

3-D Stochastic Modeling of the Sediment Texture in Unconsolidated Sediments for Prediction, Uncertainty Quantification, and Parameter Estimation

Alberto Albarrán Ordás

Vollständiger Abdruck der von der TUM School of Engineering and Design der Technischen Universität München zur Erlangung eines

Doktors der Ingenieurwissenschaften (Dr.-Ing.)

genehmigten Dissertation.

Vorsitz:

Priv.-Doz. Dr. rer. nat. habil. Arno Rein

Prüfende der Dissertation:

1. Prof. Dr. rer. nat. Florian Einsiedl
2. Prof. Florian Wellmann, Ph.D.

Die Dissertation wurde am 30.09.2024 bei der Technischen Universität München eingereicht und durch die TUM School of Engineering and Design am 04.02.2025 angenommen.

Abstract

The management of underground space and the competition for their use have become increasingly important in addressing the challenges of urbanization, land use, infrastructure, resource protection, and climate change mitigation. This is particularly pronounced in cities commonly built in unconsolidated sediments (e.g., river terraces), such as Munich (Germany), a paradigmatic example driving the thesis. Besides Munich, the research was conducted in two other geographical settings: Starnberg, located in the Bavarian Alpine foothills, and the area of Augsburg - Low Lech Valley. The geological heterogeneity of sediments is crucial for underground planning. However, the geological conditions are often unknown at the necessary level of detail, and the available subsurface data is frequently scarce and has not been optimally utilized. As a result, subsurface planning has not received adequate attention for sustainable and efficient spatial planning. However, urban areas possess a wealth of data due to extensive subsurface infrastructure development over time. The present cumulative dissertation addresses these challenges by enhancing the predictive capabilities concerning unconsolidated sediments by focusing on three key aspects: *i*) prediction of fundamental geological characteristics of these sediments in 3-D, *ii*) integration of uncertainties in input data and uncertainty quantification related to the prediction, and *iii*) ensuring the multipurpose usability of the underground space. The results were presented in four publications published in internationally recognized journals.

The construction of geological 3-D models of unconsolidated sediments rarely considers their granular composition and intergranular constituents. This leads to an oversimplification of the geological nature since the composition of such deposits can vary significantly on a local scale – e.g., mixtures of particles with different grain sizes and the presence of clay/silt infill in void spaces. The first publication of this thesis addresses this issue in Munich, aiming to predict the fundamental characteristics of these sediments in 3-D, particularly the grain-size distribution (GSD), by developing a user-defined geostatistical framework known as the D_i models method. This approach employs Sequential Stochastic Simulation to model the grain fraction for various cumulative frequencies of the hypothetical GSD. It also allows for a flexible definition of grain-size-based heterogeneities. The study highlights the possibilities of expanding the approach to conduct scenarios for applications demanding specific grain fractions, to derive grain-size-based material properties, and to carry out further analysis based on aggregations of cells for characterizing reservoir anatomical components. The geo-modeling framework was successfully applied in four other application settings: the Starnberg Road Tunnel, the U9 Subway Tunnel in Munich, the city of Augsburg, and the Low Lech Valley, all of which are located in southern Germany.

The input data used in the D_i models method are direct soil descriptions from drilled materials described in the field (drilling profiles) according to the standards for soil description. Primary data are always subject to intrinsic inaccuracies (e.g. variability of the subsurface, inherent generalizations of the standards, human errors in sampling and description). These are usually ignored in 3-D geo-modeling strategies; thus, the overall uncertainty quantification (UQ) could be underestimated. The uncertainty linked to the constructed 3-D geologic image can significantly impact the accuracy and reliability of the model outputs. Thus, it needs to be quantified to strengthen the decision-making process for practical applications. The thesis explicitly tackles these challenges in the second publication by reinterpreting the soil observations to account for potential variations due to imprecision. This is achieved by identifying all soil constituents being part of unconsolidated sediments, quantifying their proportion ranges, and finally capturing the fictive grain-size range of the sediments inferred from soil observations. This idea is adapted to the modeling framework to incorporate lithological noise. The concepts of entropy and joint entropy are applied for UQ of the main outputs of the approach. The results show a more realistic UQ and enable the reliability of different models' outputs to be compared. Moreover, valuable insights about the geostatistical implementation parameters in the approach can be inferred. The UQ measures proposed in the second publication in a domain in Munich have proved very useful in two other case study applications: identifying the most suitable regions for new drilling in the U9 Subway Tunnel and quantifying the uncertainty degree of the interconnectedness between aquifers in the city of Augsburg.

Most categorical 3-D geo-models have a fit-for-purpose design to meet the predefined specific requirements of the intended use. Schemes based on gross lithologies, lithofacies, hydrofacies, and geotechnical classes are case-specific. As such, they are built with a level of detail best suited for the stated goal but fairly underestimate the complexity of geological nature. Yet, underground space requires interdisciplinarity to face several purposes simultaneously, and this should be treated from the start of the model design. In addition, there is a need to reevaluate and use the link between grain size and properties to derive methods to identify material properties at the scale of the facies structures. Moreover, combining different lines of evidence, such as geological and numerical modeling and hydrogeochemistry, among others, benefits sustainable subsurface planning. These challenges are mainly explored in the third and fourth publications, partially also in the first published work, and the case study applications. The need to provide multiple solutions to the subsurface's interdisciplinary nature is implicitly faced by providing detailed predictions of the GSD. Specifically, multipurpose usability was explored in the following four big application fields.

a) The grain-size patterns define complex lithologic geometries and spatial relationships of geological bodies, thus constituting the architecture of reservoir bodies. The results of the first publication in Munich reveal one shallow Quaternary gravelly aquifer system interconnected with different parts of the same underlying Miocene aquifer in delimited areas. The uppermost multistory Miocene aquifer, i.e., T1, with a maximum depth of ~140 m below ground level, is

separated from three other deeper extensive aquifers, i.e., T2 to T4, by impermeable beds throughout the city. Instead, the 3-D geo-models in the Augsburg and Low Lech Valley areas show a multi-layered shallow aquifer system, which is lithologically vertically zoned and crosscut stratigraphic units. Aquifer interconnectedness may favor vertical groundwater flow, thus suggesting a higher vulnerability to anthropogenic impacts. In this regard, coupling the 3-D geo-model of Munich with hydrogeochemical data, which was addressed in the fourth publication, revealed a distinct hydrogeochemical signature for the deeper aquifer systems T2 to T4, when compared to the overlying aquifers, which qualitatively verifies the reservoir architecture. These insights constitute a significant step in providing effective regional aquifer management.

b) Estimating the fictive GSD provides predictive schemes for soil properties at high resolutions, e.g., hydraulic conductivity (K), while also averaging them within individual beds along well screens, aquifers, or aquitards. This was addressed in the third publication. Local-dependent K values are estimated using a comprehensive set of empirical formulas relating K from the grain-size range. The resulting 3-D K fields provide reliable information about the local fluctuation of K in Munich and in the Low Lech Valley case study. This motivated its use in a further application to calibrate a wide-city numerical groundwater model in Munich.

c) The approach also yields valuable parameters to assess the groundwater withdrawal and the geothermal potential for groundwater heat pumps (GWHP). In this sense, spatial hydrogeological information on groundwater thickness and K are required and are the most significant source of uncertainty in potential assessments. Whereas the aquifer thickness is derived by subtracting the aquifer basis from the groundwater surface, K ranges often come from interpolating pumping-test data. The case study conducted in Low Lech Valley poses a significant challenge for potential assessment given the lack of a continuous impermeable substratum acting as aquifer basis and the strong vertical lithological changes within the multi-layered aquifer, thus hindering the interpolation of K from pumping tests. To close these gaps, a drilling depth restriction (RDD), according to current regulatory constraints of water authorities, was implemented in 3-D to the depth of the uppermost discontinuous low-permeability bed. This aims to protect the underlying aquifers from anthropogenic alterations and enables the determination of the saturated aquifer thickness. The strong vertical lithological zonation in the aquifer was addressed by determining equivalent horizontal K values for the layered aquifer system.

d) Another emphasis for exploring model usability concerns tunnel planning, which was investigated using two case study applications based on two 3-D geo-models. These included identifying and quantifying groundwater inflows into the Starnberg Road Tunnel and optimizing a drilling campaign for the U9 Subway Tunnel in Munich.

In conclusion, the findings of this thesis yield valuable results to help planners, regulators, urban decision-makers, and cities to characterize the 3-D geology in unconsolidated sediments, which is crucial to support data-driven decision-making for sustainable management of the near-surface

underground space as a multifunctional resource. Thus, it may be concluded that the main objective of the thesis, namely the improvement of the prediction capability of the characteristics of unconsolidated sediments in 3-D with a multipurpose framework to secure sustainable underground management, has been successfully achieved.

Zusammenfassung

Angesichts der Herausforderungen von zunehmender Urbanisierung, Flächennutzung, Infrastruktur, Ressourcenschutz und des Klimawandels hat die Raumplanung des geologischen Untergrundes, auch hinsichtlich miteinander konkurrierender Untergrundnutzungen und gegenseitiger Beeinflussungen, an Bedeutung gewonnen. Dies gilt insbesondere für Städte wie München (Deutschland), welche häufig auf Lockergesteinssedimenten (z.B. Flussterrassen) errichtet wurden, welche als Modellbeispiel für diese Dissertation dient. Neben München wurden in dieser Forschungsarbeit zwei weitere Arbeitsgebiete betrachtet: Starnberg, gelegen im Bayerischen Voralpenland, und das Gebiet Augsburg - Unteres Lechtal. Die geologischen Gegebenheiten, besonders die Heterogenität der Sedimentablagerungen, sind dabei ein entscheidender Faktor für die Raumplanung des Untergrundes. Jedoch sind diese oft im erforderlichen Detailgrad unbekannt und die verfügbare Datengrundlage in der Regel begrenzt oder wird bisher nicht optimal ausgenutzt. Als Folge hat die Untergrundplanung bisher nicht die notwendige Aufmerksamkeit für eine nachhaltige und effiziente Raumplanung erhalten. Dennoch verfügen urbane Räume, aufgrund des umfangreichen Ausbaus der unterirdischen Infrastruktur, über eine Vielzahl von Daten. Die vorliegende kumulative Dissertation adressiert diese Herausforderungen durch die Verbesserung der Vorhersagefähigkeit der Heterogenität von Lockergesteinssedimenten. Der Fokus liegt hierbei auf drei wesentlichen Aspekten: *i*) die Vorhersage grundlegender geologischer Merkmale dieser Sedimente im dreidimensionalen Raum (3-D), *ii*) die Integration von Unsicherheiten in den Eingangsdaten und einer entsprechenden Unsicherheitsquantifizierung hinsichtlich der Vorhersage, sowie *iii*) der Sicherstellung einer multifunktionalen Nutzung des Untergrundes. Diese Arbeit basiert dabei auf Ergebnissen, die einem internationalen Fachpublikum in vier wissenschaftlichen Veröffentlichungen bereits zur Verfügung gestellt wurden.

Der Aufbau geologischer 3D-Modelle für Lockergesteine berücksichtigt selten die granulare Zusammensetzung und die intergranularen Bestandteile. Diese Vernachlässigung führt zu einer unzureichenden Repräsentation der tatsächlichen geologischen Beschaffenheit, da die Zusammensetzung solcher Ablagerungen lokal stark variieren kann – z.B. Mischungen von Partikeln unterschiedlicher Korngrößen, Ton-/Schluffeintrag in Zwischenräumen. Die erste Veröffentlichung dieser Dissertation befasst sich mit diesem Thema anhand eines Fallbeispiels der Stadt München und zielt darauf ab, die grundlegenden geologischen Merkmale dieser Sedimente in 3-D vorherzusagen, insbesondere die Korngrößenverteilung. Hierzu wurde ein benutzerdefinierter geostatistischer Modellierungsansatz namens D_T -Modelle-Methode entwickelt. Dieser Ansatz verwendet sequenzielle stochastische Simulationen zur Modellierung der Kornfraktionen für verschiedene kumulative Frequenzen der fiktiven

Korngrößensummenverteilungen. Die Methode ermöglicht zudem eine flexible Definition von auf Korngrößen basierten Heterogenitäten. Die Studie demonstriert die Erweiterungsmöglichkeiten des Ansatzes, um Anwendungsszenarien zu realisieren, die spezifische Kornfraktionen erfordern, um korngrößenbasierte Eigenschaften abzuleiten. Darüber hinaus können weitere Analysen auf der Grundlage von Zellaggregationen (Gruppierung von Zellen des 3D-Modells) zur Charakterisierung von Elementen des Untergrundes durchgeführt werden. Die Methode wurde erfolgreich an vier weiteren Standorten angewendet: dem Starnberger Straßentunnel, einem U-Bahntunnel (Linie U9) in München, für die Stadt Augsburg und dem Unteren Lechtal, die allesamt im Süden Deutschlands liegen.

Die Eingangsdaten der D_i -Modelle-Methode sind Bodenbeschreibungen aus Bohrmaterial (Bohrprofile), die gemäß den Standards für Bodenbeschreibung vor Ort erhoben werden. Diese Primärdaten sind jedoch inhärenten Ungenauigkeiten (z.B. Variabilität des Untergrunds, inhärente Verallgemeinerungen der Standards, menschliche Fehler bei der Probenahme und -beschreibung) unterworfen. Diese werden in 3D-Modellstrategien in der Regel ignoriert. Dies kann zur Unterschätzung der allgemeinen Unsicherheitsquantifizierung (UQ) führen. Die Unsicherheit, die sich auf die modellierte 3D-Geologie bezieht, kann die Genauigkeit und Verlässlichkeit der Modellergebnisse erheblich beeinträchtigen. Daher muss sie quantifiziert werden, um den Entscheidungsprozess für praktische Anwendungen zu verbessern. Diese Herausforderungen werden gezielt in der zweiten Publikation dieser Dissertation adressiert, indem die Bohrbeschreibungen neu interpretiert und potenzielle Variationen aufgrund von Ungenauigkeiten berücksichtigt werden. Dies wird erreicht, indem alle Bodenbestandteile der Lockergesteine, identifiziert und ihre Proportionsbereiche quantifiziert werden, um schließlich den fiktiven Korngrößenbereich der Sedimente zu erfassen. Zur Integration der lithologischen Variabilität als Hintergrundrauschen wird dieses Vorgehen entsprechend auf den Modellierungsansatz angewendet. Die Konzepte der Entropie und der Verbundentropie werden zur UQ der Ergebnisse auf den Modellierungsansatz angewendet. Die Ergebnisse zeigen eine realistische UQ und ermöglichen den Vergleich der Zuverlässigkeit der verschiedenen 3D-Modelle. Zudem können wertvolle Erkenntnisse über die geostatistischen Implementierungsparameter im Ansatz gewonnen werden. Die in der zweiten Publikation für die Fallstudie in München vorgeschlagenen Maße der UQ haben sich auch in zwei weiteren Fallstudien als äußerst wertvoll erwiesen. Sie halfen dabei, geeignete Bohrstandorte im Tunnel der U-Bahnlinie U9 zu identifizieren und den Grad der Unsicherheit hinsichtlich der Verbindung zwischen Aquiferen in der Stadt Augsburg zu quantifizieren.

Die meisten kategorisierten geologischen 3D-Modelle sind auf spezifische Zwecke zugeschnitten, um die jeweiligen Anforderungen ihrer Verwendung zu erfüllen. Die Schemata, die auf groben Lithologien, Lithofazies, Hydrofazies und geotechnischen Klassen basieren, sind fallbezogen. Sie werden mit einem Detailgrad erstellt, der für den jeweiligen Anwendungsfall zwar angemessen ist, jedoch oft die Komplexität der geologischen Gegebenheiten unterschätzt. Der geologische Untergrund erfordert jedoch einen interdisziplinären Ansatz, um mehrere Nutzungen gleichzeitig

abbilden zu können. Dies sollte bereits zu Beginn des Modellierungsprozesses berücksichtigt werden. Darüber hinaus besteht der Bedarf, das Verhältnis zwischen Korngröße und Materialeigenschaften neu zu bewerten und entsprechende Methoden zu entwickeln, die Eigenschaften von Sedimenten auf Ebene der Faziestrukturen genauer zu identifizieren. Die Kombination verschiedener Disziplinen, wie beispielsweise geologische und numerische Modellierung mit Hydrogeochemie, unterstützt die nachhaltige Planung der Untergrundnutzung. Diese Herausforderungen werden hauptsächlich in der dritten und vierten Publikation sowie teilweise in der ersten Veröffentlichung und den Fallstudien untersucht. Der Bedarf, mehrere Lösungen für die interdisziplinäre Beschaffenheit des Untergrunds bereitzustellen, wird durch detaillierte Vorhersagen der Korngrößen adressiert.

Die Mehrzwecknutzung wurde dabei in den folgenden vier Hauptanwendungsfeldern erforscht:

a) Korngrößenmuster definieren komplexe Geometrien und räumliche Beziehungen von geologischen Körpern und sind entscheidend für den Aufbau von Grundwasser-Stockwerken. Die Ergebnisse der ersten Publikation, am Beispiel von München, zeigen einen oberflächennahen quartären, kiesigen Grundwasserleiter, der in abgegrenzten Bereichen mit verschiedenen Teilen des darunter liegenden miozänen Grundwasserleiters verbunden ist. Der oberste mehrstöckige miozäne Grundwasserleiter, hier beschrieben als T1-Aquifer, mit einer maximalen Tiefe von ~140 m unter Geländeoberkante, ist von drei anderen tieferen Grundwasserleitern, T2 bis T4, durch undurchlässige Schichten im Untergrund des gesamten Stadtbereichs getrennt. Die geologische 3D-Modelle im Raum der Stadt Augsburg und im Unteren Lechtal zeigen hingegen ein mehrschichtiges oberflächennahes Grundwasserleitersystem, das aufgrund lithologischer Ausprägung vertikal unterteilt ist und stratigraphische Einheiten durchschneidet. Die Verbindung der Grundwasserleiter kann den vertikalen Grundwasserfluss begünstigen und weist somit auf eine erhöhte Anfälligkeit für die Ausbreitung anthropogener Einflüsse hin. In diesem Zusammenhang zeigte die Kopplung des geologischen 3D-Modells von München mit hydrogeochemischen Daten, wie in der vierten Publikation behandelt, eine deutliche hydrogeochemische Signatur für die tieferen Grundwasserleiter T2 bis T4 im Vergleich zu den darüber liegenden Grundwasserleitern, was die Reservoirarchitektur qualitativ bestätigt. Diese Erkenntnisse stellen einen bedeutenden Schritt zur Förderung einer effektiven regionalen Grundwasserbewirtschaftung dar.

b) Die Annahme fiktiver Korngrößenverteilungen ermöglicht die Abschätzung von Korngrößenbasierten Eigenschaften in hoher Auflösung, wie z. B. die hydraulische Durchlässigkeit (k_f -Wert), ebenso wie die Mittelung innerhalb einzelner Schichten entlang von Brunnenfiltern, Grundwasserleitern oder Grundwasserstauern. Dies wurde in der dritten Publikation abgehandelt. Lokalabhängige k_f -Werte werden unter Verwendung einer umfassenden Sammlung empirischer Formeln zur Ableitung des k_f -Werts aus dem fiktiven Korngrößenbereich geschätzt. Die resultierenden 3D- k_f -Felder liefern verlässliche Informationen über die lokalen Schwankungen des k_f -Werts im Münchner Untergrund und in der Fallstudie des Unteren Lechtals.

Dies motivierte zur Anwendung dieses Ansatzes für die Kalibrierung eines großstädtischen numerischen Grundwassermodells in München.

c) Der Ansatz liefert auch wertvolle Parameter zur Abschätzung des Potenzials zur Entnahme und thermischen Nutzung von Grundwasser. Hierbei sind räumliche hydrogeologische Informationen über die Grundwassermächtigkeit und den k_f -Wert erforderlich und stellen die wesentlichste Unsicherheitsquelle bei Potenzialabschätzungen dar. Während die Aquifermächtigkeit durch den Abstand der Aquiferbasis zur Grundwasseroberfläche abgeleitet wird, stammen die k_f -Werte oft aus der Interpolation von Pumpversuchsdaten. Die Fallstudie im Unteren Lechtal stellt eine bedeutende Herausforderung für die Potenzialabschätzung aus zwei Gründen dar. Zum einen schränkt das Fehlen einer kontinuierlichen undurchlässigen Trennschicht ihre Verwendung als Grundwasserleiterbasis ein. Zum anderen behindert die vertikal stark schwankende Lithologie innerhalb des mehrschichtigen Aquifers die Interpolation vom k_f -Wert aus Pumpversuchen. Um diese Lücken zu schließen, wurde eine maximale Bohrtiefenbegrenzung gemäß den aktuellen regulatorischen Einschränkungen der Wasserbehörden in 3-D bis zur Tiefe der obersten tiefenabhängigen undurchlässigen Schicht implementiert. Dies soll die darunter liegenden Grundwasserleiter vor anthropogenen Einflüssen schützen sowie die Bestimmung der gesättigten Grundwassermächtigkeit ermöglichen. Dabei wurde die ausgeprägte vertikale lithologische Zonierung im Aquifer durch die Bestimmung äquivalenter horizontaler k_f -Werte für das geschichtete Grundwasserleitersystem im 3D-Modell berücksichtigt.

d) Ein weiterer Schwerpunkt ist die Tunnelplanung, die durch zwei Fallstudienanwendungen basierend auf geologischen 3D-Modellen untersucht wurde: die Identifizierung und Quantifizierung von Grundwasserzuflüssen in den Starnberger Straßentunnel und die Optimierung einer Bohrkampagne für den Tunnel der U-Bahnlinie U9 in München.

Zusammenfassend liefern die Ergebnisse dieser Dissertation wertvolle Erkenntnisse, um Planungsbüros, Behörden, Träger öffentlicher Belange und kommunale Entscheidungsträger dabei zu unterstützen, die 3D-Geologie im Lockergestein zu charakterisieren. Dies ist entscheidend, um eine nachhaltige Raumplanung des oberflächennahen Untergrunds als multifunktionale Ressource zu sichern. Zusammenfassend lässt sich das Hauptziel dieser Dissertation als die erfolgreiche Verbesserung der Vorhersagefähigkeit von Merkmalen unverfestigter Sedimente in 3-D mittels eines vielseitigen Konzepts zur Sicherstellung einer nachhaltigen Untergrundbewirtschaftung beschreiben.

Declaration of authorship

Publications (ISI-listed, full research paper, peer-reviewed)

In accordance with Appendix 6, Article 6(2) of the Regulations for the Award of Doctoral Degrees at the Technical University of Munich (effective 1 January 2014), a one-page summary of each full research paper is provided below, highlighting the candidate's individual contributions to each. For concise reading, an author contribution statement is also included. For detailed information about the CRediT (Contributor Roles Taxonomy) authorship statement, please refer to doi: [10.1002/leap.1210](https://doi.org/10.1002/leap.1210).

The publications are licensed under a Creative Commons Attribution 4.0 International License, which permits use, sharing, adaptation, distribution, and reproduction in any medium or format, provided that proper credit is given to the original author(s) and source, a link to the Creative Commons license is provided, and any changes made are indicated. For detailed information on this license, please refer to <http://creativecommons.org/licenses/by/4.0/>.

The D_i models method: geological 3-D modeling of detrital systems consisting of varying grain fractions to predict the relative lithological variability for a multipurpose usability

Authors: Alberto Albarrán-Ordás & Kai Zosseder

Journal: *Bulletin of Engineering Geology and the Environment*

Dates: Received: 8 June 2021 / Accepted: 7 December 2021

doi: [10.1007/s10064-021-02538-2](https://doi.org/10.1007/s10064-021-02538-2)

CRedit authorship contribution statement: Alberto Albarrán-Ordás: Conceptualization, Methodology, Software, Validation, Formal analysis, Investigation, Writing – original draft, and Visualization; Kai Zosseder: Conceptualization, Methodology, Writing – review and Editing, and supervision.

Author Contribution: An abstract of this work is presented in Chapter 4. The publication was conducted in the framework of the GeoPot and GeoSPOT projects. I provided the main contributions of the research according to CRediT under Kai Zosseder's supervision. The conceptualization and methodology presented in this paper were suggested and conducted by myself. Kai Zosseder, as a co-conceptualizer, observed the quality of the research process in regular meetings and provided the necessary guidance. The implementation of the D_i models method using SKUA-GOCAD™ software (Emerson E&P, St. Louis, USA), formal analysis, investigation, and validation was done independently by myself. I would like to note that Kai Zosseder provided very valuable suggestions in the cross-validation procedure. As data curation is not directly visible in the publication, I want to stress the importance of this work for ensuring the transferability of the method into other geographical settings. In this sense, I developed an ArcToolbox to automate the quality control and homogenization procedures, as well as the interpretation of the borehole data provided by the Soil Information System of Bavaria (Germany). This tool was delivered to the Bavarian Environment Agency (LfU) on completion of the GeoPot project. The automation of such processes allowed the implementation of the method in various case study areas with a noticeable impact on time-saving. In addition, it leads to the identification and correction of errors detected in the database, which is exceedingly helpful in supporting the maintenance of the database. I drafted the manuscript and prepared all the figures for publication. Kai Zosseder carefully and critically oversaw the draft, which provided valuable remarks and suggestions. Last but not least, the research work presented in this paper would not have been possible without acquiring the funding to carry it out, which was an important Zosseder's contribution.

Uncertainties in 3-D stochastic geological modeling of fictive grain size distributions in detrital systems

Authors: [Alberto Albarrán-Ordás](#) & Kai Zosseder

Journal: *Applied Computing and Geosciences*

Dates: Received: 14 October 2022 / Accepted: 7 June 2023

doi: [10.1016/j.acags.2023.100127](https://doi.org/10.1016/j.acags.2023.100127)

CRedit authorship contribution statement: Alberto Albarrán-Ordás: Conceptualization, Methodology, Software, Data curation, Formal analysis, Writing – original draft, Visualization, Investigation, Validation, Writing-Reviewing, and Editing. Kai Zosseder: Conceptualization, Supervision, Funding acquisition.

Author Contribution: Similarly to the first published work, I provided the critical parts of this research. Chapter 5 gives a summary of the study. The conceptualization and methodology presented in this paper were suggested and conducted by myself. Kai Zosseder, as a co-conceptualizer, monitored the research progress in regular meetings and provided valuable guidance. I did the modeling work using SKUA-GOCAD™ software (Emerson E&P, St. Louis, USA) and independently did formal analysis, investigation, and validation. I prepared the manuscript's draft and the figures and schematic representations of the publication. Kai Zosseder contributed with dedicated suggestions, which improved the quality of the draft during the critical review of the paper. The research presented in this paper was conducted within the framework of the GeoSPOT project. Zosseder performed the funding acquisition. In this sense, I want to thank the engagement of my supervisor, Zosseder, for securing the necessary funding for conducting this research work over several years.

Estimation of 3-D hydraulic conductivity fields from fictive grain-size distributions obtained by geological 3-D modeling

Authors: Alberto Albarrán-Ordás & Kai Zosseder

Journal: *Hydrogeology Journal* (accepted for publication after scientific review)

Dates: Received: 26 February 2024 / Accepted (after scientific review): 4 September 2024

doi: -

CRedit authorship contribution statement: Alberto Albarrán-Ordás: Conceptualization, Methodology, Software, Data curation, Formal analysis, Writing – original draft, Visualization, Investigation, Validation, Writing-Reviewing and Editing. Kai Zosseder: Conceptualization, Methodology, Supervision, Funding acquisition.

Author Contribution: For a summary of this publication, please refer to Chapter 6. I provided the main contributions to this publication. According to the CRedit taxonomy, I conceptualized, implemented the methodology, and validated the study. Kai Zosseder, as a co-conceptualizer, observed the quality of the research process in regular meetings and provided the necessary guidance. In this sense, Kai Zosseder provided helpful and inspiring inputs by suggesting the inclusion of the analysis of lateral changes in the hydraulic conductivity of the aquifer in the validation procedure. I also independently performed the formal analysis, investigation, and modeling work using SKUA-GOCAD™ software (Emerson E&P, St. Louis, USA) and data curation to implement PCHIP interpolation, estimate the 3-D K fields, and prepare related diagrams. During the last phase of the work, I drafted the manuscript and prepared all the figures and tables of the publication. I also want to thank Kai Zosseder for his suggestions during the critical review of the paper and for acquiring the funding to carry out this research in the framework of the GeoSPOT project.

Interpretation of hydrogeochemistry of the Upper Freshwater Molasse (*Obere Süßwassermolasse*) in the Munich Area (Bavaria, Germany) using multivariate analysis and three-dimensional geological modelling**Authors:** Aleksandra Kiecak, Jan Huch, [Alberto Albarrán-Ordás](#), Lilian Chavez-Kus & Kai Zosseder**Journal:** *Hydrogeology Journal***Dates:** Received: 10 February 2023 / Accepted: 6 December 2023**doi:** [10.1007/s10040-023-02761-z](https://doi.org/10.1007/s10040-023-02761-z)

Author Contribution: An abstract of this work is presented in Chapter 7. I want to emphasize that Aleksandra Kiecak, the paper's main author, took the leading role in all the individual contributions following the CRediT taxonomy. As a co-author, I made various contributions to the study in the CRediT terms of conceptualization, methodology, formal analysis, investigation, visualization, and manuscript writing. At the conceptualization and methodology stages, I provided ideas and suggested steps in conducting the work about integrating the information from the geological 3-D models into the study to enhance the cluster interpretation. These ideas are based on the assignation of the aquifer systems to the wells used in the research and their further classification as "shallow" or "deep", depending on their spatial relationships and interconnectivity with the shallow Quaternary aquifer shown in the 3-D models. My formal analysis involved applying the D_i models method in a broad area located north of Munich, i.e., Model North, and synthesizing the data from both 3-D geo-models, i.e., in the city of Munich and Model North. As such, I conducted the assignment of aquifers along the well screens where samples were collected for this study, enabling the differentiation between shallow and deeper wells. This knowledge is critical to link the results of the hydrogeochemical clusters to the 3-D geo-models and to identify the well screens reaching across different groundwater systems, which were excluded from statistical analysis. Regarding the investigation, I contributed to the study by discussing the cluster interpretation enhanced by geological 3-D modeling. Therefore, first, I integrated the clusters obtained by multivariate statistical methods in the geological 3-D model. Then, I selected and generated a set of 2-D cross sections along the wells in both geological 3-D models, showing both the aquifer systems depicted from the 3-D models and the hydrogeochemical groups near the well screens, thus enhancing the interpretation of results. Herein, I prepared three figures for the manuscript. Finally, regarding the manuscript's draft, I provided texts associated with the abovementioned aspects.

Conference Proceedings

Albarrán-Ordás, A., Zosseder, K. (2019): 3D facies modelling based on particle size distributions of borehole data. A case study of georesource management in the city of Munich. 5th European Meeting on 3D Geological Modelling, 22-24 May 2019, Bern, Switzerland.

Albarrán-Ordás, A. (2022): 3D-Modellierungsansatz zur Simulation der lithologischen Heterogenität von Lockergesteinssedimenten nach ihrer Korngrößenverteilung [*A geological 3-D modeling method for simulating the lithological heterogeneity of unconsolidated soils after their grain size distribution*]. GOCAD & 3D Anwendertreffen 2022, 09.03.2022, Freiberg, Germany.

Albarrán-Ordás, A. (2022): Das 3D-Untergrundmodell von München: Entwicklung eines nutzungsbezogenen geologischen 3D-Modells für das Untergrundmanagement der Stadt [*The underground 3D model of Munich: Development of a user-related geological 3D model for the underground management*]. Geoinformationssysteme 2022, Münchner GI-Runde, Runder Tisch GIS e.V., 28.03.2022, Munich, Germany.

Albarrán-Ordás, A., Zosseder, K. (2023): 3-D stochastic geological modelling of the sediment texture in detrital systems prediction of fictive grain size distributions and uncertainty quantification. EGU 2023, 23.-28.4.2023, Vienna, Austria.

Albarrán-Ordás, A., Zosseder, K., Kiecak, A., Kerl, M., Chavez-Kus, L., Küster, S., Schmetzer, T. (2023): Optimierungsmöglichkeiten zur Festlegung der Bohrtiefenbegrenzung durch detaillierte geologische 3D-Modellierung und die Quantifizierung ihrer Auswirkungen auf die Nutzung des vorhandenen geothermischen Potenzials [*Optimization of the drilling depth limitation by detailed geological 3D modelling and quantification of its impact on the use of the existing geothermal potential*]. DGK 2023, 17.- 19.10.2023, Essen, Germany.

Acknowledgements

This dissertation feels like a journey. Every long journey begins with a spark of inspiration and thorough preparation. My journey started long before the day I enrolled in the Ph.D. program, on the day I first began working at the Chair of Hydrogeology, which years later would lead me to pursue a doctorate. As with any journey, there have been unexpected changes, surprises, enriching moments, but also some very challenging ones. In these lines, I want to remember all those who have accompanied me, in one way or another, throughout this journey.

First and foremost, I want to express my deepest gratitude to my supervisor, Dr. Kai Zosseder, and the Head of the Chair of Hydrogeology, Prof. Dr. Florian Einsiedl. Thank you for your guidance, for giving me the opportunity to work on so many projects throughout these years, and for planting the first seed of motivation in this journey. Kai, thank you so much for keeping me on the right track and for your helpful and inspiring inputs. They have guided me on the path to take and how to prepare myself for this journey. I am also sincerely grateful for your support during the difficult moments. I also want to thank my mentor Prof. Ph.D. Florian Wellmann for taking over the mentorship, being a constant source of certainty amidst uncertainties, and bringing order to the chaos of entropy at various stages of my journey.

A big thanks to my travel companions of the project teams of GEPO, GeoPot, GeoSPOT, GeoMaN, and 3D-GeoModell Berlin from the Chair of Hydrogeology. A special and heartfelt shout-out to my long-time colleagues Marco Kerl, Dr. Lilian Chavez-Kus, Dr. Aleksandra Kiecak, and Dr. Manuel Gossler, after years of working side by side. We pulled off something great together. And, of course, thanks also to Stefanie Küster, Jan Huch, Gabriella Somogyi, Patrick Kotyla, Kilian Beichel, Markus Theel, Tobias Schmetzer, and Ganesh Reddy Gajjala for the part of the journey we shared at the beginning of my stay at the Chair and during the final part of the doctorate. I don't want to forget the rest of my colleagues from the Chair of Hydrogeology throughout all these years. Thank you for your daily kindness, Dr. Arno Rein, Prof. Dr. Thomas Baumann, Christine Haas, Dr. Fabian Böttcher, Dr. Alejandra Peña, Felix Schölderle, Daniela Pfrang, Theis Winter, Dr. Florian Heine, Tamara Michaelis, Annette Dietmaier, Lilly Zacherl, Javiera Chocobar, Renate Reschetizka, Valerie Ernst, Mohamed Moursy, Mohamad Omid, Adrian Seeholzer, and all the other colleagues from TU Munich. Thanks also to Dr. Florian Konrad for rescuing me from my IT clumsiness and helping me get the modeling computer running in those early days. I want to extend a special thanks to Dr. Daniel Bohnsack for his personal and professional support over all these years and for proofreading parts of this thesis.

Thanks to the Bavarian State Ministry of the Environment and Consumer Protection (StMUV) and the Bavarian Environment Agency (LfU) for funding and supporting the GEPO, GeoPot, GeoSPOT,

and GeoMaN projects, as well as the Senate Department for Urban Mobility, Transport, Climate Action, and the Environment (SenUMVK) for funding the 3D-GeoModell Berlin project. In particular, I am grateful to Marcellus Schulze and Dr. Timo Spörlein, as contact persons from LfU, for their support and collaboration over the past few years. Thanks also to Dr. Marcus Schneider from Stadtwerke München (SWM) and the Zentrum Geotechnik at TU Munich for collaborating with us to make the 3-D geo-models for the U9 Subway Tunnel in Munich and the Starnberg Road Tunnel possible. Participating in all these projects has been a pleasure and a deeply enriching experience. I am truly grateful to have had the opportunity to apply the knowledge I developed during my Ph.D. in these projects.

Lastly, I want to express my gratitude to my loved ones for their emotional support, both from my life in Germany and my beloved León. Thank you so much for always being there, for bringing light to the darkest stretches of this journey, and for celebrating the sweetest moments with me. Last but not least, I want to thank my family for your unwavering support. I especially want to thank my parents, who have been the guiding light of my life's journey, always illuminating the way. Thank you for your kindness, your example, and your steadfast support in any circumstance.

Contents

Abstract	iii
Zusammenfassung	vii
Declaration of authorship	xi
Publications (ISI-listed, full research paper, peer-reviewed)	xi
Conference Proceedings.....	xvi
Acknowledgements	xvii
Contents	xix
List of Figures	xxiii
List of Tables	xxix
List of Abbreviations, Acronyms, and Symbols	xxx
1. Introduction	1
1.1 The role of sustainable management of the underground space	1
1.2 Understanding the heterogeneities of unconsolidated sediments	3
1.3 Motivation case study: the greater area of Munich	5
1.4 Structure of the thesis.....	10
2. Background and state of the art	11
2.1 Key terminology and fundamental geostatistical concepts	11
2.1.1 Key terminology.....	11
2.1.2 Random Variables and the Concept of the Random Function.....	12
2.1.3 Statistical inference and stationarity.....	14
2.1.4 Spatial continuity and variability.....	15
2.1.5 Local estimation and kriging paradigm	16
2.1.6 Stochastic Simulation and Sequential Stochastic Simulation	18
2.2 Principles of geological 3-D modeling	19
2.2.1 Structural modeling and the framework model.....	20
2.2.2 Property modeling and the voxel model.....	20
2.2.3 Categorization of heterogeneities in unconsolidated sediments.....	21
2.3 Uncertainties in geological 3-D modeling: classification and quantification	22
2.4 Usability of geological 3-D models: fit-for-purpose versus multipurpose	23
3. Research questions and hypothesis	25
3.1 Prediction of small-scale grain-size-based heterogeneities in 3-D	25
3.2 Uncertainty integration from input data and UQ of unconsolidated sediments	25
3.3 Ensuring multipurpose usability of the underground space.....	26
4. The D_i models method: geological 3-D modeling of detrital systems consisting of varying grain fractions to predict the relative lithological variability for a multipurpose usability	28

Abstract	28
Keywords	28
4.1 Introduction	29
4.2 Background of geological 3-D modeling and model suitability	30
4.3 Methodology	32
4.3.1 Step 1 - Conceptual model	33
4.3.2 Step 2 - Input data: lithological descriptions from borehole data	33
4.3.3 Step 3 - Spatial statistical inference	36
4.3.4 Step 4 - Spatial continuity model	37
4.3.5 Step 5 - Geostatistical simulation	37
4.3.6 Step 6 - Lithological predictability	39
4.3.7 Step 7 - Multipurpose usability	41
4.4 Application of the method in the case study in the city of Munich	43
4.4.1 Geological setting	43
4.4.2 Conceptual model and borehole database	45
4.4.3 Spatial continuity of the lithological classes	45
4.4.4 Partial percentile lithological models (D_i models)	47
4.4.5 Model Lithological Uniformity (MLU) and Most Uniform Lithological Model (MULM)	48
4.4.6 Architectural model of the Quaternary and UFM deposits	49
4.4.7 Example of application for scenario analysis: design process of a dewatering system	50
4.5 Discussion	52
4.6 Conclusions	57
4.7 Acknowledgements	58
5. Uncertainties in 3-D stochastic geological modeling of fictive grain size distributions in detrital systems	59
Graphical abstract	59
Abstract	59
Keywords	60
5.1 Introduction	60
5.2 Theory of stochastic 3-D modeling using GSD with the D_i models method	62
5.3 Material and methods	64
5.3.1 Adapted geo-modeling framework to incorporate imprecisions in soil observations	64
5.3.2 UQ measures: entropy and joint entropy	67
5.3.3 Simulation experiment	68
5.3.4 Stationarity and treatment of non-stationarities: indicator kriging algorithms	69
5.3.5 Construction and evaluation of 3-D categorical trend models	70
5.4 Results and discussion	70
5.4.1 Use of entropy for ensuring monotonically increasing GSD	70
5.4.2 Evaluation of the 3-D categorical trend models	71
5.4.3 UQ in partial percentile lithological models $D_i(u)$	73
5.4.4 UQ in the whole sediment mixture $H_{mixture}(u)$	77
5.4.5 Impact of adapting the geostatistical framework to integrate imprecise input data	77
5.5 Conclusions	80
5.6 Acknowledgements	81
6. Estimation of 3-D hydraulic conductivity fields from fictive grain-size distributions obtained by geological 3-D modeling	82
Abstract	82
Keywords	82
6.1 Introduction	83
6.2 Materials and methods	85
6.2.1 Study area and geological background	85
6.2.2 Datasets	87
6.2.3 Estimation of the fictive GSD range by log-cubic interpolation ($GSD_{predicted}$)	91

6.2.4	Estimation of 3-D K fields using empirical relationships on the fictive GSD range ($K_{\text{predicted}}$).....	93
6.2.5	Averaging K in alternating beds of heterogeneous detrital systems	94
6.3	Results and discussion.....	98
6.2.2	Estimated 3-D K fields (P10, P50, P90) in the city of Munich.....	98
6.3.2	Prediction performance in the immediate vicinity of well screens.....	101
6.3.3	Prediction performance by varying the area of influence of the wells.....	103
6.4	Conclusions.....	107
6.5	Acknowledgments	109
7.	Interpretation of hydrogeochemistry of the Upper Freshwater Molasse (<i>Obere Süßwassermolasse</i>) in the Munich area (Bavaria, Germany) using multivariate analysis and three-dimensional geological modelling	110
	Abstract	110
	Keywords.....	111
7.1	Introduction	111
7.2	Study area.....	113
7.2.1	Location, geology and hydrogeology	113
7.2.2	Geological 3D models in the greater area of Munich.....	114
7.3	Methodology	116
7.3.1	Data collection.....	116
7.3.2	Additional sampling by the Technical University of Munich (TUM)	117
7.3.3	Quality assurance and data selection scheme.....	117
7.3.4	Multivariate statistics	118
7.3.5	Classification of data from the greater area of Munich using the k -nearest neighbourhood algorithm (KNN).....	120
7.3.6	Cluster interpretation enhanced by geological 3D modelling.....	120
7.4	Results.....	121
7.4.1	Multivariate statistics for the Munich area.....	121
7.4.2	Classification of data from the greater area of Munich using the k -nearest neighbourhood algorithm (KNN)	124
7.4.3	Water isotopes.....	124
7.4.4	Cluster description	126
7.5	Discussion	133
7.5.1	Coupling the 3D geological models with hydrogeochemical data.....	134
7.5.2	Remarks on the conceptual regional hydrogeochemical model	135
7.6	Conclusions.....	136
7.7	Acknowledgements.....	137
8.	Main findings and discussion.....	138
8.1	Evaluation of transferability to other geological settings and areas of application on selected case studies	138
8.1.1	Case study: Tunnel planning of the Starnberg Road Tunnel.....	138
8.1.2	Case study: Tunnel planning of the U9 Subway Tunnel in Munich.....	142
8.1.3	Case study: Groundwater model calibration using 3-D K fields in Munich	144
8.1.4	Case study: Optimizing the reservoir architecture in the city of Augsburg.....	146
8.1.5	Case study: Estimating spatial aquifer parameters for assessing the shallow geothermal potential in a multi-layered aquifer in the Low Lech Valley	149
8.2	Discussion of main findings.....	155
8.2.1	Development of a 3-D novel approach simulating fictive grain size distributions: the D_i models method	155
8.2.2	Reinterpretation of coded soil observation data as fictive GSD	156
8.2.3	Uncertainty integration from input data using fictive GSD and UQ measures	156
8.2.4	Multiple parameter estimation and user-oriented scenario analysis based on the fictive GSD.....	157
9.	Conclusions and outlook.....	161

References	165
Appendices	186
Appendix A: Supporting information to Chapter 2	186
Appendix B: Supporting information to Chapter 4	188
Appendix C: Supporting information to Chapter 5.....	191
Appendix D: Supporting information to Chapter 6	195
Appendix E: Supporting information to Chapter 7	203
Appendix F: Supporting information to Chapter 8.....	213

List of Figures

Fig. 1:	Schematic representation of the underground space in unconsolidated sediments: Multifunctionality of the subsurface and multiplicity of scales of heterogeneity	2
Fig. 2:	Characterization of unconsolidated sediments according to grain size: a) Groups and subgroups of sediments according to grain size limits (DIN EN ISO 14688-1, 2020); b) Plot of a GSD curve and a grain-size range of two sediment mixtures	4
Fig. 3:	Illustrative figure showing the multifunctionality of the subsurface space in the city of Munich: a) Location map; b) Multiple underground functions and infrastructure in the city of Munich	6
Fig. 4:	Geological setting in the area of Munich showing different scales of geological heterogeneity: a) Simplified geological map (modified after Freudenberger and Schwerd (1996)); b) Schematic geological 2-D profile (modified after Zosseder et al. (2015)); c) Map of the Quaternary aquifer basis including terrain structures (modified after Albarrán-Ordás and Zosseder (2020)); d) Map of the drilled lithologies at the top of the underlying Miocene sediments at borehole locations drilled over time	9
Fig. 5:	Sketch illustrating key geostatistical terminology and random variables: a) Unknown real space; b) Deterministic approach; c) Probabilistic approach	12
Fig. 6:	Sketch illustrating the kriging paradigm: a) Unknown real space; b) Random variable $Z(\mathbf{u})$; c) Estimator random variable $Z^*(\mathbf{u})$ and simplified kriging system of equations	17
Fig. 7:	Overview of the multi-stage geological 3-D modeling process: a) Unknown real space; b) Structural modeling of interface geometries; c) Property modeling of lithostratigraphic classes (c1), lithofacies (c2), and gross lithologies (c3)	20
Fig. 8:	Steps 1 and 2 of the D_i models method. a) Lithological description for a drilled interval in a borehole data-base. b) Quality control (QC), data homogenization and translation of lithological descriptions into intervals of relative frequencies. c) Capturing the lower and upper cumulative distribution functions (CDF) bounds for all sediments. d) Reading and coding of lithological classes at each D_i according to conceptual model (precision of quantification and grain sizes to be modeled), modified after Albarrán-Ordás and Zosseder (2022)	34
Fig. 9:	Step 5 of the D_i models method: Estimation of the required number of geostatistical simulations for each D_i . a) Histogram and probability plot of the information entropy of the membership to a lithological class. Number of bins of histogram: 30. b) Histogram and probability plot of the information entropy of the membership to a lithological class. Number of bins of histogram: 30. c) Plot of summary statistics of the information entropy of the membership to a lithological class obtained for different number of simulations. d) Plot of sum of variation of the summary statistics obtained by increasing the number of simulations Fig. 71 provides an additional illustration of this process; modified after Albarrán-Ordás and Zosseder (2022)	39
Fig. 10:	Step 6 of the D_i models method: Lithological predictability. a) Partial percentile lithological models (D_i models). b) Location u_1 showing a low MLU value. c) Location u_2 showing a high MLU value. d) Most Uniform Lithological Model representing the distribution of lithological classes owning the highest relative frequencies in each voxel. The lithological class c is represented in different colors: $c=1$ (clay/silt) in purple, $c=2$ (sand) in orange, and $c=3$ (gravel) in yellow. Lithological descriptions according to DIN standards (DIN 4023, 2006). (S,g,tu): strongly gravelly sands with a moderate presence of silt/clay. (G,s'): slightly sandy gravels; modified after Albarrán-Ordás and Zosseder (2022)	41
Fig. 11:	Step 7 of the D_i models method: Multipurpose usability; modified after Albarrán-Ordás and Zosseder (2022)	42
Fig. 12:	Geological setting in the case study area. a) Location map. b) Simplified geological map in the Munich area showing the main lithostratigraphic units and the boundaries of the city of Munich; modified after Freudenberger and Schwerd (1996). c) Schematic geological view of the city of Munich; modified after Münichsdorfer (1922). m.a.s.l.: meters above sea level	43

- Fig. 13:** Borehole database in the case study area. **a)** Histogram showing the number of boreholes reaching a certain final depth in the city of Munich. The total number of boreholes is 20114. **b)** Location map of the area of the case study showing the location of the boreholes used and two cross sections AA' and BB', which are used to present and discuss the results 46
- Fig. 14:** Spatial continuity results of the lithological classes in the subsurface 3-D space in the city of Munich. **a)** Relation between the correlation ranges in the horizontal and vertical directions of each D_i model for each lithological class and comparison with common width/thickness (W/T) spaces of fluvial-channel bodies from Gibling (2006). The dotted lines represent different W/T ratios. **b)** Correlation ellipsoids for the lithological class "gravel" for each D_i value. **c)** Correlation ellipsoids for the lithological class "sand" for each D_i value. **d)** Correlation ellipsoids for the lithological class "silt/clay" for each D_i value 47
- Fig. 15:** 3-D views of the partial percentile lithological models (D_i models) in the city of Munich. **a)** D_{10} model. **b)** D_{50} model. **c)** D_{100} model. Modified after Albarrán-Ordás and Zosseder (2022)..... 48
- Fig. 16:** Case study in the city of Munich. **a)** 3-D view of the Model Lithological Uniformity. **b)** Cross section BB' showing the Model Lithological Uniformity. **c)** 3-D view of the Most Uniform Lithological Model. **d)** Cross section BB' showing the Most Uniform Lithological Model. **e)** 3-D view of the architectural model of the Quaternary and UFM deposits. **f)** Cross section BB' showing the architectural model, the aquifer assignation to the filter pipes and the groundwater and potentiometric surfaces (T3 almost not prominent, because it occurs mainly in the western part of Munich; m.a.s.l.: meters above sea level). Modified after Albarrán-Ordás and Zosseder (2022) 51
- Fig. 17:** Cross section AA' showing the results of the scenario analysis for the design process of dewatering systems in the Quaternary aquifer in the city of Munich. **a)** Conservative scenario representing the most demanding dewatering in view of the D_{60} model. **b)** Optimistic scenario representing the less demanding dewatering in view of the D_{40} model (m.a.s.l.: meters above sea level) 52
- Fig. 18:** Summary of results for cross validation: Bubble plot representing the fuzzy closeness of the estimated lithological classes to the true lithological classes for the D_{10} to the D_{100} models and the Most Uniform Lithological Model (MULM). Whereas the bottom right half of the bubbles represents the estimated lithological classes, the upper left half shows the collocated true lithologies. The number of locations for each true-estimate case is represented through the size of the dots. If the closeness to the true lithology was 0, the estimation was correct. These cases are represented along the dotted blue line (true=estimate). If the closeness to the true values was 1, the contiguous lithology was predicted instead of the true one. In the case that gravel was estimated instead of silt/clay, and vice versa, the closeness to the true lithology was 2 and the impact of misclassification was high. The light gray area represents the cases when the prediction underestimated the grain size of the true lithology (e.g., true=sand, estimate=clay/silt). An overestimation in the prediction occurred when the true lithology was finer than the estimated lithology (e.g., true=sand, estimate=gravel). This case is represented by a dark gray area. Modified after Albarrán-Ordás and Zosseder (2022)..... 55
- Fig. 19:** Analysis of worst-case predictions (closeness to true=2) and checking the degree of sediment mixing for correct predictions (closeness to true=0): Boxplots showing the distribution of Model Lithological Uniformity (MLU) for correct predictions and for worst cases of prediction with a high impact of misclassification. The number of locations (each location represents an interval of 10 cm) is 168,209 in the case of correct predictions and 6,178 for the worst-cases 56
- Fig. 20:** Concept of the random 3-D modeling of GSD with the D_i models method: **a)** Introduction of a series of RVs representing a grain size class for each i ; **b)** Probability distribution and assignation of a grain size class for each i 62
- Fig. 21:** Geological setting of the simulation domain. **a)** Location map. **b)** Simplified geological map in the Munich area showing the main lithostratigraphical units and the boundaries of the city of Munich. **c)** Schematic geological view of the city of Munich and the location of simulation domain (m.a.s.l.: meters above sea level). Modified from Albarrán-Ordás and Zosseder (2022)..... 65
- Fig. 22:** Exemplary soil observation used as hard data in the D_i models method: transformation of raw soil observations for their further integration in the geo-modeling framework..... 65
- Fig. 23:** Modifications in the initial concept scheme of the random 3-D modeling of GSD with the D_i models method to incorporate uncertainties from imprecise input data into the geo-modeling process: **a)** Introduction of a series of RVs representing a grain size class for each i ; **b)** Probability distribution and assignation of a grain size class for each i 66

- Fig. 24:** Domain setting and input data for simulation experiment: **a)** Full 3-D domain and subdomains Q and T showing borehole logs; **b)** 2-D example profile used throughout the study 69
- Fig. 25:** Exemplary application of the entropy-based correction for ensuring monotonically increasing GSD: **a)** Unsamplered location without correction; **b)** Unsamplered location with correction..... 71
- Fig. 26:** Fence diagrams showing the results of the 3-D trend construction for $D_{80,MIN}$ in: **a)** Simulation setup 3; **b)** Simulation setup 4; **c)** Simulation setup 5..... 72
- Fig. 27:** Results of the 3-D trend evaluation: **a)** Ratio of the variance provided deterministically by the trends and the final variance (should be no greater than 0.5); **b)** Closeness of the trend proportions to the true grain size classes from the soil observations..... 73
- Fig. 28:** Results of UQ in the partial lithological models of Simulation setup 1..... 75
- Fig. 29:** Results of UQ in the partial lithological models of Simulation setup 2..... 76
- Fig. 30:** Results of UQ in the whole sediment mixture for Simulation setups 1 to 5..... 78
- Fig. 31:** Results of UQ in the whole sediment mixture for Simulation setups 5, 6 and 7 79
- Fig. 32:** Uncertainty propagation: **a)** MULM(**u**) after Setup 5; **b)** (**upper panel**) Difference of uncertainty in the whole sediment mixture between Setups 5 and 6; **b)** (**lower panel**) Boxplot showing the distribution of the difference of uncertainty between Setups 5 and 6; **c)** (**upper panel**) Difference of uncertainty between Setups 5 and 7; **c)** (**lower panel**) Boxplot showing the distribution of the difference of uncertainty between Setups 5 and 7..... 80
- Fig. 33:** Study area of the city of Munich. **a)** Location map and simplified geological map; **b)** (left) Geological 3-D model of Munich: 3-D spatial distribution of the most dominant grain size classes in the sediment mixture with partly transparent ground surface; (center) 2-D profile AA' showing the most dominant lithologies; (right) 2-D profile AA' showing the aquifer subdivision 86
- Fig. 34:** Exemplary estimation of the fictive GSD range from the results of the D_i models method at unsampled location **u**. **a)** Results from simulation: (upper part) cross section showing the distribution of the most dominant grain size classes, (lower part) grain size classes for each cumulative percentage at location **u**. **b)** Points representing the simulated grain fractions provided by the D_i models method at location **u**. **c)** Resulting interpolated fictive GSD range at location **u** by log-cubic interpolation (PCHIP) as described in Section 6.2.3..... 88
- Fig. 35:** Location map of the testing datasets used in the study, i.e., GSD curves of soil samples ($GSD_{measured}$), and hydraulic conductivity values from pumping-test analysis (K_{pump}). Number of GSD data: 270. Number of K_{pump} data: 364, of which 306 data correspond to wells with known screen positions, and 58 data came from wells with assumed screen positions..... 89
- Fig. 36:** Available dataset from pumping-test analysis. The plot shows the spread of the K_{pump} values obtained from applying multiple pumping-test evaluation methods from one pumping-test report at every single well in the Quaternary and Miocene aquifers in the city of Munich. **a)** By lithostratigraphic unit; **b)** By deviations expressed as orders of magnitude (powers of ten). Total number of K_{pump} values: 364 (240 in the Quaternary, 124 in the Miocene)..... 90
- Fig. 37:** Boxplot showing the distribution of the deviations between the log-cubic interpolated fictive GSD with the PCHIP interpolant and the measured GSD obtained from sieving in the geological 3-D model of Munich. Total number of data: 270 sieving curves obtained from 191 wells. IQR: Interquartile range. GSD: Grain-size distribution. d : grain size in mm..... 92
- Fig. 38:** Scheme of the datasets used and the main steps involved in the study. **a)** Datasets; **b)** Estimation of the fictive GSD; **c)** Estimation of 3-D hydraulic conductivity field using multiple empirical methods (Averaging K in alternating beds, i.e., Section 6.2.5, not in figure) 94
- Fig. 39:** Visualization of the averaging process of the local-dependent hydraulic conductivities using an exemplary 2-D profile. **a)** Distribution of the most dominant lithologies; **b)** Distribution of the average estimate of K ($K_{predicted,P50}$); **b1)** K in individual beds; **b2)** Averaging K in alternating beds in the near vicinity of the well; **b3)** Averaging K in alternating beds, when varying the cone of depression 96
- Fig. 40:** Generalized scheme for estimating the predictive ability by comparing K_{pump} values from pumping-test analysis to the predicted range 97
- Fig. 41:** Estimated 3-D hydraulic conductivity fields in the city of Munich represented by the 3-D spatial distribution (left panels, with partly transparent ground surface), an example south-north 2-D profile AA' (center panels),

and the probability distribution functions (PDF) of the logarithmically (base 10) transformed hydraulic conductivities (right panels). **a)** Conservative (P10, 10th percentile); **b)** Average (P50, 50th percentile); **c)** Optimistic (P90, 90th percentile). Applying empirical methods leads to obtaining P10, P50, and P90 K -values at each voxel. The PDF represents the distribution of the K -values in the entire aquifer system 99

- Fig. 42:** Prediction performance in the immediate vicinity of the well screens in the city of Munich. **a)** (left) Cross-checking of model's predictions (K_{xeq}) with observed K values (K_{pump}) from various locations and depths; (right) CDF of the deviations; **b)** (left) Prediction performance versus the quality class of measured K_{pump} values; (right) Boxplot showing the distribution of the deviations for each quality class; **c)** (left) Prediction performance versus the number of screened intervals per well; (right) Boxplot showing the distribution of the deviations for each number of screened interval; **d)** (left) Prediction performance versus the estimated mean value of the coefficient of uniformity; (right) Boxplots showing the distribution of the coefficient of uniformity for each deviation degree 102
- Fig. 43:** Prediction performance by varying the well's radius of influence in the city of Munich. **a)** (left) Cross-checking of model's predictions (K_{xeq}) reaching extents up to 150 m with observed K values (K_{pump}); (right) CDF of the deviations with 150 m; **b)** (left) Cross-checking of model's predictions (K_{xeq}) reaching extents up to 250 m with observed K values (K_{pump}); (right) CDF of the deviations with 250 m; **c)** (left) Cross-checking of model's predictions (K_{xeq}) reaching extents up to 350 m with observed K values (K_{pump}); (right) CDF of the deviations with 350 m; **d)** (left) Cross-checking of model's predictions (K_{xeq}) reaching extents up to 450 m with observed K values (K_{pump}); (right) CDF of the deviations with 450 m; **e)** (left) Cross-checking of model's predictions (K_{xeq}) reaching extents up to 550 m with observed K values (K_{pump}); (right) CDF of the deviations with 550 m 104
- Fig. 44:** Graph representing the performance variation with increasing radius of influence, separately in Q and T. **a)** Quaternary (Q); **b)** Miocene (T) (R^2 =Coefficient of determination, PRS=Prediction rate of success, MAE=Mean average error, RD1=Rate of deviations with at least one order of magnitude). Higher values of R^2 and RPS and smaller values of MAE and RD1 signify a better agreement and are associated with green tones 105
- Fig. 45:** Location of the study area in the context of geology of southern Bavaria (cross sections A-A' and B-B' are presented in Fig. 56 and Fig. 57, respectively) 114
- Fig. 46:** Geological 3D model of the City of Munich with the subdivided aquifer systems Q and T1-T4. **a)** 3D fence diagram showing aquifer subdivision through the transparent ground surface; **b)** Subdivision scheme; **c)** Detailed view of the assignation of aquifer systems to screened wells. Modified from Albarrán-Ordás and Zosseder (2019); Zosseder et al. (2019) 115
- Fig. 47:** Methodology flow chart 116
- Fig. 48:** Locations of the groundwater sampling points in the study area 118
- Fig. 49:** Correlation matrix of 13 physico-chemical parameters 122
- Fig. 50:** Plots of: **a)** factor loadings and **b)** factor scores, for the first two factors (ML1 and ML2) obtained in the exploratory factor analysis (EFA) identified by clusters derived from hierarchical cluster analysis (HCA) (see Fig. 51 and cluster description in text) 123
- Fig. 51:** Dendrogram and pie charts for median values in the resulting clusters (size of the pie chart depends on the degree of mineralisation) 124
- Fig. 52:** Plots of $\delta^2\text{H}$ versus $\delta^{18}\text{O}$: **a)** for hydrological units, **b)** for clusters (colours indicate the clusters, for details see Fig. 51 and cluster description in text; some wells are represented by more than one data point. Notation: dashed line – GMWL, dotted line – LMWL for Germany (Stumpp et al., 2014); the ellipses are normal confidence ellipses calculated for each cluster; the black square represents precipitation after IAEA/WMO (2020) – long term mean of precipitation measured in Neuherberg near Munich; NA – Tritium not analysed 125
- Fig. 53:** The locations of wells assigned to clusters in the study area (colours indicate the clusters, for details see Fig. 51 and cluster description in text) 127
- Fig. 54:** Piper plot presenting clusters in the study area (colours indicate the clusters, for details see Fig. 51 and cluster description in text) 127
- Fig. 55:** Bi-variate plots. Notation: dashed line is 1:1 line, when not described differently; colours indicate the clusters, for details see Fig. 51 and cluster description in text 128
- Fig. 56:** Cluster interpretation for the city of Munich enhanced by geological 3D modelling: **a)** 3D view of the hydrogeological units considered in the present study adapted from the 3D architectural model of Albarrán-

	Ordás and Zosseder (2022); b) Cross section AA' showing the hydrogeological units and the cluster assignation by various examples of well screens	129
Fig. 57:	Cluster interpretation in the northern part of the study area enhanced by geological 3D modelling: a) 3D view of the prevailing lithological classes (gravel, sand and clay/silt); b) Cross section BB' showing the interpreted hydrogeological units and the cluster assignation by various examples of well screens	130
Fig. 58:	Geological setting in the Starnberg Road Tunnel: a) Location map; b) Planned tunnel course and borehole data used for geological 3-D modeling; c) Schematic 2-D geological profile	139
Fig. 59:	Geological 3-D model in the Starnberg Road Tunnel: 3-D distribution (left panel) and 2-D profile (right panel) representing the less and most demanding dewatering scenarios: a) Lithologies at the less demanding dewatering case; b) Aquifer geometries at the less demanding dewatering case; c) Lithologies at the most demanding dewatering case; d) Aquifer geometries at the most demanding dewatering case	140
Fig. 60:	Analysis of groundwater inflows in aquifer tier 2 into the Starnberg Road Tunnel based on the 3-D geo-model: a) Position of the transect divided into eight segments; b) Identification of inflow zones along the transect delimited on the top by the groundwater table and at the bottom by the confining layer	141
Fig. 61:	Setting in the U9 Subway Tunnel in Munich: a) Location map; b) Planned tunnel course and borehole data used for geological 3-D modeling; c) Schematic 2-D profile of section 1 of tunnel's course	142
Fig. 62:	Geological 3-D model in the U9 Subway Tunnel: 3-D distribution (left panel) and 2-D profile (right panel): a) Most dominant grain size classes; b) Reservoir architecture; c) Uncertainty quantification	143
Fig. 63:	Deriving fluctuations of K from the 3-D geo-model for groundwater model calibration: a) Results from simulation after applying the D_i models method and stratigraphic units shown at top view and in a 2-D profile; b) Fictive GSD range and 3-D K field at every location; c) 2-D K fields for assigning a preferred value and the variation range of K at the location of each pilot point	145
Fig. 64:	Geological setting in the city of Augsburg and the Low Lech Valley: a) Location map; b) Simplified geological map and domains for 3-D models; c) Schematic geological profile (modified after HydroConsult GmbH, 2016)	146
Fig. 65:	Geological 3-D model in the city of Augsburg: Most dominant grain size classes (left panel) and uncertainty model (right panel): a) 3-D spatial distribution; b) 2-D profile AA'; c) 2-D profile BB'	148
Fig. 66:	Geological 3-D model in the city of Augsburg. Most dominant grain size classes (left panel), including UQ (center panel), and reservoir architecture including UQ in the Miocene sequences (right panel): a) 3-D spatial distribution; b) 2-D profile AA'; c) 2-D profile BB'	150
Fig. 67:	Geological 3-D model in the Low Lech Valley. Most dominant grain size classes (left panel), reservoir architecture (middle left panel), RDD (middle right panel), and saturated thickness of groundwater in uppermost aquifer (right panel): a) 3-D spatial distribution; b) 2-D profile AA'; c) 2-D profile BB'	153
Fig. 68:	Estimated 3-D hydraulic conductivity fields in the Low Lech Valley: conservative estimate (P10, 10 th percentile) (left panel), average estimate (P50, 50 th percentile) (center panel), and optimistic estimate (P90, 90 th percentile) (right panel): a) 3-D spatial distribution; b) 2-D profile AA'; c) 2-D profile BB'	154
Fig. 69:	Map of the distribution of most dominant grain size classes at the top of the Miocene sediments from the geological 3-D model in the city of Munich	158
Fig. 70:	3-D views of the Miocene sediments from the geological 3-D model in the city of Munich: a) Most dominant grain size classes; b) Reservoir architecture, showing at its uppermost part the Miocene aquifers interacting with the overlying Quaternary	159
Fig. 71:	Illustration showing the process of quantifying the summary statistics of the information entropy of the membership to a lithological class for two simulation sets consisted of 10 and 30 simulations. The procedure is the same for the remaining sets of 20, 40, 50, 60, 70, 80, 90, etc. simulations, respectively. The minimal number of simulations required was obtained when the summary statistics converged to a constant value so that an increase in the number of realizations did not lead to a significant change in the lithological attribution in the whole model. Modified after Albarrán-Ordás and Zosseder (2022)	188
Fig. 72:	Schematic graph showing the architectural model of the Quaternary and UFM deposits in the case study in the city of Munich. UFM: Upper Freshwater Molasse. The red dots represent the different areas of preferential connectivity between aquifer tiers	189

Fig. 73: Exemplary application of the UQ measures in three soil observations from drilled material.....	191
Fig. 74: Results of UQ in the partial lithological models of Simulation setup 3	192
Fig. 75: Results of UQ in the partial lithological models of Simulation setup 4	193
Fig. 76: Results of UQ in the partial lithological models of Simulation setup 5	194
Fig. 77: Concept of the random 3-D modeling of GSD with the D_i models method: Introduction of a series of RVs representing a grain size class for each i . Modified after Albarrán-Ordás and Zosseder (2023).....	195
Fig. 78: Exemplary soil observation used as hard data in the D_i models method: transformation of raw soil observations for their further integration in the geo-modeling framework Modified after Albarrán-Ordás and Zosseder (2023)	196
Fig. 79: Step 7 of the D_i models method: Multipurpose usability. Modified after Albarrán-Ordás and Zosseder (2022)	197
Fig. 80: Averaging of hydraulic conductivity K in alternating beds in the immediate vicinity of the wells	201
Fig. 81: Prediction performance in the immediate vicinity of the well screens in the city of Munich: Relationship between predicted K_{req} and measured K_{pump} versus the proportion of each grain size class in the screened aquifer portion.....	202
Fig. 82: Location of all available data points. The colour scale indicates the number of single chemical analyses performed at a particular well or piezometer	203
Fig. 83: Location of data points associated with samples taken during three sampling campaigns in 2017–2019	203
Fig. 84: Factor loadings obtained in EFA	204
Fig. 85: Factor loadings for the exploratory factor analysis (EFA) with the maximum likelihood method and oblique (oblimin) rotation	204
Fig. 86: The location of wells assigned to clusters in the City of Munich area. Numbers 1-8 indicate clusters, number 9 indicates outliers, excluded from HCA.....	205
Fig. 87: Piper plot presenting clusters in the city area. Numbers 1-8 indicate clusters, number 9 indicates outliers, excluded from HCA.....	205
Fig. 88: Box plots for clusters associated with the whole study area	206
Fig. 89: $\delta^2\text{H}$ versus $\delta^{18}\text{O}$ for each hydrogeological unit. Tritium content is presented as follows: filled symbols (Y) – tritium is present in the water sample, empty symbol (N) – no tritium present, + (N.A.) – no tritium-data available. The colours indicate the hydrogeological unit (see Fig. 52a in the paper)	207
Fig. 90: Selected box plots.....	209
Fig. 91: Piper diagram of groundwater samples (the ellipses for each group are drawn approximately)	210
Fig. 92: Stiff diagrams.....	212
Fig. 93: Mapped results from the geological 3-D model in the Lower Lech Valley: a) Maximal allowed drilling depth (RDD); b) Saturated thickness of groundwater in uppermost aquifer up to the RDD; c) Thickness of fine-grained intercalations in uppermost aquifer up to RDD	213
Fig. 94: Calculated equivalent horizontal hydraulic conductivity in uppermost aquifer up to the RDD from the geological 3-D model in the Lower Lech Valley: a) conservative estimate (P10, 10th percentile); b) average estimate (P50, 50th percentile); c) optimistic estimate (P90, 90th percentile).....	214

List of Tables

Tab. 1: Overview of the simulation setups (SK: Simple Kriging; LVM: Local Varying Means; BK: Block Kriging; MWA: Moving Window Averaging; Q: Quaternary sub-domain; T: Miocene (Tertiary) sub-domain; GP: Global Proportions).....	68
Tab. 2: Results of statistical inference in the entire domain and in the sub-domains Q and T (<i>PDi</i> : constant global proportions for each grain fraction <i>c</i> in each domain; <i>HDi</i> <i>global</i> : entropy of the probability distribution from the constant global proportions, unit in nat; the color scale is the same as in Fig. 28 and Fig. 29, where higher and lower entropy values from global proportions are associated with red and blue tones, respectively).....	74
Tab. 3: Performance assessment after varying the radius of influence of the wells (R^2 =Coefficient of determination, <i>MAE</i> =Mean average error, <i>PRS</i> =Prediction rate of success, <i>RD1</i> = Rate of deviations with at least one order of magnitude, Q=Quaternary, T=Tertiary, Miocene. The most favorable values are indicated in bold)	105
Tab. 4: Loadings of the factor matrix (<i>italic</i> : loadings > 0.5)	123
Tab. 5: The number of objects in each cluster and hydrogeological units in the entire study area.....	126
Tab. 6: Overview of the stochastic simulation methods with their main features.....	186
Tab. 7: Literature review of the criteria used for defining the discrete values of a categorical variable when modeling unconsolidated sediments.	186
Tab. 8: Considerations of geological uncertainties according to different authors	187
Tab. 9: Overview of the aquifer systems and tiers from the architectural model of the Quaternary and UFM deposits in the case study in the city of Munich. m.a.s.l.: meters above sea level; UFM: Upper Freshwater Molasse; P10: 10 th percentile; P50: 50 th percentile; P90: 90 th percentile, M: arithmetic mean; SD: Standard deviation; min: minimum value; max: maximum value.....	190
Tab. 10: Selected empirical relationships relating hydraulic conductivity <i>K</i> and the size property of porous media used in the article.....	198
Tab. 11: Relationship between clusters and groundwater horizons from the 3D lithofacies model of the City of Munich	208
Tab. 12: Table of descriptive statistics of selected parameters (23 out of 64) calculated for Quaternary groundwater samples.....	209

List of Abbreviations, Acronyms, and Symbols

Symbol, acronym or abbreviation	Definition
A	3-D domain
BIM	Building Information Modeling
BIS	Bodeninformationssystem Bayern (in English: Soil Information System of Bavaria, Germany)
BK	Block Kriging
BTES	Borehole thermal energy storage
c	Grain size class/ lithological class
C	Number of grain size classes/ Number of lithological classes
C_c	Correlation coefficient
CCDF	Conditional Cumulative Distribution Function
CDF	Cumulative Distribution Function
C_{D_i}	Closeness of P_{D_i} to the true grain size classes from soil observation
CRediT	Contributor Roles Taxonomy
C_u	Coefficient of uniformity
d	Grain size (mm)
D	Grain size class linked to a particle diameter
DH	District heating
D_i	Grain size class linked to a particle diameter and corresponding to each cumulative frequency i
DIN	Deutsches Institut für Normung e.V. (in English: German Institute for Standardization)
DO	Dissolved Oxygen
EC	Electrical conductivity
EFA	Exploratory factor analysis
EU	European Union
FAO	Food and Agriculture Organization of the United Nations
$F(d)$	Interpolating polynomial function determining the cumulative percentage corresponding to a grain size d
GeoMaN	Acronym for research project (2024-2027) entitled "Determination of basic data and concepts for geological subsurface management in the Nuremberg area" (in German: Schaffung von Grundlagendaten und Konzepten für das <u>Geologische Untergrund-Management im Raum Nürnberg</u>)
GeoPot	Acronym for research project developed in 2016-2019 and entitled "Parameter determination for the estimation of geological utilization potentials in planning region 14 and in the Tertiary subsurface of the Greater Munich area" (in German: Parameterbestimmung für die Abschätzung der <u>geologischen Nutzungspotenziale</u> in der Planungsregion 14 und im tertiären Untergrund des Großraums München)
GeoSPOT	Acronym for research project developed in 2020-2023 and entitled "Geological utilization and storage potentials in the Quaternary and Tertiary subsurface of the Greater Augsburg area" (in German: <u>Geologische Nutzungs- und Speicherungspotenziale</u> im quartären und tertiären Untergrund des Großraums Augsburg)
GEPO	Acronym for research project developed in 2012-2015 and entitled "Development of a database for the estimation of the geothermal potential in the near-surface subsurface of the Quaternary groundwater aquifer of the Greater Munich area" (in German: Erstellung einer Datengrundlage für die Abschätzung des <u>geothermischen Potenzials</u> im oberflächennahen Untergrund des quartären Grundwasserleiters des Großraum Münchens)
GHG	Greenhouse gas
GMWL	Global Meteoric Water Line
GP	Global Proportion
GSD	Grain Size Distribution
GSHP	Ground source heat pump
GWHP	Groundwater heat pump
h	Separation vector between pairs of points
HCA	Hierarchical cluster analysis
HCG	High Conductive Gravels
H_{D_i}	Entropy of the discrete probability distribution of p_{D_i} (nat)
$H_{mixture}$	Joint entropy linked to the whole sediment mixture (nat)
i	Cumulative frequency value in the GSD
i_{D_i}	Realization of I_{D_i}
$i_{D_i,MIN}$	Finest-grained realization of I_{D_i}
$i_{D_i,MAX}$	Coarsest-grained realization of I_{D_i}

$i_{D_i}^*$	Set of realizations of I_{D_i}
$i_{D_i,MIN}^*$	Set of finest-grained realizations of I_{D_i}
$i_{D_i,MAX}^*$	Set of coarsest-grained realizations of I_{D_i}
I_{D_i}	Indicator random variable from Z_{D_i}
$I_{D_i}^*$	Estimator of I_{D_i}
IEA	International Energy Agency
IK	Indicator Kriging
IQR	Interquartile Range
ISO	International Organization for Standardization
j	Interval index used for denoting the interpolating segments when applying multiple PCHIP (Chapter 5)
K	Hydraulic conductivity (m/s)
KC	Kozeny-Carman
KMO	Kaiser-Meyer-Olkin
KNN	K-nearest neighbourhood algorithm
$K_{\text{predicted}}$	Predicted local-dependent hydraulic conductivity (m/s)
$K_{\text{predicted},P10}$	Conservative predicted local-dependent hydraulic conductivity (10 th percentile, P10) (m/s)
$K_{\text{predicted},P50}$	Average predicted local-dependent hydraulic conductivity (50 th percentile, P50) (m/s)
$K_{\text{predicted},P90}$	Optimistic predicted local-dependent hydraulic conductivity (90 th percentile, P90) (m/s)
$K_{\text{predicted},v}$	Predicted local-dependent hydraulic conductivity in each voxel (m/s)
$K_{\text{predicted},v,\text{aquifer}}$	Predicted local-dependent hydraulic conductivity in each voxel within the aquifer (m/s)
K_{pump}	Hydraulic conductivity value obtained from pumping-test analysis (m/s)
KT	Kriging with an external drift
K_{xeq}	Estimated equivalent horizontal hydraulic conductivity in each well along the well screens (m/s)
$K_{\text{xeq},\text{aquifer}}$	Estimated equivalent horizontal hydraulic conductivity vertically within an aquifer (m/s)
L	Number of realizations of a Random Variable
LfU	Bayerisches Landesamt für Umwelt (in English: Bavarian Environment Agency)
LMWL	Local Meteoric Water Line
LVM	Local Varying Means
MAE	Mean Absolute Error
MAR	Managed aquifer recharge
m.a.s.l.	meters above sea level (m)
MGP	Munich Gravel Plain
ML	Maximum likelihood
MLU	Model Lithological Uniformity
m_{aquifer}	Saturated aquifer thickness (m)
m_{min}	Minimum relative frequency value related to every linguistic code in a soil observation (%)
m_{max}	Maximum relative frequency value related to every linguistic code in a soil observation (%)
m_{true}	True relative frequency value related to every linguistic code in a soil observation (%)
m_{screen}	Sum of the well screen lengths for each well (m)
m_v	Thickness of each voxel (m)
$m_{v,\text{aquifer}}$	Thickness of each voxel with permeable material vertically within the aquifer (m)
MULM	Most Uniform Lithological Model
M	Arithmetic mean
MPS	Multiple-Point Statistics
MSA	Measure of Sampling Adequacy
MWA	Moving Window Averaging
n	Number of nearby local data
N	Total number of cumulative frequency values in the GSD
NAVFAC	Naval Facilities Engineering Command
NGS	National Geological Survey
N_{pump}	Number of hydraulic conductivity values available from pumping-test analysis
n_v	Number of voxels in the model domain when estimating the required number of simulations for each D_i
N_v	Number of voxels for each well screen
$N_{v,\text{aquifer}}$	Number of voxels vertically within the aquifer
OK	Ordinary Kriging
OMM	Obere Meeresmolasse (in English: Upper Marine Molasse)
OSM	Obere Süßwassermolasse (in English: Upper Freshwater Molasse)
p	Constant percentile step divisor of 100 in the GSD
PBA	Probability Bounds Analysis
PCHIP	Piecewise Cubic Hermite Interpolating Polynomials
PDF	Probability Distribution Function
P_{D_i}	Prior probability model for D_i (parts per unit)
p_{D_i}	Probability model for D_i from the local average of all realizations (parts per unit)

Q	Quaternary
QC	Quality Control
R	Correlation coefficient
R^2	Coefficient of determination
RDD	Restriction of the drilling depth (in German: Bohrtiefenbegrenzung)
RF	Random Function
ROS	Regression on order statistics
RPS	Rate of successful predictions
RP1	Rate of deviations of at least one order of magnitude, thus representing a rate of worst cases
RV	Random Variable
SD	Standard Deviation
SDG	Sustainable Development Goal
SE	Standard Error of the Mean
SGS	Sequential Gaussian Simulation
SIS	Sequential Indicator Simulation
SK	Simple Kriging
StMUV	Bayerisches Staatsministerium für Umwelt und Verbraucherschutz (in English: Bavarian State Ministry of the Environment and Consumer Protection)
SWM	Stadtwerke München
t	Index for each hydraulic conductivity value available from pumping-test analysis (Chapter 6)
T	Miocene (Tertiary)
T1	First Tertiary aquifer system from the Earth's surface
T1A	T1: First Tertiary aquifer system from the Earth's surface. A: Highest aquifer tier located in T1
T1B	T1: First Tertiary aquifer system from the Earth's surface. B: Second highest aquifer tier located in T1
T1C	T1: First Tertiary aquifer system from the Earth's surface. C: Third highest aquifer tier located in T1
T1D	T1: First Tertiary aquifer system from the Earth's surface. D: Fourth highest aquifer tier located in T1
T2	Second Tertiary aquifer system from the Earth's surface
T3	Third Tertiary aquifer system from the Earth's surface
T4	Fourth Tertiary aquifer system from the Earth's surface
TX	Not classified Tertiary aquifer
TGS	Truncated Gaussian Simulation
TUM	Technical University of Munich
\mathbf{u}	Vector of location being estimated
\mathbf{u}_α	Vector of location with known data
UFM	Upper Freshwater Molasse (in German: Obere Süßwassermolasse)
UK	United Kingdom
UNESCO	United Nations Educational, Scientific and Cultural Organization
UQ	Uncertainty Quantification
USBR	United States Bureau of Reclamation
UTES	Underground thermal energy storage
UUS	Urban Underground Space
v	Each individual voxel considered in the calculation of K_{xeq} and $K_{\text{xeq,aquifer}}$
VPC	Vertical proportion curve
W/T	Width-thickness ratio of fluvial-channel bodies
x	Horizontal direction
z_{D_i}	Realization of Z_{D_i}
Z_{D_i}	Random Variable of D_i
$z_{D_i,\text{MIN}}$	Finest-grained realization of Z_{D_i}
$z_{D_i,\text{MAX}}$	Coarsest-grained realization of Z_{D_i}
$z_{D_i}^*$	Set of realizations of Z_{D_i}
$z_{D_i,\text{LMIN}}^*$	Set of finest-grained realizations of Z_{D_i}
$z_{D_i,\text{LMAX}}^*$	Set of coarsest-grained realizations of Z_{D_i}
γ_{D_i}	Indicator variogram
$\sigma_{P_{D_i}}^2$	Variance provided by the trend model
σ_Z^2	Final variance of Z_{D_i}

Note 1: abbreviations c (grain size class) and C (number of grain size classes)

The original texts of Albarrán-Ordás and Zosseder (2023, 2022) adopted the abbreviations k and K for denoting the grain size class and the number of grain size classes, respectively. In order to

avoid confusion when referring to K as the hydraulic conductivity, the notations k , and K are replaced by the notations c and C in all instances in Chapters 4 and 5 of the thesis.

Note 2: abbreviations for applied geostatistics

The original texts of Albarrán-Ordás and Zosseder (2024, 2023), included in Chapters 5 and 6, adopted the practices in citation in applied geostatistics according to Deutsch (2021). However, the original text of Albarrán-Ordás and Zosseder (2022), did not adopt such practices. In order to unify notations with regard to Chapters 5 and 6, the following notations are replaced in all instances in Chapter 4 compared to the original text of Albarrán-Ordás and Zosseder (2022):

$P_{D_i}(\mathbf{u}; c)$ is used instead of $p(u; k)$

$I_{D_i}(\mathbf{u}; c)$ is used instead of $i(u; k)$

\mathbf{u} is used instead of u

$MLU(\mathbf{u})$ is used instead of $MLU(u; k)$

$H(\mathbf{u}; c)$ is used instead of $h(u; k)$

$p(\mathbf{u}; c)$ is used instead of $p_k(u)$

Note 3: use of language in Chapter 7

Unlike the publications Albarrán-Ordás and Zosseder (2024, 2023, 2022), included in Chapters 4, 5, and 6, which were written in American English, the text of Kiecak et al. (2023), included in Chapter 7, was written in British English. Although the present dissertation is written in American English, Chapter 7 is written in British English to respect the original language usage of the manuscript.

Note 4: textual modifications in Chapter 7

The following instances of the original text from Kiecak et al. (2023) have been adapted:

- “age of groundwater” has been replaced with “apparent groundwater age” (page 124).
- The value -63.9 ‰ has been adjusted to -63.9‰ (page 126).
- The unit mval has been replaced with mmol (Fig. 55).
- The text >50 mg/L has been modified to 50 mg/L (page 132).

CHAPTER 1**Introduction**

The emphasis of this chapter is on providing an overview of the problem motivating the research subject of this thesis. To address the challenges of combating climate change, ensuring resource protection, and facilitating population growth needs, i.e., land, housing, essential services, and infrastructure, the city's development, particularly the underground subsurface, plays a crucial role. Since most cities are built in unconsolidated sediments, the local-scale geological heterogeneities of these deposits are of prime concern for the suitability and sustainability of the wide range of competing and coexistent underground uses, which ultimately secures sustainable management of the subsurface. These circumstances are reflected in the area of Munich (Germany), which motivated the choice of this setting as a case study in this thesis. The last part of the chapter provides a dissertation outline.

1.1 The role of sustainable management of the underground space

Today, over half of the world's population lives in cities, which is expected to increase to almost 70 percent by 2050 (Mukim and Roberts, 2023). This situation causes more than 70 percent of energy consumption and ~70 percent of anthropogenic greenhouse gas (GHG) emissions from urban areas (Bricker et al., 2024), thus representing a significant cause of climate change. The role of cities, especially city development, is crucial to mitigate the effects of climate change.

In response to the challenges posed by the climate crisis, underground space is recognized as holding a wide range of uses that can strongly contribute to the transition to cleaner energy and carbon neutrality (Kahnt et al., 2015; UNESCO, 2022). The term *underground space*, and, more specifically, the term *Urban Underground Space* (UUS), has been defined as the physical space located underground, considering the material itself and the water and energy resource potential, thus providing a multifunctional resource (Volchko et al., 2020). Urban geology, rooted initially in engineering geology, has moved towards an interdisciplinary, solution-focused science (Bricker et al., 2024). As such, particular attention should be given to ensure adequate resource protection and balance the UUS's competing and coexisting functions. In this sense, the EU Water Framework Directive (European Parliament, 2000), which was transposed into national law by every Member State, establishes a framework for the protection of groundwater, among other water resources, promoting sustainable water use based on the long-term protection of available water resources. This is a critical issue, especially in cities, since many concurrent issues arise from urbanization. The UUS is being used increasingly more intensively, to an increasing depth, and for evermore

purposes (Schokker et al., 2017). In this context, Kahnt et al. (2015) introduced the concept of *potential utilization zone* as a possible instrument for subsurface spatial planning to assess the possible effects of competing uses in the subsurface space. Fig. 1 illustrates the problem of overlapping uses in the underground space by giving an overview of multiple underground functions. Typical urban pressures associated with the UUS, i.e., withdrawals for drinking and industrial water supply, deep excavations, such as basements and parking lots, and transport infrastructure, such as road tunnels or multiple-level underground railways, need to coexist with the sustainable exploitation of emerging energy resources, thus representing a current urban challenge (see Fig. 1). In particular, regarding the harnessing of energy, the use of shallow geothermal energy at depths ranging to 200 m may especially contribute to decarbonizing heating and cooling (UNESCO, 2022), which accounts for at least 40% of global energy consumption and CO₂ emissions (IEA, 2019). Moreover, underground structures and aquifer systems can store surplus heat from cooling processes and recover it during winter (UNESCO, 2022).

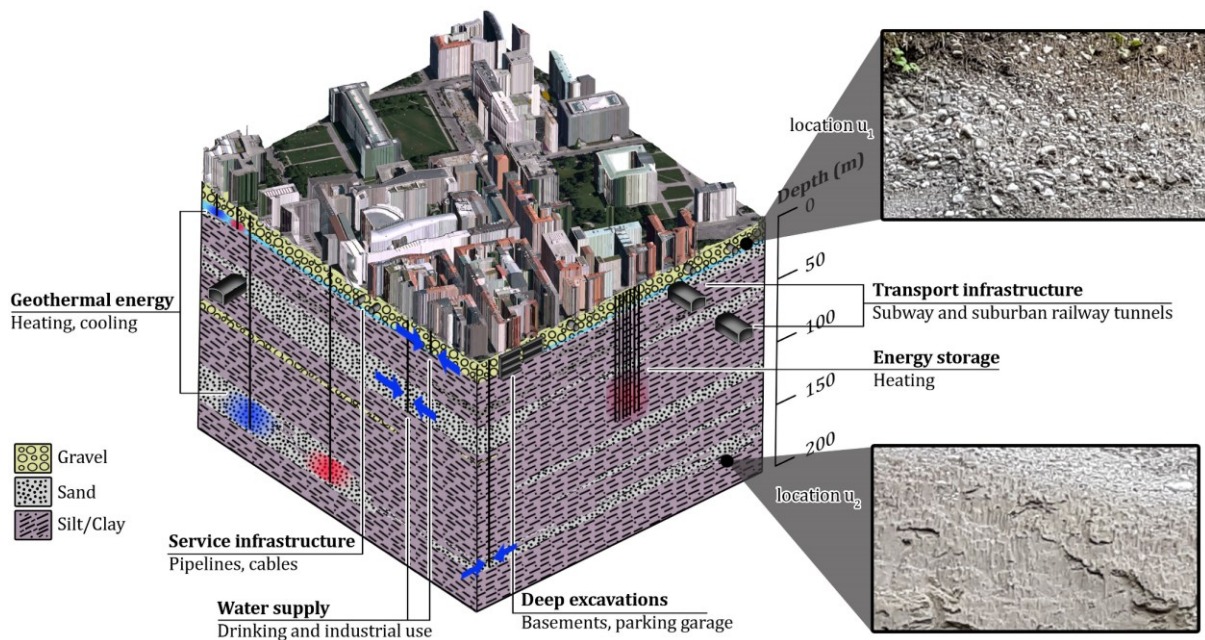


Fig. 1: Schematic representation of the underground space in unconsolidated sediments: Multifunctionality of the subsurface and multiplicity of scales of heterogeneity

Consequently, as a multifunctional resource, the underground space requires careful planning and sensitive management of its potential and value to society (Volchko et al., 2020). To address these challenges effectively, i.e., combating climate change, ensuring resource protection, and facilitating the typical UUS uses, sustainable management of the entire subsurface space is required (FAO, 2016; Kahnt et al., 2015). The geological conditions of the UUS are the key factor affecting underground space development (Bricker et al., 2024; Lai et al., 2023). At a European level, this is reflected in need to further characterize the groundwater bodies to assess their uses (European Parliament, 2000). Accordingly, this characterization shall include the extent and type

of geological units, their hydraulic and stratification characteristics, and the properties of the overlying superficial deposits in the catchment (European Parliament, 2000).

However, the physical limits of the geological features in the underground space are invisible to planners, developers, and regulators, leading to the inability to address these issues proactively (UNESCO, 2022). Hence, there is a lack of explicit mention of UUS in key policies (Bricker et al., 2024), and thus, the current practice of subsurface planning is far from ideal (Kessler et al., 2010). However, introducing the Sustainable Development Goals (SDGs) is an important step forward in recognizing the role of urban geology (Bricker et al., 2024). This requires adequate information on the 3-D geometry and properties of natural sediments at the right level of detail (Schokker et al., 2017). Detailed 3-D models that characterize near-surface deposits are most useful in urban planning and development (Campbell et al., 2010; Kessler et al., 2010, 2005). However, the complexity and three-dimensionality of the subsurface may be solely described by limited available data (Galloway and Hobday, 1983). Yet, mainly urban areas possess a great deal of geological data on the subsurface, namely soil observations of drilled materials obtained from boreholes drilled over time. In this context, most cities were built in the unconsolidated surficial deposits created by fluvial, lacustrine, glacial, deltaic, and aeolian geologic processes (Ehlers and Gibbard, 2004a, 2004b; Freeze and Cherry, 1979; Singhal and Gupta, 1999). These deposits occur in nearly all regions mantling much of the earth's surface (Freeze and Cherry, 1979), constituting the only major sources of groundwater for vast areas throughout the developing world (Bloomfield, 1994). Consequently, the characteristics of unconsolidated materials are of prime concern in securing sustainable management of the underground space.

1.2 Understanding the heterogeneities of unconsolidated sediments

The *unconsolidated sediments*, otherwise known as *non-indurated sediments* (Freeze and Cherry, 1979) or simply as *soil* in civil engineering (Terzagui et al., 1996), consist of non-cemented solid particles formed and transported to their present locations as a result of the weathering of the land accumulation, namely from fluvial, glacial, and eolian processes during Quaternary and late Tertiary time (Bloomfield, 1994; Singhal and Gupta, 1999). These water-bearing strata, such as gravelly and sand deposits, may form excellent aquifers and thus play an essential role in groundwater development (Singhal and Gupta, 1999). Their main feature is the intergranular pore space; therefore, they are classified according to the grain size of their constituents, as indicated in Fig. 2a (DIN EN ISO 14688-1, 2020). Depending on the distribution of various particle sizes, unconsolidated material can be characterized using the grain-size distribution (GSD) curve or the grain-size range based on sieve analysis data, as shown in Fig. 2b. The grain-size fractions and the grading derived from a GSD are generally summarized as the soil texture (Schuhmann et al., 2011).

The natural geological composition of most formations, including non-indurated sediments, tends to vary significantly from place to place in the subsurface, thus leading to *heterogeneity*.

Heterogeneity may occur at different scales ranging from small or microscopic to larger or megascopic scales, depending on various reservoir anatomical components (Alpay, 1972). When deposited, sediments tend to settle on their flat sides, leading to a *layered heterogeneity* (Domenico and Schwartz, 1997; Kruseman and de Ridder, 2000).

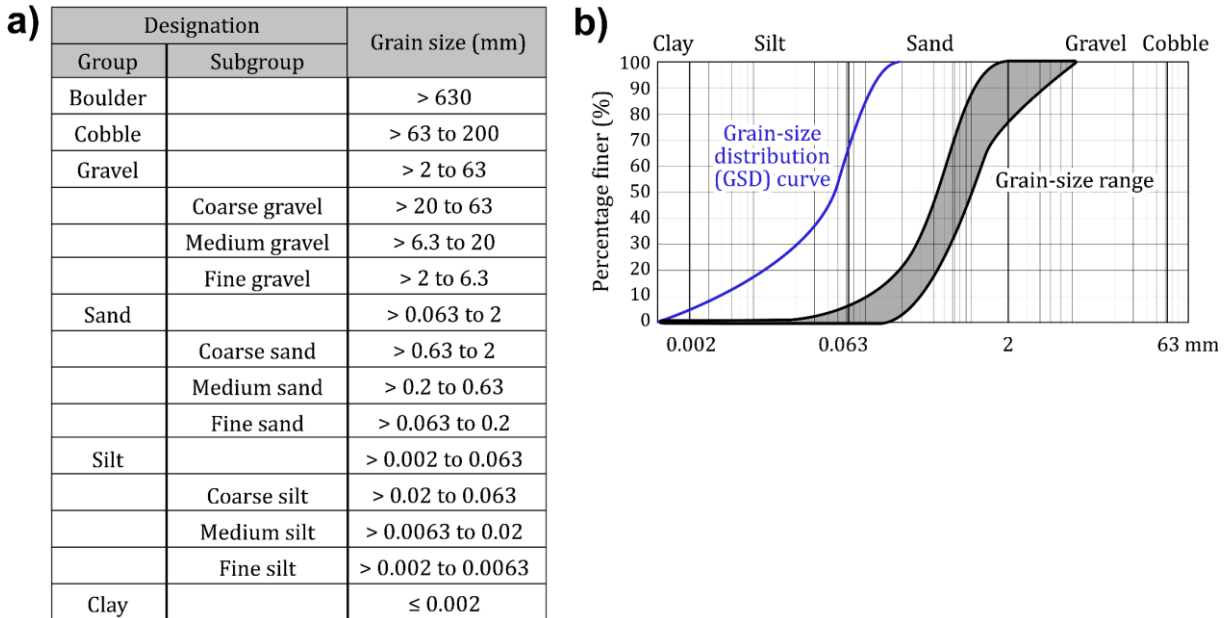


Fig. 2: Characterization of unconsolidated sediments according to grain size: **a)** Groups and subgroups of sediments according to grain size limits (DIN EN ISO 14688-1, 2020); **b)** Plot of a GSD curve and a grain-size range of two sediment mixtures

Herein, geological layers may have nonuniform stratification characteristics, pinch out, and contain intercalations of other sediments, e.g., lenses (Kruseman and de Ridder, 2000). This can be seen in Fig. 1 in the interlayered sandy deposits at various depths, which may be bounded laterally by impermeable material. In the presence of faults or large-scale stratigraphic features, such as the overburden-bedrock contact, large geological contrasts can arise, thus leading to a *discontinuous heterogeneity* (Freeze and Cherry, 1979; Woessner and Poeter, 2020). In Fig. 1, the interface between the main gravel body at the top and the underlying fine-grained sediments represents an excellent example of this scale of heterogeneity.

However, the individual layers of natural deposits are never homogeneous (Terzagui et al., 1996), thus having irregular bedding, reservoir geometries, and textural inhomogeneities (Galloway and Hobday, 1983). In this sense, a geological formation composed of unconsolidated sediments commonly shows grain size variations in their particles, both horizontally and vertically, leading to *local-scale heterogeneity* of sedimentary textures (Alpay, 1972) or a *trending heterogeneity* (Freeze and Cherry, 1979). This is represented in Fig. 1 at locations u_1 and u_2 . The reality of such deposits is then characterized by an inherent natural complexity of holding highly non-constant sediment mixtures in space. However, there is a certain reluctance to acknowledge the importance of small-scale heterogeneities since the effect operates at a scale much smaller than most models

can resolve (Ringrose and Bentley, 2015). The spatial distribution of these local-scale patterns makes up the geological systems (Freeze and Cherry, 1979), thus defining the geometries of the main geological features in geologic media, i.e., aquifers and aquitards, and ultimately also the spatial relationships between them.

The local-scale geological heterogeneity leads to a non-constant spatial distribution of petrophysical properties in the underground space, whose characterization enables assessing engineering geology constraints and evaluating geothermal and energy storage potential (Bricker et al., 2024). Herein, the granular composition profoundly affects the physical properties (Pusch, 2002). Some of them, namely the transport properties, e.g., the hydraulic conductivity (K), determine the rate and capacity of water flow through a porous medium (Domenico and Schwartz, 1997). The latter ultimately controls the suitability of various potential UUS uses highly dependent on groundwater migration, such as groundwater extraction, groundwater heat pump systems (GWHP), and underground thermal energy storage systems (UTES). Regarding thermal properties, soil composition, and porosity strongly influence thermal conductivity (Pusch, 2002). The latter property significantly affects the heat transfer process, which is essential in the efficiency of systems based on borehole thermal energy storage (BTES) (Arabkoohsar, 2023). In foundation and earthwork engineering, the design of ordinary soil-supporting structures is mainly affected by mechanical properties, which also depend on the size of the soil constituents (Terzagui et al., 1996). As mentioned in Chapter 1.1, geological property characterization is a prerequisite for current urban planning, which requires digital technologies to enable 3-D urban characterization. In this sense, Bricker et al. (2024) highlighted the urgency for geospatial data to address decarbonization, climate change, and potential assessments, i.e., geothermal, energy, and carbon storage.

1.3 Motivation case study: the greater area of Munich

The city of Munich, located in Bavaria in the southeast of Germany (see Fig. 3), serves as the case study area in this thesis. The municipality covers an area of approximately 310 km² and, with a population of 1.57 million inhabitants as of June 2023, it is the third-largest city in Germany. The population of Munich is expected to undergo considerable demographic growth, reaching approximately 1.85 million in 2040, representing an increase of 19% from 2021 (LHM, 2022). In this sense, the city of Munich has recognized its essential role as a driver of global change to achieve sustainable growth in the city (LHM, 2022). Herein, the municipality has set itself the goal of reducing the energy-related GHG emissions to 0.3 tonnes of CO₂ equivalent per inhabitant and year in the city by 2035, thus reaching carbon neutrality (LHM, 2022).

To achieve this, policymakers must address the interrelated challenges of urban growth and climate change. This implies the stresses arising from the pressure of a city's population on its supplies of land, housing, essential services, infrastructure, and environment (Mukim and Roberts, 2023). The city's sustainable development requires extensive subsurface use in response

to these needs (Volchko et al., 2020). In particular, the city of Munich attaches high priority to the investigation and use of the UUS as heat source and thermal storage and to consider potential conflicts of competing uses, e.g., with drinking water supply (Timpe et al., 2021). Fig. 3b provides an overview of the city's multiple underground uses at the beginning of the present thesis and illustrates how Munich's subsurface interacts with the interrelated challenges mentioned above, which are further discussed.

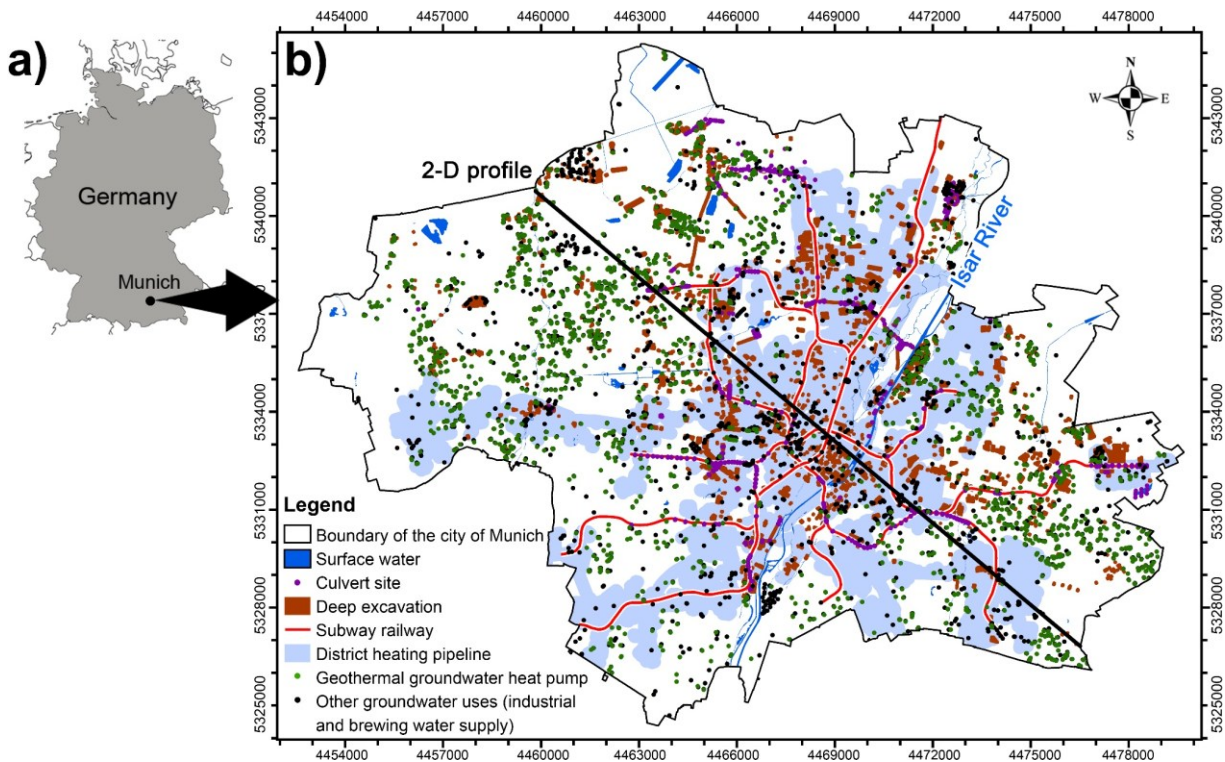


Fig. 3: Illustrative figure showing the multifunctionality of the subsurface space in the city of Munich: **a)** Location map; **b)** Multiple underground functions and infrastructure in the city of Munich

The lack of room above ground and the need to reduce traffic congestion in the inner city of Munich has motivated the introduction of underground multi-story parking systems for park-and-ride travelers in the last few years (Hönes, 2021). This trend is about to strengthen according to the measures adopted by the city of Munich to improve the parking facilities and tackle the GHG reduction in the traffic sector (Timpe et al., 2021) (see deep excavations shown in brown in Fig. 3b). Moreover, the need for further development in the UUS is even most evident in the city's public transport. The population growth is pushing current infrastructures to operate close to their capacity limits (see red lines representing the subway railways in Fig. 3b). Thus, the further development of the subway and suburban railway tunnels will be treated as a high-priority task until the 2040s (Timpe et al., 2021). Moreover, Stadtwerke München (SWM), Munich's municipal utilities company, operates the district heating (DH) network of the city of about 900 km (Fig. 3b). The expansion of this network and its renewable supply are significant aspects of the city's strategy for sustainable urban development. By 2035, SWM aims to raise the share of the city's heating market covered by DH from 35% to 50% (LHM, 2022). To achieve this, deep geothermal

energy should contribute up to 60% of the DH supply (LHM, 2022). In addition, the greater area of Munich holds a wide variety of groundwater uses in shallow and deeper aquifers up to ~300 m below ground level. Among others, groundwater is mainly used for drinking, industrial, brewing, and emergency water supply (see black dots in Fig. 3b), as well as for GWHP in open-loop geothermal systems (see green dots in Fig. 3b). The multiple culvert structures designed for managing groundwater discharge distributed across the city (see lilac dots, Fig. 3b) are increasingly used as heat sources. The construction and management of the above-mentioned underground facilities, i.e., parking systems, deep excavations, tunnels, DH network covered with deep geothermal energy, and groundwater uses, depend critically on the space availability and soil and groundwater conditions. These aspects are strongly conditioned by the UUS's competing and coexisting functions and geology's inherent spatial variability in Munich's subsurface space.

Munich lies on the Munich Gravel Plain (MGP), a glacial outwash plain comprising sandur terraces formed by melting glaciers in the Pleistocene and modern Holocene deposits from alluvial and fluvial origin (Bauer et al., 2005; Lemcke, 1988). Fig. 4a and b show a simplified geological map of the greater area of Munich and a geological 2-D profile across the city, respectively. The lithostratigraphic units relevant in this thesis are the Quaternary and the Upper Freshwater Molasse (UFM) of Miocene age, representing the most recent sediments up to a depth of ~300 m below ground level (see Fig. 4a and b). These units are composed of unconsolidated deposits and are widely exposed to the space above ground, holding most of the great deal of underground infrastructure and subsurface uses built and planned in the city, except for the mid-depth, at depths of 400-2,500 m, to deep geothermal energy in greater depths. The Quaternary aquifer of the MGP, formed mainly by coarse-grained gravels, is one of the most productive groundwater occurrences in Europe (Freudenberger and Schwerd, 1996) and has been the subject of intensive research (Kerl et al., 2012; Prösl and Anders, 2011; Zosseder et al., 2015). This aquifer is underlain by a Miocene clayed-marly slackwater and sandy substratum, which is generally considered to act as a confining layer. The relief of this boundary and its implications for the distribution of the aquifer thickness were studied by Albarrán-Ordás and Zosseder (2020). The Quaternary basis was modeled through a universal kriging procedure using borehole data, i.e., the positions of the bottom boundary of the Quaternary formation based on the vertical change in the prevailing lithology from the gravelly Quaternary to the finer-grained Miocene. This work revealed an uneven relief of channels and ridges, as shown in Fig. 4b and c. Although its valuable insights are crucial for estimating the aquifer yields or the geothermal potential for GWHP in the city of Munich (Böttcher et al., 2019; Böttcher and Zosseder, 2022), the modeled interface can be understood as an element of the discontinuous heterogeneity, as discussed in Chapter 1.2, which ignores the local-dependent textural inhomogeneities. The importance of integrating the local-scale patterns becomes evident if we consider the variations in material properties. This is particularly relevant since solute migration is strongly affected by smaller effects and the spatial dependence of hydraulic properties (Koltermann and Gorelick, 1996).

The natural heterogeneity of K has been reflected in Munich's subsurface, reaching up to three orders of magnitude in the shallow Quaternary aquifer and large steps of two orders of magnitude even at very short distances of ~ 300 m (Exler, 1967; Gebhardt, 1968; Theel et al., 2020). The cross-section in Fig. 4a shows some exemplary well screens at positions #1, #2, and #3 with K values obtained from pumping tests. The spatial interpolation in the vertical and horizontal directions of such scarce data from adjacent wells, while neglecting the smaller effects in the internal composition of the aquifer, presents many difficulties and usually forces the interpolation of the data in space accompanied by averaging or homogenization procedures (de Marsily et al., 2005). Herein, the heterogeneity treatment is only countered by the values in local measurements, thus without considering the sediment mixture. The need for further research in providing more details of the heterogeneity also becomes apparent when one observes the drilled lithologies at the top of the underlying Miocene at borehole locations drilled over time in Munich, as shown in Fig. 4d. A very heterogeneous distribution of sandy, i.e., shown by the orange dots in Fig. 4d, and clayed/silty lithologies, i.e., shown by the lilac dots in Fig. 4d, can be inferred across the city (see Fig. 4d). Whereas the silty-clayed substratum acts as a confining layer, the sandy sequences situated just below the Quaternary aquifer, i.e., the so-called *geological window structures*, may affect the reservoir architecture. Such structures may favor a vertical groundwater flow and connectivity of the Quaternary aquifer with the underlying Miocene sequences, thus impacting the regional aquifer management. Moreover, at the beginning of the present thesis, less was known about the spatial relationships of the underlying Miocene aquifers. The a priori arbitrary spatial distribution of sandy deposits shown in Fig. 4d, separated by several hundred meters, raises questions concerning their lateral extent, thickness, and interconnectivity, as expressed by the question marks in Fig. 4c. Although the local presence of sands at the top altitude of the substratum was known, especially due to the experiences and insights from subway and underground constructions over time (Blasy, 1974; Gebhardt, 1968; Schirm, 1968), they were not widely studied in a more global context in the Munich area, and the connectivity issue and the 3-D component were ignored.

The selected study area of the city of Munich exemplifies the circumstances mentioned in Chapters 1.1 and 1.2. Munich's underground space is being used increasingly intensively for more purposes ranging from transport and service infrastructure to multiple groundwater uses. The geological conditions of natural unconsolidated sediments strongly condition the sustainable development of its underground space. Therefore, this thesis aims to improve the prediction capability of the characteristics of these sediments with a multipurpose framework to secure sustainable management of the underground space of major cities, with the example of Munich.

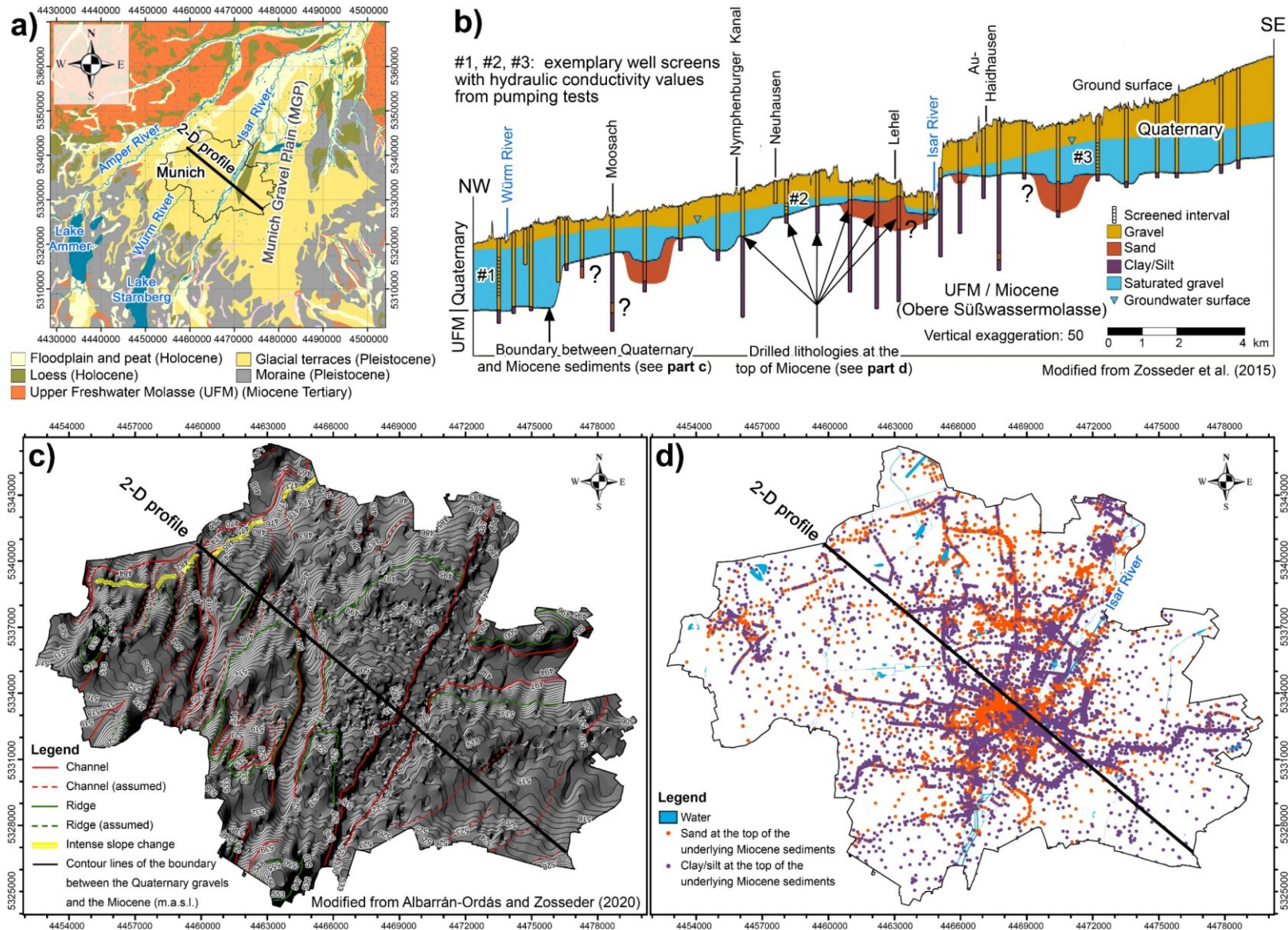


Fig. 4: Geological setting in the area of Munich showing different scales of geological heterogeneity: **a)** Simplified geological map (modified after Freudenberger and Schwerd (1996)); **b)** Schematic geological 2-D profile (modified after Zosseder et al. (2015)); **c)** Map of the Quaternary aquifer basis including terrain structures (modified after Albarrán-Ordás and Zosseder (2020)); **d)** Map of the drilled lithologies at the top of the underlying Miocene sediments at borehole locations drilled over time

1.4 Structure of the thesis

Chapter 1 underlines the need for better characterizing the local-scale heterogeneity of unconsolidated materials since they are of prime concern in securing sustainable management of the underground space. This is exemplified in the city of Munich (Germany), which was selected as the motivation case study area for this thesis.

Chapter 2 presents an overview of key geostatistical terminology used throughout this thesis and a review of the principles of 3-D geo-modeling relevant to characterizing unconsolidated sediments. Regarding the latter, the focus is first on introducing the geo-modeling process as a multi-stage sequential approach consisting of structural and voxel modeling. Then, the most commonly used criteria for categorizing the heterogeneities of unconsolidated sediments in 3-D models are briefly described. The chapter also outlines the classification and quantification of uncertainties related to geological 3-D models and the various connotations of model usability.

Chapter 3 describes the research gaps identified from Chapter 2 and subsequently formulates actions to address the gaps through the proposed research in this thesis.

Chapters 4 to 7 include four Peer-reviewed publications as integral parts of this cumulative thesis. Three are main authorship publications, and one manuscript is a co-authored work. The study in Chapter 4 proposes a 3-D geostatistical framework enabling the estimation of the fictive GSD by simulating the grain size classes for a certain number of cumulative frequencies of the GSD. Chapter 5 addresses the adaptation of the framework to incorporate uncertainties in the input data and proposes UQ measures in a simulation experiment. Chapter 6 analyses the estimation of local-dependent K -values and explores the possibilities of capturing the representativeness of the aquifer heterogeneity and spatial geometries closer to the field scale. The study in Chapter 7 aims to integrate hydrogeochemistry with the insights of the proposed geo-modeling approach.

The findings of the thesis and their limitations are presented and discussed in Chapter 8. The transferability of the results is addressed by exploring five case studies conducted in different geological contexts and applications, i.e., planning of a road and a subway tunnel, city-wide groundwater model calibration, reservoir architecture, and parameter estimation for geothermal potential assessment in a multi-layer aquifer system.

Chapter 9 reviews the conclusions and future work proposed.

CHAPTER 2

Background and state of the art

Chapter 1 underlined the need to characterize the local-scale heterogeneity of unconsolidated materials for securing sustainable management of the underground space. This chapter overviews key terminology and modeling concepts relevant to characterizing such sediments. The chapter begins with an overview of key definitions and geostatistical fundamentals (2.1). After illustrating the need for modeling the spatial distribution of attributes, the deterministic and probabilistic approaches are compared, and the concept of the Random Function is introduced. Subsequently, the paradigms underlying statistical inference, stationarity, kriging estimation, and sequential stochastic simulation of categorical variables are briefly reviewed. The second part deals with general principles of geological 3-D modeling (2.2). Geo-modeling is addressed as a multi-stage process consisting of structural and subsequent property or voxel modeling. This is followed by a review of the most used criteria for categorizing the heterogeneities of unconsolidated sediments in geological 3-D models. The classification and quantification of uncertainties in the 3-D geo-modeling process are covered in the third part (2.3). The last part of the chapter briefly reviews the current uses of 3-D geo-models and links them to the challenges of the multiple functions of the underground space discussed in Chapter 1 (2.4).

2.1 Key terminology and fundamental geostatistical concepts

This chapter provides an overview of key definitions and a background of the theory of the main geostatistical concepts relevant to this thesis. For extensive discussions and further information, one can refer to the following reference books: Goovaerts (1997), Isaaks and Srivastava (1989), Chilès and Delfiner (2012), and Deutsch (2002).

2.1.1 Key terminology

To introduce some key concepts, we will consider a spatial domain A with a given but unknown attribute $Z(\mathbf{u})$ of the geological reality, with \mathbf{u} being the location coordinate vector, and with some attribute measurements at locations \mathbf{u}_α , i.e., $z(\mathbf{u}_\alpha)$. This situation is shown in Fig. 5a and clearly illustrates the need to estimate the attribute's actual value at all locations $z(\mathbf{u})$.

A *model*, whether deterministic or probabilistic, can be defined as a simplified representation of the unknown reality carrying a set of simplifying assumptions (Koltermann and Gorelick, 1996). A *deterministic model* considers only one possible outcome to any unsampled location of the reality (see Fig. 5b). This consideration is appropriate when the fundamental processes that

generated the data are sufficiently known to accurately estimate the attribute at locations without data (Isaaks and Srivastava, 1989). Thus, the deterministic approach assumes the error to be negligible (Goovaerts, 1997) and cannot produce realistic models of uncertainty (Mariethoz and Caers, 2015).

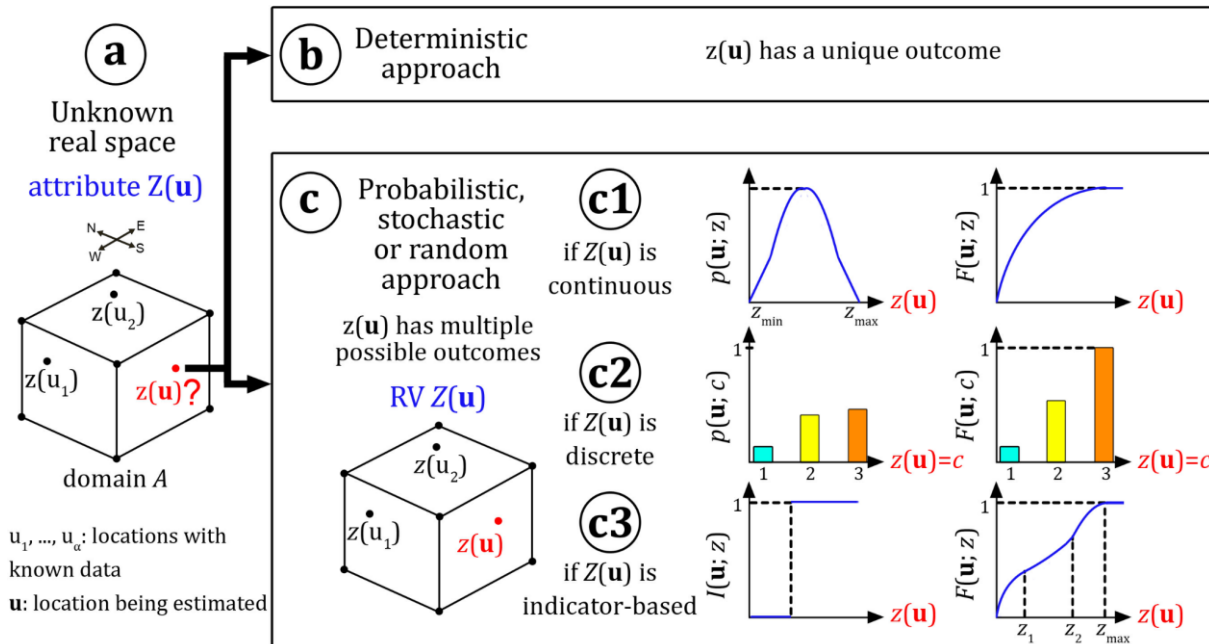


Fig. 5: Sketch illustrating key geostatistical terminology and random variables: **a)** Unknown real space; **b)** Deterministic approach; **c)** Probabilistic approach

However, in earth science, data are typically the result of complex processes. In such cases, a *probabilistic model*, also called a *stochastic* or *random model*, provides a series of possible outcomes, each with a probability of occurrence, as shown in Fig. 5c (Goovaerts, 1997). This approach considers the data as the result of some random process (Isaaks and Srivastava, 1989). In decision-making, it is critical to assess the potential error associated with prediction, and thus, the probabilistic approach is preferentially adopted to describe the uncertainty (Hong, 2010).

Geostatistics studies phenomena that fluctuate in space (Deutsch and Journel, 1997). It can be regarded as a collection of techniques that characterize spatial attributes, also known as regionalized variables, employing primarily random models. For those attributes, deterministic models are not applied because of the complexity of the natural processes (Olea, 1999).

A *geological 3-D model* or a *3-D geo-model* is a simplified 3-D representation of the geological reality with a set of assumptions. In this thesis, the reality of interest addressed is the geological composition and the property distribution in unconsolidated sediments.

2.1.2 Random Variables and the Concept of the Random Function

A *random variable* (RV) or a *regionalized variable* is one whose values can take a series of outcomes randomly generated according to some probabilistic mechanism. Consequently, a RV

can be characterized by its probability distribution (Isaaks and Srivastava, 1989). Whereas the traditional notation of a RV consists of a capital letter in italics (Deutsch, 2021), i.e., $Z(\mathbf{u})$, its outcome at any particular location is denoted by the lowercase also in italics $z(\mathbf{u})$ (see Fig. 5c). However, the observed outcomes are denoted as $z(\mathbf{u}_\alpha)$. Three types of RVs are usually distinguished: continuous, indicator, and discrete, which are shown at the right of Fig. 5c.

In a *continuous RV*, the value of the outcome may be in the interval between a minimum and a maximum value, i.e., $\{z(\mathbf{u}) \in [z_{\min}, z_{\max}]\}$, as shown in Fig. 5c1, and the RV is fully described by its univariate cumulative distribution function (CDF), denoted as $F(\mathbf{u}; z)$, thus providing the probability that the RV at any location \mathbf{u} is no greater than any threshold z (Goovaerts, 1997):

$$F(\mathbf{u}; z) = \text{Prob}\{Z(\mathbf{u}) \leq z\}; \quad \in [0, 1]; \quad \forall \mathbf{u} \in A; \quad \forall z. \quad (1)$$

However, a *discrete or categorical RV* may take a number C of mutually exclusive outcomes ($c = 1, \dots, C$) and is associated with a probability of occurrence of each outcome $p(\mathbf{u}; c)$ (see Fig. 5c2):

$$p(\mathbf{u}; c) = \text{Prob}\{Z(\mathbf{u}) = c\}; \quad \in [0, 1]; \quad \forall \mathbf{u} \in A; \quad c = 1, \dots, C; \quad \sum_{c=1}^C p(\mathbf{u}; c) = 1 \quad (2)$$

After defining a specific ordering of the discrete possible outcomes, the discrete RV can be described by its probability distribution function (PDF), denoted as $F(\mathbf{u}; c)$, providing the probability for any discrete outcome c' ordered lesser or equal to c (see at the right of Fig. 5c2):

$$F(\mathbf{u}; c) = \sum_{c'=1}^c p(\mathbf{u}; c'); \quad \in [0, 1]; \quad \forall \mathbf{u} \in A; \quad c = 1, \dots, C; \quad F(\mathbf{u}; c) \leq F(\mathbf{u}; c') \quad (3)$$

An *indicator RV* behaves as a discrete RV with only two possible outcomes, i.e., 0 and 1, and is preceded by a binary transform of the original RV, which in the discrete variant can be defined as:

$$I(\mathbf{u}; c) = \begin{cases} 1 & \text{if } Z(\mathbf{u}) = c; \\ 0 & \text{otherwise} \end{cases}; \quad \forall \mathbf{u} \in A; \quad c = 1, \dots, C, \quad (4)$$

and the PDF provides the probability that category c prevails at \mathbf{u} expressed as the expected value of the indicator RV (see Fig. 5c3):

$$F(\mathbf{u}; c) = E\{I(\mathbf{u}; c)\} = p(\mathbf{u}; c); \quad \in [0, 1]; \quad \forall \mathbf{u} \in A; \quad c = 1, \dots, C. \quad (5)$$

The binary transform of a continuous RV can be defined as:

$$I(\mathbf{u}; z) = \begin{cases} 1 & \text{if } Z(\mathbf{u}) \leq z; \\ 0 & \text{otherwise} \end{cases}; \quad \forall \mathbf{u} \in A; \quad \forall z, \quad (6)$$

resulting in a PDF providing the probability that the RV is no greater than a given threshold z , which can be expressed as the expected value of the indicator RV:

$$F(\mathbf{u}; z) = \text{Prob}\{Z(\mathbf{u}) \leq z\} = E\{I(\mathbf{u}; z); \quad \in [0, 1]; \forall \mathbf{u} \in A; \forall z. \quad (7)$$

To introduce the concept of a random function, it is necessary to consider one RV per each possible attribute in reality and for all sites (Olea, 1999). Having this idea in mind, a *random function* (RF) is a collection of the RVs in a defined domain $\{Z(\mathbf{u}), \mathbf{u} \in A\}$ (Deutsch and Journel, 1997). Just as the univariate CDF of one RV in Eq. (1), the RF is fully characterized by the set of all its multivariate CDF for any possible number Y of RVs ($y = 1, \dots, Y$) and all possible locations $\mathbf{u}_1, \dots, \mathbf{u}_Y$:

$$F(\mathbf{u}_1, \dots, \mathbf{u}_Y; z_1, \dots, z_Y) = \text{Prob}\{Z(\mathbf{u}_1) \leq z_1, \dots, Z(\mathbf{u}_Y) \leq z_Y\}; \quad \in [0, 1]; \forall \mathbf{u} \in A; \forall z. \quad (8)$$

The multivariate CDF of Eq. (8) describes the joint uncertainty about the Y number of RVs and is referred to as the *spatial law of the RF* (McLennan, 2007).

The notation conditional cumulative distribution function (CCDF) is used when the multivariate CDF is specific to some neighboring data. The draw of any outcomes from the CCDF is the heart of Monte Carlo drawings and stochastic simulation (Deutsch and Journel, 1997). A RF is *multiGaussian* or *parametric* if all CDFs are Gaussian. In this case, determining the CCDF reduces to estimating some parameters, namely the mean and variance (Goovaerts, 1997).

A RF can also be understood as the rule that assigns a realization $z(\mathbf{u}, \theta)$ to the outcome θ of an experiment S (Gómez-Hernández and Srivastava, 2021):

$$Z(\mathbf{u}) \sim \{z(\mathbf{u}, \theta); \quad \forall \mathbf{u} \in A; \forall \theta \in S. \quad (9)$$

2.1.3 Statistical inference and stationarity

The paradigm underlying the statistical inference is to substitute the unavailable repetitive realizations of the RV at unsampled locations for another replication available elsewhere in space at sample locations (Pyrz and Deutsch, 2014). Returning to our example in Fig. 5, the CDF at locations where the attribute is unknown $F(\mathbf{u}; z)$ may be inferred from sampling the distribution of z at other locations with data. This task corresponds to the *decision of stationarity*. This property of the RF model allows for defining a pool of data over which experimental averages will be calculated and assumed representative of the population as a whole (Journel, 1989).

This decision is a mathematical first and second-order assumption (McLennan, 2007). The decision of *first order* assumes that both the mean $m(\mathbf{u})$ and the variance $\sigma(\mathbf{u})^2$ are constant, independent of location, and are inferred from the global univariate CDF of the available data (see Eqs. (10) and (11)). The *second order* assumes that the covariance between all pairs of data $C(\mathbf{h})$ is translation invariant (see Eq. (12)).

$$m(\mathbf{u}) = m \text{ from } F(z); \quad \forall \mathbf{u} \in A; \forall z. \quad (10)$$

$$\text{Var}\{Z(\mathbf{u})\} = \sigma^2 \text{ from } F(z); \quad \forall \mathbf{u} \in A; \forall z. \quad (11)$$

$$F(\mathbf{u}_1, \dots, \mathbf{u}_B; z_1, \dots, z_Y) = F(\mathbf{u}_1 + \mathbf{h}, \dots, \mathbf{u}_B + \mathbf{h}; z_1, \dots, z_Y); \quad \in [0, 1]; \forall \mathbf{u} \in A; \forall z; \forall \mathbf{h}, \quad (12)$$

where \mathbf{h} denotes the separation vector between data pairs. If the bivariate distribution is not exceeded, the covariance is inferred from the \mathbf{h} -bivariate CDF depending solely on \mathbf{h} :

$$F(\mathbf{u}_1, \mathbf{u}_2; z_1, z_2) = F(\mathbf{h}; z_1, z_2); \quad \in [0, 1]; \forall \mathbf{u} \in A; \forall z; \forall \mathbf{h}, \quad (13)$$

$$C(\mathbf{u}_1, \mathbf{u}_2) = C(\mathbf{h}) = E\{Z(\mathbf{u}) \times Z(\mathbf{u} + \mathbf{h})\} - m^2; \quad \forall \mathbf{u} \in A; \forall \mathbf{h}. \quad (14)$$

Consequently, the decision of the first and two orders of stationarity and the separation vector \mathbf{h} allow us to determine the mean, the variance, and the covariance, thus leading to inference. Making a reasonable decision of stationarity is essential for building models with realistic geological heterogeneity (McLennan, 2007). In practice, this decision also includes the subdivision of the domain into zones deemed homogeneous enough, each of which is assigned a separate RF. In this sense, using a trend model relaxes the strong decision of first-order stationarity and defines the mean dependent on the sample location in the domain (Villalba and Deutsch, 2010).

2.1.4 Spatial continuity and variability

The spatial continuity of an attribute represents the similarity or dissimilarity between data as a function of distance, represented by the separation vector \mathbf{h} . It can be characterized by the covariance $C(\mathbf{h})$, the correlogram $\rho(\mathbf{h})$, and the semivariogram $\gamma(\mathbf{h})$ functions (Goovaerts, 1997), having the following relation, which depends on the stationarity decision:

$$C(\mathbf{h}) = C(0) \times \rho(\mathbf{h}) = C(0) - \gamma(\mathbf{h}); \quad \forall \mathbf{u} \in A; \forall \mathbf{h}, \quad (15)$$

where $C(0)$ is the covariance at $\mathbf{h}=0$, thus equaling the variance σ^2 of the RF:

$$C(0) = E\{Z(\mathbf{u}) \times Z(\mathbf{u} + \mathbf{0})\} - m^2 = E\{Z(\mathbf{u})^2\} - m^2 = \text{Var}Z(\mathbf{u}) = \sigma^2; \quad \forall \mathbf{u} \in A. \quad (16)$$

The *semivariogram* is the most traditional measure of spatial variability (Isaaks and Srivastava, 1989). Unlike the covariance, which is a measure of similarity, the experimental semivariogram $\gamma(\mathbf{h})$ measures the average dissimilarity between pairs of data separated by \mathbf{h} , where $N(\mathbf{h})$ is the number of data pairs separated by \mathbf{h} :

$$\gamma(\mathbf{h}) = \frac{1}{2 \times N(\mathbf{h})} \sum_{\alpha=1}^{N(\mathbf{h})} [z(\mathbf{u}_\alpha) - z(\mathbf{u}_\alpha + \mathbf{h})]^2; \quad \forall \mathbf{h}; \forall \mathbf{u} \in A. \quad (17)$$

The term *variogram* is used throughout this thesis since it is commonly used in the literature to refer to the semivariogram. The variogram generally increases as the separation distance between pairs increases. Moreover, the spatial continuity is often anisotropic; thus, the variogram must be inferred in different directions. The most essential features of the variogram are the range, the sill, and the nugget effect. Whereas the *range* represents the distance at which the variogram reaches a plateau, the *sill* is the variogram value at this plateau, which is the variance of the RF. Moreover, the *nugget effect* represents the variogram value for $\mathbf{h}=0$ in the presence of sampling errors and short-scale variability.

Fitting an analytical model to an experimental variogram is necessary for implementing estimation and simulation algorithms. The four most common analytical functions are the spherical (Eq. (18)), exponential (Eq. (19)), Gaussian (Eq. (20)), and the nugget effect (Eq.(21)).

$$\gamma(\mathbf{h}) = \begin{cases} 1.5\mathbf{h} - 0.5\mathbf{h}^3, & \text{if } \mathbf{h} \leq 1 \\ 1, & \text{otherwise} \end{cases}; \quad \forall \mathbf{h}, \quad (18)$$

$$\gamma(\mathbf{h}) = 1 - \exp(-3\mathbf{h}); \quad \forall \mathbf{h}, \quad (19)$$

$$\gamma(\mathbf{h}) = 1 - \exp(-3\mathbf{h}^2); \quad \forall \mathbf{h}, \quad (20)$$

$$\gamma(\mathbf{h}) = \begin{cases} 0, & \text{if } \mathbf{h} = 0 \\ 1, & \text{otherwise} \end{cases}; \quad \forall \mathbf{h}. \quad (21)$$

2.1.5 Local estimation and kriging paradigm

The *local estimation* of the real attribute $Z(\mathbf{u})$, also referred to as *kriging*, is a well-established methodology that provides the best linear unbiased estimate and its variance at each unsampled location obtained from the linear combination of the original nearby data $z(\mathbf{u}_\alpha)$ available.

If we consider the real and unknown attribute $Z(\mathbf{u})$ (see Fig. 6a), we can apply the concept of the RF presented in Chapter 2.1.2 to consider a RV $Z(\mathbf{u})$, which, under the assumption of stationarity of first and second order has constant mean and variance values, as well as a translation dependent covariance as shown in Fig. 6b.

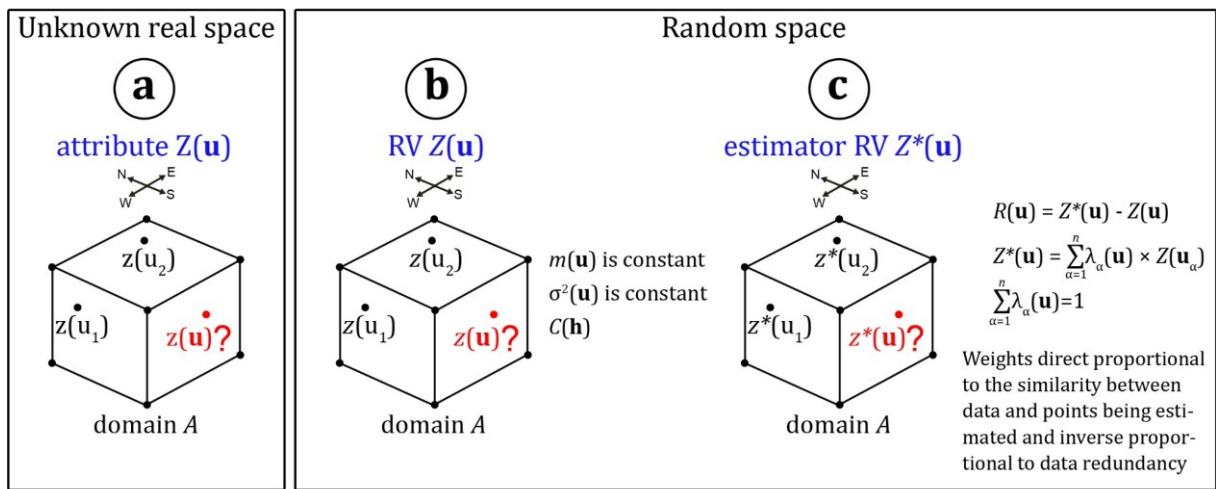
We can now consider a *kriging estimator* of a RV $Z^*(\mathbf{u})$ as a linear combination of all the RVs within a given neighborhood (see Fig. 6c):

$$Z^*(\mathbf{u}) - m(\mathbf{u}) = \sum_{\alpha=1}^n \lambda_\alpha(\mathbf{u}) \times [Z(\mathbf{u}_\alpha) - m(\mathbf{u}_\alpha)]; \quad \forall \mathbf{u} \in A; \alpha = 1, \dots, n, \quad (22)$$

where λ_α are the kriging weights assigned to the data, and $m(\mathbf{u})$ and $m(\mathbf{u}_\alpha)$ are the mean values. Thus, the kriging estimator depends on the known data and their weights, and both may change from one location to another. Various kriging variants can be considered depending on how the mean values are treated in Eq. (22). Whereas *simple kriging* (SK) considers the mean to be known

and constant, the *ordinary kriging* (OK) variant assumes an unknown and constant mean. Both *kriging* algorithms *with an external drift* (KT) and *universal kriging* introduce a function providing a mean fluctuation, although a polynomial function gives the latter. In the case of *indicator kriging* (IK), a binary transformation of the data is applied. Goovaerts (1997) provides a detailed description of kriging's flavors. For simplification purposes, only the OK estimator is presented, which considers the mean to be constant in a local neighborhood centered on the location \mathbf{u} being estimated:

$$Z^*(\mathbf{u}) = \sum_{\alpha=1}^n \lambda_{\alpha}(\mathbf{u}) \times Z(\mathbf{u}_{\alpha}); \quad \forall \mathbf{u} \in A; \alpha = 1, \dots, n. \quad (23)$$



u_1, \dots, u_n : locations with known data; \mathbf{u} : location being estimated; RV: Random variable; $R(\mathbf{u})$: estimation error; $\lambda_{\alpha}(\mathbf{u})$: kriging weights

Fig. 6: Sketch illustrating the kriging paradigm: **a)** Unknown real space; **b)** Random variable $Z(\mathbf{u})$; **c)** Estimator random variable $Z^*(\mathbf{u})$ and simplified kriging system of equations

We can define another RV for the estimation error or residual, expressed by $R(\mathbf{u})$, obtained from the difference between the estimator RV $Z^*(\mathbf{u})$, and the RV $Z(\mathbf{u})$, that is, $R(\mathbf{u}) = Z^*(\mathbf{u}) - Z(\mathbf{u})$ as shown in Fig. 6c, at right. The estimation error is minimized under the constraint of unbiasedness, implying that $E\{Z^*(\mathbf{u}) - Z(\mathbf{u})\} = 0$. The stationary first order assumes that $E\{Z(\mathbf{u})\}$ is constant. Consequently, the kriging system of equations can be described as follows:

$$\begin{cases} \sum_{\alpha=1}^n \lambda_{\alpha}(\mathbf{u}) \times C(\mathbf{u}_{\alpha} - \mathbf{u}_{\beta}) + \mu = C(\mathbf{u}_{\alpha} - \mathbf{u}) \\ \sum_{\alpha=1}^n \lambda_{\alpha}(\mathbf{u}) = 1 \end{cases}; \quad \forall \mathbf{u} \in A; \alpha = 1, \dots, n, \quad (24)$$

where μ is the Lagrange parameter, and $\lambda_{\alpha}(\mathbf{u})$ are the kriging weights. The kriging weights are inversely proportional to the similarity between pairs of points $C(\mathbf{u}_{\alpha} - \mathbf{u}_{\beta})$, thus accounting for the data redundancy, and directly proportional to the similarity between the data and the locations being estimated, that is, $C(\mathbf{u}_{\alpha} - \mathbf{u})$.

The resulting *kriging variance* at a given location \mathbf{u} can be expressed as the reduction of the prior variance σ^2 of the RV due to the similarities between the known data and the location \mathbf{u} :

$$\sigma_{OK}^2(\mathbf{u}) = \sigma^2 - \sum_{\alpha=1}^n \lambda_{\sigma}(\mathbf{u}) \times C(\mathbf{u}_{\alpha} - \mathbf{u}) - \mu; \quad \forall \mathbf{u} \in A; \alpha = 1, \dots, n. \quad (25)$$

2.1.6 Stochastic Simulation and Sequential Stochastic Simulation

Stochastic simulation refers to the generation of multiple equiprobable representations (called realizations) of the spatial distribution of an attribute using spatial statistical methods of geostatistics (Koltermann and Gorelick, 1996). Various algorithms are available to create stochastic simulations, mainly grouped into object-based and cell-based techniques (Ringrose and Bentley, 2015). Tab. 6 of Appendix A provides an overview of these methods, which may vary in the types of input statistics, the ability to honor them, and ease of implementation (Pyrzcz and Deutsch, 2014). No simulation algorithm is best for all cases, but rather various alternatives from which to build the algorithm best suited for the problem at hand (Gómez-Hernández, 1997). The *object-based* methods are neither cell nor variogram-based and are suitable when geo-bodies geometries are well understood (Hassanpour and Deutsch, 2010). They provide a more geometrical representation of the shapes of the sedimentary bodies based on predefined geometries but cannot reproduce high-resolution trends (Pyrzcz and Deutsch, 2014). Instead, *cell-based* methods assign properties on a cell-by-cell basis. These techniques are, in turn, divided into two types, namely variogram-based, requiring complete 3-D variogram interpretations (Gringarten and Deutsch, 1999), and texture-based, using training images recreating the desired geological architecture, e.g., Multiple-Point Statistics (MPS). Variogram-based approaches remain the most widely used and underlie several simulation algorithms, such as the LU decomposition, the probability field (*p*-field) (Froidevaux, 1992), the simulated annealing, and the sequential simulation. The latter, i.e., *sequential simulation*, is the most common technique, involving modeling the CCDF of the RF and randomly sampling it at every location with a random sequence (Coburn et al., 2006). This process is conditional to the data and all values simulated at previously visited locations (Goovaerts, 1997). Conditional simulation methods can be grouped mainly into Sequential Gaussian Simulation (SGS) and Sequential Indicator Simulation (SIS).

The problem of predicting the geological composition at any unsampled location \mathbf{u} using only data available $z(\mathbf{u}_{\alpha})$ over the study area A is commonly addressed by introducing and simulating a categorical variable $Z(\mathbf{u})$ differentiating groups of common behavior. These groups are considered more geologically and statistically homogeneous (Deutsch, 2006). Thus, the real geological composition is categorized mathematically into a discrete number C of integer values for modeling purposes ($c= 1, \dots, C$), whose differentiation intends to better describe the prevailing heterogeneity to be modeled in 3-D space (Wellmann and Caumon, 2018). In this context, SIS is a widely used non-Gaussian simulation technique for categorical variable models (Deutsch, 2006; Deutsch and Journel, 1997; Journel, 1983), which applies the formalism of indicator RVs

presented in Eqs. (4) and (6) in a random sequence where an outcome is simulated by drawing the CCDF by Monte Carlo simulation.

The discrete values of a categorical variable are mutually exclusive and, thus, can be modeled by an indicator RV $I(\mathbf{u}; c)$ introducing a binary transformation into 1s or 0s, depending on whether the discrete value c is present at the location or not (see Eq. (4)). The mean of the indicator RV for each class is equal to the proportion of c (see Eq. (26)) and the variance of the indicators can be expressed as a function of the mean (see Eq. (27)).

$$m(\mathbf{u}; c) = E\{I(\mathbf{u}; c)\} = p(\mathbf{u}; c); \quad \forall \mathbf{u} \in A; c = 1, \dots, C, \quad (26)$$

$$Var\{I(\mathbf{u}; c)\} = \sigma^2(\mathbf{u}; c) = p(\mathbf{u}; c) \times [1 - p(\mathbf{u}; c)]; \quad \forall \mathbf{u} \in A; c = 1, \dots, C, \quad (27)$$

The covariance of the indicators can be expressed as:

$$C(\mathbf{h}; c) = E\{I(\mathbf{u}; c) \times I(\mathbf{u} + \mathbf{h}; c)\} - [p(\mathbf{u}; c)]^2; \quad \forall \mathbf{u} \in A; c = 1, \dots, C; \forall \mathbf{h}. \quad (28)$$

The indicator kriging estimator $I^*(\mathbf{u}; c)$ in the presence of n nearby local data can be expressed as follows as in Eq. (22):

$$I^*(\mathbf{u}; c) - p(\mathbf{u}; c) = \sum_{\alpha=1}^n \lambda_{\alpha}(\mathbf{u}; c) \times [I(\mathbf{u}_{\alpha}; c) - p(\mathbf{u}_{\alpha}; c)]; \quad \forall \mathbf{u} \in A; c = 1, \dots, C, \quad (29)$$

where $p(\mathbf{u}; c)$ and $p(\mathbf{u}_{\alpha}; c)$ are the mean values of the indicator RV for each class c at locations being estimated and data locations, respectively, $\lambda_{\alpha}(\mathbf{u}; c)$ are the indicator kriging weights, and $I(\mathbf{u}_{\alpha}; c)$ are the indicator RVs at data points. $I^*(\mathbf{u}; c)$ provides the local conditional probability for each discrete value c at an unsampled location, which is integrated into a CCDF for implementing Monte Carlo sampling of the CCDF (Hadavand and Deutsch, 2017). The various SIS variants relate to using the mean of the indicator RV in Eq. (29) (Deutsch, 2006). They include stationary SK, OK, and non-stationarity SK using local varying means, among others (Deutsch, 2006; Goovaerts, 1997). SIS can easily incorporate hard data from the boreholes and integrate secondary information (soft conditioning). Secondary data overcome the stationarity that probabilistic algorithms assume as a default (Ringrose and Bentley, 2015) and introduce geological patterns by providing a deterministic trend in different forms: horizontal, vertical, or 3-D spatial trends.

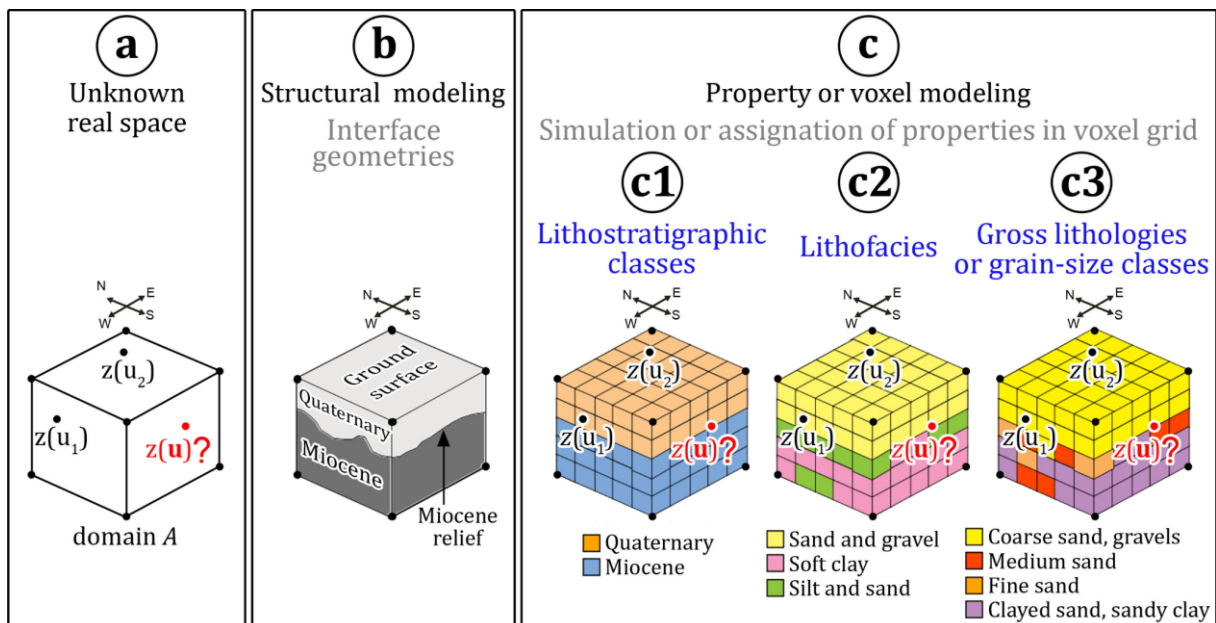
2.2 Principles of geological 3-D modeling

The process of *geological 3-D modeling* addresses creating spatial and spatiotemporal models of the physical nature of portions of the Earth's crust (Turner, 2006). Different authors describe geological modeling methods' current state and challenges (Pyrzcz and Deutsch, 2014; Turner, 2006; Wellmann and Caumon, 2018). Depending on the purpose of the model, they may have different goals. They can be used to predict interface geometries, i.e., stratigraphic boundaries and faults, the variation in the internal composition of geological bodies, and their spatial relationships (Turner, 2006). Therefore, this process usually consists of a multi-stage sequential approach

where the interfaces are modeled first. Secondly, the properties are predicted per unit of volume defined by the voxel or cell size. Both approaches are usually combined in the geological 3-D modeling process and exemplified in Fig. 7.

2.2.1 Structural modeling and the framework model

Structural modeling, also called *geometry*, *layer*, or *framework modeling*, aims to determine the interpreted surfaces stacked in stratigraphic order (Enemark et al., 2022), thus yielding surfaces and internally 3-D solid bodies representing both the stratigraphic boundaries and layers (see Fig. 7b). It is sometimes cited as *large-scale reservoir modeling* since it focuses on modeling the reservoir container. However, this latter term is usually used in oil, gas, and geothermal reservoirs. Moreover, in the literature, it can often also be referred to as *lithostratigraphic modeling* since it is commonly based on stratigraphic distributions of the modeling domain (Kearsey et al., 2015). Depending on the geological setting, several variants exist for structural models: (1) *layered models* (or *layer-cake models*), appropriate for stacked sedimentary strata; (2) *fault models*, if the model has discontinuities such as fractures or faults; and (3) *complex systems* without layered sequences (Turner, 2006). Arpat (2005) states that models consisting of homogeneous layers are convenient for basic reservoir engineering calculations, such as mass balances, but cannot provide the detail required by modern flow simulation applications.



u_1, \dots, u_a : locations with known data; u : location being estimated

Fig. 7: Overview of the multi-stage geological 3-D modeling process: **a)** Unknown real space; **b)** Structural modeling of interface geometries; **c)** Property modeling of lithostratigraphic classes (**c1**), lithofacies (**c2**), and gross lithologies (**c3**)

2.2.2 Property modeling and the voxel model

The resulting layers or volumes can be then discretized in a structured mesh of volumetric pixels (voxels) that are assigned specific property distributions (Enemark et al., 2022), i.e., the geological

composition, petrophysical or hydrogeological properties, and uncertainty. The assignment of properties is usually preceded by applying geostatistical methods within the voxel grids (see Chapter 2.1.6). Therefore, *property modeling*, also called *predicting* or *voxel modeling*, aims to describe the entire 3-D parametric space at each location of the subsurface, as shown in Fig. 7c. Instead, the term generally used in oil, gas, and geothermal reservoirs is *reservoir modeling* (Pyrzcz and Deutsch, 2014). In addition to discretizing the various layers, voxel-based approaches allow modeling the internal heterogeneity of the subsurface. Therefore, they are becoming increasingly crucial for underground spatial planning, even at regional and national levels (Hademenos et al., 2019; Stafleu et al., 2011). Moreover, their flexibility for deriving 3-D attributed parameterized models with geotechnical, hydrogeological, and other properties provides them multi-purpose usability and fosters a culture of multidisciplinary integration (Campbell et al., 2010). Voxel models also sometimes serve as a discretized space to transfer the probability at each voxel of being crossed by each interface in a structural model and the associated uncertainty.

2.2.3 Categorization of heterogeneities in unconsolidated sediments

SIS is widely used for categorical variable models (Deutsch, 2006; Journel, 1983). This cell-based simulation algorithm is commonly applied in voxel models in which the geological composition is categorized into discrete classes. The discrete integer values categorize the geological heterogeneities and must be established prior to modeling continuous properties (Pyrzcz and Deutsch, 2014). They represent understanding a particular geological setting, should not oversimplify the geological reality (Lindsay et al., 2012), and are case-specific (Silva, 2018). Much effort has been made to categorize the heterogeneities in unconsolidated sediments. However, this process is not standardized and may be based on different classifications (see Tab. 7 of Appendix A). A categorization based on *lithofacies* according to the sedimentary environment, as shown in the simplistic example of Fig. 7c2, has been used in many 3-D geo-models (Bianchi et al., 2015; Høyer et al., 2015; Jørgensen et al., 2010; Stafleu et al., 2011). Another option is to use a strict *lithostratigraphic scheme* (see Fig. 7c1), such as Merritt et al. (2007), Royse (2010), Stafleu et al. (2011), Høyer et al. (2015), and Hademoos et al. (2019). This typically precedes lithostratigraphic modeling, i.e., structural model. However, as shown in Fig. 7c3, other authors focused on a scheme based on differentiating *gross lithologies* or most prevailing *grain-size classes* (Hademenos et al., 2019; Kearsley et al., 2015; Stafleu et al., 2011), using existing classification schemes defining sediment classes, generally by established standards, such as the Wentworth (1922) or national classification systems, such as the REGIS scheme in The Netherlands (Vernes and van Doorn, 2005). A hydrofacies scheme is sometimes applied, focusing on introducing a discrete variable based on lithological facies with distinctive hydraulic properties (Comunian et al., 2011). Other works, e.g., Khojasteh (2013), considered geotechnical soil classes for unconsolidated sediments based on geotechnical norms (DIN 18196, 2023).

2.3 Uncertainties in geological 3-D modeling: classification and quantification

Uncertainty is crucial in understanding the reliability of the geological 3-D models and, therefore, in the decision-making processes when determining the distributions of properties while assessing a proposed application (Pakyuz-Charrier et al., 2018b; Potter et al., 2010; Turner, 2006). Over the years, different authors analyzed the geo-modeling process's types and sources of uncertainties. The available literature on this topic often mentions the early contributions of Mann (1993), who introduced three types of uncertainties (see Tab. 8 of Appendix A). However, the separation between the categories is not completely clear (Wellmann and Caumon, 2018). Jones et al. (2004) and McCaffrey et al. (2005) focused on understanding the uncertainties arising during geological mapping and noted the need for further development of methods that consider uncertainties associated with geological field data and interpretations. Further investigations in the classification of uncertainties have been done in recent years. Wellmann et al. (2010) adapted the three types of uncertainties of Mann (1993) to 3-D structural modeling. Wellmann and Caumon (2018) provided different levels of uncertainties arising in the construction of 3-D structural models, namely at the levels of (1) conceptual model, (2) structure of the mathematical model, (3) parameters of mathematical model, and (4) input data.

Significant efforts have been made toward uncertainty quantification in geological 3-D modeling in recent years. Different methods provide a scalar measure of uncertainty. In the case of continuous properties, two major cases can be defined. Regarding structural modeling, the realization of a set of multiple simulations in a discretized space enables the determination of the probability of each voxel being crossed by each interface. It is important to note that, in this way, the uncertainty transferred into a voxel-based space is related to the features of a structural model. Some work has been done here to integrate uncertainties in the position of input data, model parameters, and interpolation parameters in 3-D structural models, such as the concept of *geological inversion* of structural data (Wellmann et al., 2010). Lindsay et al. (2012) use the concept of *geological perturbation* to introduce model realizations with perturbed measurements. Wellmann and Caumon (2018) have a complete review of the works. However, in property modeling, summary statistics based on normally distributed data, such as the mean, standard deviation, and quantiles, are particularly effective and provide concrete information values about the distribution's spread (Potter et al., 2013). Similarly, this information can also be transferred into a discretized 3-D space, as mentioned above. In the case of categorical properties, the use of summary statistics is limited, and it is only possible if the ordering and addition of the variables are possible (Potter et al., 2013). Several theories have been developed in recent decades to address unordered categorical variables (Wellmann and Caumon, 2018). Some methods are based on the concept of the *theory of possibility* (Bárdossy and Fodor, 2001; Zadeh, 1978), which measures the uncertainty by capturing the degree of possibility and necessity of each discrete class. Other methods consider the concept of *information entropy* (Shannon, 1948) or normalized information entropy (Leung et al., 1992) to measure the discrete distribution's randomness. In this sense, additional measures of information entropy, such as joint entropy, conditional entropy,

and mutual information, can be used for analyzing spatial correlations of uncertainty and potential uncertainty reduction in space (Wellmann, 2013). Lindsay et al. (2012) introduced the concept of *stratigraphic variability*. The latter concept is used as a proxy for uncertainty and indicates the record of stratigraphic units found at discrete locations calculated from multiple model realizations with perturbed measurements. These approaches have been applied and highlighted in different publications for geological purposes almost exclusively on 3-D structural modeling (Bianchi et al., 2015; Bond et al., 2007; Pakyuz-Charrier et al., 2018a; Schweizer et al., 2017; Wellmann and Regenauer-Lieb, 2012).

2.4 Usability of geological 3-D models: fit-for-purpose versus multipurpose

3-D geo-models are always built for a purpose, and the objective should be clear from the start (Pyrzcz and Deutsch, 2014). Various uses may be considered, covering the prediction and visualization of the geometries of geological structures, their spatial relationships, their internal composition, property distributions, and displacements by tectonic forces (Turner, 2006).

However, most models have a *fit-for-purpose* design to meet the specific requirements of the intended use (Ringrose and Bentley, 2015). In this sense, the geological 3-D models are built with a level of detail suitable for the stated goal (Pyrzcz and Deutsch, 2014). Based on the specific purpose, the discrete integer values considered in the categorical modeling approaches address the intended use (Chapter 2.2.3). The introduction of a categorization scheme in *fit-for-purpose* models is then case-specific (Silva, 2018). The model parametrization largely depends on the level of detail introduced by the categorical variable defined. The different classes will be parametrized with constant geotechnical, hydrogeological, or petrophysical properties from published literature or with field data to address an individual application. Focusing on a specific goal implies that some details of the heterogeneity will inevitably be lost, which would be helpful when dealing with other purposes. In addition, the opportunities to effectively parameterize with multiple properties are considerably reduced. In this sense, 3-D geo-models have been applied in the last years in a wide range of applications in fields as varied as hydrogeology (Bianchi et al., 2015; Campbell et al., 2010; Ross et al., 2005), hydrochemistry (Raiber et al., 2012; Royse, 2010), resource assessment (Maljers et al., 2015; van der Meulen et al., 2007, 2005), seismic microzonation (Kruiver et al., 2017) and environmental risk assessments (Wycisk et al., 2009).

However, urban geology has moved towards an interdisciplinary, solution-focused science. Hence, the subsurface space often needs to face several purposes and challenges at a time. The *fit-for-purpose* models cannot answer questions they were not designed to answer (Ringrose and Bentley, 2015). This is particularly critical in the UUS since it is a multifunctional resource and should also be treated as such from the start of the reservoir model design. In other words, geotechnical characteristics or thermal properties may be as crucial as hydraulic characteristics in underground management. In response to this issue, some 3-D geo-models with a multipurpose framework have been developed recently, such as the GeoTOP model in the Netherlands (Stafleu et al., 2011; Stafleu and Dubelaar, 2016). Moreover, as de Marsily et al. (2005) stated, it is

necessary to derive methods to identify the material properties at the scale of the facies structures. In this sense, the link between grain size and hydraulic properties needs to be re-evaluated and used.

CHAPTER 3

Research questions and hypothesis

The present chapter describes the research gaps identified in Chapter 2 and formulates the research hypothesis to address these gaps.

3.1 Prediction of small-scale grain-size-based heterogeneities in 3-D

Open research question

The only use of 3-D geo-models in their structural approach is limited to modeling the subsurface's internal heterogeneity due to its inability to understand small-scale effects (Chapter 2.2.1). The voxel-based 3-D geo-models present some areas of improvement since the categorization schemes of heterogeneities in unconsolidated sediments oversimplify, importantly, their geological nature (Chapter 2.2.2). Such deposits are never homogeneous and consist of highly non-constant mixtures of particles of different grain sizes in space. Categorical schemes based on gross lithologies have limitations since natural deposits never consist of sediments of one unique grain size. Lithofacies, hydrofacies, and geotechnical schemes are rather purpose-specific, thus leading to limitations in the subsequent model usability while underestimating the complexity of reality.

Research hypothesis

The essential features of unconsolidated sediments, specifically the fictive grain-size distribution (GSD), can be effectively predicted with a compartmentalization of the underground space into voxels, which allows for a detailed discretization level and for capturing small-scale effects, and with a new categorization scheme for heterogeneities at a grain-size scale, which enhance the modeling of gradual variations in clast mixtures.

3.2 Uncertainty integration from input data and UQ of unconsolidated sediments

Open research question

The uncertainty conditions the reliability of the model outputs for practical decision purposes. The input data used to address the heterogeneities in unconsolidated sediments are soil observations from drilled materials described in the field. The standards for soil classification are subject to systematic imprecisions in quantifying the lithological components associated with inherent generalizations and on-site personnel's subjectivity. Regarding integrating such uncertainties in the modeling process, whose typology was discussed in Chapter 2.3, the intrinsic

inaccuracies from input data are usually ignored in 3-D geo-modeling strategies, and the overall UQ could be significantly underestimated. In addition, the uncertainty is relevant to the underlying parameters of the developed RF model. As discussed in Chapter 2.3, most of the methods addressing the UQ in 3-D geo-models focus on the membership of each location to a unit or layer, i.e., related to 3-D structural modeling. Discretizing uncertainties in a voxel model for visualization is quite frequent in achieving this. However, more is needed to address the uncertainty of the detailed composition of unconsolidated sediments. Consequently, exploring and developing UQ measures for the particularities of small-scale grain-size-based heterogeneities is necessary.

Research hypothesis

The hypothesis of this research is double:

The reinterpretation of soil observations as fictive GSD enables the interpretation of different valid combinations of the soil components whose statistical dispersion introduces uncertainties.

The prediction of small-scale grain-size-based heterogeneities in unconsolidated sediments posited in Chapter 3.1 can integrate uncertainties, ensuring their propagation throughout the geo-modeling process, and entropy-based methods, typically used in structural modeling as discussed in Chapter 2.3, can be adapted for effectively quantifying the uncertainty of the modeling outputs in sediment mixtures.

3.3 Ensuring multipurpose usability of the underground space

Open research question

The UUS is a multifunctional resource with a wide variety of potential uses. Thus, there is a need to work across customized solutions for underground management (cf. Chapter 1.1). However, geological 3-D models commonly have a fit-for-purpose design fulfilling a specific goal. Focusing on individual goals leads to the inability to answer questions they were not designed to answer. The case-specific categorization of heterogeneities implies that some heterogeneity details will inevitably be lost, and the opportunities to effectively parameterize the underground space with multiple properties are considerably reduced. These aspects present significant challenges for the level of detail required in the model design to secure sustainable UUS management. In addition, current model design approaches do not allow for the effective prediction of the relative amounts of user-defined grain fractions on a cell-by-cell basis.

Research hypothesis

This research hypothesizes that *a multipurpose approach can be developed to design and address the multifunctional uses in the UUS by identifying material properties at the scale of facies structures of unconsolidated sediments.* By predicting the essential features of unconsolidated sediments,

specifically the fictive grain-size distribution (GSD), it is anticipated that this approach will enhance the ability to *predict multiple properties linked to grain size*. Furthermore, the relative quantification of grain fractions is hypothesized to enable *user-defined scenario analyses*, identifying minimum and maximum mass contents for each grain fraction, thereby providing conservative, realistic, and pessimistic estimates *for further detailed applications*.

CHAPTER 4

The D_i models method: geological 3-D modeling of detrital systems consisting of varying grain fractions to predict the relative lithological variability for a multipurpose usability

Alberto Albarrán-Ordás^a, Kai Zosseder^a

^a Technical University of Munich, Arcisstraße 21, 80333 Munich, Germany

(Please refer to Notes 1 and 2 in List of Abbreviations, Acronyms, and Symbols)

Abstract

The coexistence of a wide variety of subsurface uses in urban areas requires increasingly demanding geological prediction capacities for characterizing the geological heterogeneities at a small-scale. In particular, detrital systems are characterized by the presence of highly varying sediment mixtures which control the non-constant spatial distribution of properties, therefore presenting a crucial aspect for understanding the small-scale spatial variability of physical properties. The proposed methodology uses the lithological descriptions from drilled boreholes and implements sequential indicator simulation to simulate the cumulative frequencies of each lithological class in the whole sediment mixture. The resulting distributions are expressed by a set of voxel models, referred to as D_i models. This solution is able to predict the relative amounts of each grain fraction on a cell-by-cell basis and therefore also derive a virtual grain size distribution. Its implementation allows the modeler to flexibly choose both the grain fractions to be modeled and the precision in the relative quantification. The concept of information entropy is adapted as a measure of the disorder state of the clasts mixture, resulting in the concept of “Model Lithological Uniformity,” proposed as a measure of the degree of detrital homogeneity. Moreover, the “Most Uniform Lithological Model” is presented as a distribution of the most prevailing lithologies. This method was tested in the city of Munich (Germany) using a dataset of over 20,000 boreholes, providing a significant step forward in capturing the spatial heterogeneity of detrital systems and addressing model scenarios for applications requiring variable relative amounts of grain fractions.

Keywords

Geological 3-D modeling, geostatistics, Sequential indicator simulation, Lithological heterogeneity, underground management.

4.1 Introduction

The development of cities implies a growing demand of space and natural resources spreading in depth in both the horizontal and vertical in-depth directions. With the aim of achieving orderly urban growth and ensuring both sustainable and coexisting use of the various natural resource deposits and underground infrastructures, there then exists a clear need to manage the subsurface space (Campbell et al., 2010; Schokker et al., 2017). This need is especially relevant in detrital depositional environments consisting of sediment mixtures of differing grain sizes, since many urban areas around the world are built on such deposits. Underground management will be even more accentuated in the next years given the straightforward integration of geological subsurface into the building information modeling (BIM) method, which will be mandatory within the timeframe of 2021–2025 at a national level in some countries (Wehrens and Volken, 2019).

The highest possible level of knowledge of the geological subsurface properties is desirable for this purpose, but it is unfortunately not available in most cases. These properties condition the suitability of a wide variety of geological potentials in the underground space, e.g., heat supply, storage, water resources, and as space for urban infrastructure. Direct soil observations from drilled materials constitute the most common types of geological data available. Borehole data, which are often very scarce and qualitatively heterogeneous, are most abundant in urban areas. These data have become available for further analysis due to the increasing level of digitalization and represent a potential big data source for geological analysis in favor of spatial planning (Marti, 2019). Alongside the common lack of knowledge, geology also possesses an inherent natural complexity of holding highly non-constant properties in space (de Marsily et al., 2005). These facts often result in conservative procedures for managing the use of geological potentials with respect to legislative requirements. Understanding geological natural media implies acknowledging and accounting for their spatial heterogeneity (de Marsily et al., 2005). Added to this, the wide range of potential uses that the subsurface space might hold requires a flexible methodological approach that is able to address multi-functional specifications (Volchko et al., 2020). Both the 3-D spatial delimitation and the appropriate small-scale parameter assignments significantly constrain the suitability of both geological subsurface potentials and their sustainable and coexistent use.

In order to address these challenges, the use of massive borehole data and the digitalization of geological mapping in a more general sense (Jones et al., 2004) and, more concretely, geological 3-D models, in their different forms and approaches, are gaining importance over the last decades - not only for visualization purposes but also as a planning and forecasting tool. This is evidenced by the fact that geological mapping is currently undergoing a transformation from traditional 2-D to 3-D, with geological 3-D modeling becoming a key priority for national geological surveys (NGS) (Berg et al., 2011).

Within the broad field of 3-D geo-modeling approaches performed in order to face the aforementioned challenges, two key aspects will be addressed in the present paper: the predictive

ability of geology with respect to heterogeneity and multi-purpose usability. This is all intended to be accompanied by a flexible and user-defined implementation.

4.2 Background of geological 3-D modeling and model suitability

The general term of “3-D structural modeling” constitutes the preliminary step of any geological 3-D model and addresses the definition of the accurate geometry of the geological domain as well as the integration of uncertainties associated with the geometrical input data (Pyrzcz and Deutsch, 2014; Turner, 2006). In this respect, Wellmann and Caumon (2018) have provided a very complete description of the current state and challenges of 3-D structural modeling. Therein, the sole consideration of structural geometric features by means of, e.g., layer-cake models or geometric 3-D models could be used as framework models (Wellmann and Caumon, 2018), but they are considered to be an approximation for understanding the small-scale effects and heterogeneities involved. The resulting geometrical model is commonly discretized in volume elements of the tetrahedron type or of a variety of voxel configurations with the ultimate goal of providing subdivisions in which property distributions can be predicted (Turner, 2006).

The prediction of both the geological composition and continuous properties (petrophysical, geotechnical or hydrogeological) in 3-D space is addressed by means of 3-D property modeling in voxelized domains. Property predictions based on voxel models enable modeling of the internal heterogeneity of the subsurface and are becoming increasingly important (Hademenos et al., 2019; Stafleu et al., 2011). In this regard, Kearsey et al. (2015) compared a 3-D model consisting of lithostratigraphic units, each of which possesses a unique dominant lithology, with a lithological 3-D model, thus providing a lithological prediction in each voxel. He concluded that the minor lithologies occurring within the units commonly represent a significant proportion of the lithological composition, which underlines the relevance of the small-scale geological variability. Focusing on the geological composition, the predictive ability of the model commonly depends upon the introduction of a categorical variable whose stationary classes represent subdivisions which are more geologically and statistically homogeneous (Deutsch, 2006). Commonly used categorical variables may thus be based on lithofacies classes, such as in the 3-D model for the glacial and postglacial deposits underlying the city of Glasgow in the UK (Bianchi et al., 2015) and in the 3-D lithofacies distributions of Zeeland in the Netherlands (Stafleu et al., 2011; Stafleu and Dubelaar, 2016). Alternatively, the grain sizes (or rather the lithological classes) can be considered, i.e., the 3-D lithological distributions also implemented in the models mentioned earlier (Kearsey et al., 2015; Stafleu et al., 2011), as well as for the Belgian Continental Shelf (Hademenos et al., 2019). Lithological and stratigraphical information can be also combined to subdivide the geological space into lithostratigraphic units (Hademenos et al., 2019; Royse, 2010; Stafleu et al., 2011). Another option is offered by hydrofacies classes showing lithological facies with distinctive hydraulic properties (Comunian et al., 2011; Theel et al., 2020). The categorical variable chosen largely controls the degree of geological variability which the model may achieve, and it has strong implications for the quantification of model uncertainties and model usability

(Potter et al., 2013). The introduction of this categorical variable is case-specific (Silva, 2018), and the variable should be fixed in such a way that it does not oversimplify the geological reality (Lindsay et al., 2012) in addition to counting for the subsequent usability of the model - which should have a multi-purpose nature, if possible.

In regard to usability, geological 3-D models may be used based on pure visualization, the definition of geometric architecture of geo-bodies, to multi-parameter estimation for various specific applications (Ross et al., 2005) like groundwater flow numerical modeling. Regarding the geometric architecture of geo-bodies, this commonly implies the definition of their lateral extension, thickness, and three-dimensional connectivity. The latter feature is of utmost importance to correct flow and transport predictions, especially when dealing with contamination assessments (de Marsily et al., 2005). This interconnectedness is provided by analyzing the geometrical dependences between the geological bodies. Multi-parameter estimation largely depends on the level of detail introduced by the categorical variable defined. A lithological description as precise as possible is needed, on the basis of which properties will be assigned (de Marsily et al., 2005). The various stationary classes into which the geological reality is subdivided, whether they be lithologies, lithofacies, hydrofacies or lithostratigraphical units, will be parametrized with constant geotechnical, hydrogeological, or petrophysical properties from the published literature, or with field data. In this regard, if the categorical variable considerably oversimplifies the geological reality; the constant parameters derived from it would also be misrepresented. This was demonstrated by Kearsley et al. (2015) by using a lithologically-derived model compared with a lithostratigraphic model while modeling the glaciofluvial deposits in the city of Glasgow. In this sense, 3-D geomodels, most of them based on a structural approach, have been applied in the last years in a wide range of applications in fields as varied as hydrogeology (Bianchi et al., 2015; Campbell et al., 2010), hydrochemistry (Raiber et al., 2012; Royse, 2010), resource assessment (Maljers et al., 2015; van der Meulen et al., 2007, 2005), seismic microzonation (Kruiver et al., 2017), geotechnics (Merritt et al., 2007), and environmental risk assessments (Wycisk et al., 2009).

The extended use of the subsurface in its wide variety of competing and coexisting functions - together with the inherent spatial variability of geology - motivates the need for underground management. This is being increasingly addressed by the digitalization of the geological space, which has resulted in significant progress in advanced geological 3-D models in recent years. The current modeling methodologies implemented in detrital systems introduce a categorical variable which tends to assume a stationary prevailing class (lithologies, lithofacies, hydrofacies, etc.) in each voxel for both predicting the final image of geology and further parameterizing the model with property distributions. In this sense, the presence of highly variable sediment mixtures ultimately controls the non-constant spatial distribution of properties in detrital systems. Our understanding of this small-scale spatial lithological variability can be improved by deepening the knowledge regarding the prediction of 3-D distributions of relative amounts of the grain fractions composing the sediment mixture.

This paper proposes a 3-D modeling approach which provides substantial contributions for improved modeling detrital depositional environments. On the one hand, this novel method addresses the prediction of the geological composition of detrital systems, considering these as clasts mixtures with quantifiable variable amounts of grain fractions. This approach is implemented by introducing a user-definition of the grain fractions being considered into the sediment mixture and the precision of the relative amounts of each grain fraction. On the other hand, this approach aims to address multi-functional specifications for different purposes. Special efforts have been made to combine model scenarios for applications requiring different relative frequencies of grain fractions.

After an explanation of the modeling method, its implementation in the city of Munich will be described using a large data set to display the geological prediction and the multi-user opportunities.

4.3 Methodology

In order to better understand the small-scale geological variability of sediment mixtures, a novel 3D-geological modeling approach is presented to, on the one hand, improve the spatial prediction of the lithology distribution and, on the other hand, to provide a flexible interpretation of the modeled lithological distribution for user-specified applications. The cornerstone of this method is the lithological heterogeneities in detrital sedimentary systems being able to be described as grain size distributions. This distribution of cumulative frequencies of grain fractions can be geomodeled in 3-D space in a geostatistical simulation framework by means of a set of partial percentile lithological models, referred to herein as D_i models. This set of models in turn defines the cumulative frequencies of each lithological class in each voxel after defining a constant frequency. The relative amounts of grain fractions are thus also inferred. They refer to the lithological stages of the subsurface, being equivalent to the reference passing diameters D_i of a grain-size distribution with same percentile distances, whereby the subscript i defines the cumulative frequency of the total sediment mixture. This can be read as the grain size distribution curve at every voxel.

Based on this principle, the modeling approach uses a stochastic simulation framework by way of the Sequential Indicator Simulation (SIS) method to reproduce (1) the hard data, which are truth measurements from the lithological descriptions from existing boreholes, (2) inferred spatial statistics in the distribution of grain sizes proportions, and (3) the spatial continuity of each lithological class for each D_i . This process results in a multi-voxel solution in which many partial percentile lithological models as reference diameters D_i are defined. On this basis, the concept of “Model Lithological Uniformity” is proposed, as a measure of the homogeneity of the grain sizes in the detrital mixture. The “Most Uniform Lithological Model” can be directly derived, and it represents the distribution of lithologies possessing the highest relative frequencies in the detrital mixture.

For a clear explanation of each methodological step, we have added some short examples of the case study in Munich.

4.3.1 Step 1 - Conceptual model

The first step of the proposed methodology includes:

- i) Construction and discretization of the geometrical framework of the 3-D space being modeled.
- ii) Definition of the grain fractions to be modeled in the detrital mixture. The grain fractions to be considered are defined by a categorical variable according to the grain sizes.
- iii) Definition of the percentiles of interest of the grain size distribution, denoted as D_i . In this context, D represents the grain diameter expressed by the lithological class, and the subscript i is an integer indicating the percentile of interest. For example, the percentile of interest D_{10} denotes the lithological class below which the 10% finest grain fraction falls. The set of i values is defined so that the grain size distribution is divided into equal frequency groups. This is done by defining a constant step p between percentiles, e.g. the p^{th} percentile, the $(p+p)^{\text{th}}$ percentile, the $(p+2p)^{\text{th}}$ percentile, the $(p+3p)^{\text{th}}$ percentile, etc. This implies a total number of N percentiles of interest considered (where $N=100/p$). For instance, if we consider a step of $p=10$, then $i=10, 20, 30, 40, 50, 60, 70, 80, 90, 100$ and we obtain $N=10$ percentiles of interest. The number of percentiles can be adjusted by selecting a smaller or bigger step p , which increases respectively decreases the number N (e.g., $N=20$ for $p=5$). As a consequence, the percentile step p sets also the precision in the frequency quantification that the model is able to account for.

On this basis, the construction of N percentile lithological models is addressed using a geostatistical simulation approach. These models, which are linked to each percentile of interest of the sediment mixture, can be expressed as D_i models.

To illustrate this, the conceptual model for the case study in Munich considers three grain fractions to be modeled (clay/silt, sand, and gravel), although a finer graduation is conceivable which also includes minor lithological components. In our case, the construction of ten partial percentile models ($N=10$) was required in order to obtain a lithological prediction with a precision of 10% ($p=10$). These are linked to the following ten reference diameters: D_{10} , D_{20} , D_{30} , D_{40} , D_{50} , D_{60} , D_{70} , D_{80} , D_{90} , and D_{100} of the whole sediment mixture.

4.3.2 Step 2 - Input data: lithological descriptions from borehole data

The proposed method is intended for and already being applied to process large amounts of lithological descriptions from boreholes. This information is the basic input for the modeling approach. Given the conceptual model and, more specifically, once the grain fractions and the

precision of the model are set, the lithological descriptions are prepared and interpreted for each described borehole section in the available dataset accordingly to constrain the partial percentile models as hard data. Borehole data might be stored in databases, which are normally managed at the national or regional level, and they include information about the intersected geology. One common aspect of all databases is that the borehole descriptions consist of coded information representing the geological composition for each drilled interval in terms of (1) the geological nature and (2) the degree of intensity or presence of the lithological components. In this respect, the use of common codes information for soil description is promoted at the European level by European standards EN ISO 14688-1 and EN ISO 14688-2. Beyond this, additional information based on regional or national guidelines, e.g. DIN 4023 (2006), might be also used. The workflows adopted in this approach for data acquisition and preparation were adapted to the borehole database used for the present case study in the city of Munich (Germany) using the integration of the aforementioned European references into the German standards (DIN EN ISO 14688-1, 2020; DIN EN ISO 14688-2, 2020; DIN EN ISO 14689, 2018), and the DIN standards (DIN 4023, 2006). Section 4.4.2 summarizes the features of this database.

Steps 1 and 2 of the methodology, the data acquisition to the interpretation ready-to-use in geostatistical simulations is illustrated below (Fig. 8) by the following lithological description as an example: (gG,s,o). This can be translated into moderately sandy (s) coarse gravels (gG) with a presence of organic material (o).

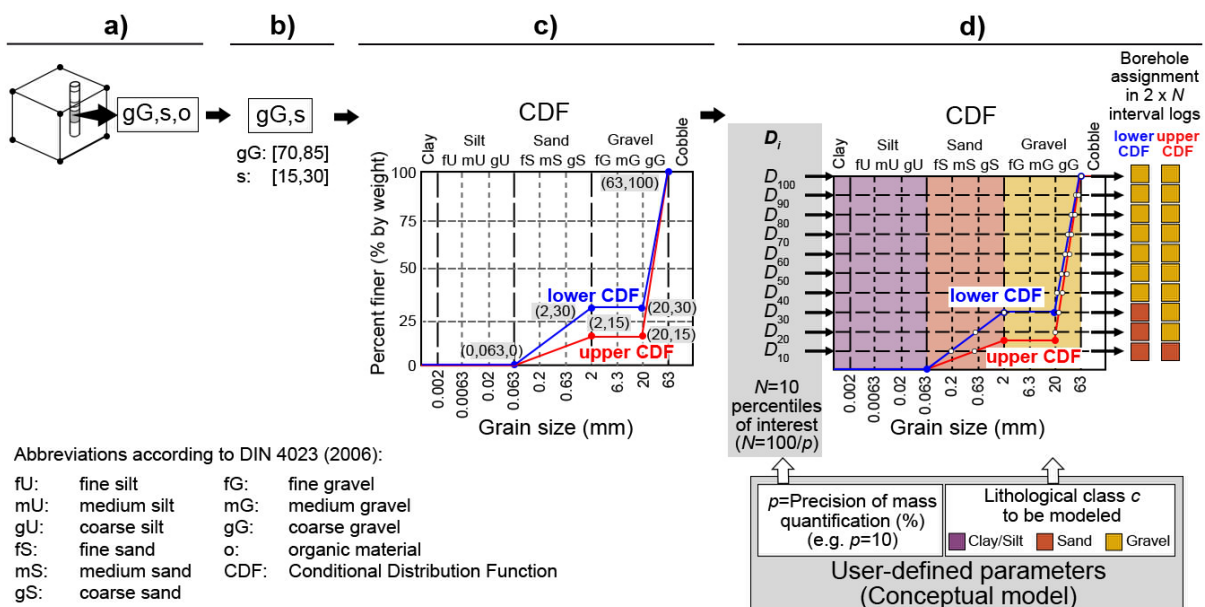


Fig. 8: Steps 1 and 2 of the D_i models method. **a)** Lithological description for a drilled interval in a borehole database. **b)** Quality control (QC), data homogenization and translation of lithological descriptions into intervals of relative frequencies. **c)** Capturing the lower and upper cumulative distribution functions (CDF) bounds for all sediments. **d)** Reading and coding of lithological classes at each D_i according to conceptual model (precision of quantification and grain sizes to be modeled), modified after Albarrán-Ordás and Zosseder (2022)

In order to achieve a grain-size based, consistent database, the borehole descriptions were firstly subject to quality control (QC), a plausibility analysis, and homogenization, because the borehole descriptions in the databases generally include unnecessary or implausible information. In our example, and as a consequence of the QC, the latter component from the description (gG,s,o) was discarded, resulting in (gG,s), since the presence of organic material does not provide grain-size based relevant information (see Fig. 8b). Every linguistic code indicating a lithology was converted into an interval in the form of $[m_{\min}, m_{\max}]$, representing its possible imprecise region of relative frequency values in which the true value (m_{true}) lies. These ranges arise from the inherent generalizations linked with the soil description schemes used, which provide reference values for the minimal and maximal relative frequencies for each code. Hence, in order to obtain a homogeneous data set for the further use, a correction process of not plausible borehole descriptions ignoring the inherent frequency classification scheme (e.g., describing a lithological frequency over 100%) was also accomplished. In the classification schemes, the true relative quantification of the soil components was bounded between some intervals. Following this interval arithmetic, the borehole description in our example (gG,s) indicates that the relative frequency (%) of the clasts in the range of grain sizes between 20 and 63 mm lies in the interval [70, 85] and, in the case of the clasts between 0.063 and 2 mm, lies in the interval [15, 30](Fig. 8b).

Based on these intervals, cumulative distribution functions (CDF) of the different grain fractions are built. Therefore, the grain-size distribution curve is equal to the discrete cumulative distribution of the lithological classes. The CDF are considered as synthetic distribution functions, since they are not based on results from a real particle size sieve analysis.

Since the intervals describe a range and not a precise percentage of the lithological components, the intervals of relative frequencies are used to build upper and a lower CDF curves representing the most coarse-grained and most fine-grained interpretations of the lithological descriptions. Similar to the Probability Bounds Analysis (PBA)(Aughenbaugh and Paredis, 2007), these curves represent the interpreted bounds between which all possible distributions might lie. Returning to our example, the point (63,100) in Fig. 8c indicates that 100 percent of all grain fractions are finer than a cobble. At the 20 mm abscissa position, two points are represented, one for each minimal and maximal relative frequencies for the sands mentioned earlier. Whereas point (20,15) shows that 15% of all grain fractions are finer than a coarse gravel, point (20,30) indicates a relative amount of 30% being finer than the aforementioned lithology. The first point then belongs to the most coarse-grained interpretation from the borehole descriptions, and the latter to the most fine-grained interpretation. Lastly, at the 0.063 mm abscissa position, two points are represented in the same position, indicating that there are no particles finer than a sand. The grain fractions which were not included in the borehole descriptions are represented by horizontal steps in the shape of both CDF curves, since they do not provide any cumulative relative amounts. We observe in Fig. 8c that this occurs for the following grain fractions: clay, silt, fine to medium gravel, and cobble. The exact distribution within a grain size composed of several minor grain fractions (in this case, e.g., between 0.063 and 2 mm), is unknown when using a lithological scheme as

described above. As a result, the proportions of fine-grained to coarse-grained sands are interpolated by applying a linear equation between two pairs of values for a semi-log plot with an abscissa axis logarithmically scaled.

In order to constrain the partial percentile models, both the lower and upper CDF bounds are read at each of the N reference diameters of the sediment mixture representing the cumulative frequencies. The reading process is implemented according to the parameters defined in the conceptual model: three grain fractions (gravel, sand, and clay/silt) and a precision p of 10% (see Fig. 8d). A set of two recorded lithological classes for each reference diameter D_i is obtained, one from the most fine-grained interpretation from the borehole descriptions, i.e. the lower CDF, and another from the most coarse-grained borehole descriptions, i.e. the higher CDF. This set is then coded into categories, in our example into: 1 (clay/silt), 2 (sand), and 3 (gravel). In this way, the information initially contained in the borehole descriptions for each drilled interval, given as linguistic codes, was converted into a set of data in the format of three rows (D_i , lithological class for lower CDF, lithological class for upper CDF) and by as many columns as the D_i values defined. These data sets describe the interpreted existing lithological class at the specific D_i values for the upper and lower CDF interpretation and can be easily imported into the discretized 3-D space as input data in the form of interval-logs (see Fig. 8d).

4.3.3 Step 3 - Spatial statistical inference

This step includes the spatial analysis of geological trends in the distributions of the grain size proportions detected in the available geological data. As a result, “soft” information on areal trends in the distribution of the proportions of the lithological classes are provided. The integration of the trends or “soft” data is a necessary step prior to geostatistical simulation (Pyrzcz and Deutsch, 2014). The application of all geostatistical algorithms implicitly considers the assumption of stationarity underlying the variable in question - in this case the prevailing lithology from all possible grain sizes defined in the conceptual model. The introduction of deterministic trends overcomes these assumptions (Ringrose and Bentley, 2015). Although a wide range of techniques are used in order to account for trends, no purely objective method for trend modeling exists (Pyrzcz and Deutsch, 2014). Areal trends and vertical proportion curves (VPC) provide a 2-D insight into the spatial distribution of the variables under consideration. In contrast, the 3-D trends combine both in-depth and areal information and account for a fully three-dimensional trend model. Currently, the most common practice consists of subdividing the modeling domain into different large-scale units, e.g. lithostratigraphic units, and inferring the proportions of the categorical variable from the available borehole data in each separated volume (Kearsey et al., 2015; Stafleu et al., 2011).

This modeling approach enables the superimposition of trends, in all their variants, onto the simulation. The type of kriging chosen by the modeler conditions the treatment of stationarity (Ringrose and Bentley, 2015). The trends were addressed separately for each of the reference

diameters D_i . In order to account for the interpretation from both the lower and upper CDF (see Step 1), each D_i value required two trends, one for each CDF bound. Trends were then applied as inputs to constrain the geostatistical simulation in the following form $P_{D_i}(\mathbf{u}; c)$, where $c=1, 2, 3$ and $P_{D_i}(\mathbf{u}; c)$ is the continuous probability between 0 and 1 of lithological class c at location \mathbf{u} .

4.3.4 Step 4 - Spatial continuity model

Step 4 of the methodology concerned the quantification of spatial correlation by means of 3-D variogram analysis, providing the understanding of the spatial continuity of the lithological classes from the hard data, which is the continuity of the indicator variables $I_{D_i}(\mathbf{u}; c)$. For instance, Goovaerts (1997) and Gringarten and Deutsch (1999) provide a comprehensive description of variogram interpretation and modeling.

The spatial geological variance in the borehole data was investigated both for each reference diameter D_i and for the lithological classes considered in the conceptual model. The hard data in interval-logs (see Fig. 8d) needed to be adapted in the form of indicator data in order to use it for the 3-D variogram analysis, and to feed the geostatistical simulations (Step 5). To do this, if we consider the categorical variable under study (which is in this case the lithological class), as well as their mutually exclusive and discrete c values, we can express the indicator categorical variable as (Deutsch, 2006):

$$I_{D_i}(\mathbf{u}; c) = \begin{cases} 1 & \text{if lithological class prevails at location } \mathbf{u} \\ 0 & \text{otherwise} \end{cases}; \quad c = 1, 2, 3, \quad (30)$$

where:

\mathbf{u} : location being estimated.

c : lithological class.

$I_{D_i}(\mathbf{u}; c)$: indicator variable for the lithological class c in the location \mathbf{u} .

Consequently, the hard data are coded into 1s if the lithological class prevails, and into 0s if it does not.

4.3.5 Step 5 - Geostatistical simulation

The modeling approach considers the geostatistical simulation of the lithological class for each D_i in 3-D space. Geostatistical simulation is preferred over estimation in order to generate multiple equiprobable models (Pyrcz and Deutsch, 2014). This is intended to include the various equiprobable interpreted lithologies of the lower and upper CDF bounds for each D_i (see Fig. 8d). The integration of the lithological classes for both bounds ultimately implies the introduction and propagation of uncertainties from the borehole descriptions. In order to ensure an equal

representation of both valid interpretations for each D_i model, it was necessary to fix the same number of simulations for the lower CDF bound as for the upper bound.

Among other possibilities for the geostatistical simulation, the SIS algorithm was selected. This choice was influenced by a variety of aspects. The presence of dense conditioning well data (Hassanpour and Deutsch, 2010) and the lack of clear genetic shapes of the sedimentary bodies (Deutsch, 2006) prioritize the use of SIS and may limit the use of object-based methods. Its voxel-based character also enables the incorporation of high-resolution trends as secondary data (Step 3), as well as the reproduction of small-scale features (Pyrcz and Deutsch, 2014). SIS methods apply indicator kriging (IK) for the simulation of categorical variables (Deutsch, 2006; Goovaerts, 1997), and they introduce heterogeneity using a sequential random path for visiting unsimulated locations in order to draw Gaussian realizations using an indicator transform (Ringrose and Bentley, 2015). SIS visits (iteratively and one-by-one) all unsampled locations until all locations are informed by a simulated value (Journel, 1989). Further, SIS reproduces the hard data from the boreholes (Step 2), the inferred spatial statistics (Step 3), and the spatial continuity of the indicator categorical variables of each lithological class (Step 4). Most SIS variations relate to how the trends are superimposed on the simulation. The general remarks of the different options are summarized in detail in Deutsch (2006).

The application of SIS honors the conceptual model taking place separately for each of the reference diameters defined (D_i). The required number of realizations concerning each D_i is estimated through the analysis of the frequency distribution of the assigned lithological class in the whole model domain. Based on a certain number of simulations, the frequency distribution does not vary significantly. Various simulation sets are run for this purpose, each of them having a different number of realizations. The effort then focused on observing from which simulation set an increase in the number of realizations did not lead to a significant change in the lithological attribution in the whole model. In the example shown in Fig. 9, a total of ten sets are considered. The starting set consisted of 10 realizations and was increased by steps of 10 simulations, reaching a maximal number of 100 for the last set. For each simulation set, the information entropy of the membership to a lithological class was calculated for all voxels of the whole model domain. Fig. 9 illustrates the process of estimating the number of simulations required for each D_i . Fig. 9a and b show the histogram and the probability plot for the information entropy for 10 and 30 simulations, respectively, from which the summary statistics can be computed. The minimal number of simulations was obtained when the entropy summary statistics converged to a constant value. Fig. 9c shows how the aforementioned summary statistics vary when increasing the number of simulations by steps of 10 realizations. We observe that the mean has an initial value of 0.4 and becomes stabilized at a value of 0.5 when at least 30 simulations are run. The simulation process also shows that the 10th, 50th and 90th percentiles of the values obtained vary widely when running simulations sets of 10 and 20 realizations and reach a stable value when the simulation reaches a number of 30 realizations. We can also appreciate this stabilization but less intensively in the case of the standard deviation and the standard error of the mean. In this

example a minimum number of 30 simulations is satisfactory. Fig. 9d represents the sum of the variation of all aforementioned summary statistics between contiguous simulations sets and shows clearly the simulation set from which the information entropy associated to the membership to a lithological class did not vary significantly. Fig. 71 of Appendix B provides an additional illustration of this process.

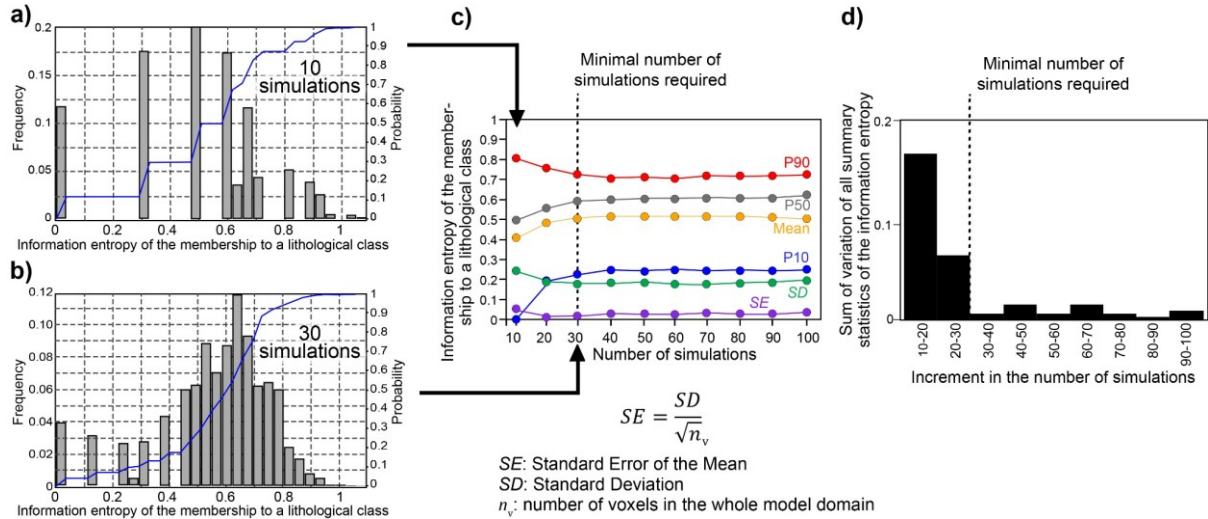


Fig. 9: Step 5 of the D_i models method: Estimation of the required number of geostatistical simulations for each D_i . **a)** Histogram and probability plot of the information entropy of the membership to a lithological class. Number of bins of histogram: 30. **b)** Histogram and probability plot of the information entropy of the membership to a lithological class. Number of bins of histogram: 30. **c)** Plot of summary statistics of the information entropy of the membership to a lithological class obtained for different number of simulations. **d)** Plot of sum of variation of the summary statistics obtained by increasing the number of simulations Fig. 71 provides an additional illustration of this process; modified after Albarrán-Ordás and Zosseder (2022)

4.3.6 Step 6 - Lithological predictability

Partial percentile lithological models (D_i models)

The D_i models represent the lithological class associated with each cumulative frequency of the total detrital mixture in each voxel. Fig. 10a illustrates a schematic example of a set of D_i models. The relative frequency value remained constant and corresponded to the precision p defined in the conception model (10% in this example; see Step 1). There are as many partial lithological models as the number N of percentiles of interest considered. The probability distribution of lithological classes for each D_i in each voxel was calculated as a result of the stochastic simulation. For each D_i , the multiple probability field was encoded on a representation of the most probable lithological classes. The sum of the relative frequencies of each grain fraction can be directly inferred and is shown for two locations, in Fig. 10b and Fig. 10c.

Model Lithological Uniformity (MLU)

The proposed methodology introduces the concept of “Model Lithological Uniformity” as a measure of the degree of the lithological composition homogeneity of a clasts mixture. Fig. 10b and Fig. 10c show the Model Lithological Uniformity values at two locations based on the relative frequencies obtained from the D_i models. The concept of information entropy (Shannon, 1948) has been used in geological 3-D models as an objective measure of uncertainty (Goovaerts, 1997; Wellmann and Regenauer-Lieb, 2012). This concept was adapted to the particular context of clasts mixtures and understood as a measure of the disorder state of a detrital system at a grain-size level in each voxel. The greater the lithological disorder, the higher the lithological entropy, so the entropy equals zero if the heterogeneity has a maximum value, and the lithological uniformity thus reaches a minimum value. In this context, the standardized lithological heterogeneity (normalized to 1) can be expressed as the ratio between the estimated lithological entropy in the presence of three possible lithological classes as well as the upper bound of the lithological entropy ($\log c$). This can be expressed as follows:

$$MLU(\mathbf{u}) = 1 - \frac{H(\mathbf{u}; c)}{\log c} = 1 - \left[\frac{-\sum_{c=1}^C p(\mathbf{u}; c) \times \log [p(\mathbf{u}; c)]}{\log c} \right] \quad [0, 1], \quad (31)$$

where:

$MLU(\mathbf{u})$: Model Lithological Uniformity at location \mathbf{u} .

\mathbf{u} : location being estimated.

c : lithological class.

C : largest lithological class ($C=3$ for gravel in the default case).

$H(\mathbf{u}; c)$: lithological entropy of the membership to a lithological class c at location \mathbf{u} .

$p(\mathbf{u}; c)$: relative frequency of lithological class c at location \mathbf{u} based on the D_i models.

Most Uniform Lithological Model (MULM)

By applying the concept of “Model Lithological Uniformity” (MLU), the relative frequencies of each lithological class were computed based on the D_i models. To illustrate this, Fig. 10b and Fig. 10c show the resulting relative frequencies at two random locations, u_1 and u_2 with differing degrees of lithological homogeneity. In each location of the 3-D space, the lithological classes possessing the highest relative frequency, e.g. $c=2$ (sand) for u_1 and $c=3$ (gravel) for location u_2 , conform with the Most Uniform Lithological Model of the system (see Fig. 10d). This model itself does not show the complexity of the geological reality in each voxel (the clast mixture), but rather represents the distribution of the most dominant lithology.

$$MULM(\mathbf{u}) = c \text{ with } \max(\{p(\mathbf{u}; c) : c = 1, \dots, C\}), \quad (32)$$

where:

\mathbf{u} : location being estimated.

c : lithological class.

C : largest lithological class ($C=3$ for gravel in the default case).

MULM(\mathbf{u}): Most-Uniform Lithological Model in the location \mathbf{u} .

$p(\mathbf{u}; c)$: relative frequency of lithological class c at location \mathbf{u} based on the D_i models.

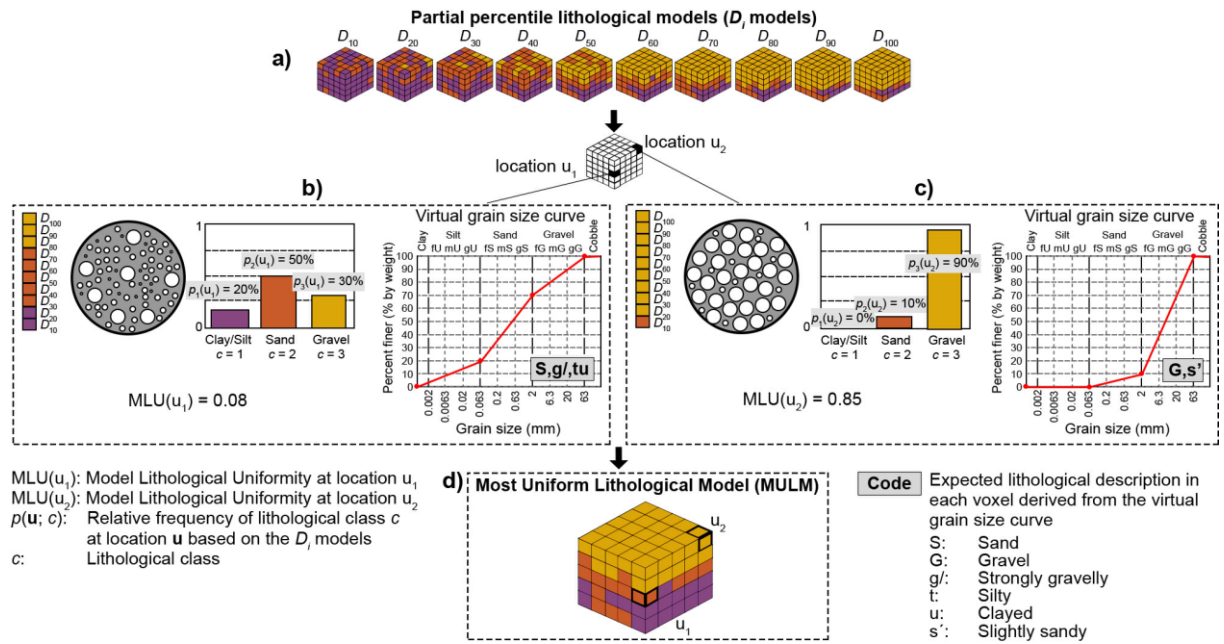


Fig. 10: Step 6 of the D_i models method: Lithological predictability. **a)** Partial percentile lithological models (D_i models). **b)** Location u_1 showing a low MLU value. **c)** Location u_2 showing a high MLU value. **d)** Most Uniform Lithological Model representing the distribution of lithological classes owning the highest relative frequencies in each voxel. The lithological class c is represented in different colors: $c=1$ (clay/silt) in purple, $c=2$ (sand) in orange, and $c=3$ (gravel) in yellow. Lithological descriptions according to DIN standards (DIN 4023, 2006). (S,g,tu): strongly gravelly sands with a moderate presence of silt/clay. (G,s'): slightly sandy gravels; modified after Albarrán-Ordás and Zosseder (2022)

4.3.7 Step 7 - Multipurpose usability

As shown in Step 6, the relative frequencies of each grain fraction given by the conceptual model were directly inferred from the D_i models. This is shown at the center of Fig. 10b and Fig. 10c. A synthetic grain size distribution curve can thus also be derived at each location (see at right of the preceding figures) or extracted along virtual wells. The availability of synthetic grain size curves in individual voxels strongly encourages the model usability from various points of view, which are summarized in Fig. 11. The lithological classes can be reclassified on a cell-by-cell basis, with categories for sediment mixtures, lithofacies types, soil classes for civil engineering purposes, or from cut-offs from numerical property distributions (Fig. 11a3). If needed, the expected lithological composition at a voxel scale can be expressed as coded information according to

regional or national guidelines (see the examples in Fig. 10). Moreover, the numerical attribution and modeling of property distributions is not limited to the mere parameterization of assignments based on the literature or field/laboratory data (Fig. 11a1). The D_i models approach enables derivation of empirical parameters that are dependent on the virtual grain size variations at each model location, e.g. hydraulic conductivity (Beyer, 1964; Hazen, 1892; Seelheim, 1880), effective porosity (Marotz, 1968), and geotechnical parameters. Alternatively, the aforementioned grain size-dependent parameters can be calculated from the CDF bounds of the lithological descriptions along the drilled boreholes. The 3-D property distributions can then be modeled, if required (Fig. 11a2). Whatever the choice made, it then leads to a prediction of the property distributions of such parameters more accurately in 3-D space than those obtained with the straightforward attribution.

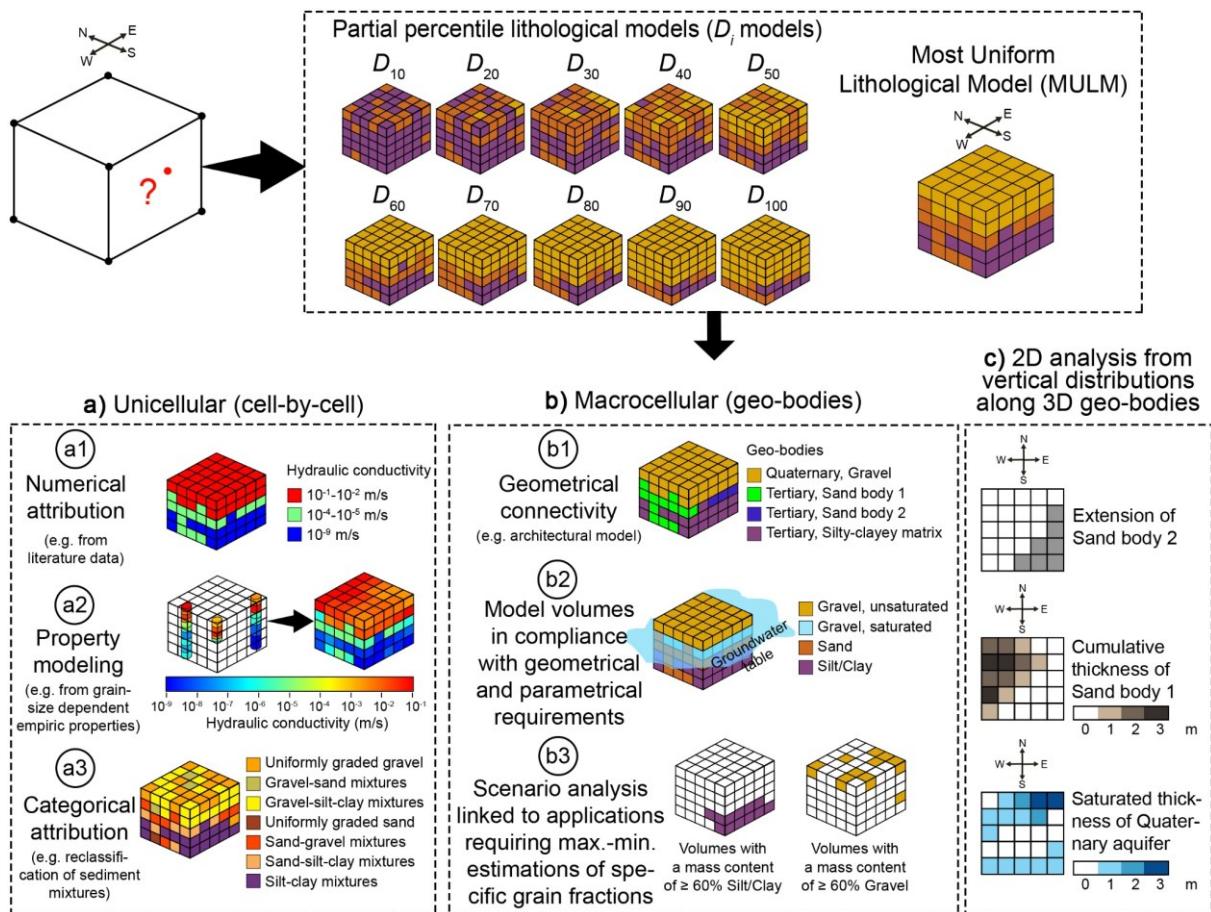


Fig. 11: Step 7 of the D_i models method: Multipurpose usability; modified after Albarrán-Ordás and Zosseder (2022)

In addition, building linkages or groundwater related issues between model cells based on geometrical or parametrical constraints is the basis for identifying groups of cells in compliance with some requirements. This is, for example, the case when analyzing the connectivity of geological bodies in order to determine a reservoir architecture (see Fig. 11b1), or when capturing the saturated aquifer parts overlying a confining layer owing to a certain thickness (Fig. 11b2).

The identification of pessimistic, realistic, and optimistic scenarios for the distribution of specific lithologies in space on the basis of modeled grain-size fractions can be of benefit to applications demanding the geometries of, e.g., confining layers or aquifers (see Fig. 11b3), or for civil engineering issues like tunnel construction. Given that the modeling of lithology distribution always includes uncertainties (caused by non-optimal spatial distribution of input data, imprecise lithological descriptions, etc.), a conservative representation of the lithology geometry of interest (e.g., the maximal lithology distribution with a higher permeability) can support practical assessments like the calculation of dewatering regarding underground structures (to name one example). In this example, a conservative representation of the lithology of interest means that lithology having a higher degree of permeability (gravel, sand), thus causing a higher water encroachment, is modeled with a larger spatial occurrence in order to be on the safe side for the further dewatering calculations. For example, we would in this use case propose a specific D_i model (e.g. 60th percentile) as a representation of the lithology distribution. The aforementioned unicellular and macrocellular workarounds are susceptible to further analysis by means of classical 2-D computations combining features from both approaches.

4.4 Application of the method in the case study in the city of Munich

4.4.1 Geological setting

The proposed methodology was tested on a city-wide scale in Munich (Germany), which is located in the North Alpine Foreland Basin in the southern part of Germany (Fig. 12a). This typical asymmetric foreland basin, also known as Molasse basin, dips southwards underneath the Alps and is filled with up to 5,000 m of sediments belonging to several marine to continental transgressive/regressive sequences (Lemcke, 1988). The most recent deposits in this basin are formed mainly by Quaternary coarse-grained gravels from glacio-fluvial origin, and they cover a total surface area of 2,250 km² along the so-called Munich Gravel Plain (MGP) (see Fig. 12b).

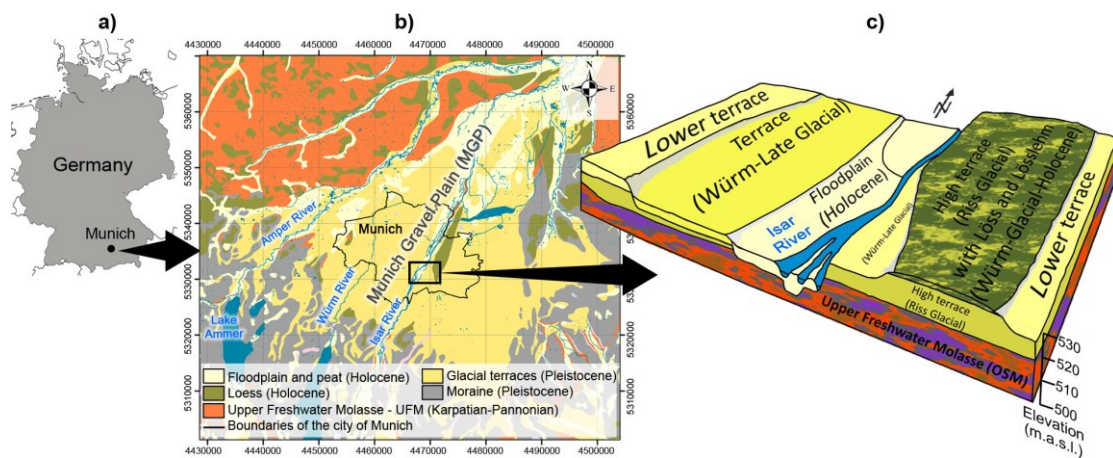


Fig. 12: Geological setting in the case study area. **a)** Location map. **b)** Simplified geological map in the Munich area showing the main lithostratigraphic units and the boundaries of the city of Munich; modified after Freudenberger and Schwerd (1996). **c)** Schematic geological view of the city of Munich; modified after Münichsdorfer (1922). m.a.s.l.: meters above sea level

In the city of Munich, the MGP comprises various sandur terraces as well as the floodplain of the Isar River, formed by gravel deposits having a thickness from few meters up to several decameters. Most of the deposits in the MGP were formed during the Pleistocene glacial cycles of Riss and Würm. The melt waters of the Isar-Loisach glacier resulted in the formation of braided rivers which piled up gravelly deposits to huge outwash plains (Bauer et al., 2005). The Quaternary aquifer constitutes one of the most productive groundwater occurrences in Europe (Freudenberger and Schwerd, 1996) and conforms with the principal shallow aquifer in the region, which hosts a wide variety of coexisting groundwater uses, such as industrial water, drinking water, or groundwater heat pumps (GWHPs) for open loop geothermal systems. The city of Munich, covering an area of approximately 310 km² of the total extent of the MGP, is situated in the central part of this outwash plain (see Fig. 12b) and concentrates the majority of uses (e.g., over 2800 GWHPs were recorded in 2020). This relevance has led to an increasing number of scientific activities in recent years addressing various aspects of this aquifer in the Munich area, e.g., its hydrogeological classification like hydrofacies characterization of the gravelly deposits (Theel et al., 2020) and the geostatistical relief modeling of the geometry of the aquifer basis (Albarrán-Ordás and Zosseder, 2020), or characterization for geothermal purposes (Böttcher et al., 2019).

These deposits are underlain by fluvio-lacustrine successions in erosive discordance, representing the last Tertiary sedimentation stage of the basin (see Fig. 12c). This deposition occurred during the Middle and Late Miocene and is represented by the Upper Freshwater Molasse (UFM) (Bachmann and Muller, 1992). The filling deposits of UFM are several hundred meters thick and comprise grey or brownish, and partly also reddish clayed-marly slackwater sediments and sandy to coarse-grained river channel deposits. The mica-bearing clayed and sandy sediments are fairly characteristic of the UFM deposits. The latter are yellowish grey to brownish and are commonly known as *Flinz*. Since these formations consist almost exclusively of unhardened fluvio-terrestrial sediments, the lithological differentiation represents the distinctive criterion for subdividing the UFM into major lithostratigraphical units, which are in turn classified into the Western and the Eastern Molasse facies (Doppler et al., 2005; Schwerd et al., 1996). The UFM includes relevant but less-explored groundwater occurrences and are characterized by their high level of geological complexity, which poses a major challenge to characterizing their geometric architecture and geological composition. The groundwater from this aquifer system is exploited at different depths for a wide variety of uses. Among others, it is mainly used for public and drinking water, but also as an industrial and brewing water supply. In addition, this aquifer is conceived for facilitating emergency water supply, if required. A great deal of infrastructure has been built in both the Quaternary and the Tertiary units, e.g., pipework systems, tunnels, and the deeper subway structures. The coexistence of this diverse range of uses and influences as well as the high natural variability of these deposits highlight the need for their long-term groundwater management. Due to its relevance, the latter formation has also been subject of research in recent years (Prösl and Anders, 2011; Zosseder et al., 2019).

4.4.2 Conceptual model and borehole database

A borehole database from the Soil Information System of Bavaria (Germany), abbreviated as BIS, was considered in the present case study. This database is a comprehensive soil inventory managed by the Bavarian Environmental Agency and is typical of the datasets provided by governmental institutions, e.g. geological surveys. This database includes, among other issues, information on an exhaustive borehole database from the drilling operations during recent decades (Kresse and Danko, 2012). Consequently, the workflows adopted for the data acquisition and preparation were adapted to the peculiarities of this borehole database. However, as mentioned in Section 4.3 (Step 2), the workflow can be adapted to other borehole databases as needed.

The borehole descriptions contained in the BIS database consist of coded information representing the geological composition for each drilled interval and according to the following standards: DIN 4023 (2006), DIN EN ISO 14688-1 (2020), DIN EN ISO 14688-2 (2020), and DIN EN ISO 14689 (2018). These standards define the symbolic codes used for soil description. The dataset used is comprised of the lithological descriptions from 210,322 drilling intervals. This information corresponds to a total number of 20,114 boreholes amounting to a density of approximately 64 boreholes per km² on average (see Fig. 13). The lithological descriptions from the boreholes sum up to a total of 347 km of drilled materials with lithological information to process.

The framework model consisted of a grid covering an area of 27 by 21 km. This was comprised of approximately 23 million voxels, each of which had a resolution of 100 by 100 meters in the horizontal axis, and 1 m in the vertical direction. The modeling domain had a maximal depth of 170 meters above sea level (m.a.s.l.), and the highest voxel was at a height of 590 (m.a.s.l.). The model holds a very variable thickness, since the ground surface has a marked downward slope towards the north. The user-defined categorization of the lithological classes resulted in three types, depending on the particle grain sizes: 1 for clay and silt (≤ 0.063 mm), 2 for sand ($> 0.063 - 2$ mm), and 3 for gravel (> 2 mm). This decision was primarily based upon selecting the lithological classes with more practice-oriented implications. In addition, a precision p of 10% in the relative amounts of grain fractions was defined as previously mentioned by way of example in Section 4.3.

4.4.3 Spatial continuity of the lithological classes

To describe the spatial correlation of each lithological class (1, 2, 3), the variograms were estimated from the available interval-based lithological information of the 210,322 borehole descriptions. The points in Fig. 14a show the relationship between the maximal horizontal correlation ranges and the vertical correlation ranges for all D_i values and all lithological classes. Although the variogram ranges are not the same as the element body sizes (Ringrose and Bentley, 2015), a set of dotted lines was also plotted in order to visualize different reference width-

thickness ratios (W/T) and to compare the correlation ranges obtained with the dimensions of fluvial-channel bodies. The W/T ratio defines the broadness or narrowness of architectural elements of fluvial systems (Miall, 2014). Gibling (2006) emphasized in the study of the 3D geometry of fluvial channels bodies proposing twelve different types of channel bodies and valley fills based on more than 1500 bedrock and fluvial bodies for which width and thickness were recorded. A comparison between the correlation ranges obtained and the results from Gibling (2006) indicated that the correlation ranges of the gravels can be attributed to the common W/T spectrum of values for meandering rivers (see Fig. 14a), which are result of the juxtaposition of deposits from different courses. These fluvial channel bodies typically have ranges from 4 to 20 m in thickness, from 0.3 to 3 km in width, and W/T values from 7 to 940. Similarly, we can also observe that the narrower correlation ranges of the sands very closely fit the dimensions of fixed river systems (see Fig. 14a). These deposits may represent single-channel or braided-sand bed networks (Gibling, 2006) and typically have a W/T from 2.5 to 150, a thickness of between 3-15 m, and widths of between 15-300 m.

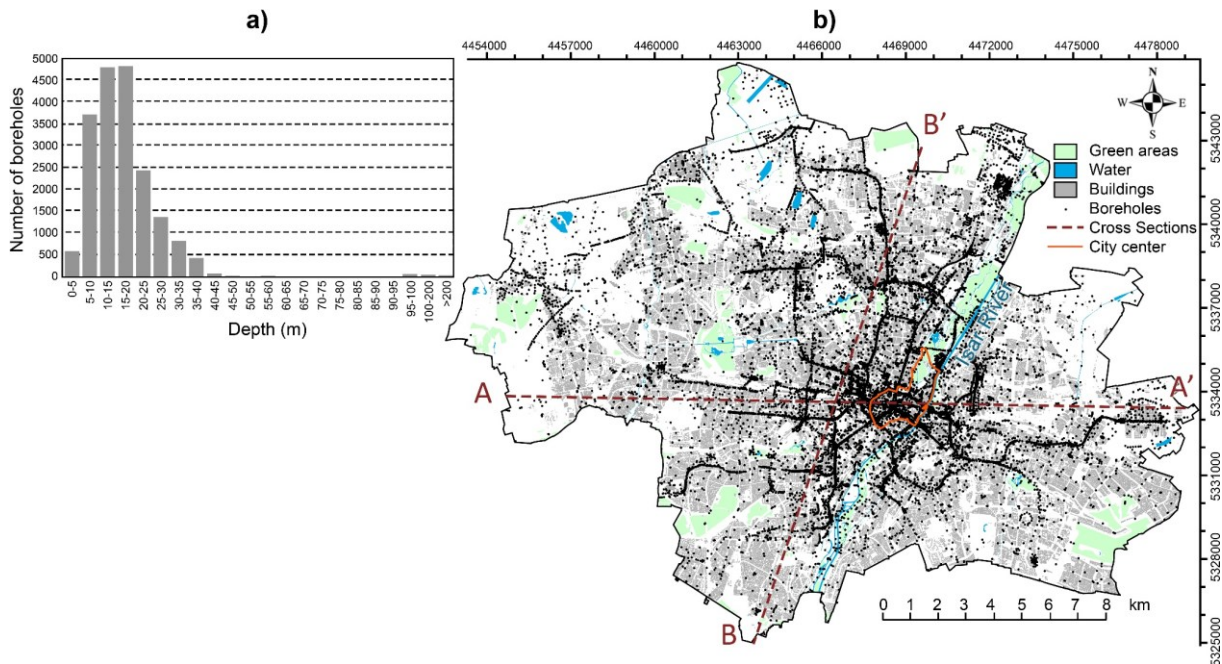


Fig. 13: Borehole database in the case study area. **a)** Histogram showing the number of boreholes reaching a certain final depth in the city of Munich. The total number of boreholes is 20114. **b)** Location map of the area of the case study showing the location of the boreholes used and two cross sections AA' and BB', which are used to present and discuss the results

On the other hand, Fig. 14b, Fig. 14c, and Fig. 14d illustrate the spatial continuity in the horizontal direction by means of the ellipsoidal representations regarding the direction of maximal correlation and correlation ranges in the horizontal direction for the three lithological classes as well as each D_i reference diameter.

The variogram analysis showed that the gravels have high horizontal-vertical ratios for almost every D_i (Fig. 14a) and, at the same time, they have high horizontal correlation ranges, especially

from the D_{40} value (Fig. 14b). Although most variograms are less anisotropic, the prevailing angles of maximal correlation are E-W. In the case of sands, lower ranges in both figures were evident, indicating a priori narrower geometries associated with this lithology (Fig. 14c). Except for D_{10} , D_{20} , and D_{100} , all of the maximal horizontal correlation ranges were smaller than approximately 200 m, with correlation angles approximately along the 100° line.

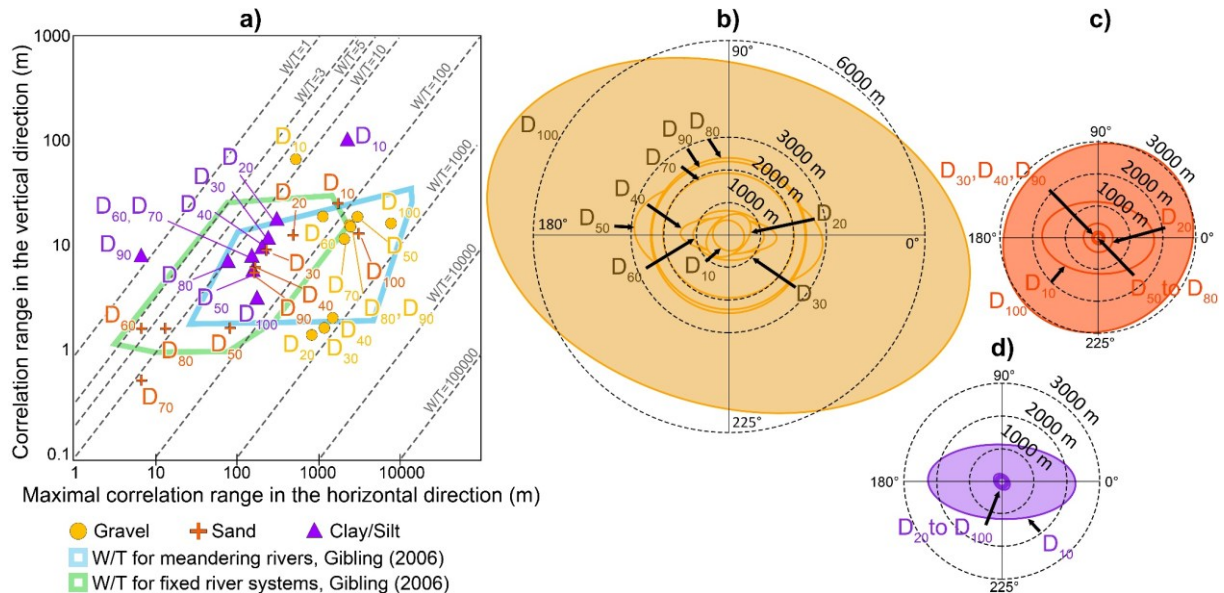


Fig. 14: Spatial continuity results of the lithological classes in the subsurface 3-D space in the city of Munich. **a)** Relation between the correlation ranges in the horizontal and vertical directions of each D_i model for each lithological class and comparison with common width/thickness (W/T) spaces of fluvial-channel bodies from Gibling (2006). The dotted lines represent different W/T ratios. **b)** Correlation ellipsoids for the lithological class “gravel” for each D_i value. **c)** Correlation ellipsoids for the lithological class “sand” for each D_i value. **d)** Correlation ellipsoids for the lithological class “silt/clay” for each D_i value

4.4.4 Partial percentile lithological models (D_i models)

The distribution of lithological classes 1, 2, and 3 was modeled for each fixed D_i value of the cumulative frequencies. The D_{10} , D_{50} and D_{100} lithological models are shown in Fig. 15 as an example of the set of D_i models. Behind each D_i model, the probability of occurrence of each lithological class in each voxel based on 50 stochastic simulations for each D_i model will remain for further interpretation.

As might be expected, an increment in particle size of the sediments became clearly evident as the cumulative frequency of the whole sediment mixture increased from D_{10} to D_{100} . The distribution of lithological classes obtained for the D_{10} model indicated that the 10% of the finest particles in both the Quaternary and UFM units are mostly composed of clays and silts and, to a lesser extent, of sands. The gravelly areas in this model are extremely rare and reflect deposits made of at least 90% gravel, which are only present very locally in the Quaternary and a deep UFM formation. The D_{50} model shows that the 50% of the finest sediments in the UFM are still mostly fined-grained. The Quaternary, in contrast, is characterized by a picture dominated by the presence of gravels,

indicating that all areas marked as yellow are expected to own relative percentages of gravels of at least 50%. The last partial lithological model shown here, this is the D_{100} model, shows clearly the presence of clayed/silty successions in the UFM, which means expected relative percentages of 100% of the same lithologies. These impermeable beds are likely to behave as aquifuges between the different confined aquifers in the UFM, mostly composed of sands. In this case, the Quaternary sediments are almost completely formed by at least a small relative percentage of gravels.

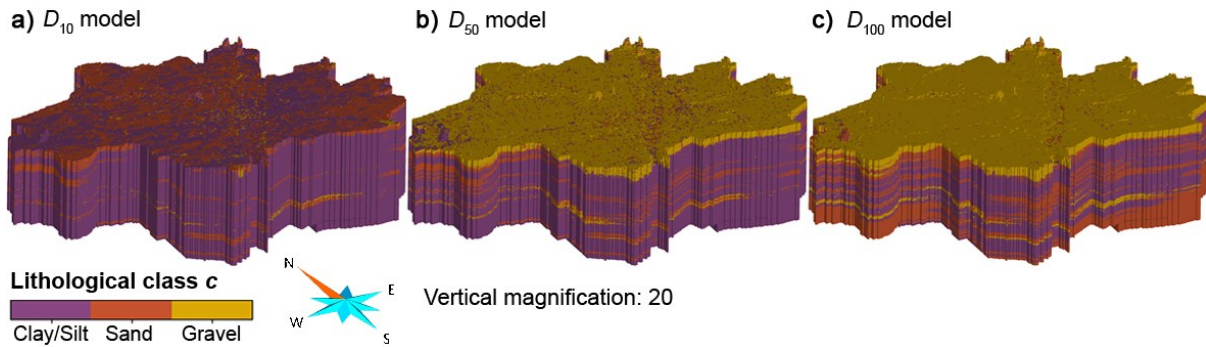


Fig. 15: 3-D views of the partial percentile lithological models (D_i models) in the city of Munich. **a)** D_{10} model. **b)** D_{50} model. **c)** D_{100} model. Modified after Albarrán-Ordás and Zosseder (2022)

4.4.5 Model Lithological Uniformity (MLU) and Most Uniform Lithological Model (MULM)

Based on the D_i models shown above, the Model Lithological Uniformity and the Most Uniform Model are derived as described in Step 6 in Section 4.3. Fig. 16a and Fig. 16b show the Model Lithological Uniformity of the detrital mixtures in Munich's subsurface, representing the degree of homogeneity of the clastic mixtures present in the Quaternary and UFM deposits (see Section 4.4). The lithological classes owing the highest relative frequencies in each voxel in the city of Munich constitute the Most Uniform Lithological Model presented in Fig. 16c and Fig. 16d.

The results clearly highlight a main gravel body at the top, holding a median Model Lithological Uniformity of 0.38. Only 10% of the Quaternary gravels show extremely high MLU values above 0.54. This volume covers, with a median thickness of 13 m, the first meters from the topographical relief and corresponds with the Quaternary glacio-fluvial deposits. Moreover, the bottom surface of this geo-body exhibits a variable relief composed of meander-shaped channels and plateaus (Albarrán-Ordás and Zosseder, 2020). The thickness distribution of the Quaternary deposits is highly variable and only locally interrupted at Tertiary hills, such as the "Aubinger Lohe", a spot at the western end of the city or along the slope edges of the Isar River crossing the city of Munich from south to north (see Fig. 12b, Fig. 13b, and Fig. 16c). As we can see, the gravelly sediments in the Quaternary are interrupted in depth by a prominent erosive discordance below which the sandy, silty and clayed lithologies of the UFM become predominant. As a result, wide areas of the quaternary gravels along this discordance are directly underlying of sandy UFM-sediments and

hence, showing a potential hydraulic interaction area between quaternary and tertiary aquifers (so called hydraulic windows). Below, we can distinguish the UFM as a system consisting of a series of more coarse-grained (sandy) geological bodies alternating with fine-grained successions. Fine-grained deposits can reach significant thicknesses and they separate the numerous coarse-grained geo-bodies one another. The coarse deposits are mainly composed of sands and in greater depths of approximately 300-350 m.a.s.l. the content of gravel bodies increases importantly. As shown in Fig. 16a and Fig. 16b, the Model Lithological Uniformity values are highest in many clayed and silty formations in the UFM, which correspond with the areas mentioned in Section 4.4.4, when describing the D_{100} model. The MLU decreases to 0.2-0.4 in the Tertiary sandy-dominated aquifers. Almost 25% of the deposits in the UFM, most of them fine-grained, reach the highest MLU values and about the same percentage are below 0.54. Compared to the Quaternary sediments, a larger dispersion of the MLU values is observed in the UFM (IQR of 0.46 versus only 0.26 in the Quaternary). The increased thickness of these fine-grained homogeneous deposits increased the median of the MLU to 0.7 in the whole UFM.

4.4.6 Architectural model of the Quaternary and UFM deposits

As previously mentioned in Section 4.4.1, both the wide variety of existing and potential future subsurface uses and the inherent non-constant geological properties of the fluvio-glacial and lacustrine deposits underlying the city of Munich will require a long-term management of the underground space. The challenge for a successful underground management is to identify geo-bodies having specific potentials and their connection or separation to others, like the connection between different aquifers and potential hydraulic interactions. For this purpose, it is critical to analyze the geometrical continuity of the prevailing lithologies shown in Fig. 16c. This leads to a subdivision of the modeling space into different geological bodies according to their geometrical associations to ultimately determine the reservoir architecture (Fig. 16e and Fig. 16f). Immediately prior to analyze the geometrical continuity of the lithological distribution of the model shown in Fig. 16c and Fig. 16d, a Moving Window Filtering (windows size of 5 cells in the three directions) was applied. The aim of this filtering is to exclude isolated cells, such as e.g. small isolated sand lenses, in the architectural model. The excluded cells were not considered to be relevant for the purposes of the architectural model due to their isolated nature and minimum extension.

The application of the D_i models method and the subsequent interconnectivity analysis resulted in four extensive coarse-grained geological bodies separated from one another by fine-grained silty and clayed successions in the UFM. This subset of bodies was termed as T1 to T4, from shallower to greater depths, respectively. At the top, the T1 geo-body consists of a multistory and laterally extended sand body with a maximum depth of 138 m below ground level. Within the T1 body additional separations were made which exist only in some spatial parts. Hence, T1 was identified in tiers, named herein T1A to T1D, which have a variable extension and thickness but remain, as a whole, geometrically connected in the city area presenting different areas of

preferential connectivity at various depths. As we can see in Fig. 16e and Fig. 16f, the gravelly sediments in the Quaternary are interrupted by a prominent erosive discordance. As a result of the erosion processes, some of the old deposits of UFM are only present locally and not throughout the whole modeling area, which can be seen, for instance, in Fig. 16f, where the T1A geo-body (highlighted in dark blue) in the northern half of the city is missing. Based on the reservoir architecture, differentiated erosion at the Quaternary aquifer base ultimately leads to a connection of this aquifer with different underlying aquifer parts of the UFM in multiple areas throughout the city (see Fig. 16f). The coarse-grained sandy body T1 (A-D) hosts the main aquifer systems exploited at different depths in the UFM in a complex structure. In contrast, the deeper aquifers T2-T4 of the UFM can be clearly separated and have no further hydraulic interlinkage to other aquifers. Therefore, reservoir architecture derived by the D_i models method and its consequences in terms of aquifer interactions constitute a significant step forward in understanding and ultimately providing an effective ground-water management system. Both a schematic graph and a detailed description of the aquifer systems and tiers from the architectural model are shown in Tab. 9 and Fig. 72 of Appendix B.

The wide range of groundwater uses present in UFM aquifers was mentioned earlier in Section 4.4.1. In order to properly manage these and future applications and characterize the aquifer systems in the UFM, it will be necessary to itemize the current exploitation status of the different aquifers. This can be done by means of analyzing the filter pipes length and depth for a number of nearly 4,500 existing wells and groundwater stations installed in the Munich subsurface. A short extract of this process is illustrated in Fig. 16f. This itemization enables the selective grouping of groundwater measurements together for each separated aquifer system and support ultimately the generation of reasonable hydraulic potentiometric surface maps for each aquifer. Hence, individual hydraulic potential maps for the aquifer sections T1A-D and T2 were produced in the city of Munich based on the modeled underground architecture, as Fig. 16f shows. The potentiometric surface maps were generated using geostatistical interpolation methods (Universal Kriging) and relied on an elaborate groundwater measurement campaign performed in April 2018 within the framework of the GeoPot research project (Geopotentials of the Tertiary subsurface in the wider area of Munich, Germany) (Zosseder et al., 2019). The individual analysis for each aquifer provided by this approach also enables individually addressing a water chemistry characterization of each aquifer in subsequent steps. This was also accomplished in the aforementioned research project and showed significant variations for the different aquifer sections.

4.4.7 Example of application for scenario analysis: design process of a dewatering system

The set of D_i models offers a flexible system for a scenario analysis in determining both coarse-grained and fine-grained geological deposits for various applications.

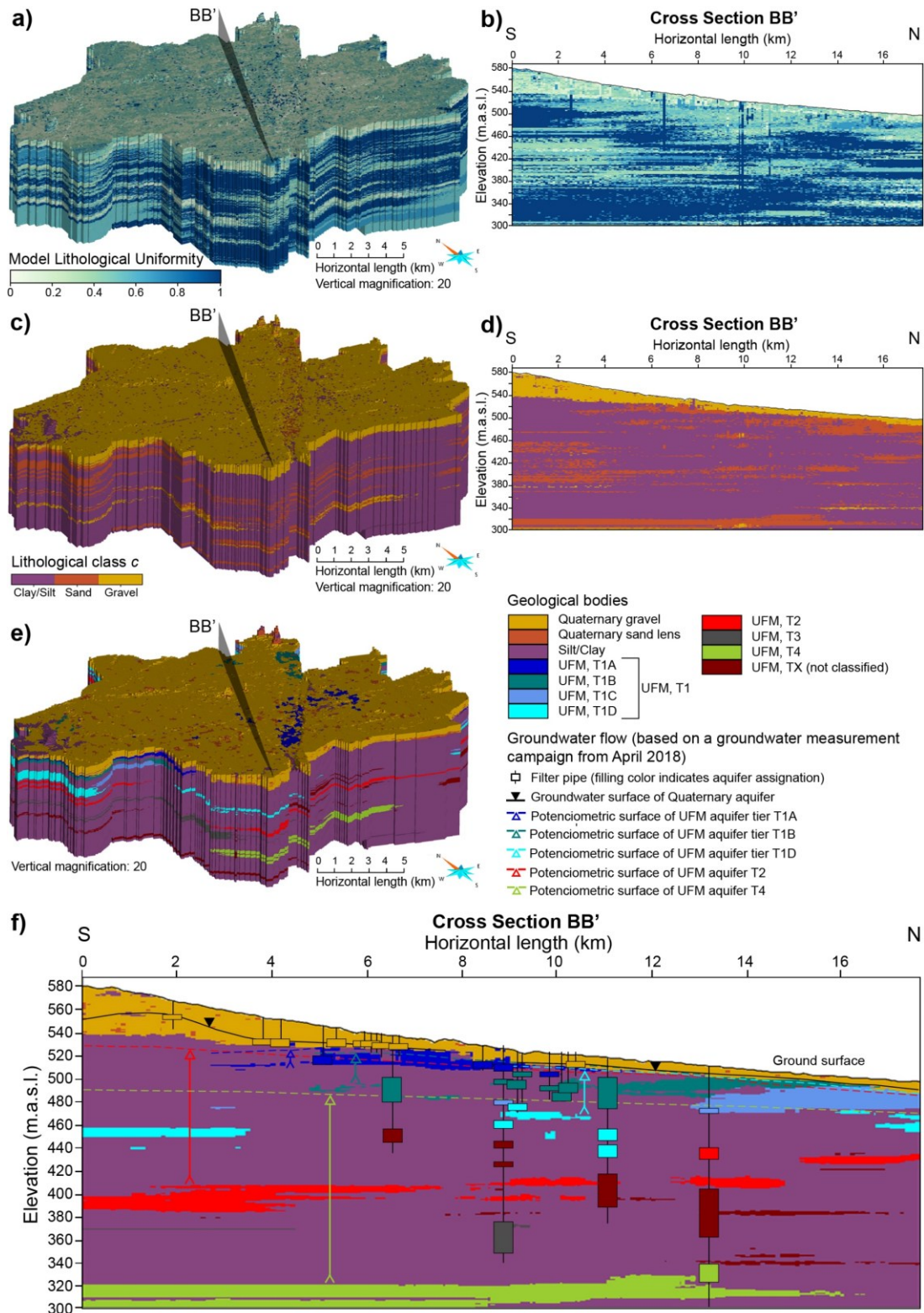


Fig. 16: Case study in the city of Munich. **a)** 3-D view of the Model Lithological Uniformity. **b)** Cross section BB' showing the Model Lithological Uniformity. **c)** 3-D view of the Most Uniform Lithological Model. **d)** Cross section BB' showing the Most Uniform Lithological Model. **e)** 3-D view of the architectural model of the Quaternary and UFM deposits. **f)** Cross section BB' showing the architectural model, the aquifer assignment to the filter pipes and the groundwater and potentiometric surfaces (T3 almost not prominent, because it occurs mainly in the western part of Munich; m.a.s.l.: meters above sea level). Modified after Albarrán-Ordás and Zosseder (2022)

In this example, the ultimate goal consists of determining the parts of the gravelly Quaternary aquifer that influence the design process of a dewatering system for an excavation in an urban area based on conservative assumptions. To this end, we considered the groundwater contour map of the Quaternary aquifer obtained from a detailed measurement campaign containing over 6,000 groundwater wells performed in April 2014 (Albarrán-Ordás and Zosseder, 2020; Böttcher et al., 2019; Zosseder et al., 2015). In this case, the conservative scenario (in terms of the most demanding dewatering), was estimated by capturing the aquifer geometries holding a maximum expected amount of water-saturated coarse-grained sediments (gravels). According to the standards for soil description used in this case study (see Section 4.4.2), gravel-dominated deposits were characterized by a minimum relative amount of 40% of gravels. Thus, water-saturated aquifer volumes holding 40% of gravels can be therefore considered as the most demanding dewatering scenario. These volumes can be assessed by estimating the groundwater which fills the gravelly sediments below the water table in the D_{60} model, which can be identified in Fig. 17a. By contrast, the aquifer parts holding at least 60% of gravels may represent an optimistic forecast regarding a better situation for dewatering shown in Fig. 17b. The latter scenario can be inferred by the water-saturated gravelly volumes in the D_{40} model. The results show that the conservative scenario for the most demanding dewatering design resulted in a substantial increment representing an 83% increase in the water-saturated areas along the cross section (represented in blue).

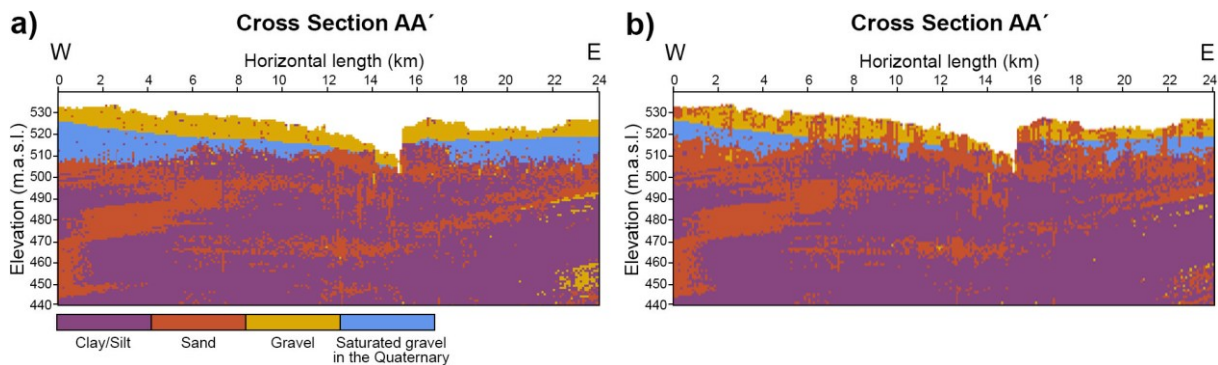


Fig. 17: Cross section AA' showing the results of the scenario analysis for the design process of dewatering systems in the Quaternary aquifer in the city of Munich. **a)** Conservative scenario representing the most demanding dewatering in view of the D_{60} model. **b)** Optimistic scenario representing the less demanding dewatering in view of the D_{40} model (m.a.s.l.: meters above sea level)

4.5 Discussion

The modeling approach presented herein aims at better capturing the lithological variability of detrital systems at a voxel scale. This is achieved by estimating relative proportions of mass fractions of the lithological classes, and thus reducing significantly the stationary assumption in each voxel. The current modeling methodologies tend to assume a stationary prevailing class (lithologies, lithofacies, hydrofacies, etc.) in each voxel in predicting the final image of geology (Hademenos et al., 2019; Kearsley et al., 2015; Stafleu et al., 2011). They are commonly applied in

combination with stochastic simulations, thus providing probabilities of occurrences from multiple realizations which actually do not represent the relative quantification of the classes in the sediment mixture (Stafleu and Dubelaar, 2016). The aforementioned assumption is even more notable in lithostratigraphic models, in which constant properties are assigned to each unit (Kearsey et al., 2015). In contrast, the proposed methodology predicts the lithological classes associated to cumulative frequencies of the whole clasts mixture in each voxel after defining a constant frequency or precision p (e.g., 10% in the case study). Herein, the stationarity space lies only within the lithology assigned to each cumulative frequency, so no quantification of lithological classes is possible below the defined precision. The introduction of the concept of Model Lithological Uniformity (MLU) expresses the degree of homogeneity presented in the clasts mixture in each voxel based on all cumulative frequencies. This concept arises from the adaptation of the concept of information entropy as a measure of the disorder state of a detrital system. The concept of information entropy, which has been applied successfully as an objective measure of uncertainty in geological 3-D models (Bianchi et al., 2015; Wellmann and Regenauer-Lieb, 2012), is then used in a different context. The quantitative aspect of this method benefits from high borehole densities and high levels of detail in the lithological descriptions. If no grain-size-based descriptions are available, then the method loses its added predictive value in terms of relative amounts of lithologies. The user-defined character of this method may result in an overly arduous process if the number of grain fractions being modeled and the precision are unrealistically high.

One common aspect of 3-D geomodels in detrital systems is obtaining a 3-D distribution of the most dominant or prevailing lithological classes. This representation, sometimes referred as a mean model (Pyrzcz and Deutsch, 2014), holds the categories most likely present in each voxel. Current methods address this by assigning the most probable distribution of classes from the stochastic simulation, and this constitutes the main modeling objective. The proposed method can directly derive a Most Uniform Lithological Model (MULM), with the distribution of classes owning the highest relative frequency in the clasts mixture. The MULM has been successfully implemented in the city of Munich. This is the basis for the architectural model representing the reservoir configuration in the Quaternary and UFM deposits and the subsequent itemization of the current exploitation status of the various aquifers (Section 4.4.6).

In order to discuss the predictive ability of the presented methodology, a cross validation procedure was implemented for the estimation of lithological classes in the case study. This technique was based on the elimination of some hard data - a number of boreholes and their known lithological descriptions - and the ulterior re-estimation of the lithological composition at those locations where the true lithology is known from the remaining borehole data (e.g., Isaaks and Srivastava, 1989). The subsequent analysis of the discrepancies indicates the quality of prediction of the modeling process (Pyrzcz and Deutsch, 2014). Special attention was given to the impacts of misclassification and to the ability of the modeling approach to predict different degrees of lithological homogeneity given by the Model Lithological Uniformity.

In a first step, 5% of all hard data was randomly excluded. This amounted to a total number of 1,000 boreholes covering 19,022 m of lithological descriptions. To this end, the excluded data comprised boreholes at different depths distributed throughout the whole model. The 3-D modeling process was run with the same model setup and the spatial continuity model of the indicator categorical variables of each lithological class as those described in Sections 4.3.2 and 4.3.3. The superimposition of trends was adapted so as to ignore the lithological descriptions of the excluded 1,000 boreholes.

The quality of prediction was checked along the excluded boreholes to their final depths at intervals of 10 cm along the 1,000 boreholes. This checking process was developed qualitatively by measuring the fuzzy closeness of the estimation to the truth lithological classes. The fuzzy closeness accounted for the fact that the impact of misclassifications was different in the sense that assigning “sand” instead of “gravel” is less consequential than assigning “silt/clay” instead of “gravel”. The closeness of the prediction to the true lithologies was calculated for each 10 cm interval. As a result, if the closeness to the true lithology was 0, the estimation was correct because the predicted lithology corresponded to the true value. However, if the closeness to the true values was 1, the contiguous lithology was predicted instead of the true one. Although the prediction was incorrect, the impact of misclassification was less consequential (e.g. true=sand, estimate=silt/clay). In the case that gravel was estimated instead of silt/clay, the closeness to the true lithology would be 2. In this case, the prediction is incorrect and far from the true class, so the impact of misclassification is high. This made it possible to account for the worst cases of prediction.

Fig. 18 illustrates a bubble plot representing a closeness matrix of the estimated and true lithological classes in the collocated intervals for the partial percentile models and the Most Uniform Lithological Model presented in Sections 4.4.4 and 4.4.5. This plot enables calculation of the success rate of prediction. We observed that more than 83% of the estimated lithologies coincided with the true ones for all the partial percentile models, except for the D_{10} and D_{20} models, where the percentage of success reaches 67% and 69%, respectively (see closeness to true=0 in Fig. 18). In the case of the Most Uniform Lithological Model (MULM), the lithological prediction was correct in 89% of the intervals. Of the remaining predictions, only 3% of the estimated classes (corresponding to 6,178 intervals of 10 cm) showed higher impacts of misclassifications.

The measure of the fuzzy closeness also makes it possible to identify the misclassifications in the form of underestimations and overestimations. In this context, if the true lithological class was coarser than the estimated one (e.g., true=sand, estimate=clay/silt), the prediction underestimated the grain size of the true lithology. These cases are represented by a light gray area in Fig. 18. In contrast, an overestimation in the prediction occurred when the true lithology was finer than the estimated lithology (e.g., true=sand, estimate=gravel). This situation is represented by a dark gray area in Fig. 18. We can also observe that the uncorrected predictions were equally represented in overestimations and underestimations for all models, except for the

D_{10} and D_{20} models. In the latter cases, an overestimation was noticed mostly in terms of a prediction of sand instead of clay/silt, which will be discussed below.

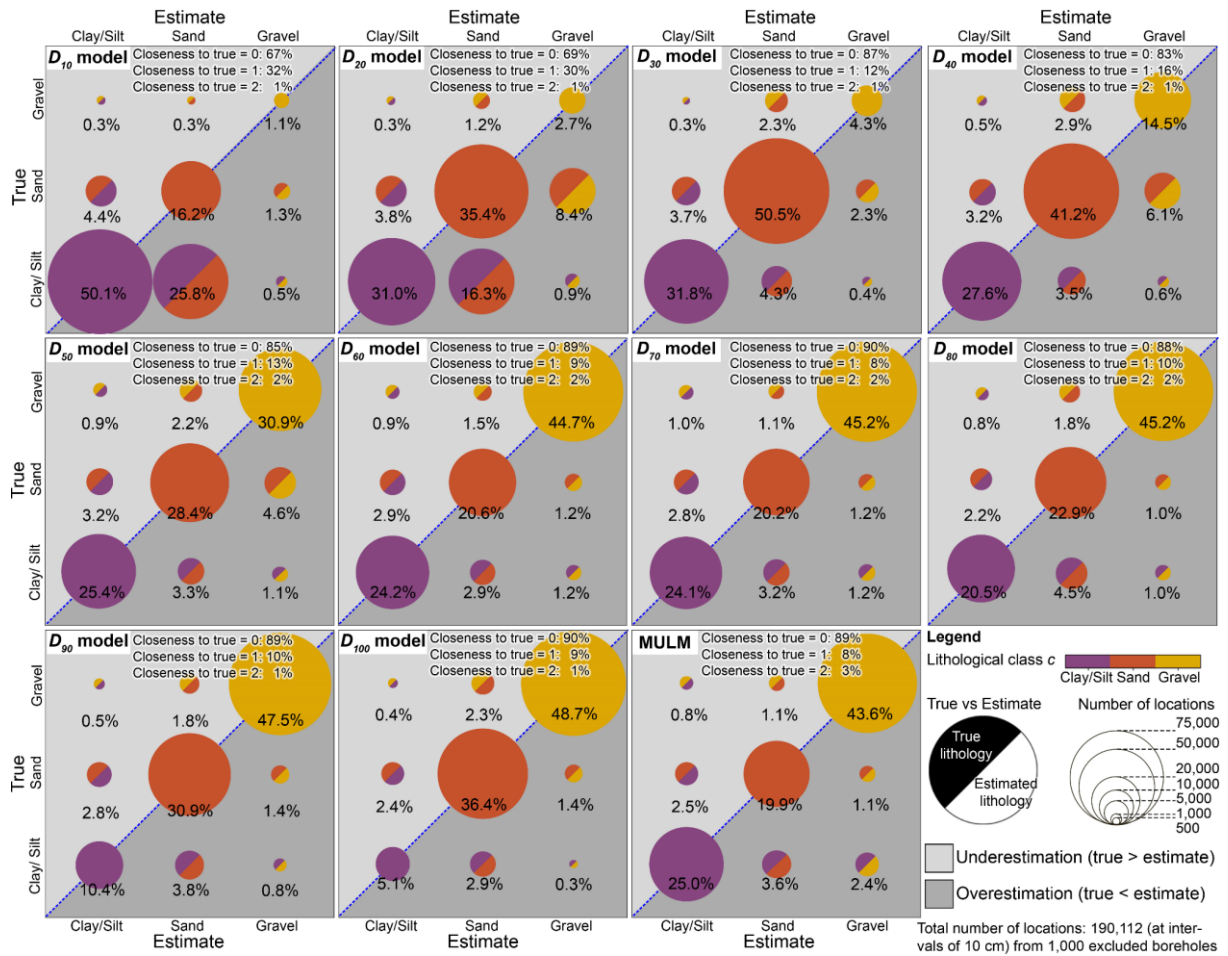


Fig. 18: Summary of results for cross validation: Bubble plot representing the fuzzy closeness of the estimated lithological classes to the true lithological classes for the D_{10} to the D_{100} models and the Most Uniform Lithological Model (MULM). Whereas the bottom right half of the bubbles represents the estimated lithological classes, the upper left half shows the collocated true lithologies. The number of locations for each true-estimate case is represented through the size of the dots. If the closeness to the true lithology was 0, the estimation was correct. These cases are represented along the dotted blue line (true=estimate). If the closeness to the true values was 1, the contiguous lithology was predicted instead of the true one. In the case that gravel was estimated instead of silt/clay, and vice versa, the closeness to the true lithology was 2 and the impact of misclassification was high. The light gray area represents the cases when the prediction underestimated the grain size of the true lithology (e.g., true=sand, estimate=clay/silt). An overestimation in the prediction occurred when the true lithology was finer than the estimated lithology (e.g., true=sand, estimate=gravel). This case is represented by a dark gray area. Modified after Albarrán-Ordás and Zosseder (2022)

Emphasis was placed on those locations of the cross validation showing drastically different lithological classes in the Most Uniform Lithological Model. Specifically, locations possessing a misclassification of two orders of magnitude (closeness to true=2), specifically predictions of clay/silt instead of gravel, and vice versa, were further investigated due to their major impact on the model interpretation. These locations were contrasted with the Model Lithological Uniformity presented in Section 4.4.4. As shown in Fig. 19, the distribution of the MLU for the worst-cases

was more or less positively skewed having a median of 0.18. Almost 25% of the locations show Model Lithological Uniformities below 0.06 and only 25% of the locations are above 0.54. Not surprisingly, this highlights that the worst-cases in the prediction were pre-dominantly associated with deposits having lower MLU values and the greater lithological variability thereby.

In view of the above issue, one might wonder whether the model is able to predict only deposits having high Model Lithological Uniformity and less complexity. For this reason, the distribution of the MLU values at locations where the estimation is correct was also analyzed in order to explore the ability of the model to predict the true lithologies in different degrees of sediment mixing. The results are represented in Fig. 19 and show a median of 0.44, indicating an almost centered distribution of the locations. This implies that the mass of the distribution of corrected predictions was not concentrated in areas neither of greater lithological variability nor with more uniform lithological composition. The 25% quantile, with 0.18, and the 75% quantile, with 0.70, also showed a wider range of uniformity values.

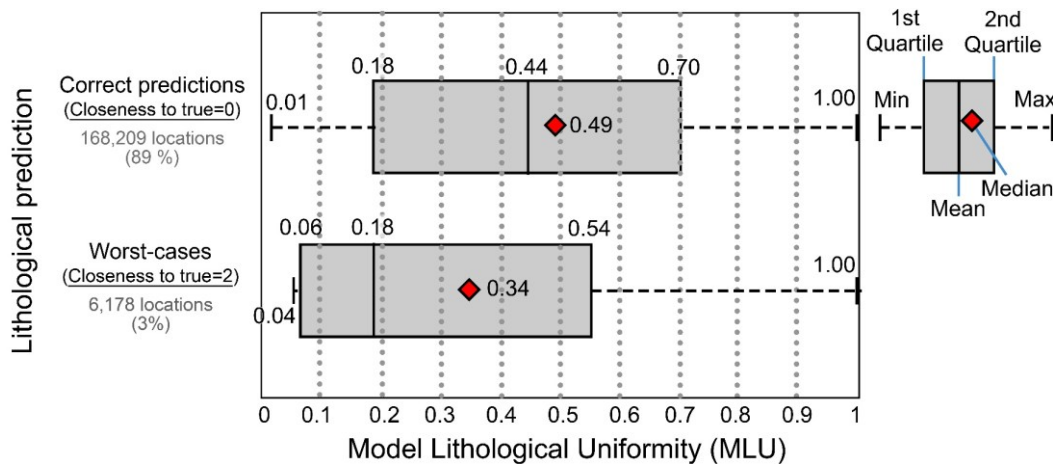


Fig. 19: Analysis of worst-case predictions (closeness to true=2) and checking the degree of sediment mixing for correct predictions (closeness to true=0): Boxplots showing the distribution of Model Lithological Uniformity (MLU) for correct predictions and for worst cases of prediction with a high impact of misclassification. The number of locations (each location represents an interval of 10 cm) is 168,209 in the case of correct predictions and 6,178 for the worst-cases

The predictive ability of the method was proven in the case study, showing a successful prediction of the MULM at 89% of the tested locations for a wide range of Model Lithological Uniformity values. Only 3% of the locations tested showed worst-case predictions and were associated with highly heterogeneous deposits having very low MLU values (mean: 0.18). In the case of the partial percentile models, a success rate of between 83% and 90% was ascertained, except for D_{10} and D_{20} (67-69%). Most of the latter discrepancies show up as misclassifications of sand instead of clay/silt (Fig. 18). This effect can be explained by a significant increase in the horizontal correlation ranges of sand identified in the spatial continuity models (Fig. 14c). The spatial variation of lithologies inferred from 3-D variogram analysis was assumed for the whole modeling domain. More accurate 3-D variogram models from large-scale subdivisions of the model volume showing similar depositional conditions may resolve these issues.

Regarding model usability, the classical, straightforward attribution of numerical values from the literature or field data on lithology or sediment mixtures (see Fig. 11a1) commonly oversimplifies the property distributions in 3-D space. This method provides synthetic grain size curves at a voxel scale, which can then lead to (i) direct derivation of empiric parameters dependent on the grain size variations at each voxel, or (ii) 3-D modeling of the property distributions of such parameters based on the information available on existing boreholes. Whichever alternative is chosen, this method enables a more accurate 3-D modeling of property distributions in space than those obtained using the straightforward attribution (see example in Fig. 11a2).

This methodology makes use of stochastic simulations for generating the most probable classes for each partial percentile model related to a different cumulative frequency, where the stationarity is assumed. Additionally, this allows the integration of imprecisions associated with the inherent generalizations for soil description. The advantage thereby is that the uncertainty contributions present in the lithological descriptions are propagated along the modeling process, which is commonly more or less ignored in all of the current modeling strategies. The development of a comprehensive measure of uncertainty based on the perspective of this method in detrital mixtures will require further study.

4.6 Conclusions

The need to manage the subsurface space especially in detrital depositional environments requires approaches for improving the capabilities of geological 3-D modeling and, among other aspects, in preserving geological realism, integrating uncertainties in the modeling process to avoid underestimations in the reliability of the model and aspiring to provide a multi-purpose, user-oriented framework. The D_i models method proposes substantial contributions to these aspects based on the cornerstone that the lithological heterogeneities in detrital systems, understood as being mixtures of clasts of a wide range of particle sizes, can be geomodeled in 3-D space. These contributions have been proven in a case study in the city of Munich (Germany). Following this premise, a multi-voxel modeling solution is presented which uses massive lithological descriptions of borehole data and is able to predict, at a grain-size scale and with a user-define implementation, the relative amounts of each grain fraction and, therefore, the full lithological composition on a cell-by-cell basis. In conducting this approach, uncertainties due to imprecise soil description associated to the inherent generalizations are integrated by interpreting different equally valid combinations of the soil components and are ultimately propagated along the modeling process through the stochastic simulations. The further development of the D_i models method includes the introduction of the concepts of Model Lithological Uniformity (MLU) and the Most Uniform Lithological Model (MULM). The predictive quality is evaluated in a cross validation process showing a success rate of prediction in the Most Uniform Model of 89% of cases considering 1,000 boreholes which amount 19 km of lithological descriptions. The combined analysis of quality of prediction and Model Lithological Uniformity

highlights the ability of the method to capture the complexity of geological reality for a wide range of MLU values and, therefore, a wide level of sediment mixing.

The multi-voxel character of this approach provides the relative amounts of each grain fraction in all voxels and encourages its flexibility of use for further applications. On the one hand, it enables an understanding of the small-scale effects present on a cell-by-cell basis derived from the sediment mixing by, e.g., attributing numerical values from the literature or field data to sediment mixtures, thus deriving empiric parameters dependent on the grain-size variations (effective porosity, hydraulic conductivity, share-wave velocity) and modeling property distributions more accurately. On the other hand, macrocellular approaches based on geometrical or cell-by-cell parametrical linkages between cells enable an understanding of complex reservoir architectures, e.g., multistory, laterally extended sand bodies like those presented in the UFM. In the case study in the city of Munich, this process ultimately led to an itemization of approximately 4,500 filter pipes classified according to eight aquifers in which they are installed, and the subsequent individual hydrogeological characterization of the groundwater systems by delineating its hydraulic characteristics and their water chemistry.

Equally, this approach has been shown to be very useful when the identification of different relative amounts of grain fractions is needed. The quantification of cumulative frequencies of lithologies can be used in the scenario analysis associated with conservative or optimistic assumptions supporting assessments for specific applications, e.g. groundwater management or civil engineering issues (Section 4.4.7). This was shown in an example of application for determining the water-saturated parts of the Quaternary aquifer that might influence the design process of a dewatering system of an excavation on conservative assumptions in the city of Munich. This flexibility has great potential for many other applications requiring a high degree of lithological variability in each voxel. Moreover, the variability captured by this method may lead to a more closely definition or modeling of continuous properties in 3-D, as well as for deriving grain-size-based dependent properties or for finer model parameterization.

4.7 Acknowledgements

This research work was conducted within the framework of the GeoPot research project, supported by the Bavarian State Ministry of the Environment and Consumer Protection (StMUV). We gratefully acknowledge the Bavarian Environment Agency (LfU) for their support and collaboration and for the access to the borehole database of the Soil Information System of Bavaria. We would like to thank especially Prof. Florian Wellmann for his constructive comments and discussions, which helped to improve the manuscript. Finally, we acknowledge Emerson E&P for providing licenses for the Software product SKUA™ Engineering Modeling in the scope of the Emerson Academic Program, which supported the results of this publication.

CHAPTER 5

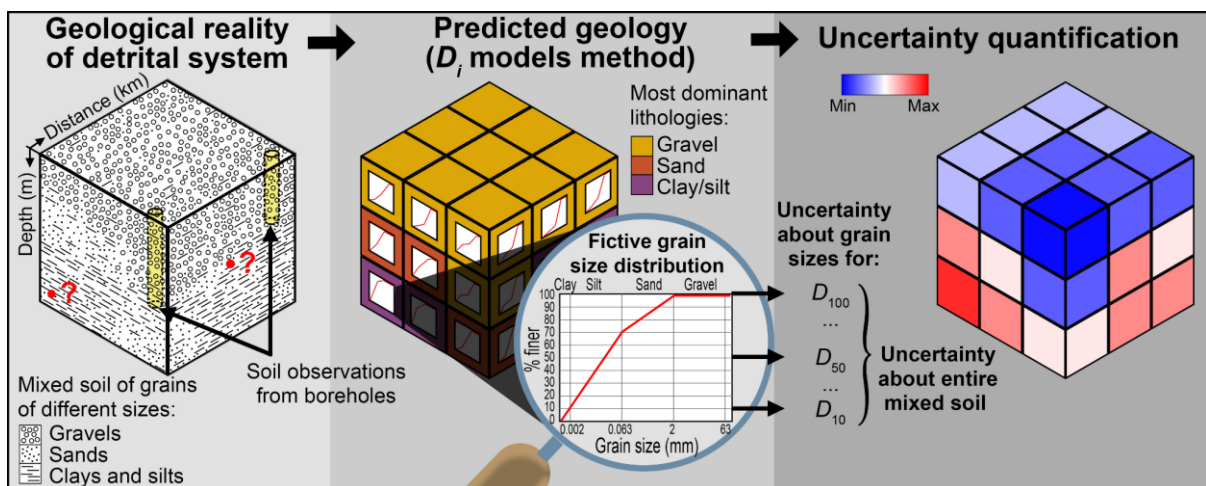
Uncertainties in 3-D stochastic geological modeling of fictive grain size distributions in detrital systems

Alberto Albarrán-Ordás^a, Kai Zosseder^a

^a Technical University of Munich, Arcisstraße 21, 80333 Munich, Germany

(Please refer to Note 1 in *List of Abbreviations, Acronyms, and Symbols*)

Graphical abstract



Abstract

Geological 3-D models are very useful tools to predict subsurface properties. However, they are always subject to uncertainties, starting from the primary data. To ensure the reliability of the model outputs and, thus, to support the decision-making process, the incorporation and quantification of uncertainties have to be integrated into the geo-modeling strategies. Among all modeling approaches, the novel D_i models method was conceived as a stochastic approach to make predictions of the 3-D lithological composition of detrital systems, based on estimating the fictive grain size distribution of the sediment mixture by using soil observations from drilled materials. Within the present study, we aim to adapt the geo-modeling framework of this method in order to incorporate uncertainties linked to systematic imprecisions in the soil observations used as input data. Following this, uncertainty quantification measures are proposed, based on entropy and joint entropy for the main outcomes of the method, i.e., the partial percentile

lithological models, and for the whole sediment mixture. Both the ability of the uncertainty quantification measures and the uncertainty propagation derived from the extension of the method are investigated in the model outcomes in a simulation experiment with real data conducted in a small-scale domain located in Munich (Germany). The results show that this adaptation of the D_i models method overcomes potential bias caused by ignoring imprecise input data, thus providing a more realistic assessment of uncertainty. The uncertainty measures provide very useful insight for quantifying local uncertainties, comparing between average uncertainties and for better understanding how the implementation parameters of the geo-modeling process influence the property estimation and the underlying uncertainties. The main findings of the present study have great potential for providing robust uncertainty information about model outputs, which ultimately strengthens the decision-making process for practical applications based on the implementation of the D_i models method.

Keywords

Geological 3-D modeling, uncertainty quantification, entropy, geostatistics, sequential indicator simulation, geomathematics.

5.1 Introduction

Geological 3-D models are common tools used in geoscience for predicting the geology present in the underground space, understood as a multifunctional natural resource (Volchko et al., 2020). In this regard, while some 3-D categorical modeling approaches are based on lithofacies (Bianchi et al., 2015; Stafleu et al., 2011), lithologies (Hademenos et al., 2019; Kearsley et al., 2015) or hydrofacies (Comunian et al., 2011; Theel et al., 2020), other authors focus on 3-D modeling the grain size distribution in the subsurface (Albarrán-Ordás and Zosseder, 2022; Roberson and Weltje, 2011). Among the latter, the D_i models method was conceived for predicting the geological heterogeneity of detrital systems composed of mixed soils (Albarrán-Ordás and Zosseder, 2022). This is achieved through a geostatistical framework, which simulates the grain size class linked to each cumulative frequency in the fictive grain size distribution (GSD) of the mixed soil.

In this context, it is well known that geological 3-D models are subjected to uncertainty (Bárdossy and Fodor, 2004), which conditions the reliability of the model outputs for practical decision purposes (Caers, 2011; Potter et al., 2010). The classification of uncertainties in the geo-modeling process is not completely clear (Wellmann and Caumon, 2018) and different types/levels of geological uncertainties are discussed in the literature (Mann, 1993; Wellmann et al., 2010; Zimmermann, 2000). Jones et al. (2004) and McCaffrey et al. (2005) noted the need for further development of methods considering uncertainties associated with geological field data and their interpretations to better estimate the overall model uncertainty. The uncertainty quantification (UQ) should start at the level of the input data, because otherwise significant uncertainty contributions might be ignored, and the overall uncertainty could be importantly underestimated (Bárdossy and Fodor, 2004). The input data used in the D_i models method are direct soil

observations from drilled materials described in the field according to the standards for soil description (Albarrán-Ordás and Zosseder, 2022). These data do not rely on laboratory tests, e.g., sieve analysis, and comprise a sequence of symbols marking the soil in terms of the types of the observed grain sizes and their proportion range (%) in the soil. Consequently, the soil observations are subject to the natural geological variability and also to the systematic imprecisions associated with the inherent generalizations of the standards used and to the subjectivity of on-site personnel. Other possible sources of uncertainty are inaccurate spatial positions of borehole data, i.e., the location and height (McCaffrey et al., 2005).

However, focusing merely on uncertainties in the input data is clearly insufficient. In this sense, the uncertainty is a property of the developed random function (RF) model and is only relevant to the underlying implementation parameters of the mathematical model (Rossi and Deutsch, 2014; Wellmann and Caumon, 2018). This includes the stationarity/non-stationarity decisions, such as the incorporation of deterministic trends (McLennan, 2007). Trends are geologically rational and expected for geostatistical prediction of categorical variables (Deutsch, 2002; Manchuk and Deutsch, 2011), but they need to be incorporated in a relatively straightforward way (McLennan, 2007). Although the introduction of 3-D trends is not commonly addressed in geostatistical modeling, their incorporation may avoid poor property prediction (Pyrzcz and Deutsch, 2014), especially when no further domain subdivision is possible. However, their construction and validation are still challenging (Babak et al., 2014; McLennan, 2007). In this sense, Section 5.2 gives special attention to the random variables (RVs), the stationarity/non-stationarity decision and the implementation parameters in the D_i models method.

Significant efforts have been made to provide a scalar measure for UQ in geological 3-D models (Wellmann and Caumon, 2018). In structural modeling, the contributions of Wellmann et al. (2010) and Lindsay et al. (2012) explore the concepts of geological inversion/perturbation. The multiple realizations of interfaces lead to the determination of the probability of being crossed by each interface at each location. This enables using the concept of entropy as an uncertainty measure associated to a probability distribution (Shannon, 1948). This was analyzed into a geostatistical context by Journel and Deutsch (1993) and has been widely used by various authors (Babak et al., 2014; Wellmann, 2013; Wellmann and Regenauer-Lieb, 2012). In the case of property modeling in voxelized domains, such as the hydraulic conductivity of an aquifer, summary statistics are particularly effective to represent uncertainty (Potter et al., 2013). By contrast, summary statistics cannot be used in 3-D categorical models and commonly the entropy is applied. However, current UQ approaches do not specifically address the uncertainty linked to each grain fraction composing the sediment mixture in a GSD. This limitation, together with the lack of the combination of scenarios with stochastic simulations in one uncertainty framework (Wellmann and Caumon, 2018), highlights the need for further research in adapting UQ measures and developing a framework for the particularities of the D_i models method.

In view of the background outlined above, this paper addresses the following research goals:

- 1) Adapting the geostatistical framework implemented by the D_i models method to integrate the uncertainties associated with imprecise input data.
- 2) Developing UQ measures linked to the main outputs of the D_i models method, i.e., the partial percentile lithological models, and the whole mixture of clasts.
- 3) Evaluating the ability of the UQ measures with different implementation parameters of the underlying RVs (stationarity/non-stationarity decisions, indicator kriging algorithms).
- 4) Exploring the uncertainty propagation and impacts on the uncertainty derived from 1).

5.2 Theory of stochastic 3-D modeling using GSD with the D_i models method

The characterization of a GSD can be described at each unknown location \mathbf{u} in a three-dimensional domain A with a discrete number C of mutually exclusive and exhaustive grain size classes ($c=1, 2, \dots, C$) so that each location \mathbf{u} corresponds to a grain size class for every cumulative frequency i . This is represented in the left part of Fig. 20a.

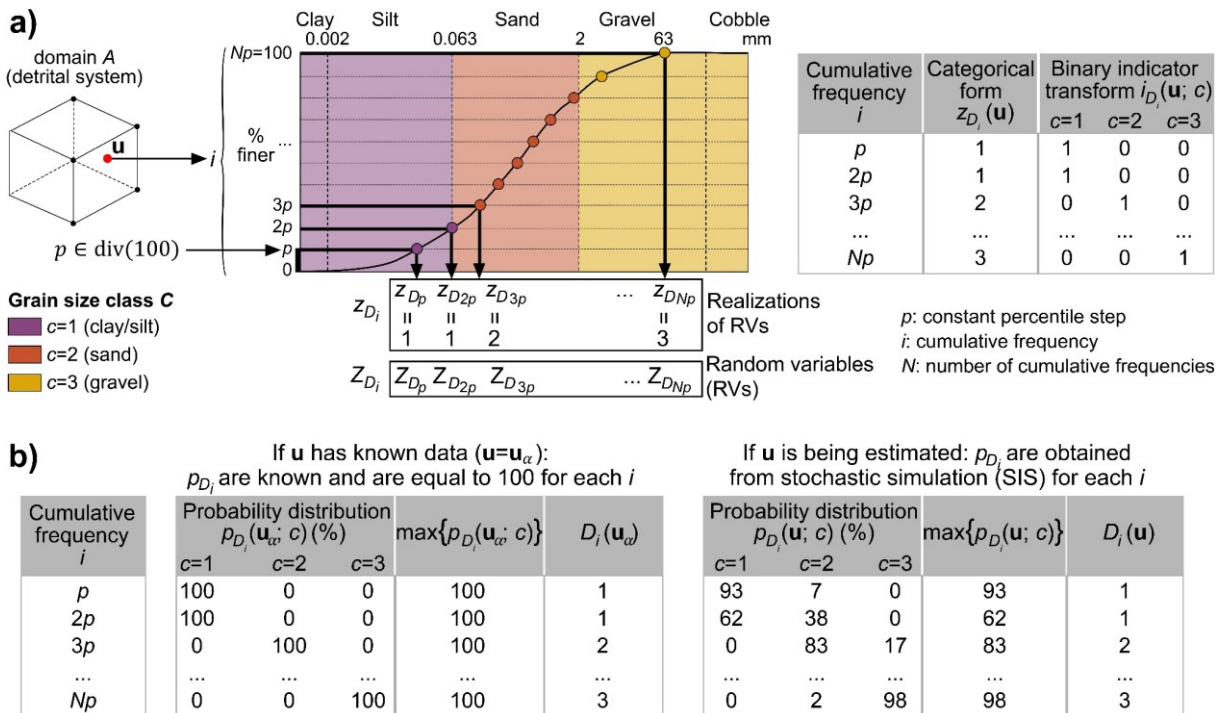


Fig. 20: Concept of the random 3-D modeling of GSD with the D_i models method: **a)** Introduction of a series of RVs representing a grain size class for each i ; **b)** Probability distribution and assignment of a grain size class for each i

We can define a set of values $i=p, 2p, 3p, \dots, Np$ in the GSD, where $Np=100$, by fixing a constant percentile step p divisor of 100 (see Fig. 20a). The GSD is then characterized by a number $N=100/p$ of cumulative frequencies. At this point, we can introduce a series of categorical RVs, denoted by a capital letter (Deutsch, 2021) as $Z_{D_i}(\mathbf{u})$ (see lower part, Fig. 20a), representing the grain size classes linked to the particle diameter, hence the notation D from diameter, assignable to each i :

$$\{Z_{D_i}(\mathbf{u}) = Z_{D_p}(\mathbf{u}), Z_{D_{2p}}(\mathbf{u}), Z_{D_{3p}}(\mathbf{u}), \dots, Z_{D_{Np}}(\mathbf{u}); \quad p \in \text{div}(100); \mathbf{u} \in A\}. \quad (33)$$

For instance, considering a constant step of $p=10$ will result in $N=10$ ($i=10, 20, 30, \dots, 100$), each of which is assigned a grain size class $Z_{D_i}(\mathbf{u}) = Z_{D_{10}}(\mathbf{u}), Z_{D_{20}}(\mathbf{u}), Z_{D_{30}}(\mathbf{u}), \dots, Z_{D_{100}}(\mathbf{u})$. Whereas the corresponding lowercase letter $z_{D_i}(\mathbf{u})$ (see part immediately below the GSD, Fig. 20a) represents the grain size class for each i at any unknown location, $z_{D_i}(\mathbf{u}_\alpha)$ denotes the known hard data. Since per definition the GSD is a monotonically increasing function, the following condition has to be fulfilled:

$$Z_{D_p}(\mathbf{u}) \leq Z_{D_{2p}}(\mathbf{u}) \leq Z_{D_{3p}}(\mathbf{u}) \leq \dots \leq Z_{D_{Np}}(\mathbf{u}). \quad (34)$$

The discrete grain size classes are mutually exclusive and, as such, the categorical RVs $Z_{D_i}(\mathbf{u})$ can be also expressed as a series of indicator RVs in Eqs. (35) and (36). The notations $i_{D_i}(\mathbf{u}; k)$ (see at right of Fig. 20a) and $i_{D_i}(\mathbf{u}_\alpha; k)$ express the indicator transforms of the discrete grain size classes for all i about every unsampled and data location, respectively.

$$I_{D_i}(\mathbf{u}; c) = I_{D_p}(\mathbf{u}; c), I_{D_{2p}}(\mathbf{u}; c), I_{D_{3p}}(\mathbf{u}; c), \dots, I_{D_{Np}}(\mathbf{u}; c). \quad (35)$$

$$I_{D_i}(\mathbf{u}; c) = \begin{cases} 1 & \text{if } Z_{D_i}(\mathbf{u}) = c \\ 0 & \text{otherwise} \end{cases}; \quad c = 1, \dots, C; \mathbf{u} \in A. \quad (36)$$

A set of C indicator variograms need to be inferred for each cumulative frequency:

$$\gamma_{I_{D_i}}(\mathbf{h}; c) = \frac{1}{2} E \left\{ [I_{D_i}(\mathbf{u} + \mathbf{h}; c) - I_{D_i}(\mathbf{u}; c)]^2 \right\}, \quad (37)$$

where \mathbf{h} denotes the separation vector between pairs of points. The indicator kriging estimator in presence of n nearby local data is written as follows:

$$I_{D_i}^*(\mathbf{u}; c) - P_{D_i}(\mathbf{u}; c) = \sum_{\alpha=1}^n \lambda_{\alpha D_i}(\mathbf{u}; c) [I_{D_i}(\mathbf{u}_\alpha; c) - P_{D_i}(\mathbf{u}_\alpha; c)] \quad c = 1, \dots, C, \quad (38)$$

where $P_{D_i}(\mathbf{u}; c)$ are the prior models of local proportions at the points being estimated, $P_{D_i}(\mathbf{u}_\alpha; c)$ are the prior models of local proportions at the known data points and $I_{D_i}(\mathbf{u}_\alpha; c)$ are the indicator RVs at the known data points that condition the indicator kriging.

The estimators $I_{D_i}^*(\mathbf{u}; c)$ provide the local conditional probability for each c at an unsampled location, which is integrated into a conditional cumulative distribution function (CCDF) for implementing Sequential Indicator Simulation (SIS) by sampling of the CCDF (Deutsch and Journel, 1997). SIS is implemented N times independently for all i considered. The results of SIS, expressed by the notation $z_{D_i}^*(\mathbf{u})$, represent the set of possible equiprobable realizations of the categorical RVs at any location. Over a large number of realizations L , the probability of each grain

size class at each location is calculated for each i according to Eq. (39) (see Fig. 20b). These probability models, called E-type models (Bassani and Costa, 2022; Pyrcz and Deutsch, 2014), are denoted as $p_{D_i}(\mathbf{u}; c)$ and inform the probability for any location that a specific grain size class prevails:

$$p_{D_i}(\mathbf{u}; c) = \frac{1}{L} \sum_{l=1}^L z_{D_i}^{*l}(\mathbf{u}; c); \quad \mathbf{u} \in A. \quad (39)$$

Grain size classes at a location with the highest probabilities constitute the partial percentile lithological models or D_i models, $D_i(\mathbf{u})$ (see Fig. 20b), expressed as follows:

$$D_i(\mathbf{u}) = c; \text{ if } \max\{p_{D_i}(\mathbf{u}; c)\} = p_{D_i}(\mathbf{u}; c); \quad c = 1, \dots, C; \quad \mathbf{u} \in A. \quad (40)$$

Derived from the latter, the distribution of the most dominant grain size classes for the whole GSD at each location can be expressed by the Most Uniform Lithological Model, denoted by MULM(\mathbf{u}) (Albarrán-Ordás and Zosseder, 2022).

5.3 Material and methods

In regard to the methodology used, first the specific procedure for incorporating uncertainties from the systematic imprecisions in the input data into the modeling method is addressed (5.3.1). Then the UQ measures are described for the main outcomes of the D_i models method (5.3.2). Subsequently a simulation experiment with real data is conducted in a small-scale domain located in the Munich area (Germany) (see Fig. 21) (5.3.3). The aim of the experiment is to investigate both the ability of the UQ measures and the propagation of systematic uncertainties from the input data in the main model outcomes. The following sections (5.3.4, 5.3.5) address the applied methods for incorporating non-stationarity into prediction and 3-D trend modeling.

5.3.1 Adapted geo-modeling framework to incorporate imprecisions in soil observations

Most data available for 3-D geological modeling inherently entail some observational errors or imprecisions in the geological composition (Bárdossy and Fodor, 2004). The input data used in this study were collected from the borehole database gathered by Bavarian Environment Agency (LfU) (Germany). The standards for soil description used in this database, i.e., DIN 4023 (2006), DIN EN ISO 14688-1 (2020), DIN EN ISO 14688-2 (2020) and DIN EN ISO 14689 (2018), do not exactly quantify each grain size fraction, but provide relative proportion ranges, thus leading to uncertainty. To illustrate this, Fig. 22 shows how hard data, by means of an exemplary raw soil observation (G,s), are transformed for their further use in the D_i models method.

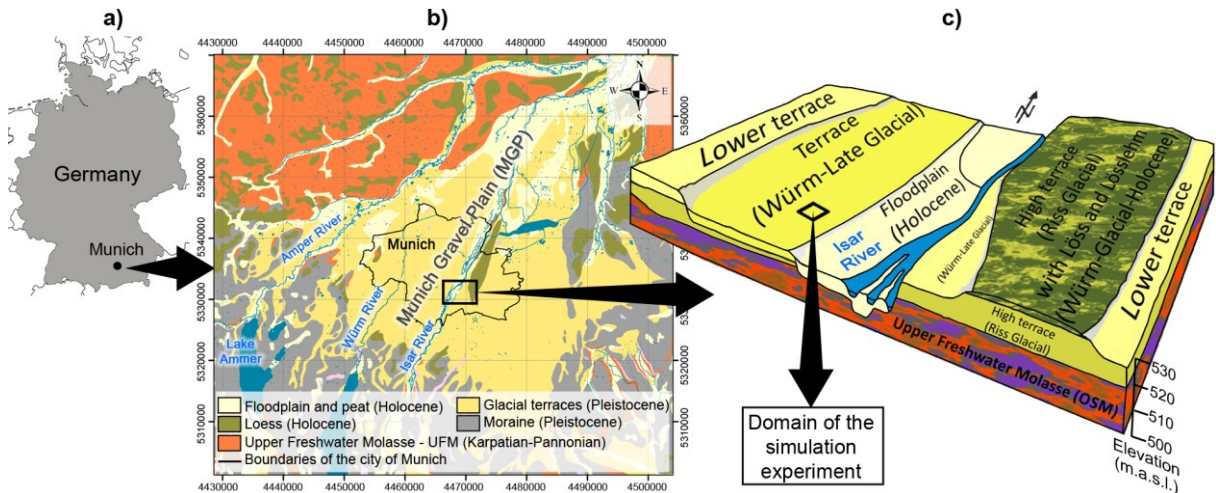
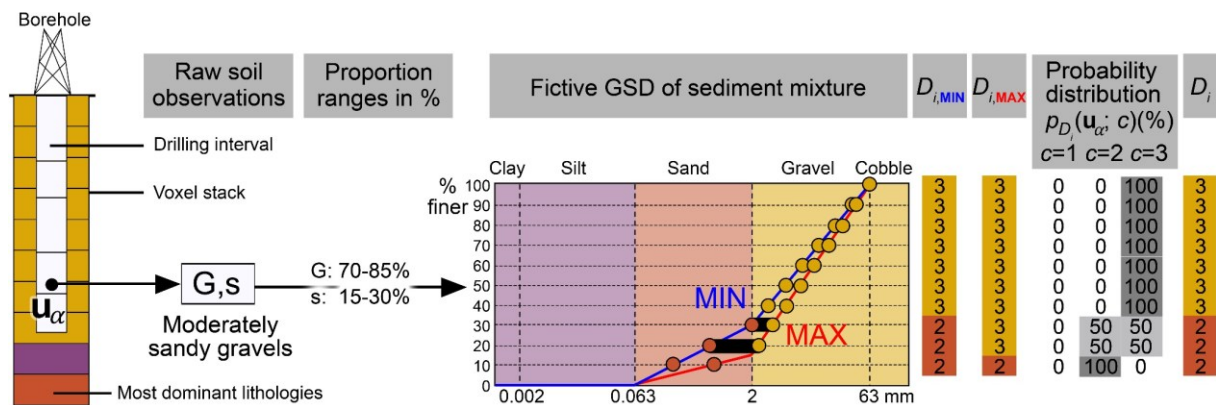


Fig. 21: Geological setting of the simulation domain. **a)** Location map. **b)** Simplified geological map in the Munich area showing the main lithostratigraphical units and the boundaries of the city of Munich. **c)** Schematic geological view of the city of Munich and the location of simulation domain (m.a.s.l.: meters above sea level). Modified from Albarrán-Ordás and Zosseder (2022)

Whereas characters with capital letters designate main soil components with relative percentages between 40% and 100%, e.g., G for gravel, secondary soil components are represented by lowercase letters followed by a quantifier denoting the relative percentage (no quantifier: 15-30%) (see at left of Fig. 22). Based on these intervals, fictive grain size ranges of the different grain fractions are built, representing the coarsest-grained (MAX) and finest-grained (MIN) interpretations of the soil observation (see Fig. 22, central part). The imprecise proportion ranges leave some room for variation, since the gravel fraction may vary between 70% and 85% and the sand fraction also fluctuates considerably (15-30%).



If two grain size classes have the most frequent occurrence (see D_{20} and D_{30}), the class with the lowest value, in this case $c=2$, prevails. The uncertainty associated remains in the discrete probability distributions

Grain size class C
 c=1 (clay/silt) c=2 (sand) c=3 (gravel)

Abbreviations and proportion ranges (%):
 G: gravel (40-100%), s: sandy (15-30%)

Fig. 22: Exemplary soil observation used as hard data in the D_i models method: transformation of raw soil observations for their further integration in the geo-modeling framework

This imprecise description leads to obtain two different equiprobable grain size classes at some cumulative frequencies, indicated by the black bars in Fig. 22. This translates into uncertainty in some cumulative frequencies and, thus, in the entire GSD, as discussed in next section.

The consideration of one unique GSD for characterizing the lithological heterogeneity shown in Section 5.2, either a MIN/MAX curve individually or a hypothetical MEAN curve between them, ignores these uncertainties. Therefore, the concept shown in Fig. 20 needs to be extended to integrate and propagate these uncertainties. Fig. 23 illustrates the changes after this adaptation.

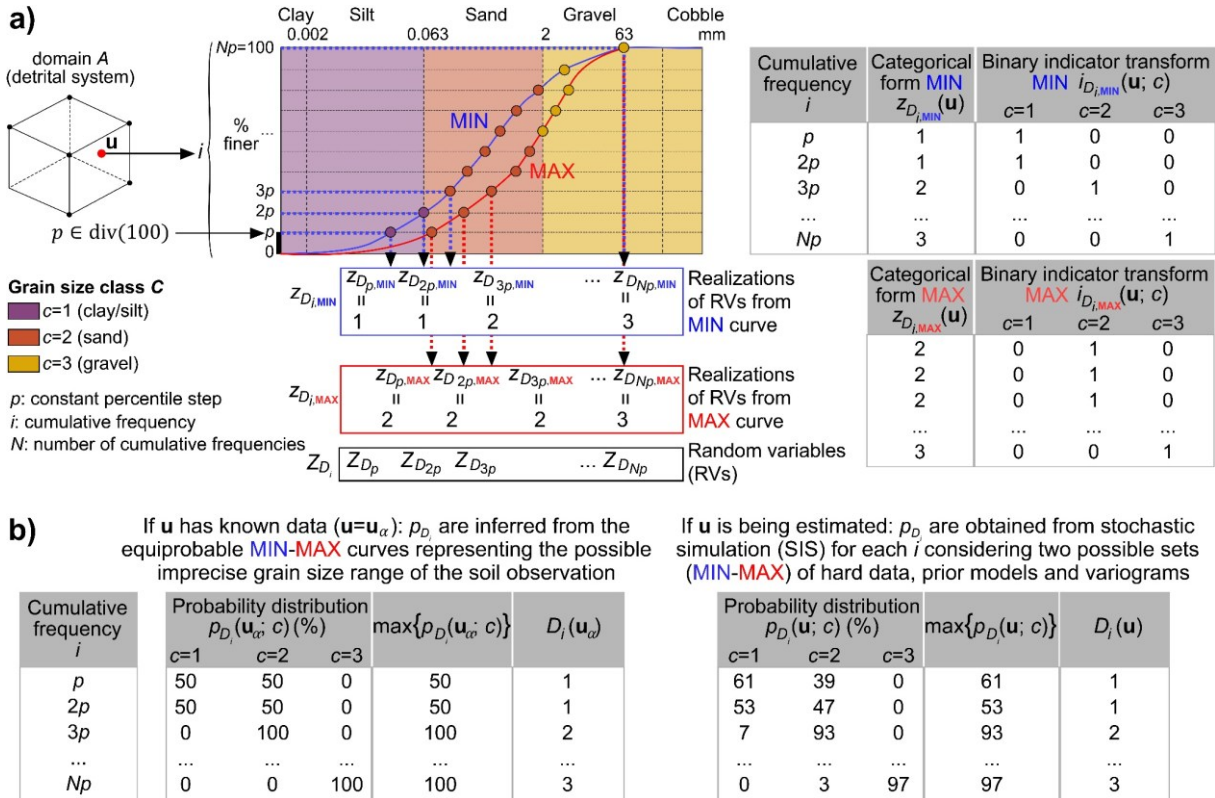


Fig. 23: Modifications in the initial concept scheme of the random 3-D modeling of GSD with the D_i models method to incorporate uncertainties from imprecise input data into the geo-modeling process: **a)** Introduction of a series of RVs representing a grain size class for each i ; **b)** Probability distribution and assignation of a grain size class for each i

As mentioned in the previous example, the imprecise proportion ranges of each lithological component are addressed by considering two curves for the GSD, thus defining a range representing the coarsest-grained and finest-grained interpretations (see blue and red curves denoted as MIN and MAX, respectively, Fig. 22 and Fig. 23a). This extension necessarily leads to introduce two equiprobable sets of input data $z_{D_i,MIN}(\mathbf{u}_\alpha)$ and $z_{D_i,MAX}(\mathbf{u}_\alpha)$ representing the two grain size classes assignable to each i . The problem of stochastic modeling the GSD is then addressed from a twofold perspective, introducing two indicator RVs per each i considered: $I_{D_i,MIN}(\mathbf{u})$, $I_{D_i,MAX}(\mathbf{u})$ (see at right of Fig. 23). To ensure the propagation of the imprecise input data, an equal number of realizations $z_{D_i,MIN}^*(\mathbf{u})$ and $z_{D_i,MAX}^*(\mathbf{u})$ is selected. Moreover, simulation

is conditioned to both possible hard data $z_{D_i, \text{MIN}}(\mathbf{u}_\alpha)$ and $z_{D_i, \text{MAX}}(\mathbf{u}_\alpha)$, both prior models of local proportions $P_{D_i, \text{MIN}}(\mathbf{u}; c)$ and $P_{D_i, \text{MAX}}(\mathbf{u}; c)$ and both indicator 3-D variograms. As shown in Fig. 23b, this leads to obtain two possible prevailing grain size classes with equal probability at some cumulative frequencies at data locations (see probability distribution for $i=p$ and $i=2p$ in Fig. 23b).

5.3.2 UQ measures: entropy and joint entropy

The entropy is a natural measure of uncertainty (Deutsch, 2021), enabling the quantification of the randomness of a discrete distribution. As mentioned in Eqs. (39) and (40), $D_i(\mathbf{u})$ are obtained from the grain size classes with the highest probabilities after simulation. Thus, we can express the uncertainty at each location \mathbf{u} for each D_i in terms of the entropy of the discrete distribution as the sum of all products of probabilities for each possible grain size class c with its logarithm:

$$H_{D_i}(\mathbf{u}) = -\sum_{c=1}^C p_{D_i}(\mathbf{u}; c) \ln[p_{D_i}(\mathbf{u}; c)]; \quad c = 1, \dots, C; \quad \mathbf{u} \in A. \quad (41)$$

The choice of the logarithmic base influences only the choice of a unit for measuring information (Shannon, 1948). In this case, the natural logarithm is used and the resulting units are nats. The entropy is at its minimum when the highest probability of occurrence is 1, thus causing complete certainty. In contrast, the entropy reaches its maximum when all probabilities have the same value and are equal to $1/C$. The average uncertainty in an entire domain A is calculated as an average of all n locations:

$$\overline{H_{D_i}} = \frac{1}{n} \sum_{\alpha=1}^n H_{D_i}(\mathbf{u}_\alpha); \quad \mathbf{u} \in A; \quad \alpha = 1, \dots, n. \quad (42)$$

With regard to the UQ about the entire GSD, we can compare this issue with the problem of quantifying the uncertainty about the information required for describing the exact state of a combined system formed by a collection of RVs. The latter case is given by the joint entropy, which is expressed by the chain rule for entropy (MacKay, 2003). If we consider the random modeling of the GSD as a collection of RVs following the logical order of sieving, we can express the joint entropy as follows:

$$H_{\text{mixture}}(\mathbf{u}) = H \left[Z_{D_{100}}(\mathbf{u}), Z_{D_{100-p}}(\mathbf{u}), \dots, Z_{D_p}(\mathbf{u}) \right] = \sum_{i=p}^{100} H \left(Z_{D_{100}}(\mathbf{u}) \middle| Z_{D_{100-p}}(\mathbf{u}), \dots, Z_{D_p}(\mathbf{u}) \right). \quad (43)$$

As revealed in Section 5.2, SIS is implemented independently for each i , which makes the RVs conditionally independent. Consequently, the joint entropy is the sum of the marginal entropies:

$$H_{\text{mixture}}(\mathbf{u}) = H \left[Z_{D_{100}}(\mathbf{u}), Z_{D_{100-p}}(\mathbf{u}), \dots, Z_{D_p}(\mathbf{u}) \right] = H[Z_{D_{100}}(\mathbf{u})] + H[Z_{D_{100-p}}(\mathbf{u})] + \dots + H[Z_{D_p}(\mathbf{u})]. \quad (44)$$

Fig. 73 illustrates an exemplary application of the UQ measures in soil observations.

5.3.3 Simulation experiment

Tab. 1 provides an overview of the model setups proposed. The simulation experiment was divided into two parts and seven setups. The first part comprised the model Setups 1 to 5 and consisted of testing the UQ measures described in Section 5.3.2 with five different underlying RFs. In these five cases the geo-modeling framework included the integration of imprecise input data described in Section 5.3.1. While Setups 1-2 implement stationary Simple Kriging (SK), they differ in the number of chosen domains (see Tab. 1). In contrast, Setups 3 to 5 assume non-stationarity in the domains and are differentiated solely by the trends used (see Tab. 1). For clarification purposes, the implications of the assumption of stationarity/non-stationarity in the context of D_i models method are briefly addressed in Sections 5.3.4 and 5.3.5.

The second part of the experiment explored the impact on the UQ of adapting the geostatistical framework of the D_i models method to integrate imprecise soil observations. This impact is quantified by comparing the obtained uncertainty when considering these imprecisions against the uncertainties obtained when ignoring them. For this purpose, two additional model setups (6-7) were produced with an identical configuration as for Setup 5, but without adapting the geo-modeling process to integrate imprecisions. Setups 6-7 consider the finest-grained and coarsest-grained interpretation of the hard data, respectively (blue and red curves in Fig. 22 and Fig. 23).

Tab. 1: Overview of the simulation setups (SK: Simple Kriging; LVM: Local Varying Means; BK: Block Kriging; MWA: Moving Window Averaging; Q: Quaternary sub-domain; T: Miocene (Tertiary) sub-domain; GP: Global Proportions).

Setup	Domains	Indicator kriging algorithm	3-D trend model and specifics of trend construction	Adapted geo-modeling framework
1	Full	Stationary SK	No	Yes
2	Two: Q, T	Stationary SK	No	Yes
3	Two: Q, T	Non-stationary SK (LVM)	Yes, highly overfit BK, 10x6 blocks, search radius: 300 m	Yes
4	Two: Q, T	Non-stationary SK (LVM)	Yes, slightly overfit BK, 10x6 blocks, search radius: 300 m, MWA: 5x5x1, smoothed with GP (0.2)	Yes
5	Two: Q, T	Non-stationary SK (LVM)	Yes, non-overfit BK, 10x6 blocks, search radius: 300 m, MWA: 5x5x1, smoothed with GP ($D_{10,MIN,MAX} = D_{30,MIN,MAX} = D_{40,MIN,MAX} = D_{80,MAX} = D_{90,MIN,MAX} = D_{100} = 0.2$; $D_{20,MIN,MAX} = 0.4$; $D_{50,MIN,MAX} = D_{60,MIN} = D_{70,MIN,MAX} = 0.5$; $D_{60,MAX} = D_{80,MIN} = 0.55$)	Yes
6	Two: Q, T	Non-stationary SK (LVM)	Same as Setup 5 but only MIN trends	No, finest-grained
7	Two: Q, T	Non-stationary SK (LVM)	Same as Setup 5 but only MAX trends	No, coarsest-grained

The simulation was conducted in a small-scale exemplary domain located within the city limits of Munich (Germany). The choice of this geographical setting was based on the high density of borehole data available, comprising of over 20,000 boreholes with soil observations in the area of Munich (Albarrán-Ordás and Zosseder, 2022), and on the detrital nature of the most recent deposits in this basin, the so-called Munich Gravel Plain (MGP). The MGP comprises Quaternary

glacio-fluvial coarse-grained gravels, which are underlain by Miocene clayed-marly slackwater sediments and sandy deposits (Bachmann and Muller, 1992). The geological setting of the entire MGP, the city of Munich and the simulation domain is included in Fig. 21. A detailed description of the model area used is given in Albarrán-Ordás and Zosseder (2022).

Fig. 24 shows the domain, the input data and the setting for the 2-D profile used throughout the study. The domain has dimensions of 765x580x133 m in the easting, northing and vertical directions, respectively, and a cell size of 25x25x1 m. The dataset used is comprised of 416 boreholes with direct soil observations in the same format as shown in Fig. 22. The full domain can be replaced by two sub-domains named Q (Quaternary) and T (Miocene, Tertiary) (see Fig. 24). The boundary surface between the sub-domains was obtained from geostatistical relief modeling (Albarrán-Ordás and Zosseder, 2020). All setups are conceptually identical in regard to the cumulative frequencies i and the considered grain fractions C . The grain-size range is discretized in three classes: $c=1$ for clay and silt (≤ 0.063 m), $c=2$ for sand (>0.063 -2.0 mm) and $c=3$ for gravel (>2.0 mm) and a constant step in the GSD of $p=10$ was fixed. The latter results in $N=10$ cumulative frequencies. An equal number of 100 realizations was run for each $z_{D_i,MIN}^*(\mathbf{u})$ and $z_{D_i,MAX}^*(\mathbf{u})$, respectively. The indicator variogram models are also identical for all the setups.

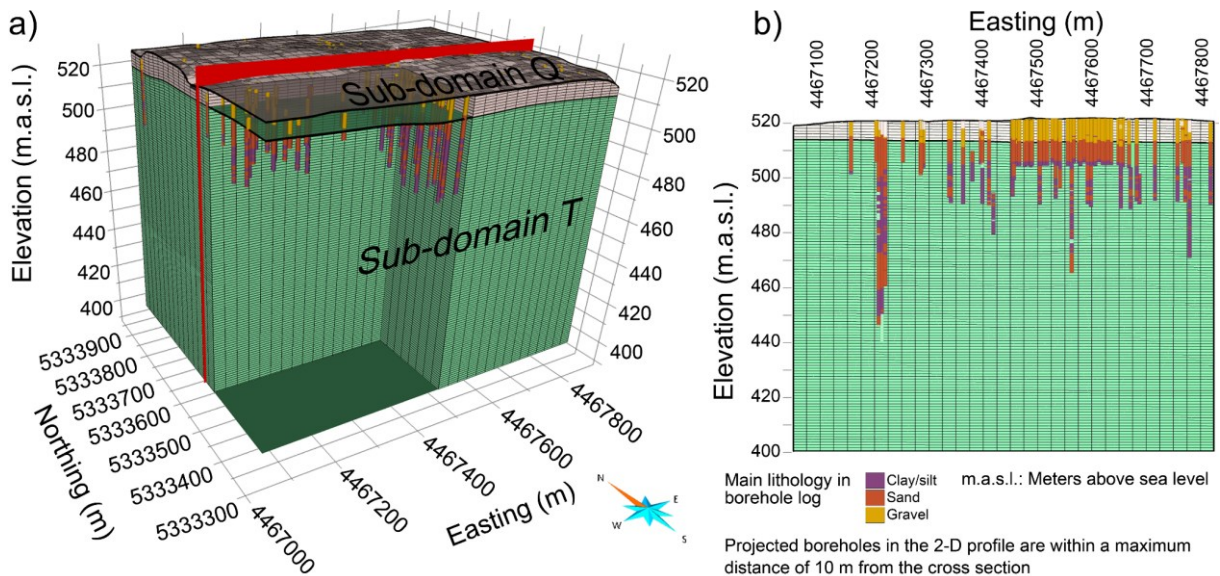


Fig. 24: Domain setting and input data for simulation experiment: **a)** Full 3-D domain and subdomains Q and T showing borehole logs; **b)** 2-D example profile used throughout the study

5.3.4 Stationarity and treatment of non-stationarities: indicator kriging algorithms

Stationarity can be defined as a decision involving the intervention of: 1) the choice and modeling of the domains based on logical geological divisions, and 2) deterministic trends (McLennan, 2007). Depending on this decision, the prior models in Eq. (38) can be provided in various ways. On the one hand, the implicit assumption of stationarity implies consideration of the prior

proportions to be constant. These are provided by the global mean probabilities of each grain size class in each domain (stationary SK), denoted by $P_{D_i}(k)$ (Deutsch, 2002):

$$I_{D_i}^*(\mathbf{u}; c) - P_{D_i}(c) = \sum_{\alpha=1}^n \lambda_{\alpha_{D_i}}(\mathbf{u}; c) [I_{D_i}(\mathbf{u}_{\alpha}; c) - P_{D_i}(c)]; \quad c = 1, \dots, C. \quad (45)$$

$$P_{D_i}(c) = E\{I_{D_i}(\mathbf{u}; c)\} = \frac{1}{n} \sum_{\alpha=1}^n I_{D_i}(\mathbf{u}_{\alpha}; c); \quad c = 1, \dots, C; \alpha = 1, \dots, n. \quad (46)$$

$P_{D_i}(c)$ are the arithmetic averages of the indicator variable for the same grain fraction c at data locations \mathbf{u}_{α} (Hadavand and Deutsch, 2017).

On the other hand, opting for integrating non-stationarities implies that the prior local proportions are location-dependent (Deutsch and Journel, 1997) and the estimator remains unchanged as in Eq. (38). The prior means are given by a 3-D categorical trend model consisting of locally varying proportions. Once the trend is constructed, it can be incorporated into modeling in various ways (Deutsch, 2006). The locally varying mean (LVM, non-stationary SK) option was chosen from all the options, since this is the most theoretically correct (Deutsch, 2006).

5.3.5 Construction and evaluation of 3-D categorical trend models

As revealed in Section 5.3.3, the model Setups 3 to 5 are based on non-stationarity assumptions. Tab. 1 provides an overview of the specifics of the constructed trends. Each of the sets of 3-D trends were generated in accordance with recommended practices (McLennan, 2007) by applying a block kriging scheme combined with a relatively large global search and a block discretization. To enhance their smooth nature, the trends constructed for Setups 4-5 also included a MWA of 5x5x1 cells and were combined with the global trends. The conditioning data are the indicator transforms of the two equiprobable sets of input data $i_{D_i, \text{MIN}}(\mathbf{u}_{\alpha}; c)$ and $i_{D_i, \text{MAX}}(\mathbf{u}_{\alpha}; c)$. The works of González et al. (2007) and Pyrcz and Deutsch (2014) provide a detailed description of methods for trend construction. However, trends are subjective (McLennan, 2007) and their reasonableness must be evaluated according to the following criteria (Hong and Deutsch, 2009): closure relation, reproduction of the global mean proportions, exactitude, fairness and overfitting. The common approaches for trend checking are described in detail in the following works: Hong and Deutsch (2009), Pyrcz and Deutsch (2014), Deutsch (2002), McLennan (2007) and Machuca-Mory and Deutsch (2009).

5.4 Results and discussion

5.4.1 Use of entropy for ensuring monotonically increasing GSD

As exposed in Eq. (34), the grain size classes constituting the D_i models, i.e., $D_i(\mathbf{u})$, need to be monotonically increasing with respect to the cumulative frequency i in order to comply with the

characteristics of soil GSD. However, since the RVs are simulated individually, the assignment of the most probable grain size class after simulation might not always fulfill this condition. To illustrate this, Fig. 25 shows the grain size classes obtained from simulation (see column D_i) at two unsampled locations u_1 and u_2 . Whereas at location u_1 the D_i values comply with the increasing nature of the GSD (see Fig. 25a), the simulation results at location u_2 show a violation of the aforementioned condition having values of $D_{70}=2$, $D_{60}=1$, $D_{50}=2$, $D_{40}=2$ and $D_{30}=1$ (see Fig. 25b). The possible logical corrections would be either make $D_{60}=2$ or make both D_{50} and D_{40} equal to 1. The solution is addressed by proposing a correction based on the estimated entropy of the discrete distribution. In particular, we propose that the highest uncertain discrete probability distribution of the involved D_i , i.e., the discrete distribution of D_{60} with an entropy value of $H_{D_{60}}(u_2) = 0.83$, indicates the cumulative frequency to implement the correction. In our example, D_{60} is then corrected from 1 (clay/silt) to 2 (sand) (see Fig. 25b).

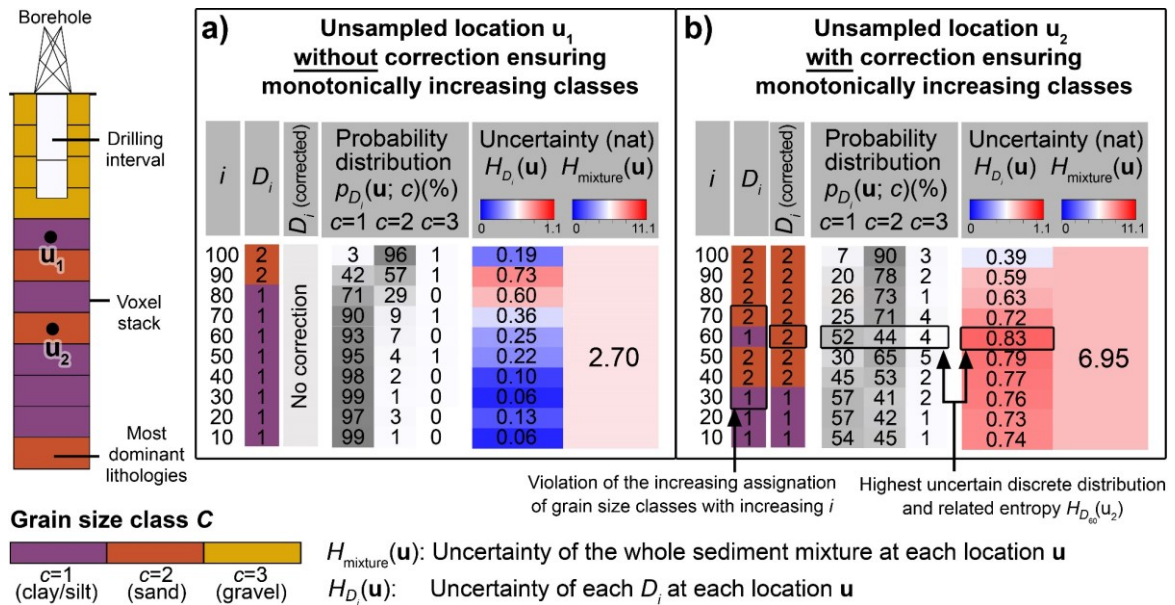


Fig. 25: Exemplary application of the entropy-based correction for ensuring monotonically increasing GSD: **a)** Unsampled location without correction; **b)** Unsampled location with correction

5.4.2 Evaluation of the 3-D categorical trend models

As an example of the constructed 3-D trends, Fig. 26. illustrates a fence diagram showing the trends for $D_{80,MIN}$ for all setups.

Subsequently, the trends were evaluated based on the named criteria (see Section 5.3.5). In all cases the trends ensure closure and reasonably reproduce the global mean proportions. The differences between the global means given by Eq. (46) and the arithmetic average of the trend model probabilities reflect values smaller than 17% in both sub-domains, which are similar to those considered to reasonably reproduce the input proportions in other studies reported in the literature (Hong, 2010; Silva, 2018). In addition, the 3-D trend models for Setup 5 have the lowest departures from global proportions.

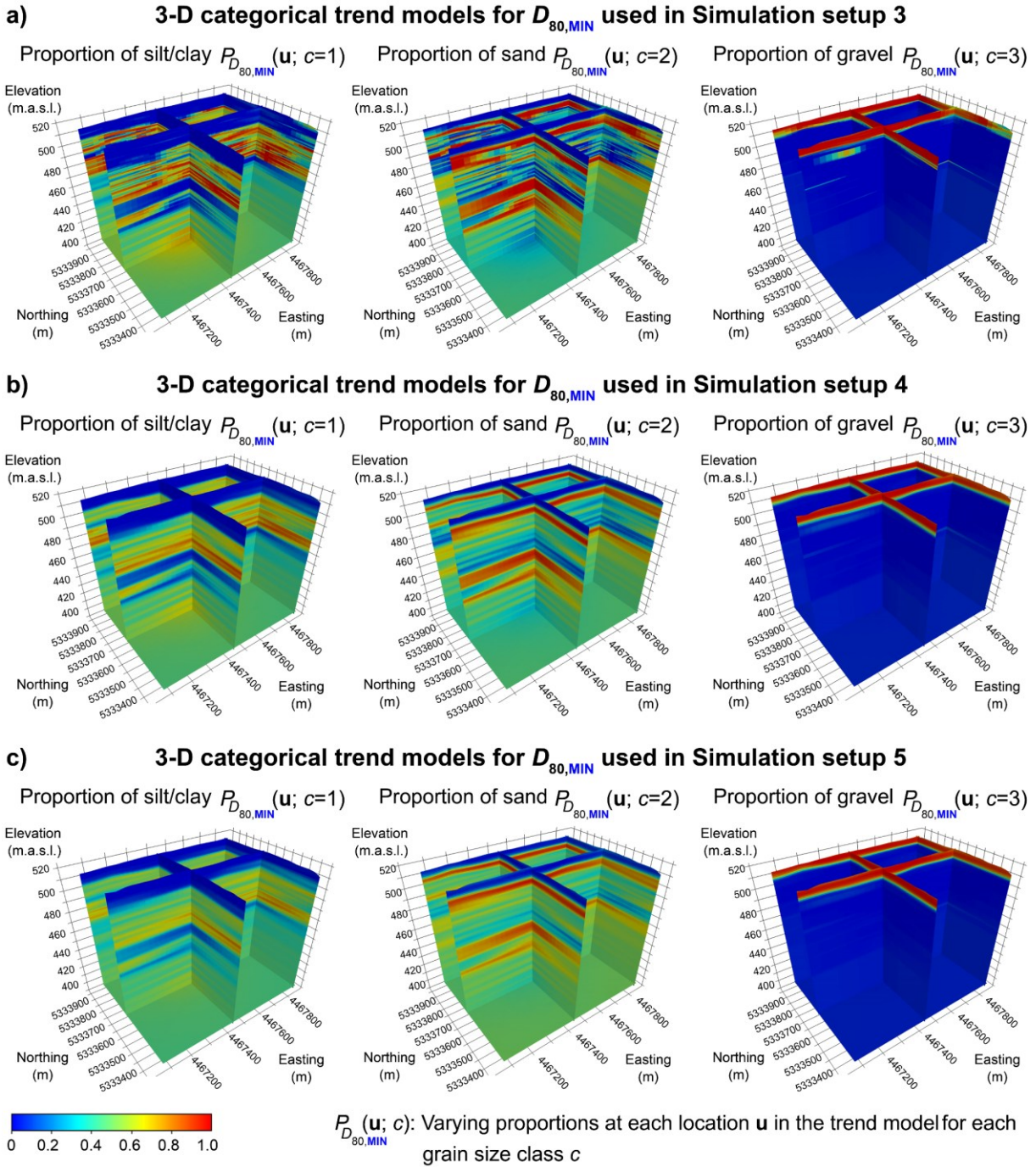


Fig. 26: Fence diagrams showing the results of the 3-D trend construction for $D_{80,MIN}$ in: **a)** Simulation setup 3; **b)** Simulation setup 4; **c)** Simulation setup 5

Moreover, all the trends are considered to be fair, since the fairness plots are sufficiently close to the ideal situation of falling on the 45° line. Regarding the balance between deterministic and stochastic variability, the trend variance contribution to the final variance is estimated and represented in Fig. 27a. As we can see, the deterministic variability exceeds the critical threshold of 50% defined by McLennan (2007) for Setups 3 and 4. Furthermore, the exactitude of hard data reproduction is evaluated by calculating the closeness of the trend proportions to the true grain

size classes from the soil observations (see Fig. 27b). The aforementioned trends also show the highest closeness to the known data (see Fig. 27b), thus denoting higher trend exactitudes, which is not desired (McLennan, 2007).

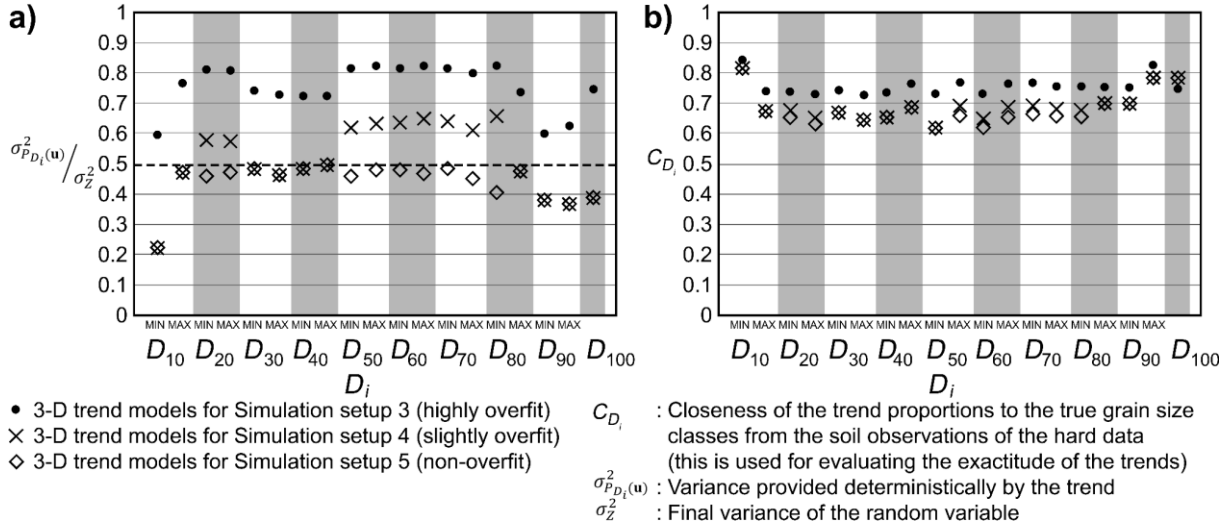


Fig. 27: Results of the 3-D trend evaluation: **a)** Ratio of the variance provided deterministically by the trends and the final variance (should be no greater than 0.5); **b)** Closeness of the trend proportions to the true grain size classes from the soil observations.

Both the tasks of constructing/evaluating the 3-D trends and their straightforward incorporation into geostatistical prediction (Babak et al., 2014; McLennan, 2007) were demonstrated to be very laborious and time-consuming in the context of the D_i models method. This is justified by the large number of trends required by this method, e.g., nineteen for this simulation experiment. Although technically possible, the incorporation of 3-D trends might be a critical issue when dealing with large 3-D models having high grid resolutions and with a more complex conceptual model. Their integration into stochastic modeling should be therefore considered on a case-by-case basis and might be particularly interesting, when no further domain subdivisions are available, as in the present case in the subdomain T.

5.4.3 UQ in partial percentile lithological models $D_i(u)$

The UQ of the D_i models provides the uncertainty associated with the grain size classes simulated for each i in the GSD. The results obtained from stationarity SK in the entire domain (Setup 1) and in separated sub-domains (Setup 2), as well as from superimposing various trends (Setups 3 to 5) are in Fig. 28, Fig. 29, Fig. 74, Fig. 75 and Fig. 76.

As mentioned in Section 5.4.2, all trends reasonably reproduced the global proportions in each sub-domain. To facilitate the discussion for the different setups, Tab. 2 shows the global proportions P_{D_i} inferred from the available sample data intersecting the entire domain and sub-domains. The inferred uncertainty about the probability distribution of the grain size classes is given by $H_{D_i}^{global}$, with a maximal value of $\ln(C) \sim 1.1$ nat. These values are also incorporated at the

right of each 2-D profile in Fig. 28 and Fig. 29. Tab. 2 shows that the entire domain hides the presence of sub-domains with differentiated lithological composition, leading to a distortion of the statistics. This is reflected in the UQ when comparing Fig. 28 and Fig. 29, since in all i the RVs fluctuate to the inferred statistics of the chosen domain/sub-domains. Consequently, the UQ from considering the entire domain (Setup 1, see Fig. 28) differs considerably from that deemed from considering subdivisions (Setups 2-5 in Fig. 29 and in Fig. 74, Fig. 75 and Fig. 76). This leads to a lack of lithological representativeness and a higher uncertainty in Setup 1 for each i . This can be clearly seen in the more marked pixel effect and higher entropy present in T in Fig. 28, compared to Fig. 29.

Tab. 2: Results of statistical inference in the entire domain and in the sub-domains Q and T (P_{D_i} : constant global proportions for each grain fraction c in each domain; $H_{D_i}^{global}$: entropy of the probability distribution from the constant global proportions, unit in nat; the color scale is the same as in Fig. 28 and Fig. 29, where higher and lower entropy values from global proportions are associated with red and blue tones, respectively)

D_i		Setup 1				Setups 2 to 5							
		Entire domain				Sub-domain Q				Sub-domain T			
		$P_{D_i}(c)$			$H_{D_i}^{global}$	$P_{D_i}(c)$			$H_{D_i}^{global}$	$P_{D_i}(c)$			$H_{D_i}^{global}$
		$c=1$	$c=2$	$c=3$		$c=1$	$c=2$	$c=3$		$c=1$	$c=2$	$c=3$	
D_{10}	MIN	0.87	0.12	0.01	0.39	0.71	0.26	0.03	0.64	0.92	0.08	0.00	0.26
	MAX	0.56	0.43	0.01	0.68	0.30	0.66	0.05	0.71	0.64	0.36	0.00	0.61
D_{20}	MIN	0.56	0.43	0.01	0.68	0.30	0.66	0.05	0.71	0.64	0.36	0.00	0.61
	MAX	0.38	0.55	0.08	0.82	0.04	0.71	0.25	0.65	0.49	0.49	0.02	0.70
D_{30}	MIN	0.49	0.49	0.03	0.72	0.21	0.72	0.07	0.69	0.57	0.42	0.01	0.65
	MAX	0.38	0.47	0.15	0.92	0.04	0.47	0.49	0.76	0.49	0.48	0.03	0.73
D_{40}	MIN	0.37	0.55	0.08	0.82	0.03	0.72	0.26	0.63	0.49	0.50	0.02	0.70
	MAX	0.34	0.43	0.23	0.97	0.02	0.27	0.71	0.61	0.45	0.50	0.04	0.77
D_{50}	MIN	0.35	0.48	0.18	0.93	0.02	0.43	0.55	0.70	0.46	0.51	0.03	0.74
	MAX	0.33	0.43	0.24	0.97	0.02	0.26	0.73	0.59	0.45	0.51	0.05	0.77
D_{60}	MIN	0.34	0.48	0.18	0.94	0.02	0.42	0.57	0.70	0.46	0.51	0.04	0.75
	MAX	0.33	0.43	0.24	0.97	0.02	0.26	0.73	0.59	0.44	0.51	0.05	0.77
D_{70}	MIN	0.34	0.43	0.24	0.98	0.02	0.26	0.73	0.59	0.45	0.51	0.05	0.77
	MAX	0.31	0.45	0.24	0.97	0.01	0.26	0.73	0.57	0.41	0.54	0.05	0.77
D_{80}	MIN	0.31	0.45	0.24	0.97	0.01	0.26	0.73	0.57	0.42	0.54	0.05	0.77
	MAX	0.18	0.57	0.25	0.89	0.01	0.26	0.74	0.55	0.24	0.70	0.06	0.68
D_{90}	MIN	0.18	0.57	0.25	0.89	0.01	0.26	0.74	0.55	0.24	0.70	0.06	0.69
	MAX	0.07	0.67	0.26	0.73	0.00	0.26	0.74	0.54	0.10	0.83	0.07	0.51
D_{100}	-	0.07	0.67	0.26	0.73	0.00	0.25	0.74	0.54	0.10	0.83	0.07	0.52

Focusing on the Setups 3-5, the UQ shows a strong differentiation among i values. Subdomain Q has a higher randomness for $i \leq 30$ (see Fig. 29 and in Fig. 74, Fig. 75 and Fig. 76), which is due to the slight (5-15%) to moderate (15-30%) presence of one or several minor components, i.e., clay/silt and/or sands. Conversely, the low randomness for $i > 50$ can be explained by the presence of gravels with relative percentages of at least 40% (see Tab. 2). However, subdomain T has low uncertainties at low i values and higher uncertainties for $i=80$ and $i=90$ (see Fig. 29).

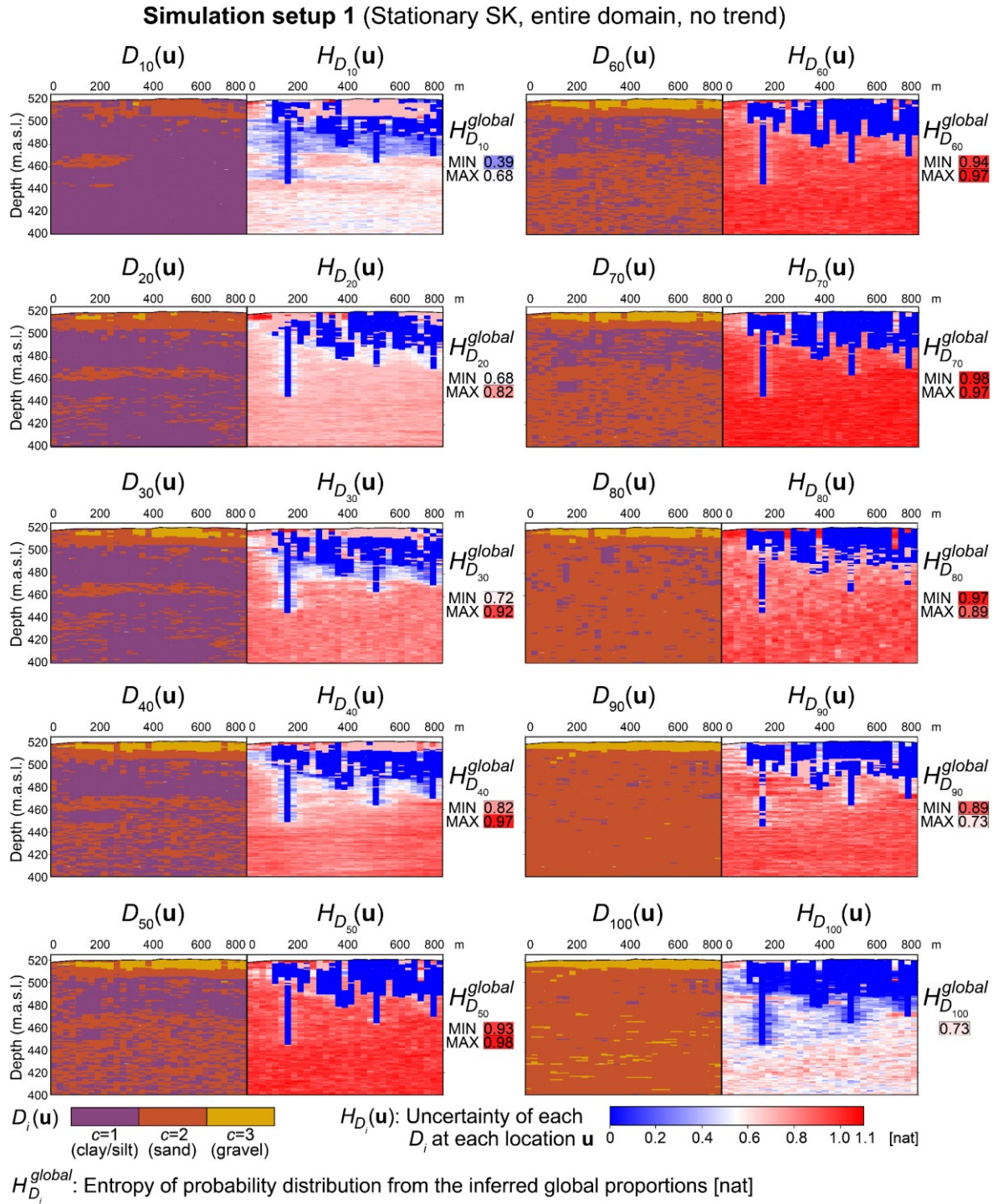


Fig. 28: Results of UQ in the partial lithological models of Simulation setup 1

This is due to the absence of gravels and the strong presence of sand or silt/clay in this subdomain, as mentioned in the description of the domain setting (Section 5.3.3). These interpretations are consistent with the higher and lower degrees of homogeneity of the clastic mixtures detected in the Miocene and Quaternary deposits, respectively, in the city of Munich (Albarrán-Ordás and Zosseder, 2022).

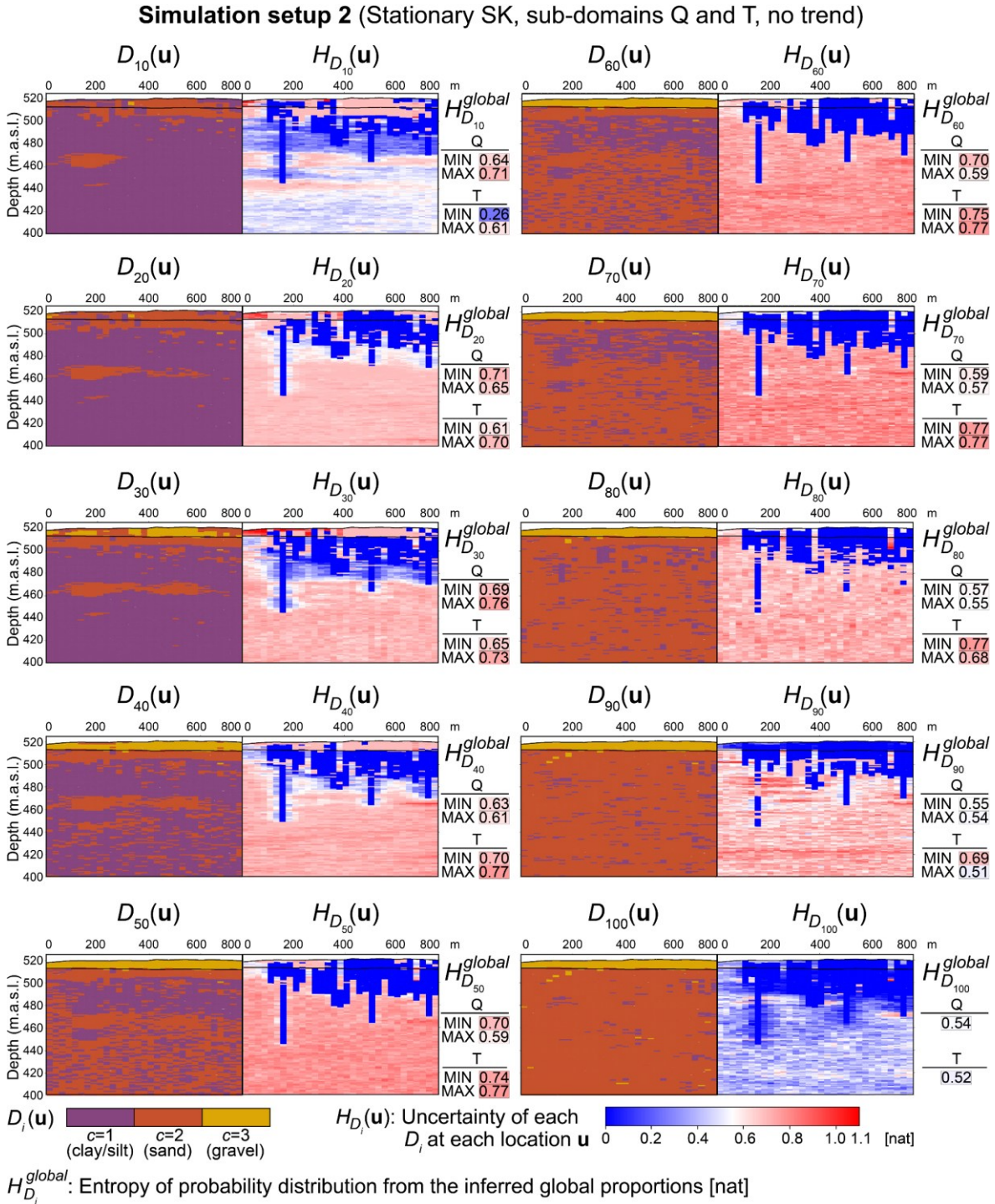


Fig. 29: Results of UQ in the partial lithological models of Simulation setup 2

The results imply that considering separate geologically homogeneous sub-domains with separate RFs in the D_i models improves the representativeness of the statistical inference, which leads to a more precise prediction of the lithological variability and a fair UQ. Thus, ignoring logical subdivisions results in lack of representativeness of the statistics, leading to large uncertainties. This is in line with the need to identify separate domains with separate RF models highlighted by McLennan (2007).

5.4.4 UQ in the whole sediment mixture $H_{\text{mixture}}(\mathbf{u})$

Fig. 30 represents the results of the UQ in the entire GSD for Setups 1-5. If no trends are used, the lack of representativeness of the global proportions inferred in the sub-domains Q and T revealed in Section 5.4.3 leads to a very poor lithological estimation (see Fig. 30a, left). This is reflected in the exaggerated presence of sand in Q in Fig. 30a, when compared to Fig. 30b to Fig. 30e. Instead, Setup 2 shows a clear reduction of the randomness in the estimation, when compared to Setup 1 (6.14 nat against 7.49 nat).

The introduction of 3-D trends significantly improves the lithological estimation (see Fig. 30c-d-e, left side) but their analysis requires much attention in the trend evaluation. This is clearly seen in Setup 3. Compared to the results from stationary SK (see Fig. 30a-b), Fig. 30c shows an apparently satisfactory prediction accompanied by very low uncertainties, especially in depths up to 450 m.a.s.l. This can be explained by the trend evaluation revealed in Section 5.4.2, since the trends for this setup hold the highest closeness (see Fig. 27b) and contribute to 70% of the final variance in most of the cumulative frequencies (see Fig. 27a). McLennan (2007) and Pyrcz and Deutsch (2014) have reported that trend overfitting may lead to an overestimation in the prediction and an unfair low uncertainty model with similar results. In the case of Setup 4, the low uncertainties may not be that obvious at first glance in Fig. 30d. However, as shown in Fig. 27a, nine of the nineteen trends created for this setup still contributed to ~60% of the total variance. The results for Setup 5 (see Fig. 30e) show a similar lithological estimation as for Setups 3-4. However, we observe a more marked pixel effect in the deeper parts, thus having a higher randomness. In this case, the trend evaluation showed contributions of the trend variance <50% (Fig. 27a). This results in trends that are not overfit and therefore Setup 5 should be the preferred approach.

Moreover, considering the whole detrital system as a combined system formed by a collection of RVs makes this UQ measure scalable. This means that by increasing the number of grain fractions ($C > 3$) or the number of cumulative frequencies N , the information needed to exactly define the combined system also increases correspondingly. This fact responds to the research need underlined by Wellmann and Caumon (2018) for developing UQ frameworks combining different possible model scenarios with stochastic simulations for the context of stochastic 3-D modeling of GSD.

5.4.5 Impact of adapting the geostatistical framework to integrate imprecise input data

Fig. 31 shows the results obtained for Setups 6-7 compared to the results of the preferred Setup 5. The impact on the UQ of the adapted geo-modeling framework is quantified by comparing the obtained uncertainty when considering the adapted framework (Setup 5) with the uncertainties captured when ignoring imprecisions (Setups 6-7).

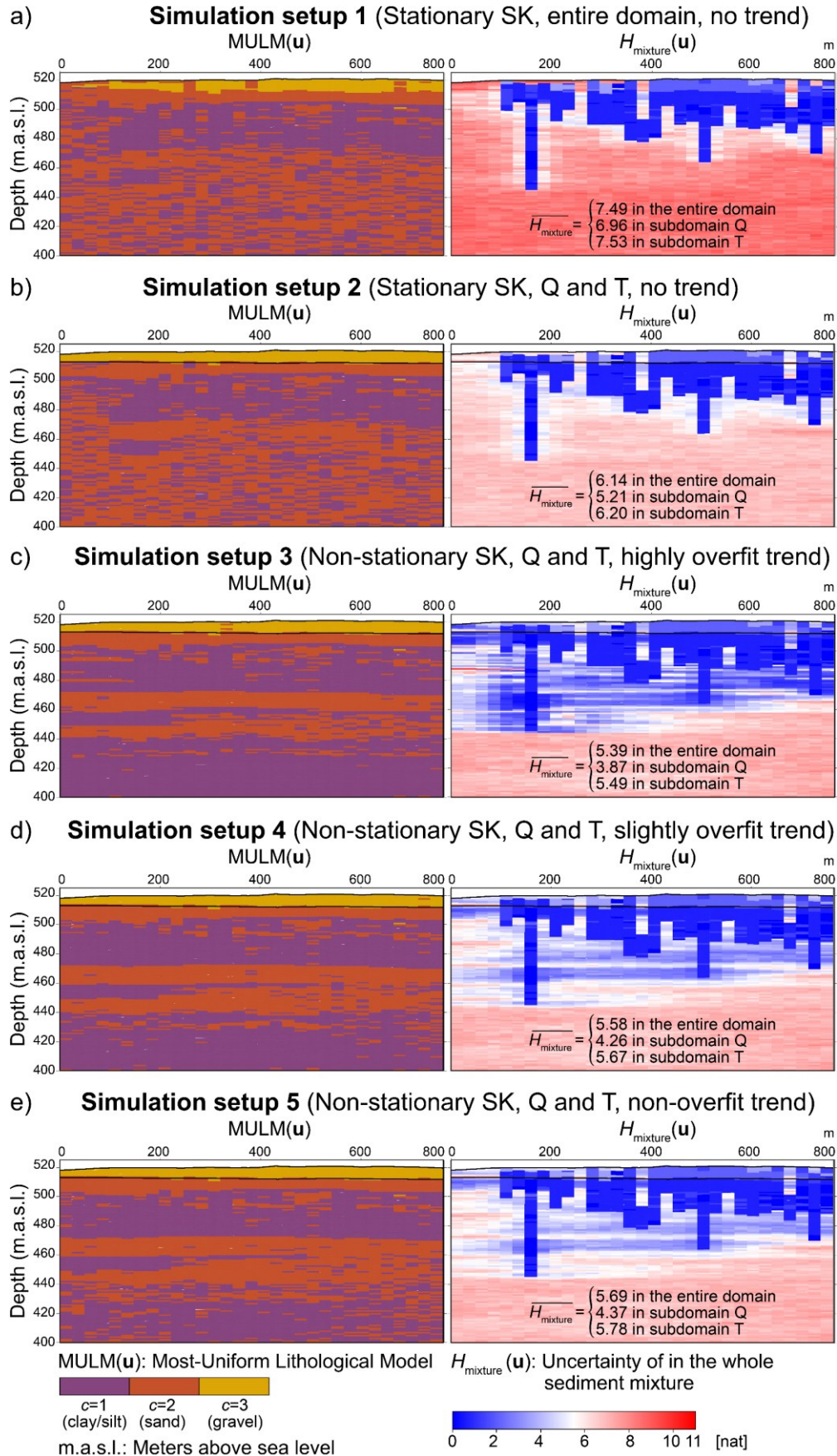


Fig. 30: Results of UQ in the whole sediment mixture for Simulation setups 1 to 5

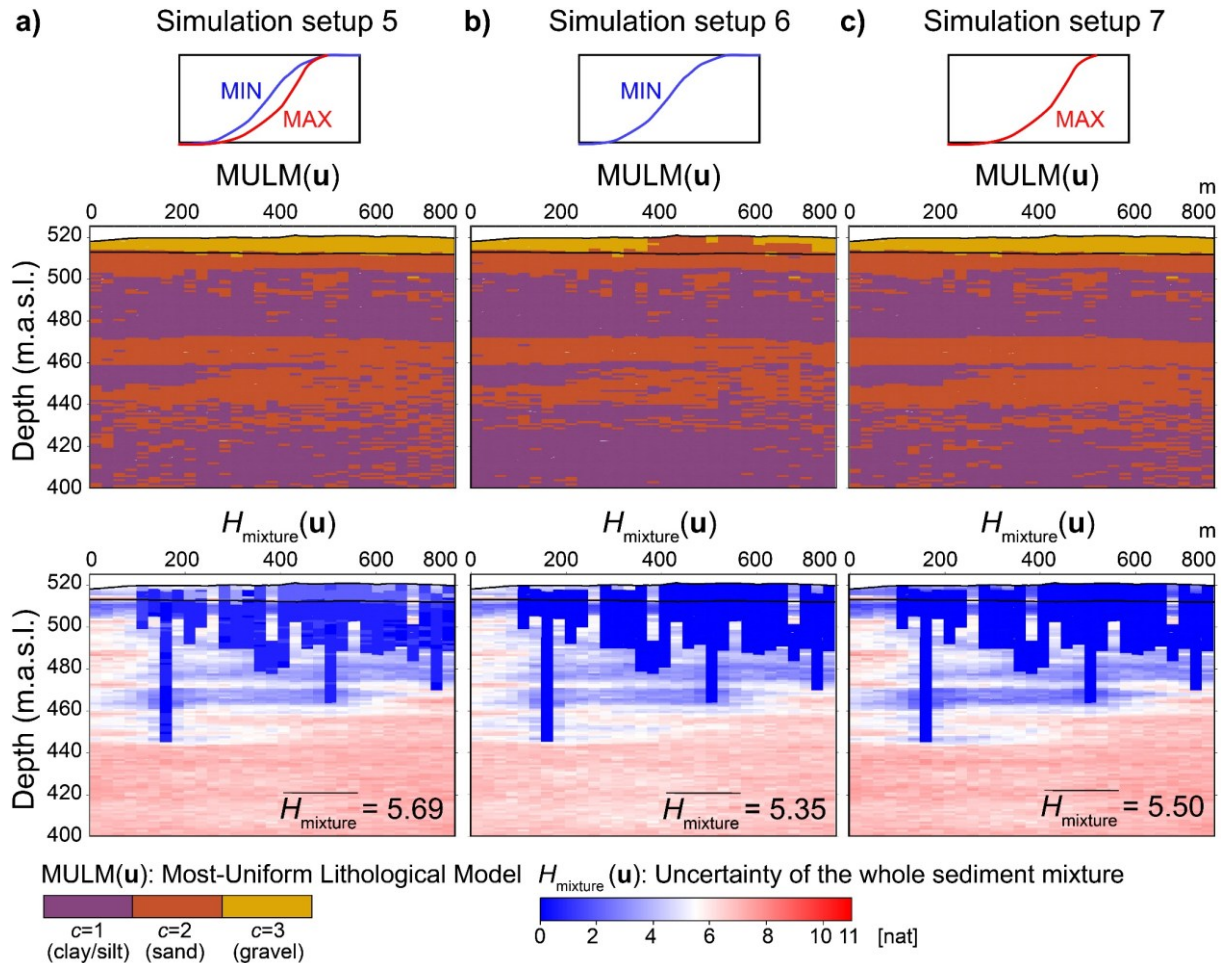


Fig. 31: Results of UQ in the whole sediment mixture for Simulation setups 5, 6 and 7

Setup 6 relies on the finest-grained interpretation from the soil observations, i.e., the blue curve shown in Fig. 23 and Fig. 31. When compared with Fig. 31a, the 2-D profile in Fig. 31b shows clearly an increased presence of sand and silt/clay in sub-domains Q and T, respectively. Instead, Setup 7 is based only on the coarsest-grained interpretation. Although no differences can be appreciated between Fig. 31a and Fig. 31c in Q, a greater presence of sand can be observed in T.

The adaptation of the D_i models method leads to an increased average uncertainty of 5.69 nat compared to 5.35 and 5.50 nat (see Fig. 31). As expected, the uncertainty at the known data in Setups 6-7 equals zero, since these setups ignore imprecise input data.

For better understanding of uncertainty propagation, we now concentrate on the estimated points. The differences of uncertainties between Setups 5 and 6 and between Setups 5 and 7, respectively, were calculated and represented in Fig. 32.

The differences from the finest-grained model show a slight increased uncertainty as the grain size of the most prevailing lithologies reduces (see lower panel, Fig. 32b). This can also be recognized in the upper panel of Fig. 32b through differences higher than 0, represented in red predominantly for clayed/silty areas in Fig. 32a. In contrast, the differences with respect to the

coarsest-grained model increase with increasing grain sizes (see boxplot, Fig. 32c). This clearly illustrates that Setup 6 considers the prediction of fine-grained sediments unfairly certain, whereas Setup 7 does likewise with coarse-grained sediments. In other words, Setup 6 introduces a bias by reducing the uncertainties with decreasing grain size of the sediments. In contrast, the bias introduced by Setup 7 reduces the uncertainty with increasing grain sizes.

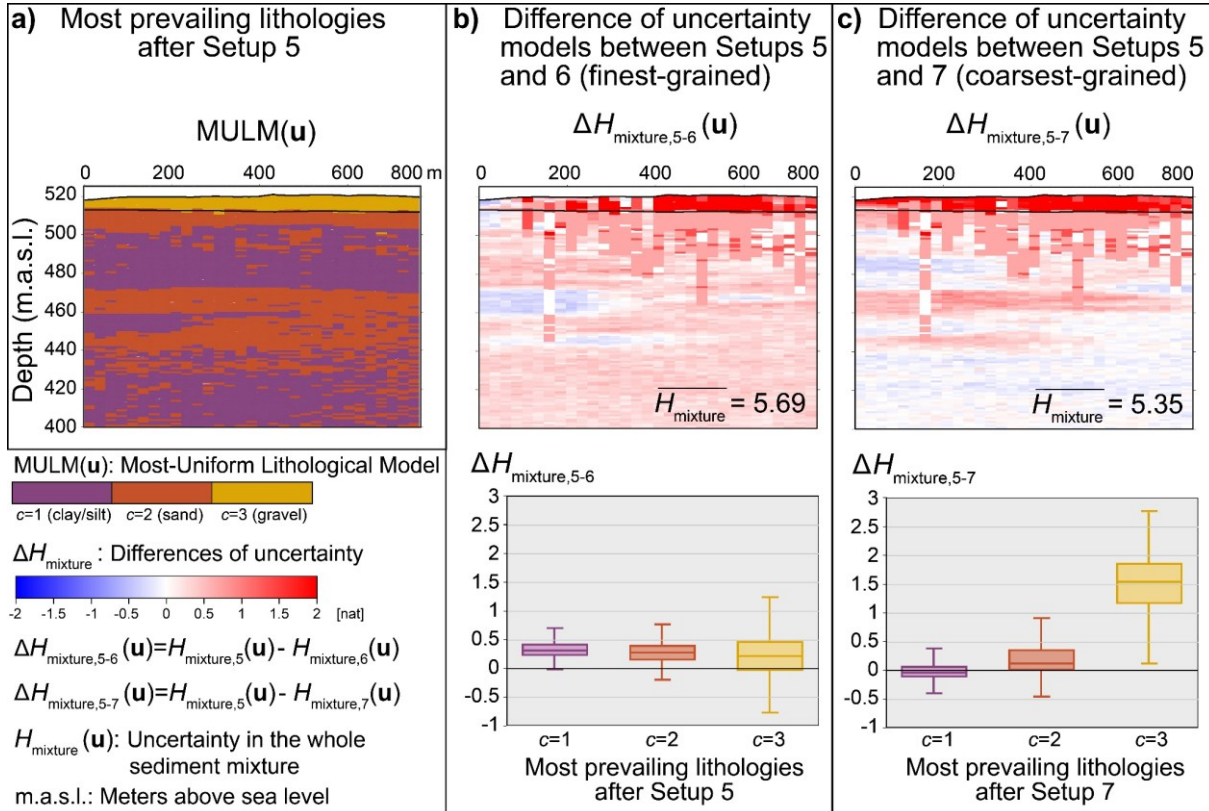


Fig. 32: Uncertainty propagation: **a)** MULM(\mathbf{u}) after Setup 5; **b) (upper panel)** Difference of uncertainty in the whole sediment mixture between Setups 5 and 6; **b) (lower panel)** Boxplot showing the distribution of the difference of uncertainty between Setups 5 and 6; **c) (upper panel)** Difference of uncertainty between Setups 5 and 7; **c) (lower panel)** Boxplot showing the distribution of the difference of uncertainty between Setups 5 and 7

This bias is overcome by adaptation of the method, leading to a higher uncertainty providing a more realistic uncertainty assessment. These findings are in line with Bárdossy and Fodor (2004), who highlighted the need to consider uncertainties in input data to avoid uncertainty underestimation. Moreover, this adaptation of the geo-modeling process introduces a lithological noise in the input data, which is conceptually consistent with the geometric model perturbation proposed in structural models (Wellmann and Caumon, 2018).

5.5 Conclusions

Based on the theory of the D_i models method, an adaptation of the method to incorporate uncertainties from imprecise input data is described. This extension focuses on integrating the uncertainties detected in the semi-quantitative and qualitative descriptions of soil observations

from drilled materials by capturing the lower and upper limits of the fictive GSD of the clastic sediments. In terms of the underlying RVs, this adaptation implies the introduction of lithological noise with two equiprobable sets of input data in the simulation, which is in turn conditioned to both hard data sets, prior models of local proportions and indicator variograms. The concepts of entropy and joint entropy are applied for UQ of the main outputs of the D_i models method. A simulation experiment conducted in a real detrital system investigates both the ability of the UQ measures and the uncertainty propagation derived from the extension of the method. The results show that this adaptation overcomes potential bias caused by ignoring imprecise input data, thus providing a more realistic uncertainty assessment. This ultimately strengthens the decision-making process for practical applications based on the implementation of the D_i models method. Moreover, both UQ measures provide very useful scalar measures for quantifying local uncertainties and for comparisons between average uncertainties. This has great potential for updating and comparing the UQ of the model outputs when fed with new data in a specific application. In addition, both concepts provide a better understanding of how the implementation parameters of the RFs, such as the stationarity/non-stationarity assumption, influence the property prediction and the underlying uncertainties. In this sense, the simulation experiment clearly reveals a significant improvement in the lithological estimation and a reasonable reduction of uncertainty, if available logical subdivisions of the domain are considered and separated RFs are defined. Furthermore, the incorporation of 3-D trend models is desirable, especially when no further subdivisions of the domain can be accomplished, since it leads to a better property prediction. However, the inclusion of trends in the D_i models method raises some difficulties and should be considered on a case-by-case basis, since the trend evaluation might be a critical issue when dealing with large 3-D models combined with high grid resolutions or with more complex conceptual models. In contrast, the scalable nature of the UQ measures seems to be very appropriate for the further application of this method with other conceptual model configurations.

5.6 Acknowledgements

We gratefully acknowledge the Bavarian Environment Agency (LfU) for the access to the borehole database of the Soil Information System of Bavaria. We would like to acknowledge Emerson E&P for providing licenses for the Software product SKUA™ Engineering Modeling in the scope of the Emerson Academic Program, which supported the results of this publication. Finally, we thank the anonymous reviewers for their careful reading of our manuscript and their valuable remarks and suggestions.

CHAPTER 6

Estimation of 3-D hydraulic conductivity fields from fictive grain-size distributions obtained by geological 3-D modeling

Alberto Albarrán-Ordás^a, Kai Zosseder^a

^a Technical University of Munich, Arcisstraße 21, 80333 Munich, Germany

Abstract

The hydraulic conductivity (K) is a crucial parameter for groundwater processes. However, it stands out by its heterogeneity and anisotropy due to differences in soil texture, thus making its area-wide estimation challenging. The common laboratory and empirical methods used, based on grain-size distribution (GSD) analysis of limited data, provide local K -measurements, thus leading to a lower representativeness of aquifer heterogeneity. Instead, pumping tests estimate an integrated K -value over an aquifer section within the cone of depression but still lack revealing spatial variations and high resolutions in K in a larger areal aquifer extent. With the D_i models method, local-dependent GSD in three-dimensional detrital systems were simulated. In this study, the possibilities to estimate K through the simulated particle-size fractions of the geological 3-D model are explored in the city of Munich. The log-cubic interpolant ensures completeness and accuracy in the fictive GSD, thus enabling the multiple application of empirical relationships for estimating K . The resulting 3-D K -fields preserve the K variability within each aquifer system. If averaged for each aquifer system separately within a different lateral extent, i.e., 50-150 m and 550 m, respectively, predictions of K show success rates of 44-47% and deviations of at least one order of magnitude in 15-19% of the cases, when compared to 364 K pumping-test data. The results underline the ability of the approach to successfully estimate K accounting for the aquifer spatial heterogeneity, enhancing its further use in groundwater modeling and potential assessments for aquifer yield and groundwater heat pump systems.

Keywords

Unconsolidated sediments, heterogeneity, hydraulic properties, geological 3-D modeling, water-resources management.

6.1 Introduction

Hydraulic conductivity (K) plays a crucial role in groundwater hydraulics since it conditions the groundwater flow in porous media (Bear, 1972; Chandel and Shankar, 2022). The knowledge of K is then needed for all evaluations, prognosis, and planning issues in groundwater use and protection, and hence for the successful management of groundwater resources (Cheong et al., 2008; Uma et al., 1989; Weight, 2001). This circumstance is reflected in the selected study area of the city of Munich, holding a wide variety of groundwater uses, such as transport and service infrastructure, drinking water, industrial water, and groundwater heat pumps (GWHP) for open loop geothermal systems.

Moreover, K is characterized by its heterogeneity, varying in nature over about twelve orders of magnitude, and its anisotropic nature, thus having a directional dependency (Domenico and Schwartz, 1997; Freeze and Cherry, 1979; Langguth and Voigt, 2004). Even within the same deposit, the expected range is several orders of magnitude (Fogg and Zhang, 2016; Galloway and Hobday, 1983). This leads to obtaining different K values in all directions for the same sequence (Domenico and Schwartz, 1997; Kruseman and de Ridder, 2000). The natural heterogeneity of K has also been reflected in Munich's subsurface of clastic sediments, reaching up to three orders of magnitude in the shallow Quaternary aquifer (Theel et al., 2020; Zosseder et al., 2022b) and four orders of magnitude in the underlying Miocene deposits (Egger, 1978; Zosseder et al., 2022b).

Therefore, various techniques have been developed to estimate K , primarily through three lines of approach: laboratory permeameter tests, field tests, and empirical methods based on grain-size distribution (GSD) data (Todd and Mays, 2005). Laboratory tests measure K from undisturbed soil cores, offering localized results with limited aquifer representativeness. Field techniques include flowmeter tests and well-testing methods like slug and pumping tests, which measure the aquifer's stress response over time (Kruseman and de Ridder, 2000; Weight, 2001). Pumping tests are more reliable and representative than slug tests but are costly and limited to well locations (Mariethoz and Caers, 2015; Prinz and Strauß, 2011; Pucko and Verbovšek, 2015; Todd and Mays, 2005). They provide an integrated K value over a specific aquifer volume, reflecting a composite of formations within the cone of depression. In this sense, K values obtained from pumping tests in wells screened in an aquifer system consisting of more than one layer, i.e., a multi-layered aquifer system, do not provide the hydraulic characteristics of the individual deposits but of an equivalent aquifer system equal to the sum of the individual deposits, assuming there are no faults (Kruseman and de Ridder, 2000). However, the presence of faults can influence the K evaluation. Empirical methods use grain-size analysis to determine K (Chandel and Shankar, 2022; Chapuis, 2012; Entenmann, 1992; Rosas et al., 2014; Storz et al., 2017; Vuković and Soro, 1992), offering quick and low-effort measurements but with less reliability for field-scale characterization (Cheong et al., 2008; Nemes and Rawls, 2006; Prinz and Strauß, 2011; Pucko and Verbovšek, 2015; Schultz and Ruppel, 2002; Shang, 2013). Moreover, since it is not generally possible to identify the best empirical method for a given sample, including different methods would be beneficial to

better indicate the range of K (Devlin, 2015). Furthermore, the greater data availability of petrographical descriptions of boreholes compared with soil samples has triggered research on using petrographical descriptions to estimate K (Fuchs, 2010). Additionally, research has focused on using sedimentological analysis to link geological properties with hydrogeological dynamics, identifying units with similar K values, called hydrofacies (Comunian et al., 2016; Theel et al., 2020).

Given the data sparsity and natural K heterogeneity, geostatistical methods have gained importance for high-resolution K distribution estimation based on the data outlined above (Domenico and Schwartz, 1997). In this sense, Williams et al. (2019) performed SGS (Sequential Gaussian Simulation) to develop a high-resolution 3-D K model in Glasgow, UK, using GSD data, reducing spatial uncertainty in groundwater flow. Similarly, Zheng et al. (2011) applied ordinary kriging (OK) to create a 3-D distribution of K at the MADE site in Mississippi from flowmeter data, emphasizing the need to map K by addressing aquifer heterogeneity beyond field methods. However, relying solely on K measurements may underestimate heterogeneity due to unintentional bias caused by the producing intervals of the aquifer dominated by high K materials (Fogg and Zhang, 2016).

Besides, in recent years, significant efforts have been made in stochastic 3-D modeling of the GSD in clastic sedimentary environments (Albarrán-Ordás and Zosseder, 2023, 2022, 2019; Roberson and Weltje, 2011). This is particularly noticeable since, the heterogeneity of K is a direct consequence of the soil texture. This is in line with Fogg and Zhang (2016), who emphasized the need for greater geologic integration into the analysis of K . Thus, estimating the fictive GSD of the sediment mixture has great potential for deriving relevant grain-size-based soil properties in general, and K in particular. In this sense, the D_i models method was conceived to simulate the grain size classes for a certain number of cumulative frequencies of the GSD at any location in a mixed soil using soil observations from drilled materials (Albarrán-Ordás and Zosseder, 2023, 2022). Obtaining a complete GSD at each location implies, in turn, the possibility of estimating K at every voxel in a three-dimensional domain. However, addressing all cumulative frequencies in the GSD of the mixed soil within the geostatistical framework will result in an overly arduous process (Albarrán-Ordás and Zosseder, 2022). This leads to the need for interpolating the missing cumulative fractions to predict the complete GSD at each location.

As stated above, despite the relevance of K in describing groundwater processes, its estimation remains challenging. Common techniques, such as laboratory, empirical, and field methods, face issues due to the lack of representativeness of aquifer heterogeneity and limited data availability from soil samples or pumping tests. These methods struggle to capture K extensively in larger aquifer volumes. Furthermore, numerical groundwater models require high-resolution K definitions, emphasizing the need for local K estimates. This study aims to address these gaps by exploring the possibilities offered by applying the D_i models method to estimate K in 3-D clastic sedimentary systems. The specific objectives include:

- 1) Achieving the completeness in the fictive GSD obtained from the D_i models method.
- 2) Estimating local-dependent values for the hydraulic conductivity (3-D K field) on the fictive interpolated GSD derived from 1) considering a comprehensive set of empirical relationships and their specific validity criteria.
- 3) Estimating equivalent representative K in alternating beds in detrital systems.
- 4) Validating the model's predictions by comparing the estimated 3-D K field with K values from pumping-test analysis.
- 5) Evaluating the effects of lateral changes in K of the aquifer on the prediction performance.

6.2 Materials and methods

6.2.1 Study area and geological background

The case study area of the presented analysis is the city of Munich, located in Bavaria in the southern part of Germany (see at left of Fig. 33a). The municipality covers an area of approximately 310 km² alongside the River Isar, lying on the so-called Munich Gravel Plain (MGP). The MGP is a glacial outwash plain comprising sandur terraces formed by melting glaciers in the Pleistocene and modern Holocene deposits from alluvial and fluvial origin (Bauer et al., 2005; Lemcke, 1988). A simplified geological map is given in Fig. 33a. The key lithostratigraphical units relevant to this study are the Quaternary and the Upper Freshwater Molasse (Obere Süßwassermolasse in German), i.e., of Miocene age. The abbreviations Q (Quaternary) and T (Miocene, Tertiary) are used throughout the study for clarification purposes. The Quaternary deposits of the MGP, formed mainly by coarse-grained gravels, constitute one of the most productive groundwater occurrences in Europe (Freudenberger and Schwerd, 1996), having an averaged hydraulic conductivity between 3.7×10^{-3} m/s (Theel et al., 2020) and 5.6×10^{-3} m/s (Zosseder et al., 2022b). The base of this unit was shaped by the drainage system over time, constituting an uneven relief of channels and ridges. This results in a variable distribution of saturated aquifer thickness in the shallow aquifer ranging between 2.5 m (1st quartile) and 10.2 m (3rd quartile) in the city of Munich, thus revealing a very heterogeneous potential for groundwater extraction (Albarrán-Ordás and Zosseder, 2020; Böttcher et al., 2019; Böttcher and Zosseder, 2022; Kerl et al., 2012). Q is underlain by clayed-marly slackwater sediments and sandy deposits of the Upper Freshwater Molasse (Bachmann and Muller, 1992). These deposits are, in turn, exploited at different depths (Zosseder et al., 2022b) and have an averaged K value between 2×10^{-5} m/s (Egger, 1978; Gebhardt, 1968) and 3.77×10^{-5} m/s (Zosseder et al., 2022b). The K range of values for both aquifer systems obtained from pumping tests is described in detail in Section 6.2.2.3. The aforementioned hydrogeological conditions have led to a noticeable proliferation of groundwater uses in both the shallow and deeper aquifers to address the energy and water demands in the area, such as service water, drinking water, emergency water supply,

and groundwater heat pumps. Thus, intensive research has been conducted in recent years to better characterize and manage the Quaternary and Miocene aquifers (Epting et al., 2020; Zosseder et al., 2022b). In this context, the D_i models method was conceived for 3-D geo-modeling of the GSD in the subsurface, which led to the development of a geological 3-D model on a city-wide scale in Munich (Albarrán-Ordás and Zosseder, 2023, 2022, 2019). Fig. 33b shows this model by means of the distribution of the most dominant lithologies in the subsurface (see Fig. 33b, left and central parts). Fig. 33b (right part) provides an overview of the reservoir configuration based on the interconnectedness of geological bodies (Albarrán-Ordás and Zosseder, 2022), which was recently qualitatively verified by considering the hydrogeochemical characteristics of the aquifers mentioned above (Kiecak et al., 2023).

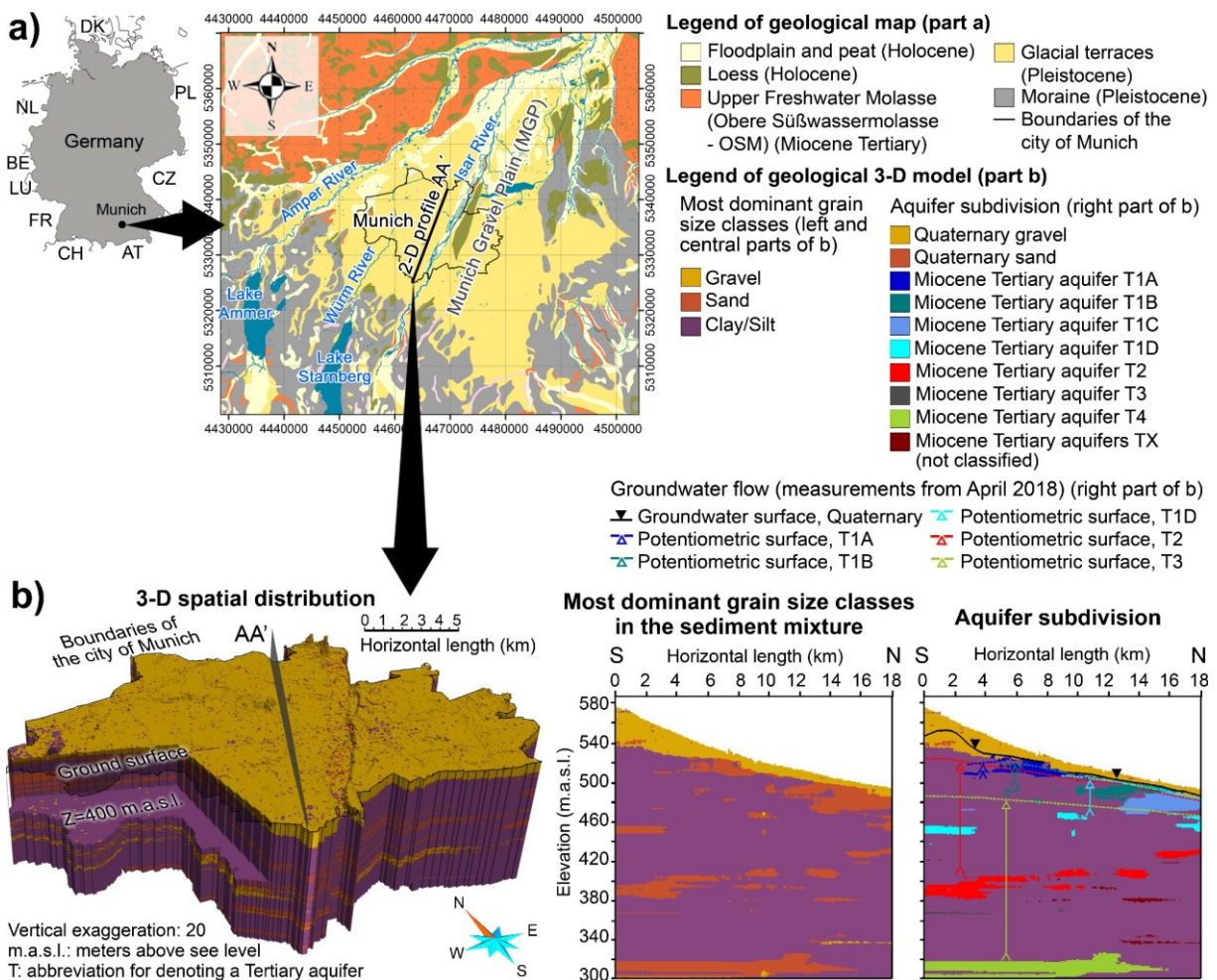


Fig. 33: Study area of the city of Munich. **a)** Location map and simplified geological map; **b)** (left) Geological 3-D model of Munich: 3-D spatial distribution of the most dominant grain size classes in the sediment mixture with partly transparent ground surface; (center) 2-D profile AA' showing the most dominant lithologies; (right) 2-D profile AA' showing the aquifer subdivision

The clastic nature of the most recent sediments occurring in the area, i.e., the Quaternary and the Miocene sequences of sediments, enables the characterization of the clastic depositional systems using the grain size range. Moreover, the study area ensures good spatial data coverage, with over

20,000 boreholes with soil observations, 270 GSD curves obtained from sieving, and 364 K values from pumping-test analysis. Additionally, the geological 3-D model developed in the last years in the study area provides simulated particle-size fractions of the GSD at each location (Albarrán-Ordás and Zosseder, 2023, 2022, 2019; Zosseder et al., 2022b).

6.2.2 Datasets

6.2.2.1 Simulation data from the geological 3-D model of Munich

The geological 3-D model of Munich covers an area with dimensions of 27 by 21 km in the easting and northing, respectively (see Fig. 33a), and approximately 300 m in the vertical direction (see Fig. 33b, at right). The grid has a resolution of 100 by 100 m aurally and 1 m vertically, comprising approximately 23 million voxels. This grid resolution successfully captures the variability present in the borehole data and subsurface materials (Zosseder et al., 2019) and presents similar values to those of other 3-D geo-models carried out at city-wide or regional scales (Bianchi et al., 2015; Enemark et al., 2022; Hademenos et al., 2019; Høyer et al., 2015; Jørgensen et al., 2010; Kearsey et al., 2015; Stafleu et al., 2011). Fig. 34a illustrates a small-scale schematic 2-D profile showing an overview of the model and the simulation data used. The model provides three ($C=3$) simulated fractions at grain-sizes limits between 0.001-0.063 mm (clay and silt), 0.063-2 mm (sand), and 2-63 mm (gravel). Herein, a constant step in the GSD of 10% was fixed. The latter results in ten cumulative percentage values (10, 20, 30, ..., 100), each of which is simulated a grain size class (see part immediately below the 2-D profile, Fig. 34a). Further details of the D_i models method, and the geological 3-D model of Munich are given in Albarrán-Ordás and Zosseder (2023, 2022, 2019). Appendix D-1 provides a more detailed summary of the main steps of the D_i models method.

To illustrate the meaning of these data, Fig. 34a shows the simulated grain fractions at an unsampled location \mathbf{u} . As indicated by the arrow flowing out of location \mathbf{u} in Fig. 34a, all the simulated grain size classes below or equal to 20% are necessarily in the particle range of sands in this example. In addition, all grain fractions from the 30% must be in the particle size range of gravel. However, the grain size range linked to the cumulative percentages between 20% and 30%, i.e., 21%, ..., 29%, were not explicitly addressed by simulation since a constant percentile step of 10% in the GSD was fixed (Albarrán-Ordás and Zosseder, 2023). This implies an unknown grain size ranging from sand to gravel for these cumulative percentages. Consequently, this uncertainty can be captured by considering a range (see grey area, Fig. 34c), thus representing the coarsest-grained and finest-grained lithological composition that can be inferred (see blue and red curves denoted as MIN and MAX (Albarrán-Ordás and Zosseder, 2023)). The interpolation procedure of both curves shown in Fig. 34c is addressed in detail in Section 6.2.3. The dataset used in the present study comprises 23 million cells with information about the simulated grain classes for the ten cumulative frequency values in the same format as shown in Fig. 34a.

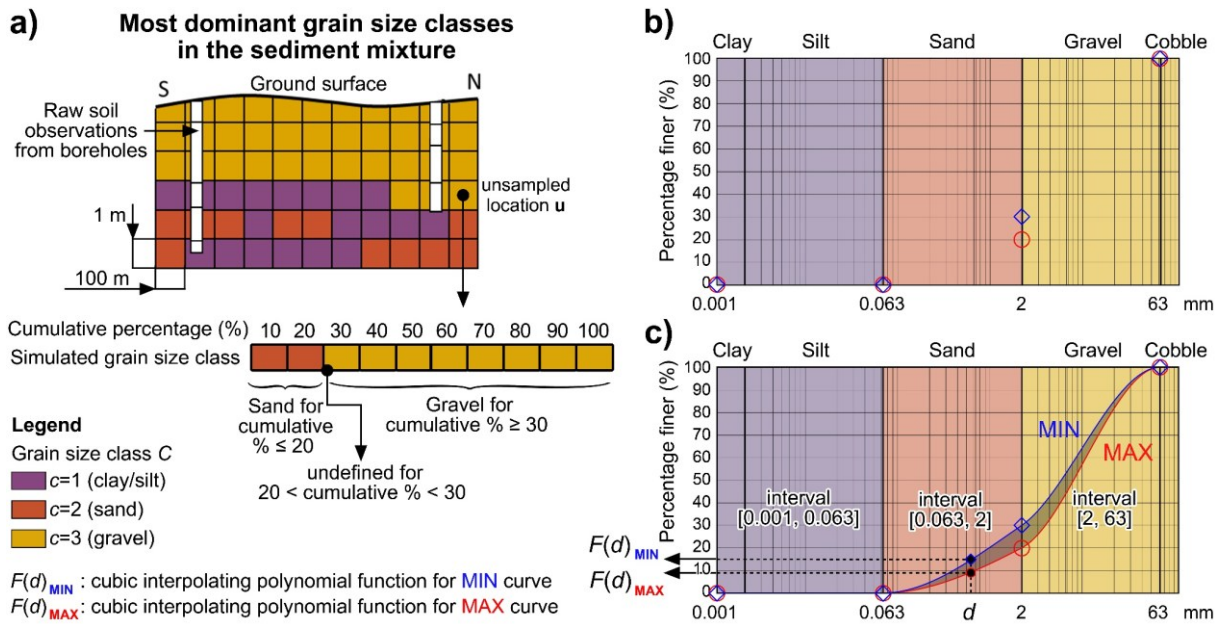


Fig. 34: Exemplary estimation of the fictive GSD range from the results of the D_i models method at unsampled location **u**. **a)** Results from simulation: (upper part) cross section showing the distribution of the most dominant grain size classes, (lower part) grain size classes for each cumulative percentage at location **u**. **b)** Points representing the simulated grain fractions provided by the D_i models method at location **u**. **c)** Resulting interpolated fictive GSD range at location **u** by log-cubic interpolation (PCHIP) as described in Section 6.2.3

6.2.2.2 GSD curves of soil samples obtained from sieve analysis ($GSD_{measured}$)

A testing dataset comprising 270 sieving curves obtained from 191 wells was used to validate the interpolated fictive GSD derived from the geological 3-D model. The location of the soil samples across the city of Munich used in this study is indicated by red triangles in Fig. 35. Soil material was taken at different depths in the Quaternary (~80%) and Miocene (~20%) deposits, respectively. The Quaternary basis, obtained from geostatistical relief modeling (Albarrán-Ordás and Zosseder, 2020), was used to assign a lithostratigraphical unit to each sample.

6.2.2.3 Hydraulic conductivity values from pumping-test analysis (K_{pump})

The present study uses 364 K values obtained from applying multiple methods for evaluating 145 pumping tests conducted in the same number of wells in both the Quaternary and the underlying Miocene aquifer systems distributed across the city of Munich. Fig. 35 (light green dots and dark green crosses) illustrates the pumping well locations. The application of multiple pumping-test evaluation methods for each pumping test produces different results, thus leading to obtaining up to ten K values at one single well from one pumping-test report, denoted here with K_{pump1} , K_{pump2} , ..., K_{pump10} . The differences in the results are due to inevitable inaccuracies in the observed or extrapolated data used in the calculations and the methods used, especially in the graphical methods (Kruseman and de Ridder, 2000). The works of Theel et al. (2020) and Zosseder et al. (2022b) provide detailed information about the data collection, digitalization, and

quality/plausibility analysis. Moreover, K values obtained from pumping tests were classified into three quality levels, i.e., high-, medium-, and low-quality, based on the measured data quality and the choice of the pumping-test evaluation method. Theel et al. (2020) reviewed the details of this quality classification.

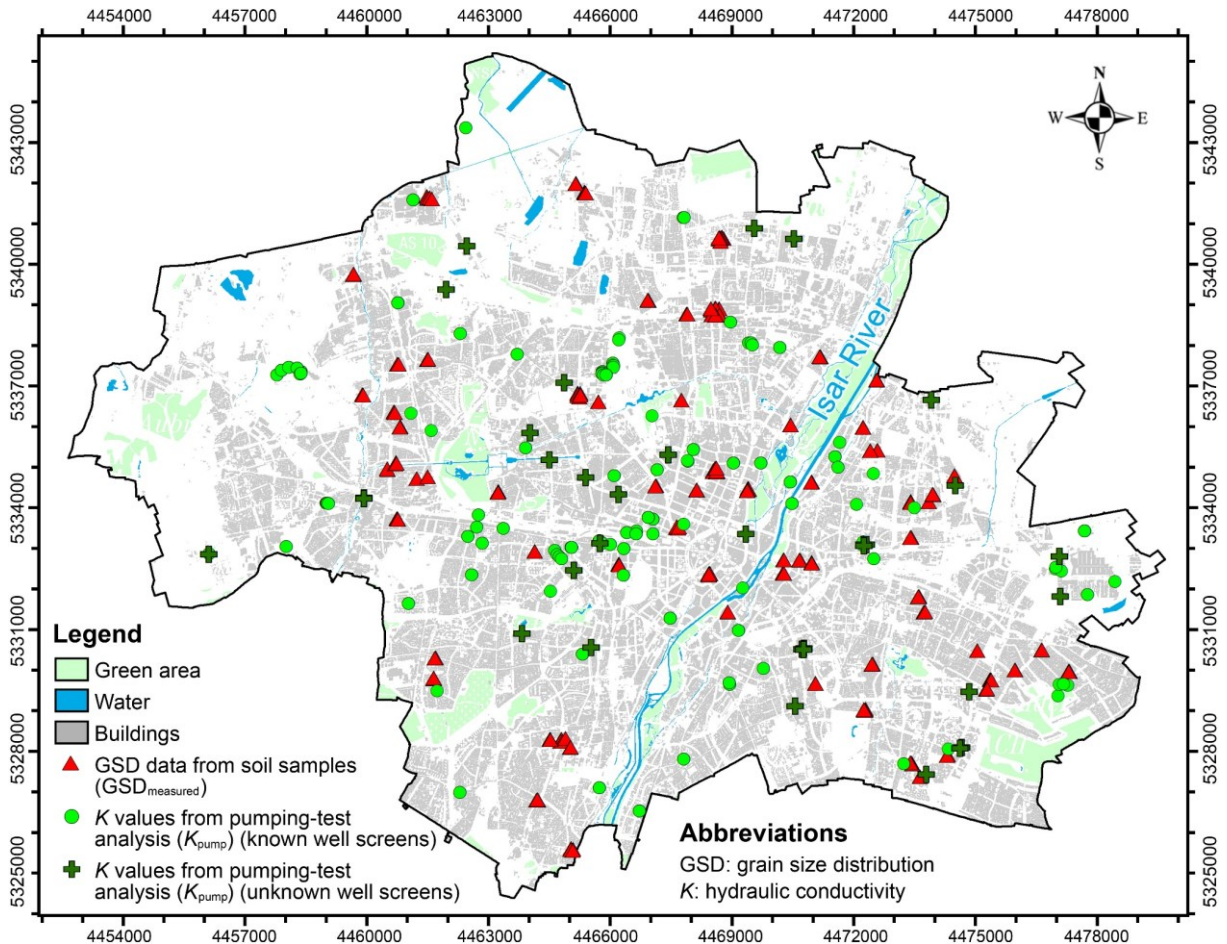


Fig. 35: Location map of the testing datasets used in the study, i.e., GSD curves of soil samples ($GSD_{measured}$), and hydraulic conductivity values from pumping-test analysis (K_{pump}). Number of GSD data: 270. Number of K_{pump} data: 364, of which 306 data correspond to wells with known screen positions, and 58 data came from wells with assumed screen positions

This dataset provides reference data to validate the estimated local-dependent K values derived from the fictive GSD obtained from the geological 3-D model (see Section 6.2.4). Thus, it is essential to have the necessary well construction information, e.g., length of the well screen and the depth at which it is placed, of the wells having K_{pump} values. In this sense, 10% of the wells, making a total of 58 K_{pump} values, lacked well screen data, except for the final well depth (see dark green crosses, Fig. 35). Herein, a position for the screened interval was to be assumed, with depths to the top and bottom set at the groundwater table and 1 m above final depth, respectively. The possible effects in the prediction performance of the aforementioned quality level and other well construction related data, such as the certainty/assumption of the well screen position and the number of screened intervals per well, are further discussed.

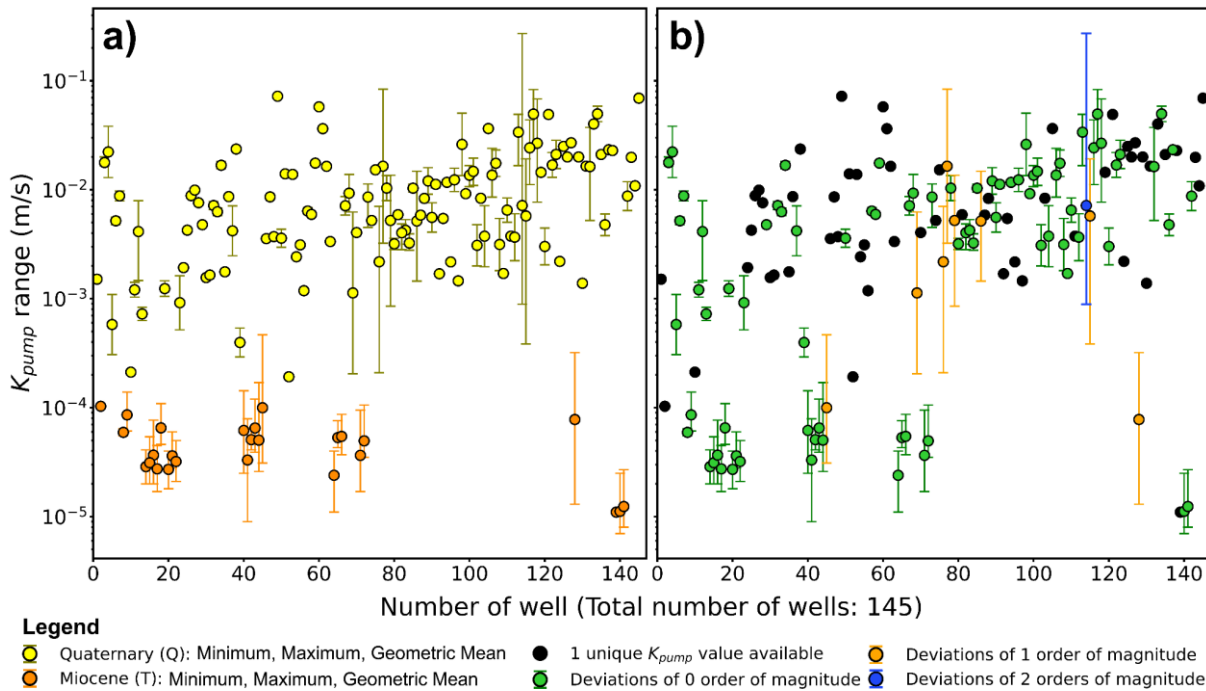


Fig. 36: Available dataset from pumping-test analysis. The plot shows the spread of the K_{pump} values obtained from applying multiple pumping-test evaluation methods from one pumping-test report at every single well in the Quaternary and Miocene aquifers in the city of Munich. **a)** By lithostratigraphic unit; **b)** By deviations expressed as orders of magnitude (powers of ten). Total number of K_{pump} values: 364 (240 in the Quaternary, 124 in the Miocene)

The scatter plots in Fig. 36 show the variability in the K_{pump} values obtained from applying multiple pumping-test evaluation methods in 145 wells. The bars in Fig. 36 indicate the spread of the K_{pump} values using the minimum, maximum, and geometric mean values obtained from one pumping-test report at each well. Meanwhile, Fig. 36a indicates the data spread separately for each lithostratigraphic unit, i.e., Q and T. Fig. 36b illustrates the deviations expressed as orders of magnitude. The graph reflects that 90% of the wells with multiple K_{pump} values obtained from applying various pumping-test evaluation methods have deviations in the same order of magnitude, represented in green bars in Fig. 36b. However, 9% of the K values amounting to 8 wells had K_{pump} estimates ranging one order of magnitude, and only in one case K_{pump} deviated in two orders of magnitude (see blue bar, Fig. 36b). The remaining 56 wells, represented as black dots in the graph, have only one K_{pump} value obtained from applying only one pumping-test evaluation method. As revealed in Section 6.1, K values obtained from pumping tests are considered the most reliable and accurate K estimates possible (Kruseman and de Ridder, 2000; Prinz and Strauß, 2011; Todd and Mays, 2005). As discussed above, K_{pump} data show an accuracy of less than one order of magnitude in most of the cases, i.e., 90% of the wells with multiple K_{pump} data (see Fig. 36b). This motivates the quantification of the rate of deviations of at least one order of magnitude between predictions and K values from pumping-test analysis (K_{pump}) to account for the worst-cases of prediction.

Furthermore, if we consider all the K data in the Quaternary sediments, a wide natural variability in K can be inferred from Fig. 36. This is in line with the findings of Exler (1967), Gebhardt (1968), and Theel et al. (2020). The latter work reported large steps of two orders of magnitude, even at very short distances (~ 300 m). Compared to Q , the K_{pump} values from the Miocene used in the present study are two to five orders of magnitude lower (Böttcher and Zosseder, 2022; Egger, 1978; Theel et al., 2020), and show less natural variability, i.e., less than two orders of magnitude (see lower part, Fig. 36).

6.2.3 Estimation of the fictive GSD range by log-cubic interpolation ($\text{GSD}_{\text{predicted}}$)

The need to achieve completeness in the fictive GSD based on the limited grain sizes provided by the D_i models method is motivated by the possibility of estimating K at every location in a three-dimensional domain. The estimation procedure of the fictive GSD range comprised the determination of the unknown fraction at grain size d from the cumulative percentage values provided, as shown in Fig. 34c. In addition, the interpolated GSD range should also meet the essential requirements of a GSD curve, i.e., respecting all provided data, and being both smooth and monotone (Shang, 2013).

The log-cubic method was used to interpolate the fictive GSD range based on multiple Piecewise Cubic Hermite Interpolating Polynomials (PCHIP) (Esfandiari, 2017; Fritsch, F.N.; Carlson, 1980; Moler, 2004). This method was favored over others, such as the log-linear method. Although the log-linear method has often been used in the past (Leij et al., 1994) and ensures monotonicity, it is not smooth (Shang, 2013) and has been referred to as not sufficiently accurate (Nemes et al., 1999).

The application of the PCHIP method to the simulation data obtained from the D_i models method implies the introduction of an interpolating polynomial function $F(d)$, which determines the cumulative percentage corresponding to a grain size d (see Fig. 34c). A number of C simulated fractions provided by the D_i models method results in $C + 1$ points in the fictive GSD. This implies consideration of a number of C interpolating segments defined in the grain size intervals expressed by $d_j \leq d \leq d_{j+1}$, where j is the interval index ($j = 1, 2, \dots, C$). The general expression of the PCHIP interpolant (Shang, 2013) can be immediately adapted to our particular case to apply piecewise for every interpolating segment $F_j(d)$ for the grain size interval $[d_j, d_{j+1}]$ as follows:

$$F(d) = F_j(d), \quad d_j \leq d \leq d_{j+1}, \quad j = 1, 2, \dots, C - 1, \quad (47)$$

$$F_j(d) = F_{j+1} \frac{3hs^2 - 2s^3}{h^3} + F_j \frac{h^3 - 3hs^2 + 2s^3}{h^3} + f_{j+1} \frac{s^2(s-h)}{h^2} + f_j \frac{s(s-h)^2}{h^2}, \quad (48)$$

where: $h = \ln d_{j+1} - \ln d_j$, $s = \ln d - \ln d_j$, and f_j and f_{j+1} represent the slope of the function at knots d_j and d_{j+1} .

To illustrate the application of PCHIP in the geological 3-D model of Munich, Fig. 34c shows the resulting interpolated fictive GSD range at an exemplary location **u**. As mentioned in Section 6.2.2.1, the model provides three simulated fractions (clay/silt, sand, and gravel), thus leading to $C=3$ interpolating segments in particle size intervals $[0.001, 0.063]$, $[0.063, 2]$, and $[2, 63]$ (see Fig. 34c). The simulated grain fractions enable deriving $C + 1 = 4$ pairs of points, marked by blue diamonds, and red circles in Fig. 34b and Fig. 34c, representing discontinuities in the second derivate of the function for the MIN and MAX curves, i.e., $F(d)_{MIN}$ and $F(d)_{MAX}$, respectively.

To assess the performance of the interpolation of the fictive GSD, the predicted values were compared against $GSD_{measured}$ data obtained from sieving of 270 soil samples from 191 wells (see Section 6.2.2.2). The boxplot in Fig. 37 illustrates the deviations between the predicted and measured data distributions at each of the ten cumulative percentages subject to simulation.

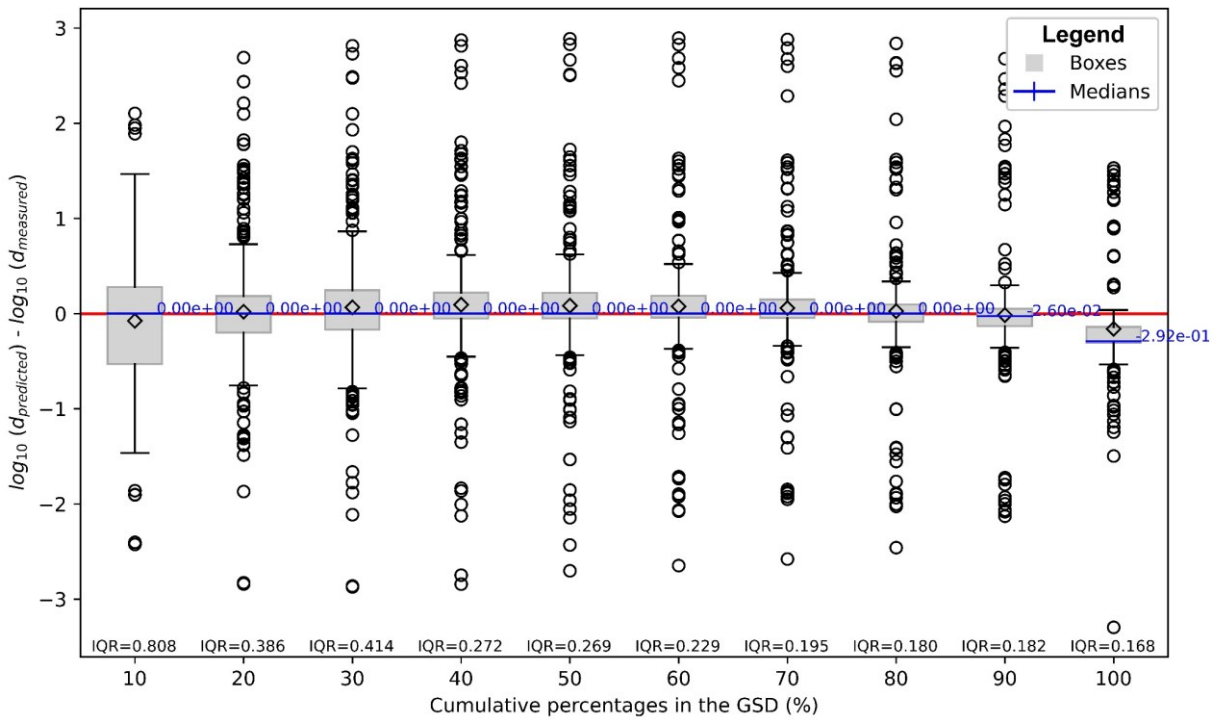


Fig. 37: Boxplot showing the distribution of the deviations between the log-cubic interpolated fictive GSD with the PCHIP interpolant and the measured GSD obtained from sieving in the geological 3-D model of Munich. Total number of data: 270 sieving curves obtained from 191 wells. IQR: Interquartile range. GSD: Grain-size distribution. d : grain size in mm

For easier comparison, and due to the logarithmic nature of the grain sizes d , the logarithm (base 10) of the data is considered. Fig. 37 shows that as the cumulative percentage in the GSD increases, the interquartile range (IQR) of the deviations between the fictive GSD and the real sieving curves decreases and, thus, the accuracy increases. Moreover, a strong prediction ability is indicated by the small median values in Fig. 37. However, we observe that the fictive GSD interpolated from the results of the 3-D model shows an overestimation in the d_{100} -value, which may be due to the consideration of the grain-size limit between 2-63 mm for gravels in the simulation setup, as

exposed in Section 6.2.2.1. Regarding the estimation of K , this is not expected to have a significant impact since the d_{100} grain diameter is not used in any empirical formulas for relating K from the grain size range.

The interpolation procedure, the estimation of the 3-D K fields (see Section 6.2.4), and related diagram preparations were performed with the NumPy (Harris et al., 2020), SciPy (Peterson et al., 2001), and Matplotlib (Hunter, 2007) packages in Python.

6.2.4 Estimation of 3-D K fields using empirical relationships on the fictive GSD range ($K_{\text{predicted}}$)

Once the full range of the fictive GSD is estimated for all voxels in the domain, as shown in Fig. 34c, grain size characteristics, such as effective grain diameters and the coefficient of uniformity, among others, can be inferred. Consequently, empirical equations relating K with the size property of porous media can be used. The relationship between K and the grain size ultimately conditions the selection of empirical methods used in the present study for K estimation. Among different sources of literature, the works of Vuković and Soro (1992), Ishaku et al. (2011), Chapuis (2012), Sahu and Saha (2016), Říha et al. (2018), and Chandel and Shankar (2021) provide a detailed and comprehensive description of the several empirical relationships for K estimation based on GSD of soil samples. The following 15 empirical methods were utilized in the present study to estimate K at each location in the geological 3-D model of Munich: Seelheim (1880), Hazen (1892), Beyer (1964), Kozeny-Carman (Carman, 1956, 1939; Kozeny, 1927), USCRO (Urumović et al., 2020), Slichter (1899), USBR (Bialas and Kleczkowski, 1970), Seiler (1973), Harleman (Harleman et al., 1963), Chapuis (2004), Sauerbrey (1932), NAVFAC (Chapuis et al., 2005), Kaubisch (1986), Shahabi (Shahabi et al., 1984), and the adaptation of Kozeny-Carman for high conductive gravels (Bianchi and Zheng, 2016). An overview of all methods used, as well as their domains of applicability and implemented criteria in the geological 3-D model, is given in Tab. 10 in Appendix D-2.

The implemented estimation procedure automatically computes all the parameters required by the empirical methods outlined above and listed in Tab. 10 in Appendix D-2 in each voxel. These parameters include the coefficient of uniformity, porosity, void ratio, as well as selected grain diameters needed for each method, i.e., d_5 , d_{10} , d_{17} , d_{25} , d_{50} , and d_{60} (see Tab. 10 of Appendix D-2). Since the GSD range is limited by two curves, i.e., the coarsest-grained, and finest-grained lithological composition (see Fig. 34 and Fig. 38b), this computation leads to obtain two sets of minimum and maximum values for each parameter. Then, the specific validity criteria of all empirical methods included in Tab. 10 in Appendix D-2 are verified for the entire GSD range at each location. This opens up the possibility of using the empirical methods several times to cover the domain of applicability in the whole grain size range. Subsequently, only the methods meeting the domains of applicability are implemented individually in each voxel. Applying multiple empirical relationships leads to obtaining a multiple estimation of K on a cell-by-cell basis.

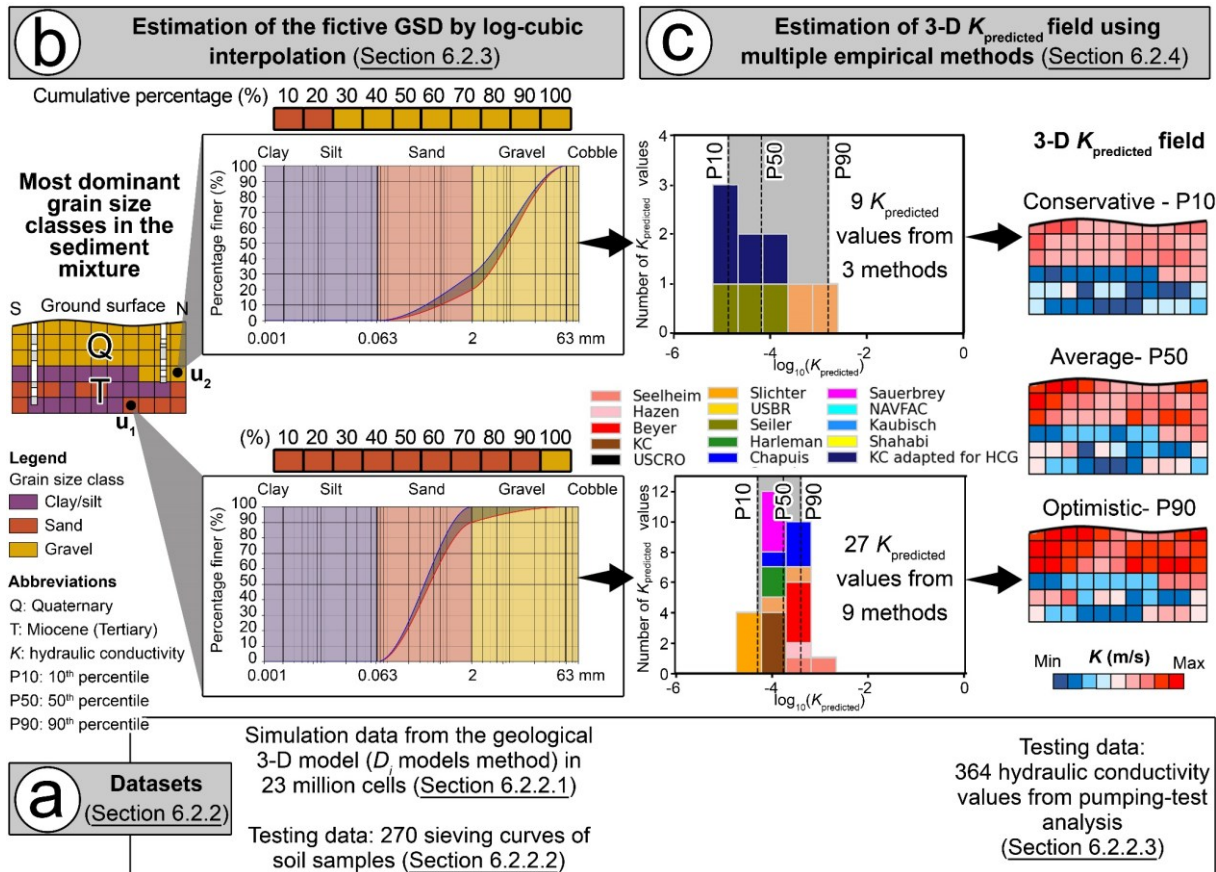


Fig. 38: Scheme of the datasets used and the main steps involved in the study. **a)** Datasets; **b)** Estimation of the fictive GSD; **c)** Estimation of 3-D hydraulic conductivity field using multiple empirical methods (Averaging K in alternating beds, i.e., Section 6.2.5, not in figure)

The fulfillment of the validity criteria results in a non-constant number of $K_{\text{predicted}}$ values at each voxel. Fig. 38b and c show how multiple $K_{\text{predicted}}$ values are estimated at two unsampled locations, u_1 and u_2 . Whereas at location u_1 27 $K_{\text{predicted}}$ values were calculated from nine empirical methods, the K estimation at location u_2 resulted in 9 $K_{\text{predicted}}$ values from three methods. Since a voxel represents an individual bed of coarse- and fined-grained sediments, and K of a particular bed is generally considered to be log-normal (Domenico and Schwartz, 1997; Freeze and Cherry, 1979), the use of the geometric mean, i.e., the mean of the log-transformed K , may be appropriate for determining an average of K at each voxel ($K_{\text{predicted},P50}$) (Prudic, 1991) (see Fig. 38c, at right). Moreover, a conservative ($K_{\text{predicted},P10}$) and an optimistic K estimate ($K_{\text{predicted},P90}$) are considered. To illustrate this, the right part of Fig. 38c presents the P10, P50, and P90 K values derived at each location.

6.2.5 Averaging K in alternating beds of heterogeneous detrital systems

The estimated 3-D K field from the 3-D model is validated against a real dataset of K values obtained from pumping-test analysis presented in Section 6.2.2.3. This validation is initially conducted in the immediate cells intersecting the well screens. Subsequently, the validation is

conducted by successively adding rings of cells laterally in the aquifer in the 3-D model, reaching extents up to 550 m. Therefore, to carry out this process, an averaging of K for the alternating beds, both vertically and horizontally, over a specific aquifer volume along the screens is required. The present section explains the averaging process in detail.

6.2.5.1 K in alternating beds in the immediate vicinity of the wells

The P10-, P50-, and P90-estimates for the local-dependent hydraulic conductivity derived from the geological 3-D model, shown schematically at the right of Fig. 38c, are further validated and discussed by comparing them to the K_{pump} values obtained from the pumping-test analysis described in Section 6.2.2.3. This ultimately leads to determining the degree of deviation of the prediction. However, as mentioned in Section 6.2.2.3, the K_{pump} values were obtained from sections of productive aquifer intervals encountered by the screened intervals of the wells. To illustrate this, Fig. 39a shows a 2-D example profile from the geological 3-D model of Munich. The cross section shows the shallow, unconfined aquifer and a well screened in approximately 4 m of the underlying confined Miocene aquifer. This implies that the vertical extent of the screened interval exceeds the voxel dimension. In our example, the screened interval overlaps four cells (see area indicated in grey, Fig. 39a and Fig. 39b). Therefore, this analysis requires averaging the $K_{\text{predicted}}$ values along the well screens to obtain a representative horizontal hydraulic conductivity against which the pumping-test measurements can be compared. This is reflected in Fig. 39b. Thus, the aquifer section in the immediate vicinity of the screen, i.e., the grey rectangle shown in Fig. 39b2, represents a layered system composed of alternating beds with different lithological composition, i.e., different fictive GSD and, thus, different $K_{\text{predicted}}$ values. At this point, the effective hydraulic conductivity parallel to the layering of sediments, i.e., in the horizontal direction x , is commonly calculated as the arithmetic mean of K of the individual beds with permeable materials weighted by the thickness of each (Bear, 1972; Domenico and Schwartz, 1997; Freeze and Cherry, 1979; Prudic, 1991; Woessner and Poeter, 2020). This can be adapted to the context of each screened well to calculate the equivalent horizontal hydraulic conductivity in each well (K_{xeq}) as follows:

$$K_{\text{xeq}} = \sum_{v=0}^{N_v} \frac{K_{\text{predicted},v} \times m_v}{m_{\text{screen}}}, \quad (49)$$

where m_v represents the thickness of each voxel v with permeable material intersecting the well screen, m_{screen} is the sum of all the well screen lengths, and N_v is the number of voxels intersecting the well screen. Fig. 80 in Appendix D provides a more detailed overview of the averaging process of K for P10 and P90 by means of an exemplary well screen. In addition, the coefficient of uniformity representative of the aquifer near the well screens was also computed as a thickness-weighted arithmetic average. This is further discussed in Section 6.3.2.

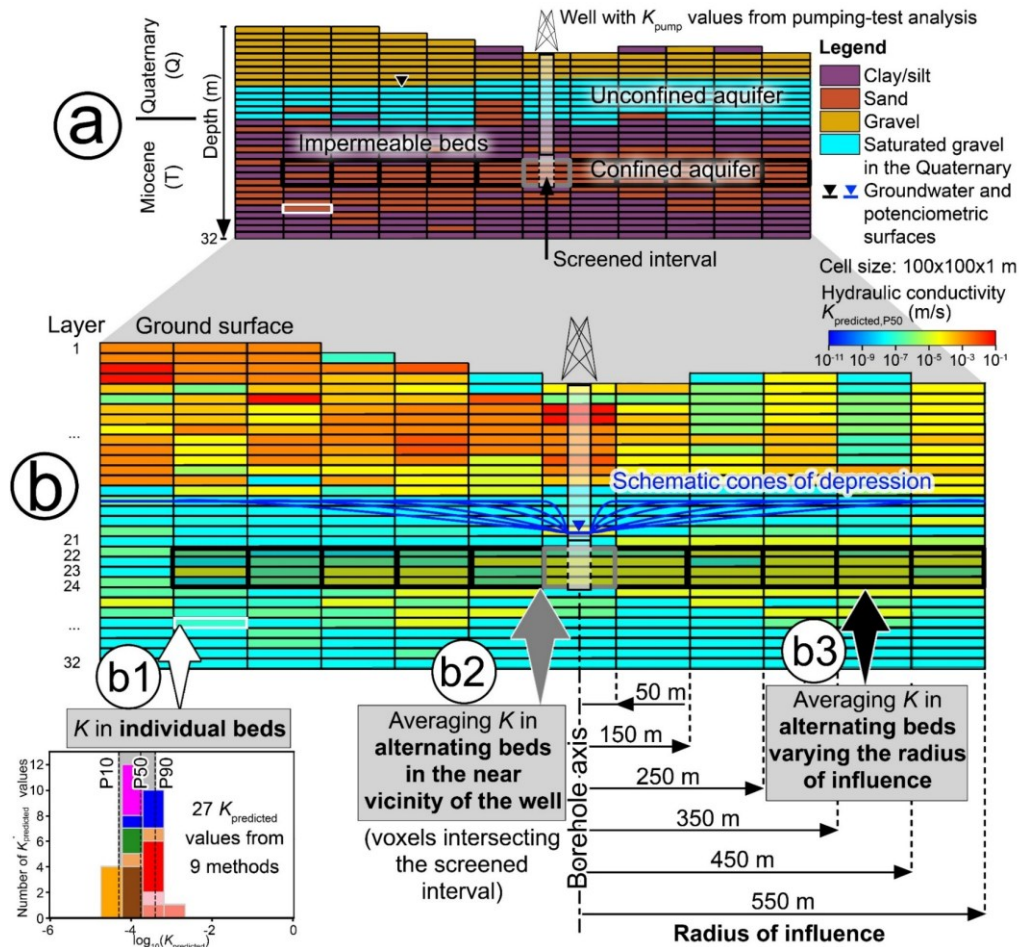


Fig. 39: Visualization of the averaging process of the local-dependent hydraulic conductivities using an exemplary 2-D profile. **a)** Distribution of the most dominant lithologies; **b)** Distribution of the average estimate of K ($K_{\text{predicted,P50}}$); **b1)** K in individual beds; **b2)** Averaging K in alternating beds in the near vicinity of the well; **b3)** Averaging K in alternating beds, when varying the cone of depression

6.2.5.2 K in alternating beds and expanding the well's radius of influence

As mentioned in Section 6.1, pumping tests provide an integrated K value over a portion of the aquifer. This volume is defined vertically by the screened interval and horizontally by the generated cone of depression. The effects of considering different lateral extents of the cone of depression on the prediction performance are also evaluated and discussed. However, this evaluation requires an averaging of the $K_{\text{predicted}}$ values not only in the vertical direction along the screened intervals, as was already described in Section 6.2.5.1, but also horizontally up to a distance beyond which flow in the wells is not supposed to affect the head in the aquifer. This case, and specifically the different lateral extents of the radius of influence considered, is represented by black rectangles in Fig. 39b. An averaging of K of the permeable materials is also needed to obtain a horizontal K value against which the K values from the pumping-test analysis can be compared when varying the well's area of influence.

In this sense, five setups were considered in the geological 3-D model of the city of Munich for this comparison, employing radii of influences of 150 m, 250 m, 350 m, 450 m, and 550 m (see Fig. 39b3). Implementing this process in a 3-D voxelized domain implies increasing the radius of influence by steps of one ring of voxels, considering a voxel size of 100x100x1 m, as discussed in Section 6.2.2.1. This translates into the five setups mentioned above as follows: 150 m (one ring of voxels), 250 m (two rings of voxels), 350 m (three rings of voxels), 450 m (four rings of voxels), and 550 m (five rings of voxels). This is illustrated in the lower part of Fig. 39b3.

The aquifer portion within each cone of depression considered, i.e., the black rectangles shown in Fig. 39b3, represents a layered system with a lateral extension of the cone of depression, thus exceeding the voxel dimension. As Prudic (1991) suggested, it may be best to approximate the K of each layer firstly using the geometric mean before converting it into an equivalent hydraulic conductivity parallel to the layering. For this purpose, the Moving Windows Averaging (MWA) method (Rossi and Deutsch, 2014) was applied for each setup and each layer separately (see layer index in Fig. 39b, left part). In our example, the screened interval is placed between layers 21 and 24. The MWA technique calculates the geometric mean of a subset of neighboring voxels defined by the radius of influence and, thus, the number of voxel rings. This ensures symmetry around the central voxel, which is intersected by the well screen. For example, considering a cone of depression of 350 m, i.e., a number of 3 rings of voxels (see Fig. 39b3), implies the computation of the geometric mean within a window with the size of $(3 \times 2) + 1 = 7$ voxels and, thus, a radius of influence of 3.5 voxels (350 m). Subsequently, the equivalent K parallel to the layering is calculated as in Eq. (49) but using the values obtained from MWA in each layer. This process was implemented over the whole volume of the geological 3-D model.

The predictive ability was estimated by comparing K values from pumping wells, i.e., K_{pump} , to the predicted ranges, i.e., the P10- and P90-estimates, of the equivalent horizontal hydraulic conductivities derived from the 3-D model. The expected range is then a series of K -values between the conservative (P10) and optimistic (P90) estimates. Fig. 40 illustrates a generalized scheme of this process. In our example, whereas two of the measured hydraulic conductivities are within the predicted range (K_{pump1} and K_{pump2}), in the remaining two measurements the prediction deviates in less than one order of magnitude (K_{pump3} and K_{pump4}).

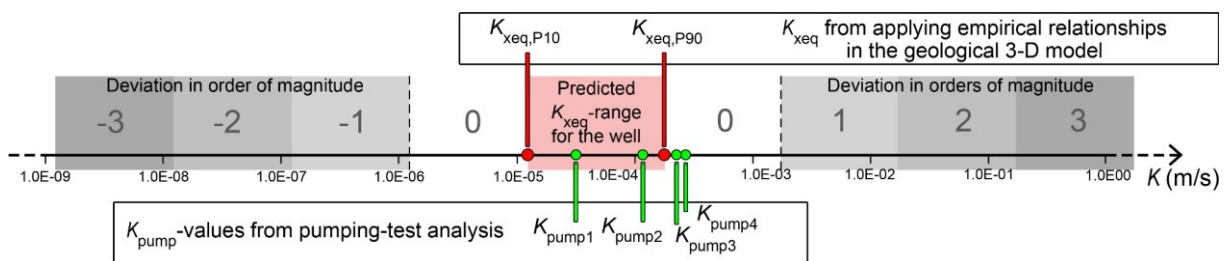


Fig. 40: Generalized scheme for estimating the predictive ability by comparing K_{pump} values from pumping-test analysis to the predicted range

The prediction performance of the five setups and the configuration in the vicinity of the wells was evaluated with two statistical parameters, i.e., the coefficient of determination (R^2), defined as the square of the correlation coefficient (R), and the mean absolute error (MAE) (Chandel and Shankar, 2022; Říha et al., 2018), defined as:

$$R = \frac{\sum_{t=1}^{N_{\text{pump}}} (K_{\text{pump}} - \overline{K_{\text{pump}}})(K_{\text{xeq}} - \overline{K_{\text{xeq}}})}{\sqrt{\sum_{t=1}^{N_{\text{pump}}} (K_{\text{pump}} - \overline{K_{\text{pump}}})^2 \sum_{p=1}^P (K_{\text{xeq}} - \overline{K_{\text{xeq}}})^2}} \quad (50)$$

$$MAE = \frac{1}{N_{\text{pump}}} \sum_{t=1}^{N_{\text{pump}}} |K_{\text{pump}} - K_{\text{xeq}}|, \quad (51)$$

where t = index for each hydraulic conductivity value from pumping-test analysis, N_{pump} = total number of K values available from pumping tests (364), K_{xeq} = estimated equivalent horizontal hydraulic conductivity in each well within the radius of influence considered, and K_{pump} = hydraulic conductivity values obtained from pumping-test analysis. Furthermore, the rate of successful predictions (RPS), and the rate of deviations of at least one order of magnitude (RD1) were considered. Higher values of R^2 and RPS, and smaller values of MAE and RD1 signify a better agreement between K_{pump} and K_{xeq} .

6.3 Results and discussion

6.2.2 Estimated 3-D K fields (P10, P50, P90) in the city of Munich

With the explained approach in Section 6.2, the hydraulic conductivity values ($K_{\text{predicted}}$) at each location of the city of Munich's subsurface up to a depth of ~ 300 m below ground level are estimated and represented in Fig. 41. As explained, these results were obtained from using 15 empirical methods on the fictive interpolated GSD at each voxel derived from the D_i models method. Using different percentiles, i.e., P10 as a conservative estimate (see Fig. 41a), P50 as an average estimate (see Fig. 41b), and P90 as an optimistic estimate (see Fig. 41c), to assess the $K_{\text{predicted}}$ -values at each voxel, three probability distributions for the K -value field in the different aquifers are available.

The reliability of the P10-, P50-, and P90-estimates for $K_{\text{predicted}}$ was tested by comparing the estimation results with K -values reported in the literature for both the Quaternary and Miocene aquifers of the city of Munich. K -value estimates were first grouped by aquifer system (see grey- and black-outlines of the aquifer systems in center panels of Fig. 41). An individualized analysis for each Miocene aquifer separately was not considered due to the lack of sufficient representative data from pumping tests for each aquifer (Zosseder et al., 2022b). Therefore, the statistical analysis is presented considering all the Miocene aquifers together.

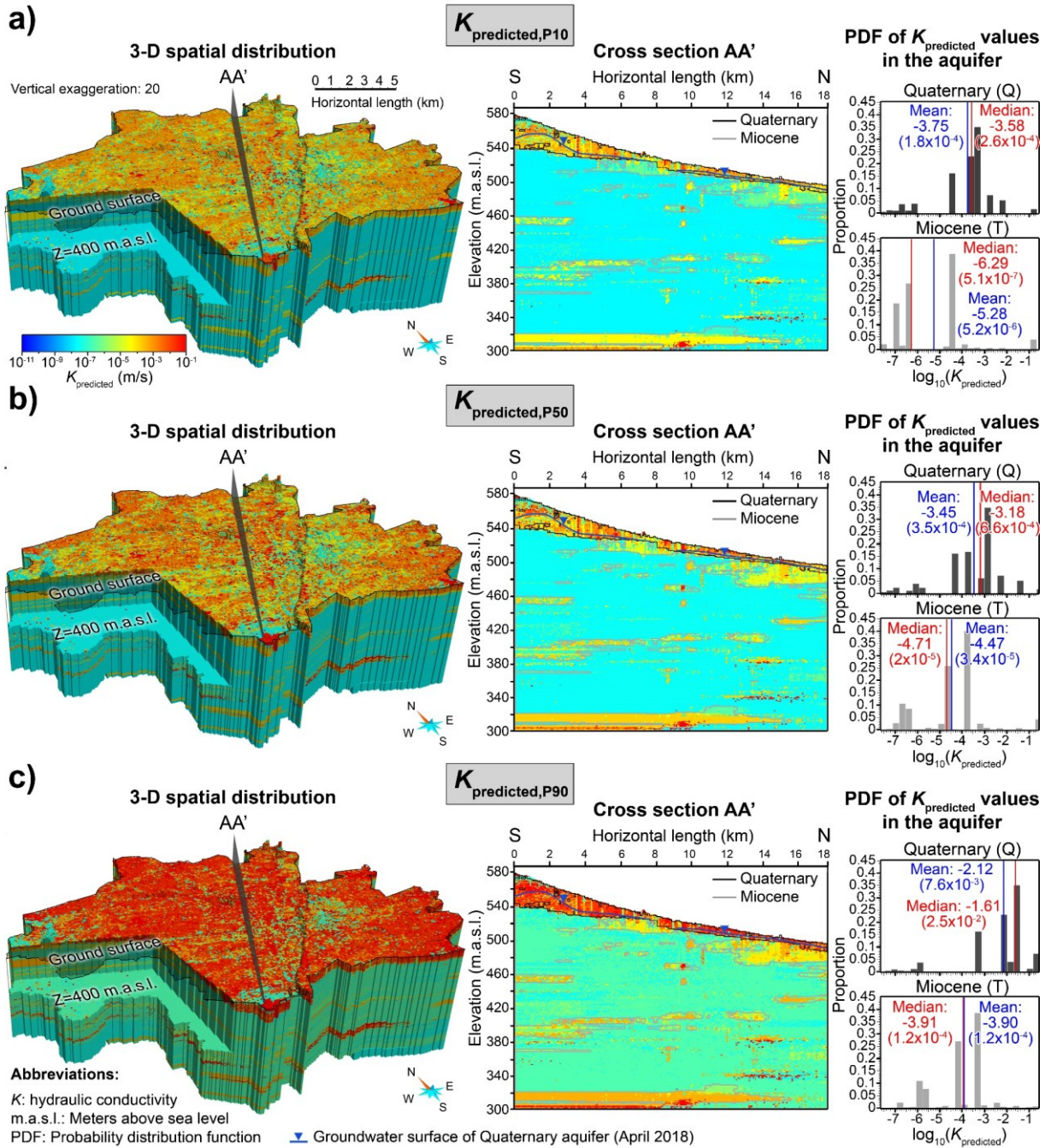


Fig. 41: Estimated 3-D hydraulic conductivity fields in the city of Munich represented by the 3-D spatial distribution (left panels, with partly transparent ground surface), an example south-north 2-D profile AA' (center panels), and the probability distribution functions (PDF) of the logarithmically (base 10) transformed hydraulic conductivities (right panels). **a)** Conservative (P10, 10th percentile); **b)** Average (P50, 50th percentile); **c)** Optimistic (P90, 90th percentile). Applying empirical methods leads to obtaining P10, P50, and P90 K -values at each voxel. The PDF represents the distribution of the K -values in the entire aquifer system

Since the distribution of K -values in aquifers is generally log-normal (Domenico and Schwartz, 1997; Prudic, 1991), the hydraulic conductivities were log-transformed (base 10) and checked for Gaussian normality (see right panels of Fig. 41). Whereas K estimates in Q follow an almost Gaussian but slightly left-skewed distribution for P10 and P50 (see Fig. 41a-b, right panels), we

observe a very marked positive tail in the distribution of P90 representing a significant proportion of very high values (see Fig. 41c, right panel). However, K estimates in T resulted in a multimodal distribution, with peaks at ~ -6.5 and ~ -4.5 (base = 10; values in m/s) for both P10 and P50 (see at the right of Fig. 41a-b), and ~ -6 and ~ -3.5 (base = 10; values in m/s) for P90 (see right panel, Fig. 41c). This hides the presence of aquifers with differentiated K distributions, which can be clearly seen, e.g., if we compare the P10-, P50- and P90-estimates in the Miocene aquifer systems in the central part of Fig. 41.

The Miocene deposits at depths of 300-320 m.a.s.l. show clearly an increase of K when compared to the overlying remaining T aquifers, thus leading to a bimodal behavior. This is not surprising due to the presence of various aquifer systems in the Miocene, as exposed in Section 6.2.1 and shown in Fig. 33b (right part) (Albarrán-Ordás and Zosseder, 2022; Kiecak et al., 2023; Zosseder et al., 2022b). Consequently, the mean of the log-transformed distributions, i.e., the geometric mean, may not actually represent the best measure of central tendency. Instead, the median was preferred for comparison, which is not strongly influenced by high or low-end outliers (Rossi and Deutsch, 2014). Furthermore, the lack of continuity in some ranges of values in the PDFs in the right part of Fig. 41 is attributed to the absence of some specific sediment mixtures in each aquifer system. For example, visible gaps for P10 between -5 and -6, for P50 ~ -5 , and P90 between -4 and -5 (base = 10; values in m/s) in the Quaternary aquifer may be justified by the absence of sandy to silty sandy deposits in this unit (see at the right of Fig. 41).

Considering Q, the right panels of Fig. 41 show that $K_{\text{predicted}}$ estimates range from 2.6×10^{-4} m/s (P10) to 2.5×10^{-2} m/s (P90), with an average of 6.6×10^{-4} m/s. In this sense, Zosseder et al. (2022b) reported expected K values from pumping wells in the entire MGP with values of P10 = 5.3×10^{-4} m/s, P50 = 5.6×10^{-3} m/s and P90 = 2.1×10^{-2} m/s. The same work also provided an average of 1.16×10^{-4} m/s specifically for the city of Munich. Regarding the hydrofacies types occurring, Theel et al. (2020) suggested an average of 3.7×10^{-3} m/s in the entire MGP.

Regarding the MGP, we may conclude that, although the results obtained in the present study for P50 are underestimated in one order of magnitude, the K variability, i.e., P10 and P90, is successfully preserved in the K estimation. In addition, the average value explicitly provided for the city of Munich (1.16×10^{-4} m/s) approximates the average obtained from estimation (6.6×10^{-4} m/s). Regarding the Miocene aquifers, the spread of $K_{\text{predicted}}$ estimates varies from 5.1×10^{-7} m/s (P10) to 1.2×10^{-4} m/s (P90), with an average of 2×10^{-5} m/s. Several studies have reported K values measured in these deposits as well. Zosseder et al. (2022b) provide an average value of 3.77×10^{-5} m/s in the Munich area obtained from pumping tests, which reasonably approximates the average from the 3-D model. Moreover, Egger (1978) analyzed 178 K values from pumping tests carried out in the Miocene aquifers in the area of Munich-Augsburg and proposed a range between 10^{-7} m/s and 10^{-3} m/s, with an average of 1 to 3×10^{-5} m/s. Gebhardt (1968) also proposed a similar average value, i.e., 2×10^{-5} m/s. The results provided by the geological 3-D model of the city of Munich suggest useful results, representing faithfully the existing trends

described in the literature. The findings outlined above reveal a satisfactory preservation of the K variability, i.e., P10 and P90, and central tendency, i.e., P50, in estimating K from the fictive GSD obtained from the D_i models method.

6.3.2 Prediction performance in the immediate vicinity of well screens

The local-dependent K estimates were further validated by comparing the equivalent horizontal hydraulic conductivity for the alternating beds along the screens, given by K_{xeq} , with the pumping-tests measurements (K_{pump}). For this purpose, only the immediate vicinity of the well screens, i.e., the voxels being intersected by the screened interval, were considered. This requires the calculation of K_{xeq} , as revealed in Section 6.2.5.1 and Fig. 39b2.

The relationship between measured K_{pump} and estimated K_{xeq} is given graphically in Fig. 42a. The position of any point in Fig. 42a indicates the deviation of the pumping-test measurement from the prediction range provided by P10-P90, as shown in Fig. 40. The straight line in the graph represents the line of perfect equality where the measurements fall in the predicted range, thus corresponding to the red rectangle in Fig. 40. This enables to determine the degree of deviation of the predictions, expressed as orders of magnitude (powers of ten). Deviations, i.e., from one to four orders of magnitude, are represented by different grey tones in Fig. 42a (left). In contrast, deviations of less than one order of magnitude are included in a white stripe between the dashed lines.

Following this, the cumulative distribution function (CDF) of the deviations was inferred (see Fig. 42a, right). Among the results obtained, 164 K values, i.e., 45% of the total number of K values, are within the line of equality (see Fig. 42a, right), and 31% showed deviations in the same order of magnitude. As seen in Fig. 42a, up to 24% of the cases showed deviations of at least one order of magnitude. These results are deemed satisfactory, compared with those obtained from soil samples with discrepancies of one or more orders of magnitude compared to K from pumping tests (Uma et al., 1989; Vuković and Soro, 1992). Moreover, deviations of four orders of magnitude occurred exclusively in wells where the screened interval was unknown and was assumed (see points marked by #2, Fig. 42a). Some deviations of two orders of magnitude are related to the same reason, i.e., an assumed position of the screen (see #1, Fig. 42a). Excluding the successful predictions, 124 K -values, i.e., 34% of the total number of K -values, lie below the equality line in Fig. 42a, thus denoting an underestimation. However, in 21% of the cases, amounting to 76 K -values, the point lies above the 1:1 line. This implies that underestimations (34%) are more common than overestimations (21%). This tendency to overestimate K when using empirical methods is in line with the suggestion that K derived from empirical methods is generally lower than K obtained from pumping tests reported in the literature (Chandel and Shankar, 2021; Cheng and Chen, 2007; Oh et al., 2013; Vuković and Soro, 1992). The work of Fuchs (2010) revealed a similar tendency to underestimate K using petrographical descriptions from drilled material.

However, the latter work compared K obtained from petrographical observations with a testing dataset of K derived from the GSD of soil samples.

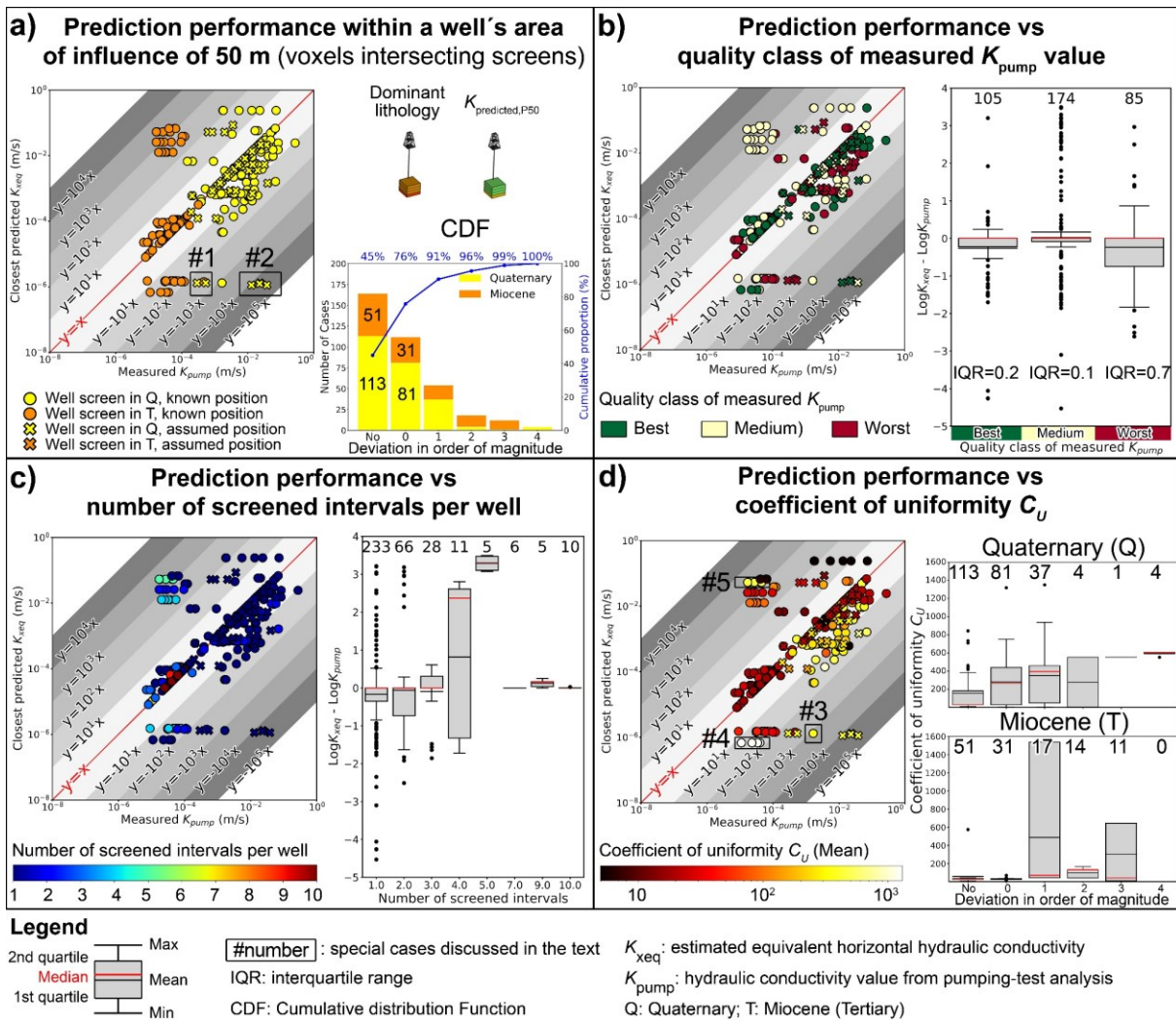


Fig. 42: Prediction performance in the immediate vicinity of the well screens in the city of Munich. **a)** (left) Cross-checking of model's predictions (K_{xeq}) with observed K values (K_{pump}) from various locations and depths; (right) CDF of the deviations; **b)** (left) Prediction performance versus the quality class of measured K_{pump} values; (right) Boxplot showing the distribution of the deviations for each quality class; **c)** (left) Prediction performance versus the number of screened intervals per well; (right) Boxplot showing the distribution of the deviations for each number of screened interval; **d)** (left) Prediction performance versus the estimated mean value of the coefficient of uniformity; (right) Boxplots showing the distribution of the coefficient of uniformity for each deviation degree

Additionally, the predictive ability was tested against three factors: (1) the quality of the pumping-test data (see Fig. 42b), (2) the number of screened intervals per well (see Fig. 42c), and (3) the mean coefficient of uniformity estimated in the voxels being intersected by the screened interval (see Fig. 42d) (see Section 6.2.5.1). Focusing on the first factor, the results show a higher spread in the deviations for the pumping-test data with the worst quality level, i.e., IQR=0.7, when compared to the rest of the data, i.e., IQR=0.2 and IQR=0.1 (see Fig. 42b at right). Not surprisingly, this leads to less accuracy in the prediction for the K_{pump} values having the lowest quality degree.

If we consider the number of screened intervals (see Fig. 42c), we observe that the lowest deviations, i.e., mean values close to 0, and the smallest spread, i.e., IQR < 1 order of magnitude, are obtained with a reduced number (up to 3 screens) and also unexpectedly with a very high number of screens (7 to 10 screens). However, Fig. 42c reveals very high deviations with mean values of two and three orders of magnitude for multiple well screens composed of 4 and 5 screens.

Regarding the coefficient of uniformity, as apparent in Fig. 42d (left), a higher deviation can be associated with the presence of a more graded soil in the Quaternary aquifer. The more graded soil in the Quaternary shown in Fig. 42d (left) is in line with the findings of Albarrán-Ordás and Zosseder (2022), who highlighted a higher degree of heterogeneity in the sediment mixture in the Quaternary sediments in the Munich area. The higher deviations with increasing coefficient uniformity are clearly seen in the Quaternary in the boxplot of Fig. 42d (right). Although this tendency cannot be appreciated in the Tertiary, some worst cases in the Miocene with deviations of one and three orders of magnitude are associated with very high coefficients of uniformity, i.e., values of 400 and higher than 1000, respectively (see points marked by #3, #4 and #5, Fig. 42d). Further, the investigation of the proportions of each grain size class within the screened aquifer portions revealed that these cases are due to the stronger presence of fine-grained sediments, i.e., 20-40% of silt and clay in average. Appendix D-4 shows the results obtained from comparing the deviations in the prediction against the lithological composition. The tendency inferred in Q and the worst cases in T are consistent with the reduced applicability of the empirical methods and the lower accuracy in K estimation with decreasing grain size of the sediments highlighted by Uma et al. (1989), Entenmann (1992) and Cornelis et al. (2001). In this sense, the accuracy of the individual empirical methods was not considered in the present approach. Given the accuracy of each method, a weighting scheme may be integrated to refine the estimate.

6.3.3 Prediction performance by varying the area of influence of the wells

The possible effects of the lateral changes in the hydraulic conductivity of the aquifer on the comparison between K -values from pumping tests and the model prediction were evaluated. Fig. 43 shows the comparison of the K values from pumping-test analysis (K_{pump}) and the representative hydraulic conductivities (K_{xeq}) computed for the five setups (see Section 6.2.5.2, 150 m, 250 m, 350 m, 450 m, 550 m radius), thus enabling a joint analysis. Each subplot illustrates the relationship between K_{xeq} and K_{pump} (left parts, Fig. 43) and the CDF of the deviations expressed in orders of magnitude (right parts, Fig. 43).

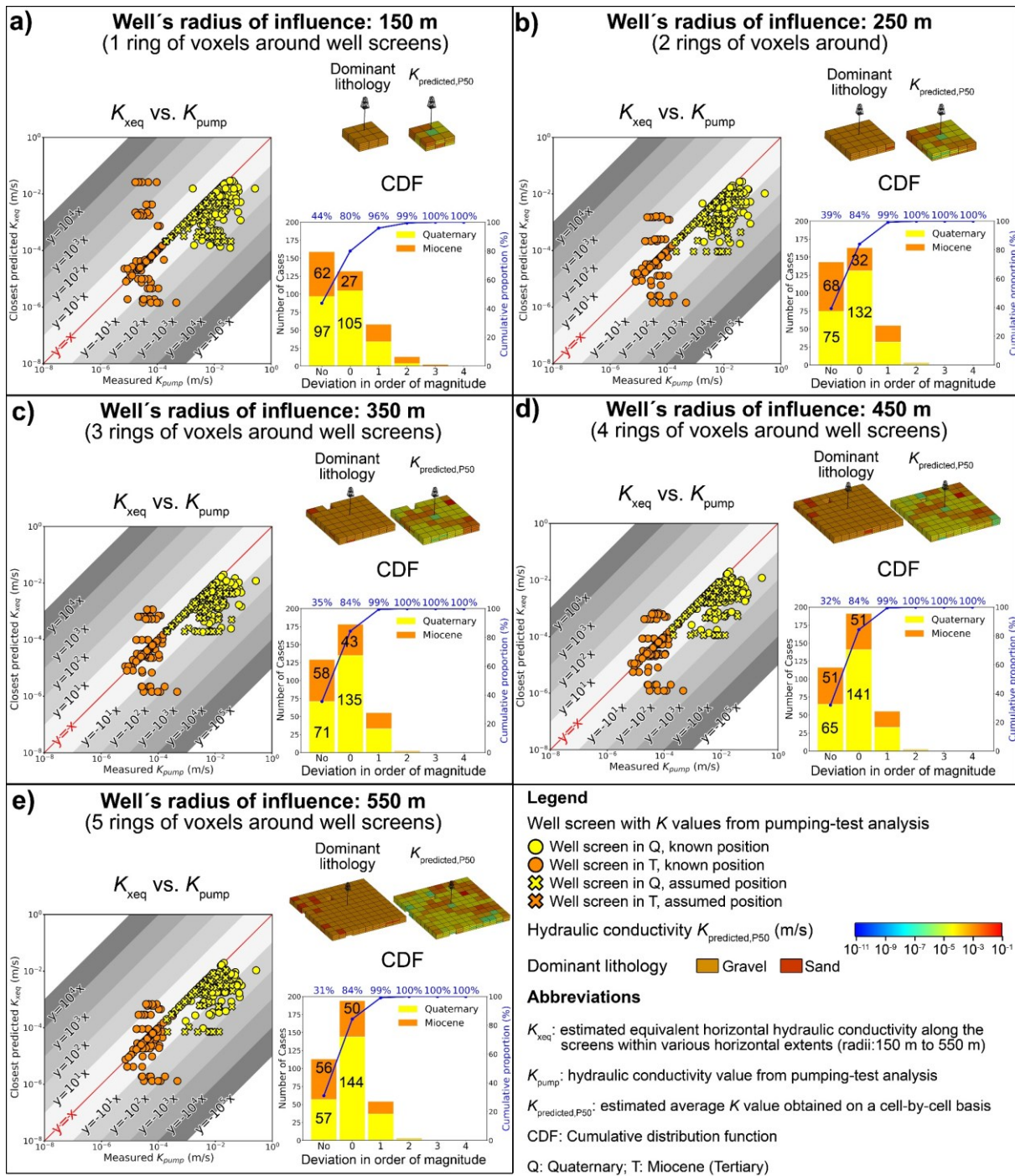


Fig. 43: Prediction performance by varying the well's radius of influence in the city of Munich. **a)** (left) Cross-checking of model's predictions (K_{xeq}) reaching extents up to 150 m with observed K values (K_{pump}); (right) CDF of the deviations with 150 m; **b)** (left) Cross-checking of model's predictions (K_{xeq}) reaching extents up to 250 m with observed K values (K_{pump}); (right) CDF of the deviations with 250 m; **c)** (left) Cross-checking of model's predictions (K_{xeq}) reaching extents up to 350 m with observed K values (K_{pump}); (right) CDF of the deviations with 350 m; **d)** (left) Cross-checking of model's predictions (K_{xeq}) reaching extents up to 450 m with observed K values (K_{pump}); (right) CDF of the deviations with 450 m; **e)** (left) Cross-checking of model's predictions (K_{xeq}) reaching extents up to 550 m with observed K values (K_{pump}); (right) CDF of the deviations with 550 m

Compared to the results obtained near the wells (see Fig. 42a), the results are closer to the equality line as the radius of influence was increased (see Fig. 43, at left). In contrast, the data in Fig. 42a were more scattered. However, the differences in the predictive ability in Q and T were addressed. This is further analyzed with the help of the CDF (see at the right of each subplot in Fig. 43) and the performance assessment, as exposed in Section 6.2.5.2. Whereas Tab. 3 provides the numerical quantification of the performance rates (see most favorable values indicated in bold), Fig. 44 graphically shows the performance variations with increasing cones of depression.

Tab. 3: Performance assessment after varying the radius of influence of the wells (R^2 =Coefficient of determination, MAE =Mean average error, PRS=Prediction rate of success, RD1= Rate of deviations with at least one order of magnitude, Q=Quaternary, T=Tertiary, Miocene. The most favorable values are indicated in bold)

Performance parameter	Setups with different well's area of influence											
	50 m		150 m		250 m		350 m		450 m		550 m	
	Q	T	Q	T	Q	T	Q	T	Q	T	Q	T
R^2	0.46	0.11	0.31	0.06	0.32	0.21	0.27	0.25	0.25	0.24	0.22	0.28
PRS	0.47	0.41	0.44	0.50	0.31	0.55	0.30	0.47	0.27	0.41	0.24	0.45
MAE	0.47	0.87	0.44	0.62	0.46	0.40	0.46	0.38	0.49	0.39	0.52	0.38
RD1	0.19	0.34	0.16	0.28	0.14	0.19	0.14	0.19	0.14	0.18	0.16	0.15

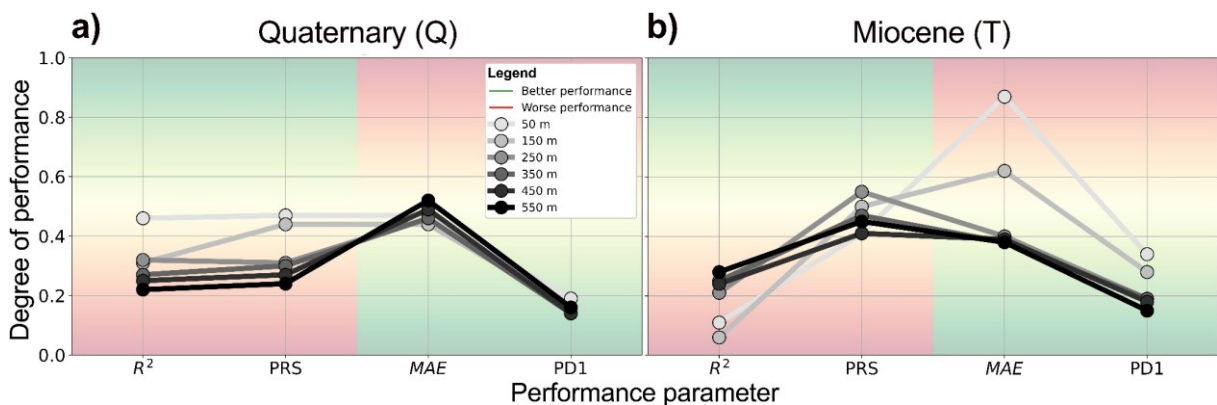


Fig. 44: Graph representing the performance variation with increasing radius of influence, separately in Q and T. **a)** Quaternary (Q); **b)** Miocene (T) (R^2 =Coefficient of determination, PRS=Prediction rate of success, MAE =Mean average error, RD1=Rate of deviations with at least one order of magnitude). Higher values of R^2 and RPS and smaller values of MAE and RD1 signify a better agreement and are associated with green tones

The results suggest that the setups with 50 m (see Fig. 42a) and 150 m (see Fig. 43a) are the most accurate to estimate K in the unconfined, shallow aquifer (Q) in the study area. A radius of 50 m provided the highest success rate, with 47% of successful predictions (see Tab. 3, PRS=0.47) and the highest coefficient of determination (R^2 =0.46). In contrast, this configuration shows an intermediate MAE value (MAE =0.47) and the highest rate of deviations of at least one order of magnitude with 19% (see RD1=0.19, Tab. 3). The more accurate prediction using a radius of 150 m relies upon a high success rate with 44%, which is very close to the highest value of 47% mentioned above, a very low percentage of worst cases, i.e., 16% with deviations of at least one order of magnitude, the lowest MAE value (MAE =0.44) and the second highest coefficient of determination (R^2 =0.32). Regarding the confined Miocene aquifers (T), the setup with 550 m shows the best performance in three of the four parameters considered. Herein, Tab 1. shows the

highest coefficient of determination ($R^2=0.28$), the lowest mean average error ($MAE=0.38$), and the lowest rate of deviations of at least one order of magnitude (0.15) for this setup. However, the success rate of predictions does not reach its greatest value ($PRS=0.45$). Given the above, the consideration of the most accurate setups for both the Quaternary, i.e., 150 m, and the Tertiary, i.e., 550 m, lead to worst cases with deviations of at least one order of magnitude limited to 16% and 15% of the estimated K values, respectively. These results are in line with Fuchs (2010), who reported a similar value of 16% when estimating K from petrographical observations but comparing them to K from soil samples, not from pumping-test analysis. Even though estimated K_{pump} values are considered the most reliable estimation of K , they are subject to inaccuracies of at least one order of magnitude in 10% of the pumping wells in the Munich area (see Section 6.2.2.3). Compared to the pumping-test analysis, the results of the current approach with differentiated radius of influence in Q and T show similar deviations in between 15% and 19% of the cases, respectively. The results are considered to reasonably approximate those obtained directly from the field. The presence of discrepancies in the prediction of K , and particularly, the presence of significant outliers, such as the 19% of predictions corresponding to 37 K values deviating by at least one order of magnitude in Q (see Tab. 3), suggests that the prediction performance of K is compromised in some cases. In this sense, 67% of the outliers are related to very high values of the coefficient of uniformity (>250) and the unknown position of the well screens. Besides these reasons, which were already discussed in Chapter 6.3.2, discrepancies can also be attributed to several factors. Firstly, they may stem from uncertainties detected in the input data used in the D_i models method, particularly in the semi-quantitative and qualitative descriptions of soil observations from drilled materials (Albarrán-Ordás and Zosseder, 2023). Secondly, as mentioned in Section 6.2.2.1, the geological 3-D model of Munich considers three grain fractions (clay/silt, sand, and gravel) with a fixed step in the GSD of 10%. In this sense, improving the prediction accuracy of the lithological composition and K could be achieved by considering more grain fractions and a finer fixed step below 10%. However, increasing the number of grain fractions and reducing the fixed step in the GSD may make the modeling process overly arduous, as highlighted by Albarrán-Ordás and Zosseder (2023, 2022). Lastly, the interpolation of the fictive GSD across a range of possible grain sizes may introduce uncertainties into the model outputs, as shown in Fig. 34.

The possible reasons for the results obtained with differentiated radius of influence are discussed hereunder. The extent of the cone of depression depends mainly on the pumping rate and the nature of the geologic materials (Kruseman and de Ridder, 2000; Weight, 2001). Herein, no comprehensive information on the pumping rates concerning the testing data used was available (see Section 6.2.2.3). Regarding the physical properties, the size of the cone of depression is affected by the storage coefficient. In this sense, the significance of the smaller storage value is that the cone of depression in a confined aquifer will generally extend farther than in an unconfined aquifer (Weight, 2001). However, in unconfined aquifers, the drawdown will normally only be measurable fairly close to the well, say not much more than about 100 m (Kruseman and

de Ridder, 2000). This is clearly in line with the results of this study. Consequently, the higher radius influence inferred in Miocene aquifers might be explained by the confining conditions with smaller storage coefficients.

The obtained results imply that considering the lateral changes in the hydraulic conductivity of the aquifer improves the prediction performance of the measured K from pumping-test analysis, thus leading to a more precise representation of the field scale. As stated by Uma et al. (1989) and Devlin (2015), estimating K based on empirical relationships of the GSD, either from soil samples or from petrographical descriptions, suffers from the lack of precise knowledge of the spatial variations of the aquifer geometry, leading to a lower representativeness of the aquifer, when compared to K from pumping tests (D'Andrea, 2001; Schultz and Ruppel, 2002).

The current approach addresses this issue from a twofold perspective. Firstly, the availability of a fictive interpolated grain-size range at each location provided by the D_i models method enables the estimation of location-dependent K based on empirical methods. Secondly, the averaging process of K within cones of depressions contributes to integrating lateral changes in the hydraulic conductivity of the aquifer. By doing so, the spatial connectivity of aquifer heterogeneity is considered, as indicated by Zheng et al. (2011). It is indeed interesting to link the results obtained with the scaling behavior of K measurements (De Bartolo et al., 2013; Fallico et al., 2012, 2010). In the present study, there was no information available regarding the pumping rates in the field data, so no information about the aquifer volume involved in the K measurements can be inferred, and these links should be considered prudently. However, K obtained from pumping tests generally involves large volumes of porous media, which is even more pronounced due to the confining conditions in the confined Miocene aquifers. The scaling effect of K measurements involves an increase in K with the scale of measurement, attributed to the heterogeneities of the aquifer, as more preferred pathways and transmissive portions are encountered (Fallico et al., 2012; Sánchez-Vila et al., 1996). In this sense, the results of the present study show that an increase in the radius of influence in the Miocene improves the prediction performance of the field data involving large aquifer volumes. These results can be attributed to a better capture of the aquifer's heterogeneity with larger aquifer volumes, aligning with the scaling effect of K measurements.

6.4 Conclusions

Based on the simulated particle-size fractions provided by applying the D_i models method in the geological 3-D model in Munich, the multiple PCHIP method was used to interpolate the fictive GSD range at each location. Subsequently, grain size characteristics were inferred, enabling the use of 15 empirical relationships for estimating K . The multiple estimation of K provides a better indication of its range and central tendency at each voxel. The obtained 3-D K field in Munich preserves the variability and average of K values from pumping-test analysis in the Quaternary and Miocene aquifer systems. Such estimations are very useful for planning groundwater

utilization and as initial calibration data for numerical groundwater models. Further, since K estimates consider the sediment texture and geological processes captured by the fictive GSD, they can be used as a secondary variable to perform collocated cokriging in geostatistical approaches, such as groundwater level interpolations. A dataset comprising 364 K values obtained from pumping tests is used to validate the 3-D K field. Herein, an averaging of K in the screened aquifer is performed. The results obtained in the near vicinity of the well screens show a satisfactory prediction with a success rate of 45%, discrepancies in the same order of magnitude in 31% of the cases, and discrepancies of at least one order of magnitude in 24% of the values. The largest discrepancies could be attributed to the missing information on the well screen position, the increasing uniformity coefficient, and the reduced applicability and accuracy of the empirical methods with a stronger presence of fine-grained sediments. The effects of the lateral changes in K in the aquifer on the prediction were evaluated by considering various cones of depressions. Herein, aquifer heterogeneity is accounted for by providing a fictive interpolated GSD at each location and averaging K within the individual beds of the lateral extents of the aquifer. The Quaternary aquifer shows a most satisfactory prediction when considering smaller radii of influence, i.e., 50 m and 150 m. Herein, success rates of 44-47% and deviations in the same order of magnitude in 31-36% of the cases were observed. However, the integration of the spatial heterogeneity of K with increasing aquifer extents up to 550 m has been proven to be more suitable in the confined Miocene aquifers, leading to a success rate of 45% and deviations of less than one order of magnitude in 40% of the cases. This demonstrates the current approach's ability to capture aquifer heterogeneity and spatial geometries at the field scale, a limitation of K estimates based on GSD analysis from soil samples or petrographical descriptions. The results show deviation rates of at least one order of magnitude between 15% and 19% of the cases. This reveals an apparently satisfactory prediction since the testing data used in the Munich area, i.e., K from pumping-test analysis, are still subject to inaccuracies of at least one order of magnitude in 10% of the wells. Furthermore, a tendency to underestimate K , similar to GSD-based estimates, is noted when compared to pumping-test analysis. The stronger presence of fine-grained sediments and high uniformity coefficients complicate the applicability and accuracy of existing empirical methods. This issue can be further investigated with multiple linear regression between measured K and sediment properties. However, K values from pumping tests relate to aquifer volumes, not individual voxels, thus limiting cell-by-cell fitting. This may necessitate excluding certain sediments, reducing high-resolution definition of K . Alternatively, stochastic modeling or weighting schemes according to the accuracy of the method can be used. Although the present approach cannot and is not intended to replace pumping tests, it provides reliable K ranges and spatial distribution, as well as estimates at every location, providing a vertically differentiated K -values field. This, together with the expected spatial aquifer geometry provided by the geological 3-D model, aids well planning. It also offers great possibilities for a better spatial prediction of K in heterogeneous aquifers, which is useful for estimating the aquifer yields or the geothermal potential for GWHP. The present approach also opens opportunities to combine and compare the K estimates with the inverse numerical modeling of K . In addition, adapting the averaging in the

vertical direction to the stratification might also be very useful in estimating the protective function of the groundwater covering. The aspects above ultimately improve groundwater resource management in clastic sedimentary systems.

6.5 Acknowledgments

We gratefully acknowledge the Bavarian Environment Agency (LfU) for the access to the borehole database of the Soil Information System of Bavaria, as well as to the pumping-test data collected and evaluated within the framework of the GEPO and GeoPOT research projects in the Munich area. We thank Valerie Ernst for her support in analyzing the deviation trends in the interpolated fictive GSD range when applying the log-linear method. The authors also thank Grundbaulabor München GmbH for providing us with data. Lastly, Emerson E&P is kindly acknowledged for providing licenses for the Software product SKUA™ Engineering Modeling in the scope of the Emerson Academic Program, which supported the results of this publication.

CHAPTER 7

Interpretation of hydrogeochemistry of the Upper Freshwater Molasse (*Obere Süßwassermolasse*) in the Munich area (Bavaria, Germany) using multivariate analysis and three-dimensional geological modelling

Aleksandra Kiecak ^a, Jan Huch ^{a,b}, [Alberto Albarrán-Ordás](#) ^a, Lilian Chavez-Kus ^a, Kai Zosseder ^a

^a Technical University of Munich, Arcisstraße 21, 80333 Munich, Germany

^b GAF AG, Arnulfstraße 199, 80634 80333 Munich, Germany

(Please refer to Notes 3 and 4 in List of Abbreviations, Acronyms, and Symbols)

Abstract

Intense use of groundwater in urban areas requires appropriate monitoring, which in turn necessitates proper data management with employment of increasingly sophisticated statistical methods and mapping tools. An example of such an urban area with intensive use of groundwater is the study area of GeoPot Project, namely Munich (Germany) and its surroundings. The aim of the presented study was to provide a description of the hydrogeochemical characteristics of the aquifers occurring in the Quaternary and Upper Freshwater Molasse (German: Obere Süßwassermolasse – OSM) sediments and to further improve the understanding of interactions between the aquifers. The focus was put on the identification of hydrochemical facies, the chemical signatures of different water types, an understanding of occurring processes, and spatial relationships between the aquifers. In order to deal with hydrogeochemical data generated for this study, as well as with data coming from existing external databanks (e.g. BIS-BY), a methodology of quality assurance was developed. The analytical methods focused on multivariate statistics. To enhance the interpretation of the obtained clusters, a recently developed three-dimensional geological model was used for better understanding and presentation. It was found that in the study area, deeper aquifer systems represent the most distinct hydrogeochemical signature of the Na – HCO₃ water type. In the remaining clusters, a transition from deeper (alkaline) to shallow (alkaline-earth) groundwater can be observed. The results of the study can be utilized for improved, sustainable groundwater management.

Keywords

Urban groundwater, hydrochemistry, groundwater statistics, sedimentary rocks, Germany.

7.1 Introduction

Urbanization is taking place all over the world and it is an emerging issue with consequences for the economy, environment and society (Kirabo Kacyira, 2012; Schirmer et al., 2013). The trend of population shifting from rural to urban areas will increase in the future and, accordingly, there is a severe need for responsible urban management that considers the availability of resources and sustainable handling of environmental impacts.

In recent years the subsurface has increasingly been recognised as a multifunctional resource providing a wide range of services (Volchko et al., 2020), which are also referred to as (geo) potentials (Bayer et al., 2019; Böttcher et al., 2019; Team GM, 2003). Intensive use of urban underground space is seen as a prerequisite for sustainable development of cities, contributing to the achievement of the 17 UN Sustainable Development Goals (Admiraal and Cornaro, 2016; Volchko et al., 2020).

One natural resource prone to susceptibility, and a significant factor in urban management, is groundwater (Vázquez-Suñé et al., 2010). Protection of this resource, including a strategy of groundwater monitoring within a dense network and intensive programme, is becoming progressively more critical. Consequently, the number of monitored sample points and data collection exercises will increase, which will lead to the need (and the opportunity) for comprehensive data management and more sophisticated data analyses, and form the basis of sustainable groundwater management.

While, most commonly, hydrogeologists must still struggle with the lack of data and an insufficient number of monitoring wells (e.g. Lo Russo and Taddia, 2009; Wakode et al., 2018), in urban areas - as in this research case - the biggest challenge is to handle very large quantities of data, which, in turn, requires meticulous descriptions as well as great efforts on quality control. Modern hydrogeological studies of regional scale are becoming more and more a link between geosciences and data science. Such comprehensive regional studies are crucial for integrated sustainable groundwater management (Raiber et al., 2012), whereas data management and data analysis, two main concepts of data science, involve knowledge of statistics, computer science, etc. (Ma, 2018).

Large data records require the application of statistical methods and tools to draw conclusions. An appropriate methodology must be developed in order to filter, process and analyse the datasets (Curtis et al., 2018). Multivariate statistical methods can provide powerful and valuable support in the investigation of hydrogeochemical patterns and processes (Menció and Mas-Pla, 2008). However, the outcomes of multivariate statistical analyses cannot be assessed without placing them in a hydrogeological three-dimensional (3D) spatial context (Raiber et al., 2012).

Therefore, developments in geological 3D modelling as well as in hydrogeochemical studies (Raiber et al., 2012), enable a new perspective of looking at geological data. An integrated approach combining multiple lines of evidence (3D geological modelling, multivariate statistics, field observations, etc.) benefitted this study in particular, but also more generally benefits the growing understanding of hydrogeochemical processes (Martinez et al., 2017). Such multidimensional approaches are particularly valuable in resource (respectively groundwater) management, where optimal and efficient use of geopotentials has to be guaranteed, assuring the best possible preservation of resources and sustainable spatial planning.

In this context, the Quaternary glaciofluvial gravel plain and the Miocene fluvio-lacustrine sediments of the Molasse Basin in Germany were the subjects of research studies (Böttcher et al., 2019; Böttcher and Zosseder, 2022; Epting et al., 2020; Zosseder et al., 2022b, 2019). Groundwater in this area is an important and intensively exploited source for drinking water, service water and for geothermal purposes (e.g. heat pumps; Kerl et al., 2012). Moreover, especially in the urban area of Munich, the Quaternary aquifer has become increasingly polluted, where, e.g. considerable quantities of chlorinated hydrocarbons were detected in the 1980s (Rauert et al., 1993). Besides the use of groundwater, the subsurface is exploited in many other ways - for subways, tunnels, infrastructure, stormwater management, etc. The increasing use of the subsurface carries the necessity for sustainable management of the subsurface (Griffioen et al., 2014), whereas extensive investigation of geological settings, resulting in their representation in 3D models, is a precondition.

The research projects and in particular the geo-modelling approach by Albarrán-Ordás and Zosseder (2022) led to the development of a geological 3D model for the municipal area of the city of Munich (Albarrán-Ordás and Zosseder, 2022, 2020, 2019; Zosseder et al., 2022b, 2019). The resulting model predicts the lithological composition in detrital systems consisting of sediment mixtures of different grain sizes. This led to the architectural model representing the interconnectedness of geological bodies with identical lithology in the Quaternary and Molasse deposits (in much greater geological and spatial complexity than previously expected), which is key to identifying and separating geopotentials and optimizing their usage. In particular, it allows an in-depth understanding of the spatial extension of aquifers and their interconnectivity, as well as their lithological configuration, and was a fundamental reference for this study. Hydrogeochemical analysis of the waters within the involved aquifers can be used to validate identified separations or connections of aquifers, which the 3D model is hinting at from a purely spatial side.

The overall aim of this study was to provide a hydrogeochemical characterization of the shallow aquifers in the greater area of Munich with an emphasis on the actual and future utilization of groundwater as a vulnerable resource. In particular, the work involved identification of the hydrochemical facies and the chemical signatures of the different water types, and an understanding of the aquifer processes and spatial relationships between the aquifers. The hydrogeochemical analyses were further used to check the plausibility of the aquifer separation derived from the

geological 3D model. The study was performed using different lines of evidence: (1) by applying multivariate statistical methods and (2) relating the outcomes to the geological 3D model by Albarrán-Ordás and Zosseder (2020, 2019) and Zosseder et al. (2022b).

7.2 Study area

7.2.1 Location, geology and hydrogeology

The study area is located in Bavaria (Germany) in the greater area of Munich and covers an area of ~550 km² (Fig. 45). The central part of the study area is the Munich Gravel Plain of fluvio-glacial origin, which consists of sandy terraces from Pleistocene glacial periods and modern alluvial and fluvial deposits (Bauer et al., 2005). Coarse-grained carbonate gravels have attained a maximal thickness of 30 m in the city of Munich and up to 60 m in the entire project area, and constitute a very productive porous aquifer (Albarrán-Ordás and Zosseder, 2020). The thickness depends on the presence of paleochannel structures carved in the underlying Neogene deposits. Depending on the local geology and the local water table, this aquifer occurs under either confined or (mostly) unconfined conditions. The average hydraulic conductivity is 5×10^{-3} m/s (Böttcher et al., 2019); however, a wide variability in hydraulic conductivity values has been reported (Theel et al., 2020).

In the south, the landscape and geology are dominated by Pleistocene sediments, including pre-Alpine moraines of four glaciations - Würm, Riß, Mindel, and Günz (from young to old) - and corresponding terraces of gravel accumulations (Doppler et al., 2011). The thicknesses vary a lot and reach mostly from a few meters up to 20 or 30 m, reaching in the south even up to 80 m (Zosseder et al., 2022b). The sediments are inhomogeneous and comprise boulders, gravels, and sands, as well as clay and silt. Local, mostly isolated and confined porous aquifers are related to lenses or layers of coarse material (Zosseder et al., 2022b).

The Upper Freshwater Molasse (German: Obere Süßwassermolasse – OSM) is the upper part of the North Alpine Foreland Basin, also termed the Molasse Basin. The sedimentary rocks range from the middle to the upper Miocene, ca. 17–11 Ma (Kuhlemann and Kempf, 2002). The OSM presents tabular geometry and contains sediments of channel deposits (sands, local gravels) and fine-grained material of the alluvial plain (clays, marls; Maurer and Buchner, 2007). The mineral composition is comprised of quartz, mica, clay minerals and minor quantities of calcite and dolomite (Rauert et al., 1993). The thickness of the OSM deposits can reach up to 700 m in the project area (southern part of Isar-valley-paleochannel) and generally increases from north to south (Zosseder et al., 2022b). The thicknesses of particular groundwater bodies may reach 200 m (Wagner et al., 2003). The OSM sediments are mostly covered by Quaternary deposits. The outcrops of the OSM are generally in the northern part of the study area, which also constitutes the northern margin of the Molasse Basin. Groundwater occurs in sand and gravel layers. Aquifers can be distinguished between “shallow” and “deeper”. This distinction, however, is of practical meaning and not linked to any specific definition of deep groundwater (e.g. as presented by Frape

et al., 2003). Shallow aquifers show evidence of anthropogenic impacts and contain relatively young, meteoric water, whereas deeper aquifers are isolated, containing older groundwater. The deeper OSM aquifers are separated and therefore protected from shallow aquifers by silty and clayey sediments, acting as an aquitard (Rauert et al., 1993). The OSM aquifer conditions are mostly confined and the hydraulic conductivity of the OSM layers is two to five orders of magnitude lower than the overlying Quaternary sediment (Böttcher and Zosseder, 2022; Jerz, 1993).

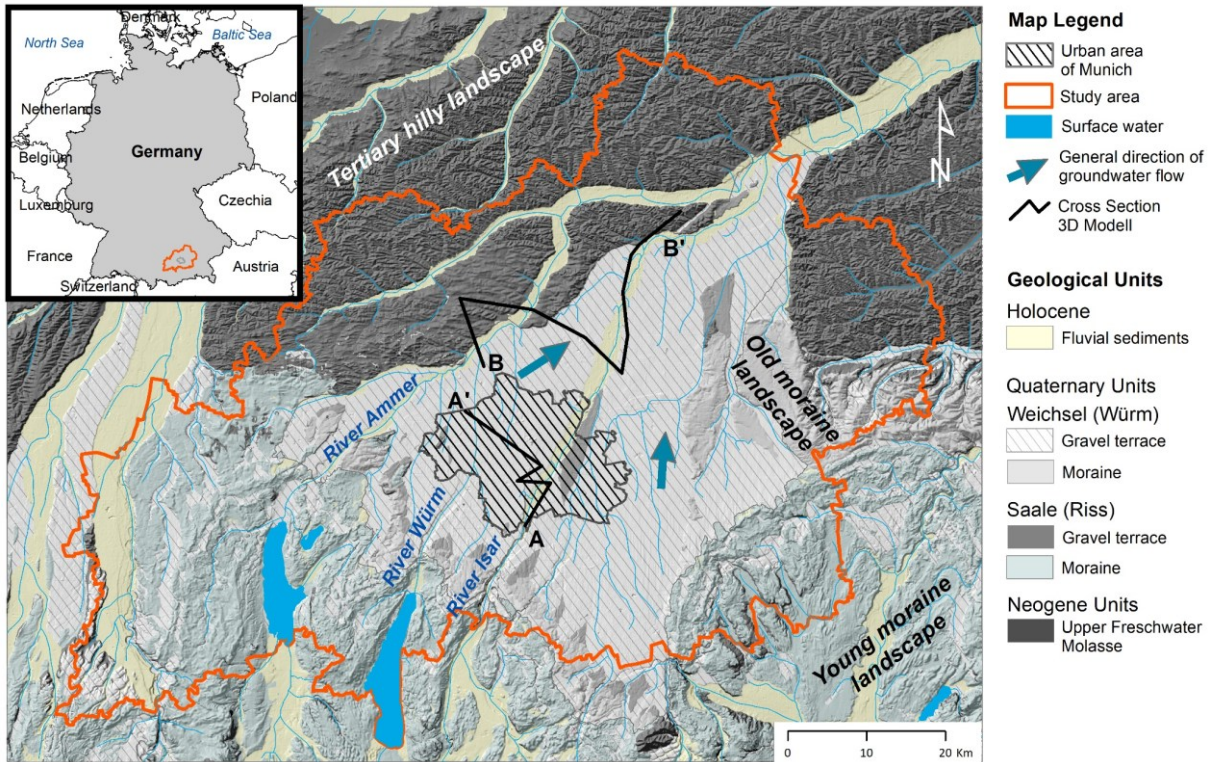


Fig. 45: Location of the study area in the context of geology of southern Bavaria (cross sections A-A' and B-B' are presented in Fig. 56 and Fig. 57, respectively)

7.2.2 Geological 3D models in the greater area of Munich

With the aim of characterizing the existing and potential uses of the subsurface space and the heterogeneity of deposits, the underground space of Munich has been the subject of geological 3D modelling in recent years (Fig. 45, the boundary of the model is almost the same as the urban area of Munich marked in grey). As a result of these works, the “ D_i models” method was conceived as a new methodology for predicting the 3D lithological variability in detrital systems and was proven in a case study in Munich. The details of the model, in particular the input data and sophisticated methodology, can be found in Albarrán-Ordás and Zosseder (2022). The same approach was also implemented in a second model in a broad area located north of Munich (Fig. 45, referred to as Model North; Zosseder et al., 2019). The models were constructed using SKUA-GOCAD™ software (Emerson E&P, St. Louis, USA). The aim of the 3D models was to identify clearly separated aquifers and detect interconnectivity between groundwater bodies.

The focus of the GeoPot project was set as the Munich area, where the need to manage the subsurface resources due to their extensive use is more accentuated, in contrast to its surroundings. Therefore, a detailed lithological and a 3D architectural model was produced for Munich, whereas in the case of the Model North, the priority was given to predicting the lithological composition and no architectural model was implemented.

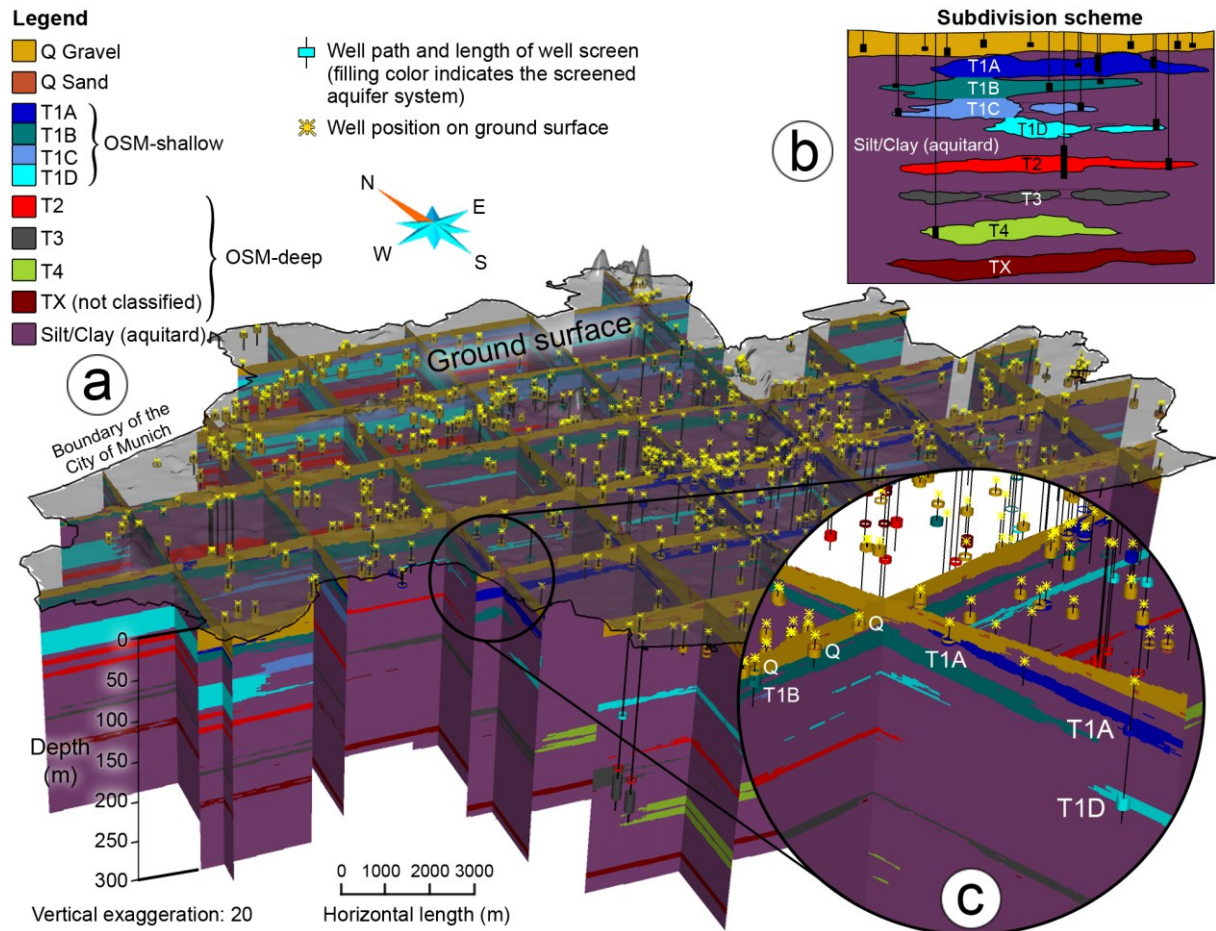


Fig. 46: Geological 3D model of the City of Munich with the subdivided aquifer systems Q and T1-T4. **a)** 3D fence diagram showing aquifer subdivision through the transparent ground surface; **b)** Subdivision scheme; **c)** Detailed view of the assignment of aquifer systems to screened wells. Modified from Albarrán-Ordás and Zosseder (2019); Zosseder et al. (2019)

The first of the models provided the prediction of the lithological composition on a cell-by-cell basis, covering a 310-km² area of Munich. This also revealed the complex reservoir configuration presented in the Quaternary and Upper Freshwater Molasse deposits by means of the 3D architectural model (Albarrán-Ordás and Zosseder, 2022). Focusing on the OSM sediments, the architectural model showed four extensive coarse-grained geological bodies in Munich that are separated by impermeable beds (Fig. 46). These four geo-bodies are termed T1–T4, from shallower to greater depths, and they host the aquifer systems with the same notation. The aquifer system T1 represents the first OSM groundwater system from the ground surface, having various aquifer tiers at different depths (referred to in a previous paper as T1A–T1D; Albarrán-Ordás and

Zosseder, 2022; Zosseder et al. 2019) and showing multiple hydraulic interaction areas with the Quaternary aquifer throughout the city. The architectural 3D model also indicated that the deeper aquifer systems T2–T4 are considered to be isolated from one another.

The second of the models, Model North, implemented using the D_i models method, focuses on the area of the Munich Gravel Plain situated immediately to the north of the city. The modelling area extends northwards to the uncovered molasse sediments in the Tertiary Hills region, covering a total surface area of 2,426 km² (Fig. 45).

7.3 Methodology

The methodology evolved in this study is presented schematically in a flowchart (Fig. 47) and described in detail in the following sections.

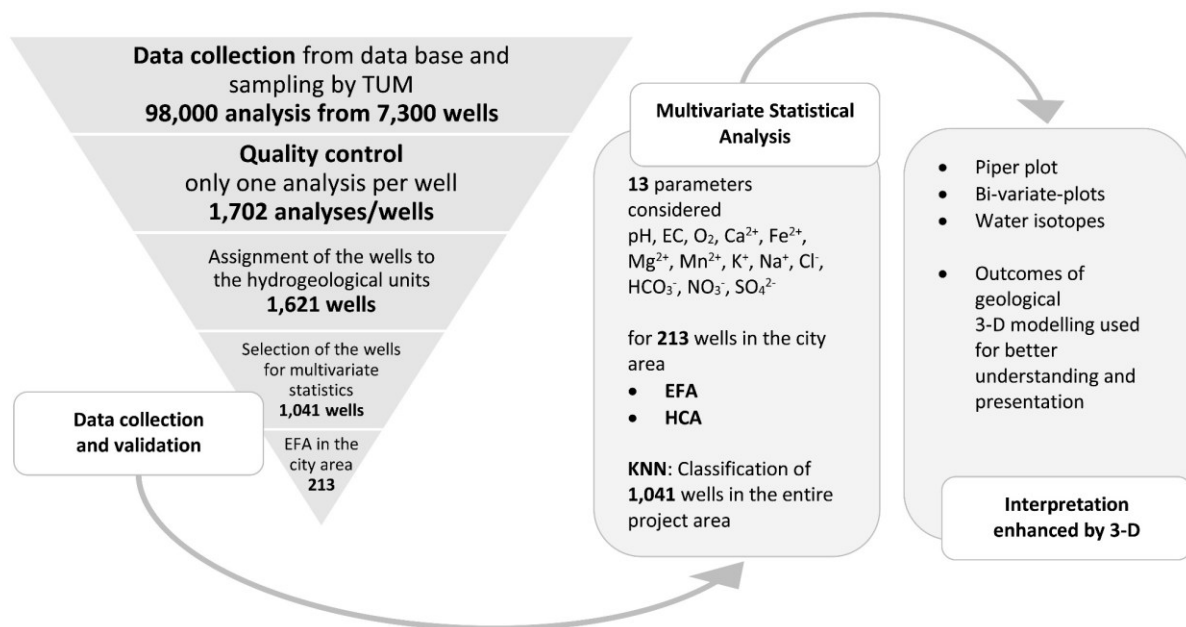


Fig. 47: Methodology flow chart

7.3.1 Data collection

A broad range of hydrogeochemical data derived from groundwater samples taken from boreholes at different depths was collected from the records of the Bavarian Environment Agency (Bayerisches Landesamt für Umwelt, LfU) and several water authorities (e.g. City of Munich). Samples revealing high anthropogenic pollution were excluded from further assessment. In particular, piezometers located by dump sites, gravel pits or polluted areas were manually selected based on their location and extreme results for certain chemical parameters (mineralisation, pH) compared to local hydrochemical conditions, and consequently expelled. However, diffuse, ubiquitous contamination from agriculture or in the urban areas were not considered as an exclusion criterion.

In total, ca. 98,000 groundwater analyses coming from 7,300 sampling locations were collected. It is important to note that each sampling location represents one well screen section in a borehole. For clarity, hereafter only the term “well” is used, despite the type of borehole (well, piezometer, etc.). Each level of the multilevel groundwater systems was also treated as a separate “well”.

7.3.2 Additional sampling by the Technical University of Munich (TUM)

In addition to the data collection from reviewed literature and external databases, groundwater sampling was carried out in three sampling campaigns during 2017–2019. Samples were collected at 108 sites, which covered private and municipal drilled wells (32), piezometers (21), and springs (55) of the OSM - Fig. 83 in Appendix E. Sampling locations were selected mostly outside the city area, in regions that had previously had a less dense programme of sampling, in order to complement the existing data. In-situ measurements were performed by multiparameter field meters (WTW Multi 3430, Xylem Analytics, Weilheim, Germany) for temperature, pH, electrical conductivity, and dissolved oxygen. Groundwater samples were analysed for 46 parameters, including major and minor ions and trace constituents at the Bavarian Environment Agency. The actual design of the applied analytic methods is described in Chavez-Kus et al. (2016). Additionally, water stable isotopes ($\delta^{18}\text{O}$ and $\delta^2\text{H}$) were measured at the TUM using a cavity ring-down spectrometer (IWA-45EP; ABB – Los Gatos Research, San Jose, USA).

7.3.3 Quality assurance and data selection scheme

The data set was extremely heterogeneous in many aspects, from the kind of raw data format to the range of analysed parameters. Additionally, the data quality, showing diverse limits of detection, varied considerably over time (data from several decades). Hence, intensive processing was essential prior to further analytical steps.

The analyses were checked for their actuality (more recent than 1978, as proposed in the study of the Bavarian Environment Agency (LfU) by Chavez-Kus et al. (2016), completeness (major ions measured) and quality (charge-balance error $\leq 10\%$). For some wells more than one analysis was available. To ensure the same weighting in spatial statistical assessment and to avoid unwanted clustering effects (e.g. Isaaks and Srivastava, 1989), only one analysis for each well was selected. The selection was performed by considering: (1) novelty (newer analyses were favoured), (2) number of analysed parameters and (3) giving priority to the analyses obtained during a sampling campaign conducted for this study case. The last criterion was introduced for the simple reason that full control over quality was possible for these samples. Finally, 1,702 analyses (coming from the same number of distinct wells) were selected. The data points were well distributed over the whole study area; however, with higher density in the city area of Munich (see Fig. 48).

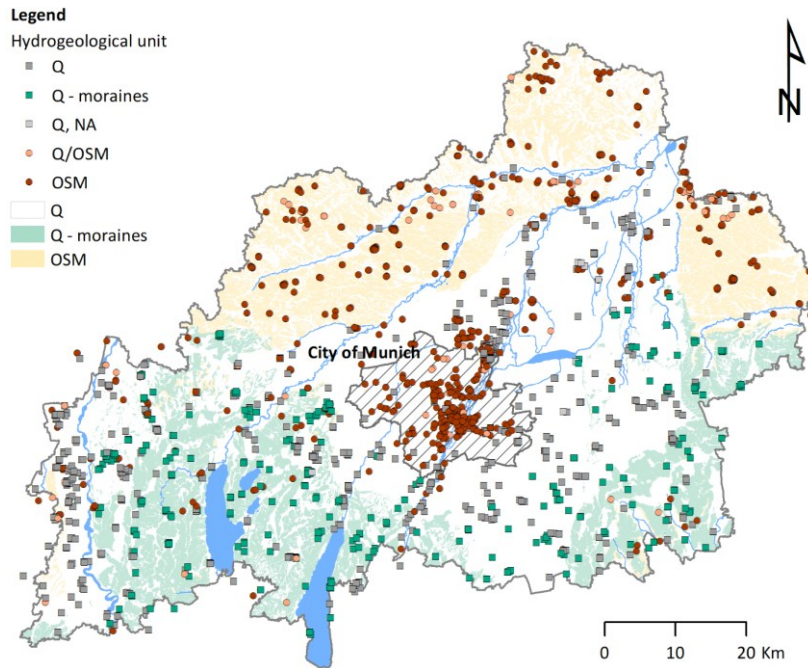


Fig. 48: Locations of the groundwater sampling points in the study area

After careful evaluation of each well (in particular: examination of available geological maps and bore logs, as well as analysing the screen lengths and depths in the geological 3D model), the wells were assigned to the hydrogeological units: (1) Quaternary (612 wells), (2) Quaternary – moraines (320), (3) OSM – shallow (581), and (4) OSM – deep (108). The locations of the wells selected for further assessment are presented in Fig. 48. Additionally, the locations of all available wells along with the number of analyses, as well as the position of sampled points in the aquifers, are shown in Fig. 82 in Appendix E. In this step, 81 wells were excluded from statistical analysis, namely the boreholes having more than one well screen section, each of them at different depth intervals, therefore, belonging to more than one hydrogeological unit. This facilitated the description of the characteristics of each hydrogeological unit (results presented in Appendix E-2). In the multivariate analysis, however, the wells capturing more than one hydrogeological unit (or geobody derived from 3D modelling) were saved in order to capture the mixing effects.

7.3.4 Multivariate statistics

Multivariate statistical methods were employed in order to capture the variability of the great amount of data for selected parameters derived from groundwater found in complex hydrogeological conditions. These multivariate statistical methods included exploratory factor analysis (EFA) and hierarchical cluster analysis (HCA), followed by the application of a machine learning algorithm. The calculations and diagram preparations were performed with the statistical program R (R Core Team, 2021) using the packages stats (integrated in R), class (Venables and Ripley, 2002), corrplot (Wei and Simko, 2021), psych (Revelle, 2020), and ggplot2 (Wickham, 2009). Besides, for the Piper diagram preparation, the package hydrogeo (English, 2017) was used.

EFA is a statistical method that aims to explore the correlation structure among measured variables and identify relationships between them (Goretzko et al., 2019). The dimensionality of variables is reduced by clustering (Hajji et al., 2021), so the data can be summarized in a smaller set of factors for prediction purposes. Because factor analysis uses a correlation matrix, underlying concerns affecting the correlation should be examined prior to the factor analysis: sample size, missing data, normality, linearity, and outliers (Schumacker, 2016). Firstly, because it has implications for the selection of the correlation method, the statistical normality of the data was analysed with the Shapiro-Wilk test. The data size was first validated with the Kaiser-Meyer-Olkin test (KMO should be > 0.5). Next, the Bartlett test of sphericity was performed to identify whether the correlations in the matrix were statistically significant (significance level > 0.05; Backhaus et al., 2016). Community is a measure of how well the variance of each variable is described by a specific set of factors. A measure of sampling adequacy (MSA) shows the proportion of variance in the variables caused by underlying factors (Goretzko et al., 2019). The optimal (lowest) number of factors was determined by generating a scree plot (eigenvalues versus eigenvectors; Conway and Huffcutt, 2003). To optimize, variance rotation is applied for better interpretation (e.g. by the oblimin oblique rotation method; Cloutier et al., 2008; Yong and Pearce, 2013). As a factor extraction method, maximal likelihood might be preferred (Goretzko et al., 2019).

HCA is a data classification technique, in which the relative positions of all objects in the multidimensional variable space are determined (Odziomek et al., 2017) and distance is used for identification of naturally-occurring groups (clusters). No a priori assumption about the data is made and the classification of the objects into clusters is based on their similarity. In HCA, the squared Euclidean distance metric and Ward's linkage method were implemented, similar to the methodology presented in Güler et al. (2002) and Cloutier et al. (2008). The Euclidean distance is a measure of similarity performed over all variables included in HCA and is used to identify outlier clusters. Ward's linkage rule creates separate clusters based on analysis of variance and was next applied to link all nonresiduals into distinct clusters (Raiber et al., 2012). The number of clusters was estimated via elbow-, silhouette-, and gap-statistic methods (Kassambara, 2017). The HCA results were then visualised in a dendrogram. Cluster analysis allowed grouping of samples in reference to similarities detected by the algorithm.

EFA and HCA were first conducted for the samples in the area Munich, as the most detailed data as well as a detailed 3D architectural model from the geological 3D modelling were available there (Albarrán-Ordás and Zosseder, 2022, 2020). A similar methodological approach to the ones presented by Cloutier et al. (2008), Gilabert-Alarcón et al. (2018) and Heine et al. (2021) was implemented. In this part of the study, 13 parameters were considered - pH, electrical conductivity (EC), dissolved oxygen (DO), calcium, iron, magnesium, manganese, potassium, sodium, chloride, hydrogen carbonate, nitrate, and sulphate - observed in 213 wells. The choice of the wells resulted from the prerequisites of the multivariate statistics; in particular, and also to avoid the concerns of missing data, only the wells for which all 13 parameters were available were selected (Cloutier

et al., 2008). Moreover, all wells were directly spatially linked to one of the geological bodies identified in the 3D architectural model of the Quaternary and OSM deposits by Albarrán-Ordás and Zosseder (2022, 2020, 2019). This shortened database comprised data from the time period 1992–2019, representing all the geological bodies and aquifer systems as presented in the preceding 3D model study. HCA procedures were applied using the *psych* package from the R library (Revelle, 2020). For the purpose of the multivariate statistical analysis, the parameters with concentrations lower than the detection limit were replaced with a proxy value '0'.

In order to evaluate the characteristics of each cluster more accurately, descriptive statistics were calculated as replenishment for cluster analysis (Ghesquière et al., 2015). The analysis was done on further constituents (e.g. trace elements and water isotopes) not included in the multivariate statistics.

7.3.5 Classification of data from the greater area of Munich using the *k*-nearest neighbourhood algorithm (KNN)

In order to check if the water types from outside of the city can be grouped in the same water type clusters detected for the city area, the records from Munich's surroundings were fitted to the clusters created for the city. For the classification of data from the entire project area, a *k*-nearest neighbourhood (KNN) algorithm was used. KNN is a supervised machine learning algorithm (Rebala et al., 2019). A total of 828 wells were considered in this step (together with wells from the city area – 1,041 wells, Fig. 47). It is assumed that similar items are closer to each other. The algorithm was first "trained" and tested on the data from the city area and then applied to the data from Munich's surroundings. The features were scaled to ensure equal contribution while calculating distance. For each row of the test set, the $k = 1$ nearest training set vectors were found and classified (Venables and Ripley, 2002).

7.3.6 Cluster interpretation enhanced by geological 3D modelling

Firstly, the geological 3D models were used in different forms to enhance the understanding of hydrogeological and hydrogeochemical conditions, by the assignment of hydrogeological units and distinguishing between shallow and deeper wells. A set of 2D cross sections along the wells in both Munich and in the area situated to the north of the city (Model North) was selected and generated from the models. These 2D representations show the predicted prevailing lithologies in the vicinity of the well screens where the samples for this study were collected. Analysis of this picture of the continuity of the lithologies resulted in the assignment of the aquifers "OSM-shallow" and "OSM-deep" to the screened well sections. This was inferred individually for each well screen along the 2D profiles.

For simplification purposes, within the present study, the aquifer systems in the OSM are sorted into one of the following two notations - OSM-shallow or OSM-deep. The first group denotes the

aquifer system T1, which presents wide interaction areas with the overlying Quaternary aquifer, whereas the second group refers to the aquifer systems T2, T3, and T4, which have no hydraulic interlinkage to other shallow aquifers. The distinction between the aquifer systems T1-T4, i.e. the 3D architectural model, was implemented in 3D only in the city area. However, in order to facilitate the cluster interpretation with depth also in the northern part of the study area, an interpretation of the OSM-shallow and OSM-deep aquifers along the cross section in Model North is provided.

7.4 Results

7.4.1 Multivariate statistics for the Munich area

The statistical normality of the data, analysed with the Shapiro-Wilk test, showed that no variable represented the normal distribution. Therefore, a correlation matrix was calculated with the Spearman method because it is nonparametric and used to perform rank-based correlation analysis (Kassambara, 2017).

Relevant relationships among the variables are presented as a correlation matrix (Fig. 49), which allows one to distinguish the following relationships: (1) strong positive correlations among chloride, sulphate, nitrate, EC and calcium (0.61–0.83), (2) strong positive correlations between DO and nitrate (0.65), DO and calcium (0.58), iron and manganese (0.53), carbonates and calcium (0.58), and (3) negative correlation of pH and calcium, EC, nitrate, chloride or carbonates (0.52–0.74).

The KMO test gave a moderate overall measure of sampling adequacy (MSA) of 0.71, indicating that the sample size is adequate for factor analysis. In the Bartlett test, high values of chi-squared ($\chi^2 = 2,068$, p -value $\approx 0,78$ degrees of freedom) were achieved, indicating that statistically significant correlations exist within the matrix. The determinant of the correlation matrix was positive. Internal consistency reliability was measured by Cronbach's alpha reliability (Revelle, 2020) and demonstrated to be good (0.72).

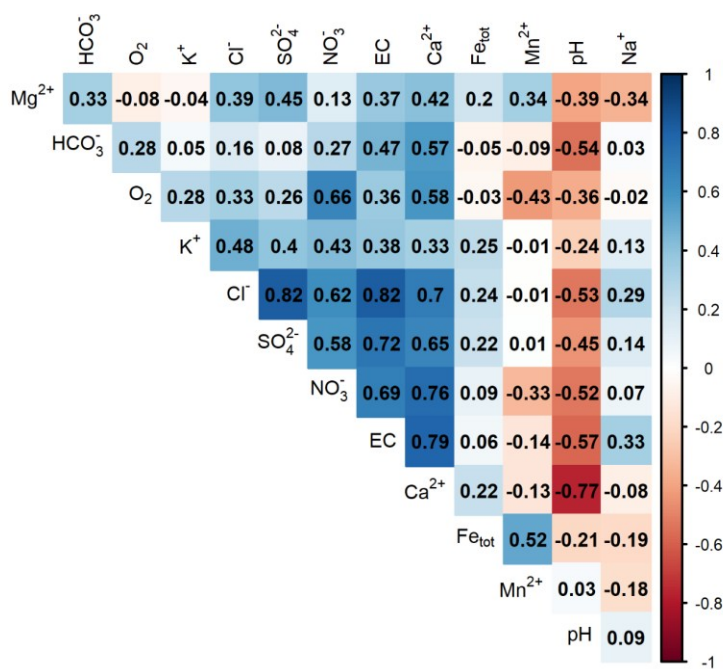


Fig. 49: Correlation matrix of 13 physico-chemical parameters

The ideal number of factors in this case was determined by three methods. The scree-elbow plot of eigenvalues and the empirical Kaiser criterion were in favour of four factors, whereas the parallel analysis favoured five. Finally, by trial and error, a number of three was chosen, giving the most satisfying results: minimum number of variables per factor of four and item to factor ratio of 4.3:1.

Maximum likelihood (ML) was implemented as a factoring method and an oblimin oblique rotation method, allowing the resulting factors to be correlated. The Bartlett method was used for factor scores.

Communalities of individual parameters vary between 0.26 and 1.00 (Tab. 4 of Appendix E). The factor loadings and factor scores for the first two factors obtained in the EFA are presented in Fig. 50 (see also Fig. 84 of Appendix E). The three factors explain 60% of the total variance; moreover, factors ML1 and ML2 are correlated at 0.47 (Fig. 85 of Appendix E).

Factor ML2 explains 27% of the variance and shows the highest loading (>0.7) for positive correlated parameters: Cl⁻, SO₄²⁻ and EC, and also for Na⁺, K⁺ and NO₃⁻. This factor matches the concentrations of anions Cl⁻, SO₄²⁻, and cations Na⁺, K⁺, to the EC, which is known to be related to the total mineralisation.

DO, Ca²⁺, and HCO₃⁻ load high regarding factor ML1. Also, NO₃⁻ and DO load secondarily to this factor, as well as pH (negatively). The opposite loadings for HCO₃⁻ and pH possibly imply that carbonate solubility is controlled by pH (Newman et al., 2016); moreover, the opposite loadings of Ca²⁺ and Na⁺ reveal the importance of the cation exchange process.

Tab. 4: Loadings of the factor matrix (*italic*: loadings > 0.5)

Parameter	Factor ML2	Factor ML1	Factor ML3	Communality	Uniqueness	Complexity
pH	-0.21	<i>-0.62</i>	-0.13	0.57	0.434	1.3
EC	<i>0.7</i>	0.33	-0.06	0.81	0.186	1.4
DO	0.05	<i>0.58</i>	-0.43	0.54	0.463	1.9
Ca ²⁺	0.3	<i>0.82</i>	0.01	1	0.005	1.3
Mg ²⁺	0.21	0.26	<i>0.56</i>	0.47	0.527	1.7
Na ⁺	<i>0.59</i>	-0.48	-0.33	0.44	0.555	2.5
K ⁺	<i>0.51</i>	-0.01	-0.07	0.26	0.739	1
Fe _{tot}	0.17	0.12	<i>0.52</i>	0.33	0.671	1.3
Mn ²⁺	0.04	-0.15	<i>0.75</i>	0.58	0.421	1.1
Cl ⁻	<i>0.95</i>	0.04	0.09	0.95	0.051	1
HCO ₃ ⁻	-0.15	<i>0.71</i>	0	0.43	0.571	1.1
SO ₄ ²⁻	<i>0.78</i>	0.11	0.14	0.71	0.295	1.1
NO ₃ ⁻	0.4	<i>0.5</i>	-0.28	0.67	0.331	2.5

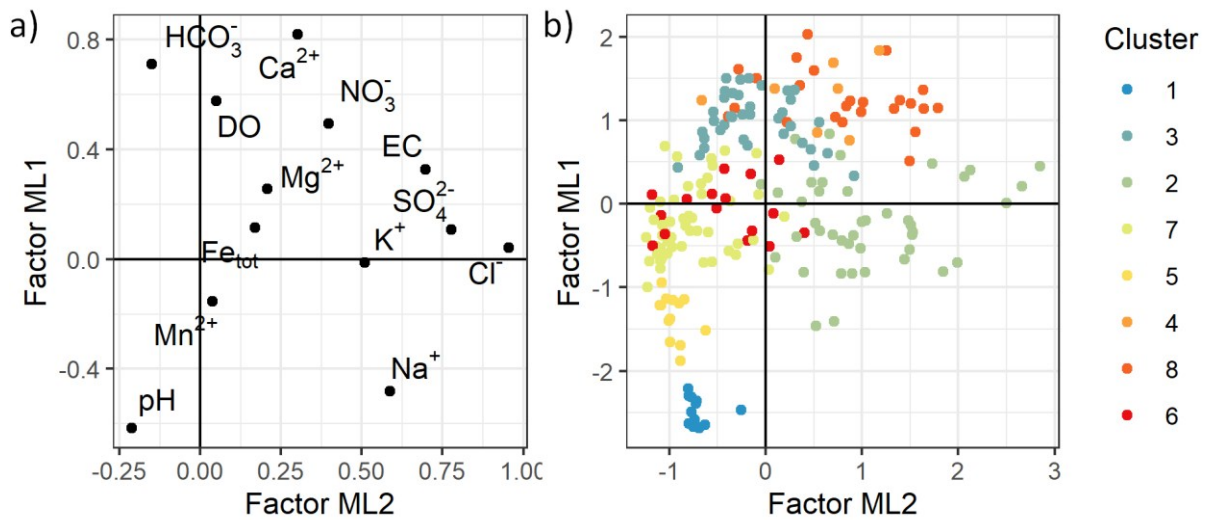


Fig. 50: Plots of: **a)** factor loadings and **b)** factor scores, for the first two factors (ML1 and ML2) obtained in the exploratory factor analysis (EFA) identified by clusters derived from hierarchical cluster analysis (HCA) (see Fig. 51 and cluster description in text)

Mn²⁺ has the highest factor loading on the third factor ML3. Similarly, Fe_{tot} and Mn²⁺ load to ML3. This factor may be connected to the redox conditions in the aquifers, especially with respect to the (admittedly low but not negligible) negative loading of DO.

The estimated number of clusters was diversified depending on the method used (6, elbow method, 4, silhouette method, 9, gap statistics). Therefore, finally, the number was determined arbitrarily on eight clusters and these clusters were the basis for the proceeding interpretation. The cluster analysis allowed grouping of the groundwater samples in reference to similarities in their physicochemical characteristics. In the first attempt at building clusters (not shown), five outliers were identified and excluded from further analysis. The dendrogram in Fig. 51 concerns the remaining 208 data points. This graphical representation of HCA as a dendrogram is presented in combination with pie charts showing the major ions contents.

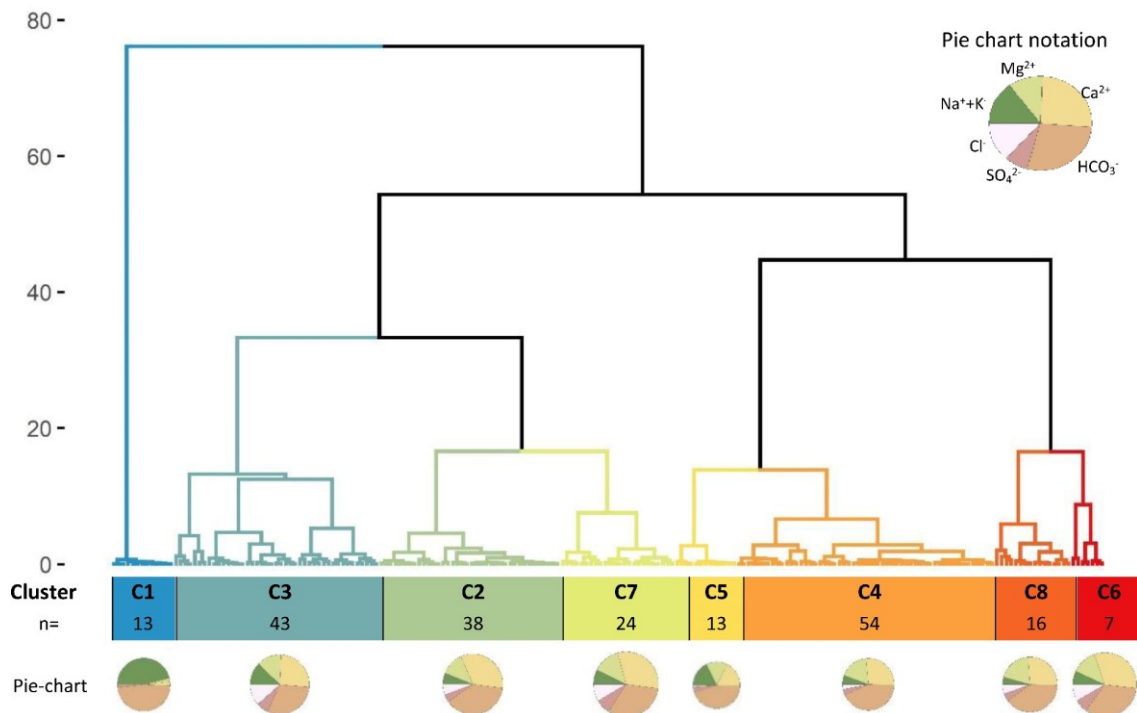


Fig. 51: Dendrogram and pie charts for median values in the resulting clusters (size of the pie chart depends on the degree of mineralisation)

7.4.2 Classification of data from the greater area of Munich using the *k*-nearest neighbourhood algorithm (KNN)

The clusters built for the city area, resulting from the previous step, were used for the classification of the wells from the entire project area. The classification was performed with the KNN-algorithm. The *k*-value, which indicates the count of the nearest neighbours, was found in an iterative selection process. For *k*=1 the accuracy score of KNN equal to 80% was found to be satisfactory (95% confidence interval: 69.14, 88.78), with *p*-value < 2.2e⁻¹⁶ and Kappa = 0.7598; hence, KNN was further used to classify the wells.

7.4.3 Water isotopes

Stable isotopes of oxygen and hydrogen in groundwater (expressed as isotope ratios $\delta^2\text{H}$ and $\delta^{18}\text{O}$, respectively) are used, among others, to analyse groundwater flow pathways, including paleo-groundwater and mixing processes (Tweed et al., 2019). For instance, the values of $\delta^2\text{H}$ and $\delta^{18}\text{O}$ for water infiltrating to the subsurface in the Pleistocene period were several per-mill lower than the present (Tweed et al., 2019). Additionally, measurements of the radioactive hydrogen isotope tritium (^3H) provide further insight into the mean apparent groundwater age (Małoszewski et al., 1983; Zuber et al., 2001).

Fig. 52 presents the stable isotope values, as well as the Global Meteoric Water Line (GMWL) and local meteoric water line (LMWL) calculated for Germany (Stumpp et al., 2014), with the formulae:

$$\text{GMWL: } \delta^2\text{H} = 8 \cdot \delta^{18}\text{O} + 10 \quad (52)$$

$$\text{LMWL: } \delta^2\text{H} = 7.72 \cdot \delta^{18}\text{O} + 4.9 \quad (53)$$

The observations plot mostly around these lines. For comparison, an isotopic value for precipitation is presented. Long-term means for stable water isotopes in precipitation were calculated for the measurements from Neuherberg (near Munich) and have the following values: $\delta^{18}\text{O} -9.89 \pm 0.78\text{‰}$, $\delta^2\text{H} -70.5 \pm 5.8\text{‰}$, with d-excess $8.6 \pm 1.3\text{‰}$ (IAEA/WMO, 2020).

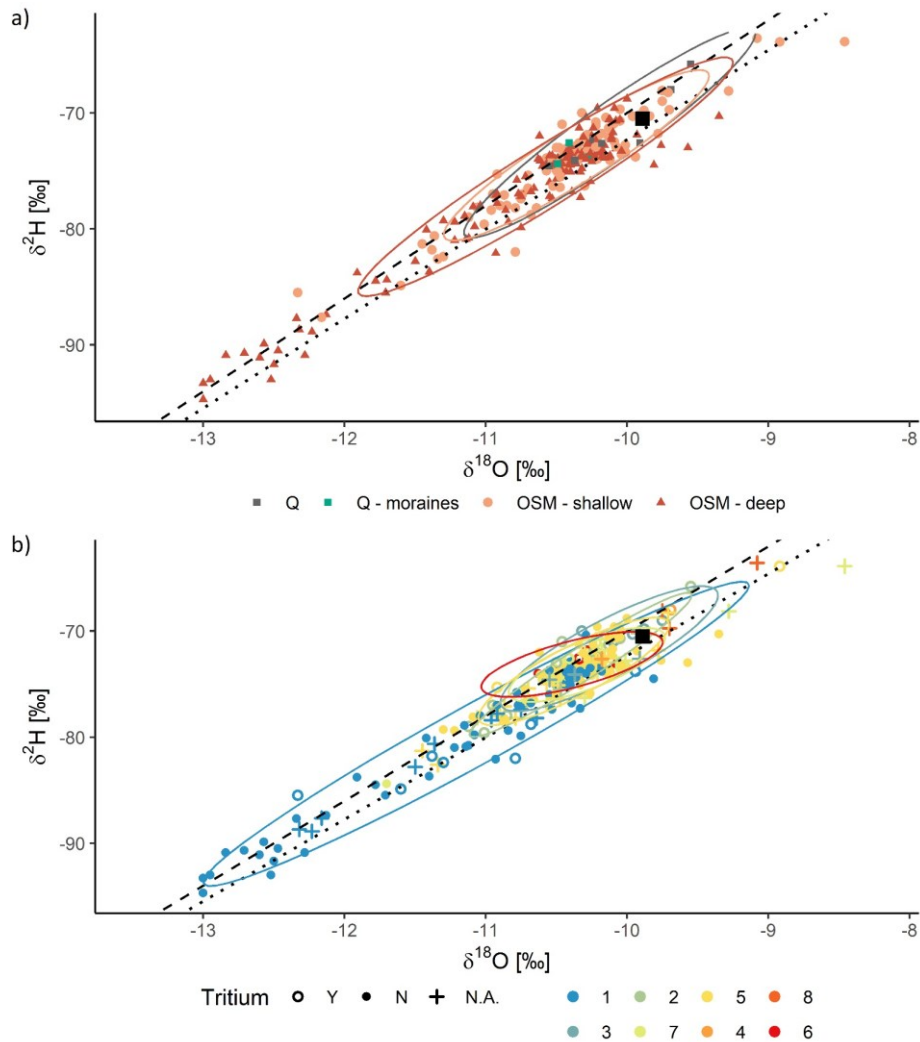


Fig. 52: Plots of $\delta^2\text{H}$ versus $\delta^{18}\text{O}$: **a)** for hydrological units, **b)** for clusters (colours indicate the clusters, for details see Fig. 51 and cluster description in text; some wells are represented by more than one data point. Notation: dashed line – GMWL, dotted line – LMWL for Germany (Stumpp et al., 2014); the ellipses are normal confidence ellipses calculated for each cluster; the black square represents precipitation after IAEA/WMO (2020) – long term mean of precipitation measured in Neuherberg near Munich; NA – Tritium not analysed

Groundwater in the study area showed water stable isotope values between -13.2 and -8.9‰ for $\delta^{18}\text{O}$ and between -94.7 and -63.9‰ for $\delta^2\text{H}$ (Fig. 52a). Water samples from Quaternary aquifers (Q and Q-moraines) plot mostly close to these values, revealing a relatively young age of groundwater in these compartments. The point cloud of OSM-shallow is spread towards lower values of $\delta^{18}\text{O}$ and $\delta^2\text{H}$, suggesting that water age reaches Pleistocene, since groundwater recharge occurred during cooler conditions from melt water or precipitation (van Geldern et al., 2014). This trend is even more visible for the wells from deeper OSM levels. The highest $\delta^{18}\text{O}$ and $\delta^2\text{H}$ values may be explained by evaporation, either natural (subsurface influx of lake water in the south of Munich) or anthropogenic (industrial cooling water) (Rauert et al., 1993). The variability of $\delta^{18}\text{O}$ and $\delta^2\text{H}$ values is greatest in cluster 1 and may reflect a spectrum of groundwater ages or mixing processes (Rauert et al., 1993). Data points of the remaining clusters concentrate mostly around the values of modern precipitation.

Regarding the tritium content (Fig. 52b; Fig. 89 of Appendix E), no occurrence was found in most of the wells of the OSM-deep. However, even in some samples associated with cluster 1, typical for deeper aquifers, tritium was observed, suggesting mixing processes. Interestingly, in some wells of shallow OSM and even in Quaternary moraines, no tritium was measured, revealing water age of more than ca. 70 years (recharged prior to the start of above-ground nuclear bomb testing in 1953), suggesting that these units in some parts of the research area are well isolated from the surface.

7.4.4 Cluster description

As described in Section 7.4.1, the primary focus was on the city area, where a detailed 3D architectural model of the Quaternary and OSM deposits was available. A map presenting locations of the wells in the Munich city area (Fig. 86 of Appendix E) and a Piper diagram for those sites (Fig. 87 of Appendix E), as well as a table of the number of wells in each aquifer system and cluster (Tab. 11 of Appendix E) are provided. The clusters described below relate to the entire area. A general overview for all observations is given in Tab. 5, Fig. 53 and Fig. 54, which present by analogy the number of wells in each aquifer and cluster, the locations of the wells within the study area, and the Piper plot.

Tab. 5: The number of objects in each cluster and hydrogeological units in the entire study area

Hydrological unit	Cluster								Total no. of objects
	C1	C3	C2	C7	C5	C4	C8	C6	
Q	-	65	155	28	2	96	4	5	355
Q-moraines	-	23	57	10	3	81	-	1	175
Q/OSM	-	18	13	4	6	17	-	9	67
OSM-shallow	3	92	39	35	41	131	28	-	369
OSM-deep	33	-	-	-	32	4	6	-	75
Total	36	198	264	77	84	329	38	15	1,041

Additionally, the box-plots obtained for the clusters are shown in Fig. 88. In Fig. 53 and Fig. 54, the groundwater samples are coloured according to their cluster. It can be seen in Fig. 53 that

clusters do not build any spatial, regional pattern in a 2D view; therefore, in the following, they are described in accordance with their occurrence in a 3D geological system. Additional information for cluster interpretation can be concluded from the bi-variate plots (Fig. 55).

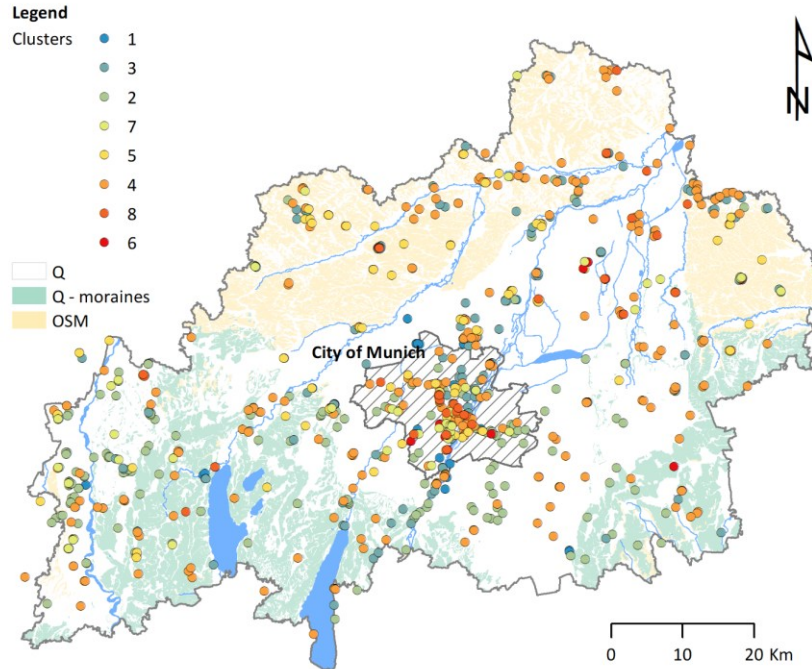


Fig. 53: The locations of wells assigned to clusters in the study area (colours indicate the clusters, for details see Fig. 51 and cluster description in text)

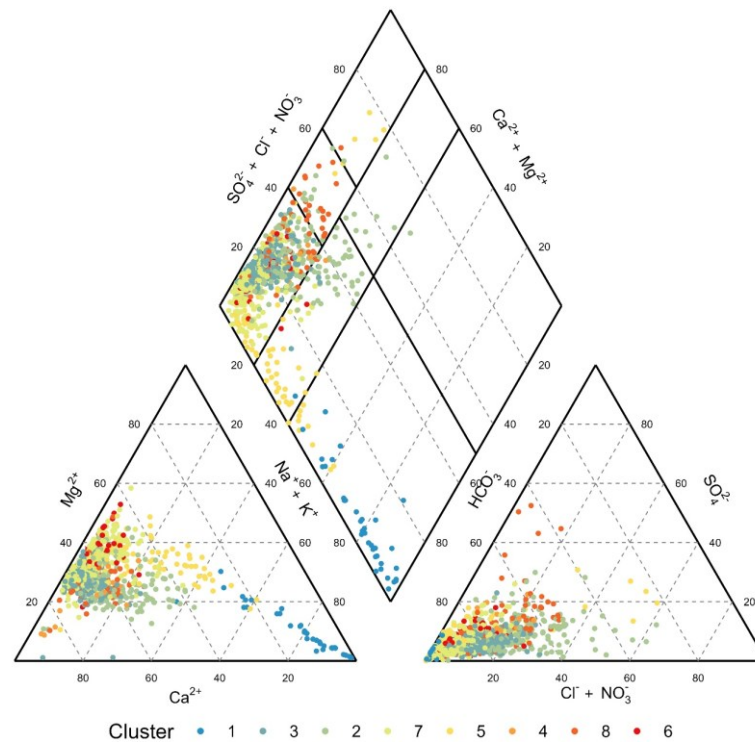


Fig. 54: Piper plot presenting clusters in the study area (colours indicate the clusters, for details see Fig. 51 and cluster description in text)

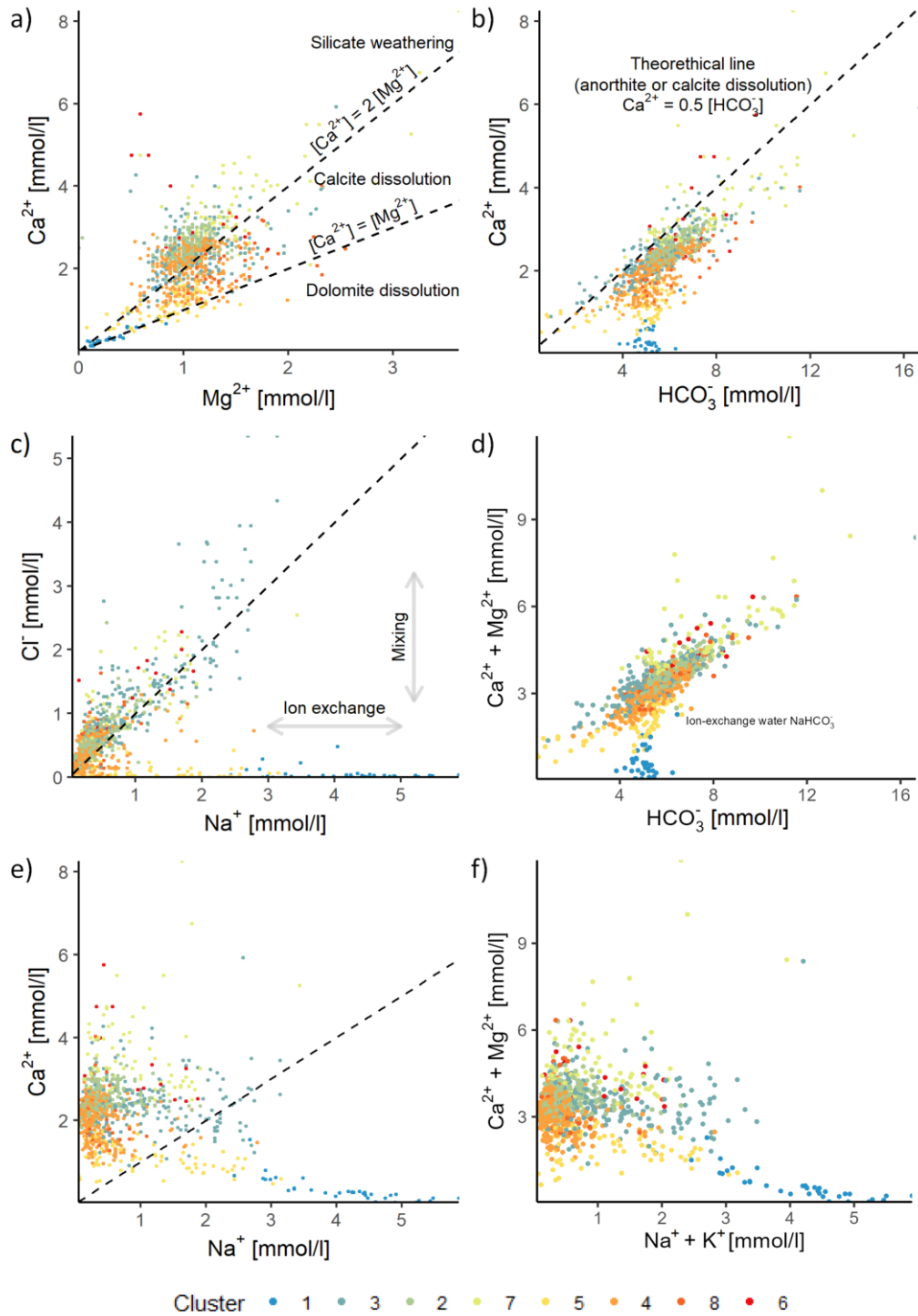


Fig. 55: Bi-variate plots. Notation: dashed line is 1:1 line, when not described differently; colours indicate the clusters, for details see Fig. 51 and cluster description in text

The cluster interpretation provided below presents various examples by means of the two geological 3D models implemented in the greater area of Munich. As mentioned in the Section 7.2.2, the models refer to (1) the city of Munich (Fig. 56), and (2) the area extending from the north of the city to the Tertiary Hills (Fig. 57). Selected examples are indicated by numbers in Fig. 56 and Fig. 57 and described in the text.

Deeper aquifers

Cluster C1 is related to well-isolated aquifer systems, with distinct chemistry, representing Na – HCO₃ water type. Due to high concentrations of bicarbonate and very small sulphate and chloride concentrations, as well as high Na content (98 mg/L), the points plot in the lower corner of the diamond on the Piper Plot (Fig. 54). In addition, Ca and Mg content are the lowest. The waters are also characterised by elevated pH (8.3–9.1), and mostly low DO. The data points of C1 (in opposite to all the remaining clusters), shown in Fig. 55b, do not follow the theoretical linear relationship of calcite dissolution (Ghesquière et al., 2015), which indicates that other processes lead to HCO₃⁻ enrichment.

The majority of deeper wells in the city belong to cluster C1, but also some well-isolated wells screened in the deeper parts of the shallow aquifer system (particularly T1D), in the south of the city (see labels 2, 3, and 4 in Fig. 56).

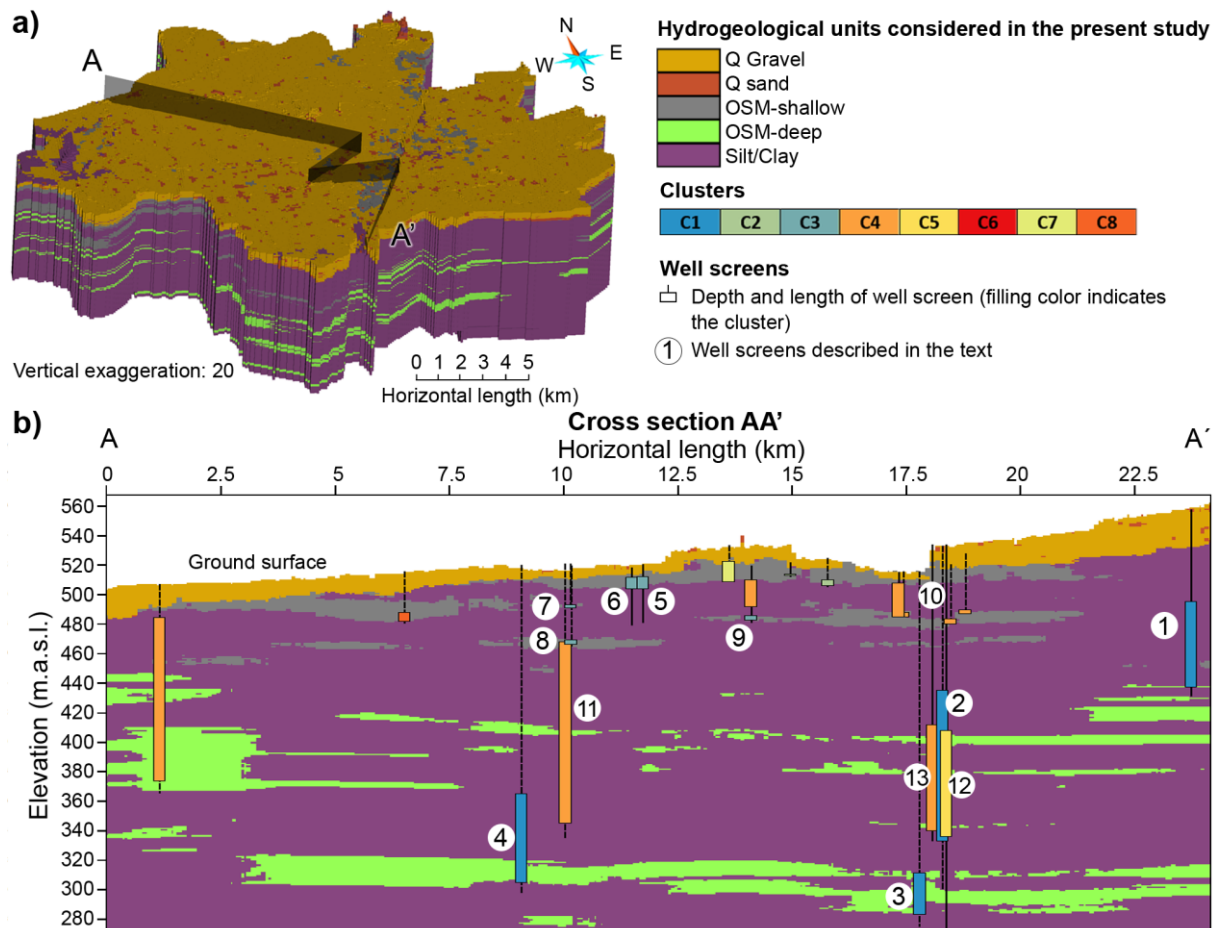


Fig. 56: Cluster interpretation for the city of Munich enhanced by geological 3D modelling: **a)** 3D view of the hydrogeological units considered in the present study adapted from the 3D architectural model of Albarrán-Ordás and Zosseder (2022); **b)** Cross section AA' showing the hydrogeological units and the cluster assignment by various examples of well screens

All the aforementioned wells are screened in the deeper aquifer system (marked in green in Fig. 56), well isolated from the overlying shallow groundwater system (marked in grey in Fig. 57). However, at well 1 (Fig. 56) at the depth of between 440 and 500 meters above sea level (m.a.s.l.), it can be observed that the well is characterized by cluster C1, although it is screened in the lower part of the OSM-shallow groundwater system (more specifically, in the aquifer system T1). This part of the shallow Neogene aquifer is very isolated from the remaining overlying aquifer tiers in the southern part of Munich, which would explain the resulting assignment of cluster C1, which typically represents deeper, clearly isolated groundwater systems. In the Munich North model, cluster C1 is observed in wells 14–18 (Fig. 57).

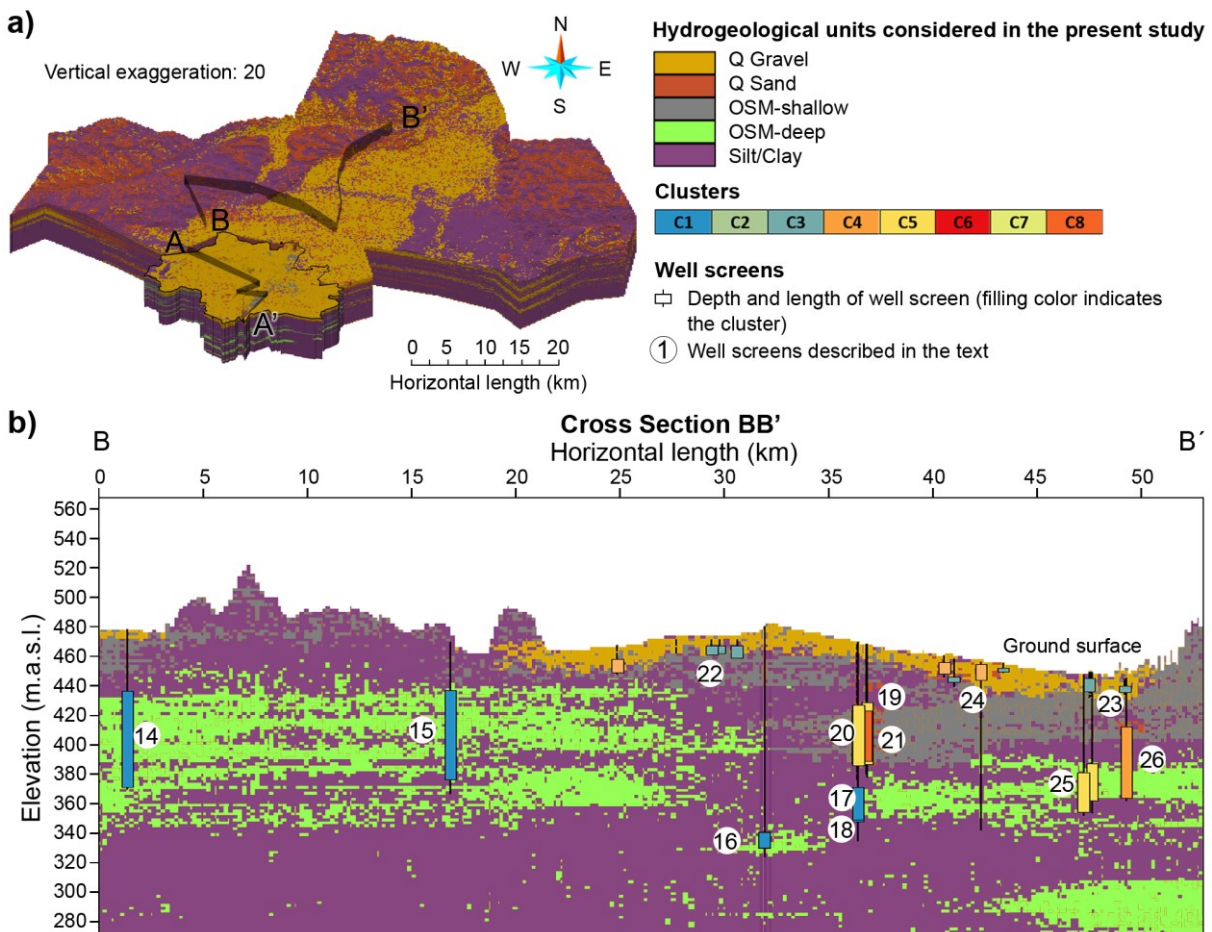


Fig. 57: Cluster interpretation in the northern part of the study area enhanced by geological 3D modelling: **a)** 3D view of the prevailing lithological classes (gravel, sand and clay/silt); **b)** Cross section BB' showing the interpreted hydrogeological units and the cluster assignment by various examples of well screens

The isolation of C1-waters is also confirmed by the values of stable water isotopes, which present much lower values than modern waters, suggesting that they were recharged during colder than present climatic conditions (Fig. 52). The majority of water samples are also free of tritium.

Ortho phosphate and fluoride concentrations are the highest in the deeper aquifers. Some trace elements (B, Ba, Li, Mo, Sr, Ti) show higher concentrations in these deeper-level samples than in

shallower-OSM samples or in the Quaternary. The opposite case is observed for uranium, for which concentrations were the lowest among the four hydrogeological units (1.3 µg/L). Concerning other trace elements, selenium and strontium analyses also reveal relatively high concentrations, which can be explained by the occurrence of weathered feldspars in the OSM sediments (Kainzmeier et al., 2007). In previous studies also from OSM, but located east of the study area (region 13-Landshut and 18-Südostbayern), the waters with low EC and DO, and high pH and specific conductivity were described as ion exchange waters (Chavez-Kus et al., 2016; Kainzmeier et al., 2007). The authors related these waters to uprising Malm waters and recalled that higher concentrations of tracer elements (B, Cz, Li, Rb, Th, Ta) present in some OSM wells are typical for Malm-waters that have undergone ion exchange.

Transition zone

A transition from deeper to shallow groundwater may be observed in the remaining clusters. With increasing depth, the content of Ca and Mg decreases and the content of Na decreases due to ion-exchange processes (Rauert et al., 1993). Cluster C5 represents mixed conditions, which is also apparent from the Piper diagram (Fig. 54), where the points representing this cluster plot between C1 and all the other points. The transition then goes further, but not as obvious, from C1 and C5 towards C7, followed by C3 and finally C4. The shift is also visible on the stable water isotopes plot (Fig. 52b).

Cluster C5 is similar to C1, except in Na content, and is characterised by low chloride, low DO and low EC. The pH values are relatively elevated, but not as distinctly as in C1. Ion exchange is the main process leading to increase of Na concentration by constant Cl content in both clusters (Fig. 55c, in contrast to the remaining clusters, where mixing and ion exchange are balanced, with small domination of mixing). Mg²⁺ and Ca²⁺ concentrations are governed predominantly by calcite weathering in cluster C5 (Fig. 55a). The ion-exchange water of Na – HCO₃-type in clusters C1 and C5 is also apparent in Fig. 55d, as data points indicate that $c(\text{Ca}^{2+} + \text{Mg}^{2+}) < c(\text{HCO}_3^-)$. In Germany, this type of water is exclusively associated with ion-exchange processes, because there are no deposits of this kind of salt in the subsurface (Hölting and Coldewey, 2013). Ion exchange is also an explanation for the deficit of Ca²⁺ in comparison to Na⁺ in clusters C1 and C5 as presented in Fig. 55e (Appelo and Postma, 2004; Ghesquière et al., 2015). The tendency is noticeably even clearer in Fig. 55f, which shows $c(\text{Ca}^{2+} + \text{Mg}^{2+})$ in comparison to $c(\text{Na}^+ + \text{K}^-)$.

The wells from this cluster are mostly screened in isolated aquifer systems; however, not as deep as C1, and the influence of younger water is noticeable. Cluster C5 lies in transition zones between deeper (C1) and shallow aquifer systems; therefore, groundwater samples of this cluster show a broader typification from Ca – HCO₃ to Na, K – HCO₃ waters. In this sense, it was observed that wells 19 and 20 (Fig. 57), which are screened in the gravel-dominant aquifer system at depths between 380 and 420 m.a.s.l., belong to cluster C5, whereas the underlying close wells 17 and 18 were assigned to cluster C1. The mixed conditions at wells 19 and 20 can be explained by the

proximity of an interaction zone between the Quaternary aquifer and the first shallow groundwater system in the OSM (from ca. 40–50 km on cross-section B–B'). It can also be observed that the aforementioned well groups 19–20 and 17–18 are separated by a fine-grained succession, thus causing an isolation of the deeper groundwater assigned to cluster C1, which is typical for isolated groundwater. Cluster C5 is also visible in four wells situated at location 25. In this case, the mixed conditions can be explained by the lateral extension of the gravel aquifer at depths of 400 m.a.s.l. It can also be observed that well 26, with a long well screen reaching the uppermost OSM groundwater system, belongs to cluster C4 and represents an exception to this interpretation.

Shallow aquifers

Clusters C3, C2 and C7 comprise wells screened in the Quaternary and shallow OSM. The dendrogram reveals some indications of similarity between these three clusters (Fig. 51). These are characterised by similar pH and EC values, as well as concentrations of Ca^{2+} , Mg^{2+} , HCO_3^- , and SO_4^{2-} . Cluster C2 is characterised by the highest DO. C3 has a higher Cl^- median concentration than C2 or C7, also with outliers.

Possibly, the anthropogenic impacts (mostly diffuse contamination sources, i.e. use of fertilizers or road-salt in winter) are visible through elevated contents of nitrate, chloride, potassium, and sodium (Wagner et al., 2011, 2003) - for example, German limit-values for nitrate in drinking water (50 mg/L) were exceeded in 30 analysed samples for C2, 18 for C3, and 15 for C7. Elevated NO_3^- concentration (including several outliers) indicates use of fertilizers in the vicinity of the wells. Elevated contents of SO_4^{2-} and Mg^{2+} are also indicators of anthropogenic contamination due to agricultural activity and wastewater release (Senbayram et al., 2015; Torres-Martínez et al., 2020). Previous studies conducted in the immediate vicinity of study area have shown that elevated concentrations of nitrate are caused by release of high amounts of manure and, to a lesser extent, synthetic fertilizers due to intensified agriculture (Wild et al., 2020, 2018).

Cluster C6 is similar to C7, but with lower DO and NO_3^- . These clusters almost overlap each other on the Piper plot (Fig. 54) and factor scores plot (Fig. 50). Cluster C7 belongs to shallow wells, screened in areas with hydraulic interaction between the Quaternary aquifer and the underlying aquifer parts of the OSM. Cluster C6 is a relatively small group of 15 wells screened at shallow depths. EC medians are the highest among all the clusters (870 and 878 $\mu\text{S}/\text{cm}$, respectively). In cluster C6, elevated Fe and Mn concentrations are noticed; moreover, the DO is relatively low, which suggests reductive conditions, as confirmed via EFA (see Section 7.4.2). Iron and manganese exceedances are generally associated with each other, as they have similar chemical behaviour, being subject to pH and redox conditions (Montcoudiol et al., 2015). Mg^{2+} and Ca^{2+} concentrations are governed predominantly by silicate weathering in clusters C6 and C7, as well as in C2 and C3 (Fig. 55a).

Clusters C4 and C8 expose some similarities and overlay each other on both Piper and factor scores plots (Fig. 50, Fig. 54). Cluster C4 represents a high variety of wells screened in different aquifer systems. These clusters are influenced by both processes of calcite dissolution and silicate weathering (Fig. 55a). Relatively high concentrations of silica are observed in the shallow OSM, which may be related to the occurrence of feldspar in the OSM sediments (Wagner et al., 2003).

As apparent on the dendrogram (Fig. 51), *clusters C6 and C8* are closely related, both being assigned to the OSM-shallow; however, C8 represents slightly greater depths. C6 has more Ca^{2+} , but less Mg^{2+} than C8 and shows higher mineralisation. The cluster interpretation enhanced by geological 3D modelling is more complex for the clusters C2, C3, C4, C6, C7 and C7, as the differences between the hydrogeochemical patterns are less distinct than for the clusters C1 and C5. On the one hand, in the model of Munich, shallow wells 5 and 6, as well as those lying a bit deeper (7, 8 and 9), belong to cluster C3. This can also be observed in the Munich North model at wells 22 and 23. On the other hand, the four wells in Munich represented by well number 10 are marked with cluster C4 and are located very close to the uppermost tier of the shallow aquifer. Similarly, one can also observe in the Munich North model (Fig. 57) that clusters C3 and C4, which are typical for shallow OSM groundwater, are found interspersed in well 24. However, an exception for cluster C4 is shown in well 11, also located in Munich, reaching great depths from 460 to 340 m.a.s.l. The latter scenario, as well as that for well 26 (Fig. 57), clearly underlines the difficulty of interpreting the results in the case of long well screens that mix groundwater from various aquifers at different depths. This can be also seen, for instance, in wells 2, 12 and 13 (Fig. 57), which are partially screened very close together at similar depths and show three different clusters (C1, C4 and C5).

Among the trace elements, the following are present: Sr with a median above 100 $\mu\text{g/L}$; B, Ba – above 10 $\mu\text{g/L}$; Cu, Cr, Li, U, Zn – above 1 $\mu\text{g/L}$. The presence of uranium above 1 $\mu\text{g/L}$ in more than 50% of samples is noteworthy, not only in the Quaternary deposits, but also in the moraines and shallow OSM. As concluded by Banning et al. (2013), uranium primarily originates from lignitic inclusions in the OSM sediment; uranium was transported to and accumulated in lowland moor peats, and nowadays get mobilised, for example, by application of agricultural fertilizer containing nitrate.

7.5 Discussion

The study and utilisation of geopotentials, in particular groundwater abstraction, and the use of shallow (as defined by Halilovic et al., 2022) and deep geothermal energy generates a great amount of data over time and space. Thus, the quality of the data and their spatial distribution may be extremely heterogeneous, so a large amount of data is not automatically a guarantee for establishing a good understanding of the local conditions. Quality assurance processes, as presented in this study, must be developed, implemented, and accordingly documented prior to analysing the data.

Further, understanding the local groundwater chemistry means developing a conceptual model and constitutes a complex problem, which may be resolved by using different lines of evidence. Privett (2019) concluded that using appropriate lines of evidence allows one to increase the understanding and solve challenging geological problems. Also, Freedman et al. (2019) stated that evolving a conceptual model should be associated with applying adequate lines of evidence and a suitable level of complexity to represent hydrogeological systems. Two main aspects resulting from the study are discussed in the following sections.

7.5.1 Coupling the 3D geological models with hydrogeochemical data

In this study, the three main lines of evidence in characterising hydrogeochemistry were: (1) multivariate statistics, complemented by (2) descriptive statistics, and finally coupled with (3) geological 3D modelling. These lines of evidence did not follow one another as listed here, but rather followed each other in a few iterative steps. Coupling the 3D geological models with hydrogeochemical data can be seen from different perspectives: first of all, the model serves as a starting point for grouping hydrochemical data, but at the same time hydrogeochemistry poses an additional validation of the model. Moreover, geological 3D modelling provides a better understanding of the geometry of the aquifers. In older studies, the main criterion for the grouping of wells was their depth. Thanks to the 3D model, other criteria can be examined such as the affiliation of wells to certain aquifers, interconnections between groundwater bodies, etc. On the other hand, the presented utilisation of the 3D geological modelling outcomes reveals a possible qualitative verification of the model, meaning that greater confidence in the model with subdivided horizons was established (after the definition of verification by Diaz-Maurin and Saaltink, 2021).

A first understanding of the hydrogeochemical characteristics of the study area was obtained by defining four main hydrogeological units and assigning objects to these units (often taking advantage of the outcomes of the geological 3D modelling), followed by calculating descriptive statistics for 46 parameters (Zosseder et al., 2022b; results described briefly in Appendix E-2). The results of this approach were satisfying but did not allow for a deepened assessment of hydrogeochemical patterns; therefore, more sophisticated multivariate statistical methods were implemented.

Multivariate statistics have successfully been applied in hydrogeochemistry studies, especially when dealing with large-scale data (e.g. Heine et al., 2021), when presenting information on human impacts on hydrogeochemistry (Menció and Mas-Pla, 2008) and distinguishing between distinct hydrogeochemical zones, as well as increasing the general understanding of hydrogeological processes (Cloutier et al., 2008). All these aspects were addressed in the presented study.

The hydrogeochemical groups (clusters) obtained by multivariate statistical methods and their dependencies could be explained using plots and diagrams, and, finally, being presented in 3D view has thus enhanced their understanding. However, the clusters were based on selected parameters. After creating the clusters by means of multiple statistical methods, it was necessary to fall back on descriptive statistics in order to characterise the hydrogeochemistry more precisely. In this way, descriptive statistics, which constitute a more traditional approach, played an important role in this study, as it enabled further insight into the hydrogeochemistry - for instance, the patterns of trace element occurrence could not be described otherwise.

The clusters obtained in this study, based on the hydrogeochemistry, were not as unambiguous as expected, because the local geology offers multiple pathways for water exchange and mixing at almost all levels and over the whole area, as has already been hinted at in the 3D model (Albarrán-Ordás and Zosseder, 2022). Therefore, the authors support the idea that the clusters actually not only present an effective way to highlight distinct water groups where possible, but they also effectively highlight relationships between mixed waters. However, some wells located close to each other and screened at almost the same depths represented different clusters, probably due to some local conditions not captured in the 3D model, or due to the long well screen lengths reaching across different groundwater systems. The latter circumstance is economically explicable, but complicates capturing the hydrogeochemistry characteristics of distinct levels - for example, Rauert et al. (1993) suspected that samples analysed in their study represented mixed waters originating from great depth intervals and, therefore, of different ages.

The two main studies highlighted so far that combined hydrogeochemistry with 3D geological modelling were reported by Martinez et al. (2017) and Raiber et al. (2012). Use of 3D geological models in these studies, similar to the one reported here, has enhanced understanding of the aquifer systems, and their spatial relationships and interconnections. Taking into account the current development of 3D modelling and its numerous applications (Albarrán-Ordás and Zosseder, 2022), and a successful implementation as presented in this study, new applications in this thematic area can be expected to follow.

7.5.2 Remarks on the conceptual regional hydrogeochemical model

A conceptual regional hydrogeochemical model was developed based on the results of multivariate statistics supported by geological 3D modelling. Based on that, the following can be stated:

- The deeper aquifers, as seen in the geological 3D models, represent the most distinct hydrogeochemical signature of the Na – HCO₃ water type. In the remaining clusters, a transition from deeper (alkaline) to shallow (alkaline-earth) groundwater can be observed.
- The dissolution of carbonate gravels present in the Quaternary layers, by recharge waters, contributes Ca²⁺ and HCO₃⁻ ions. Whereas the Mg²⁺ and Ca²⁺ concentrations are governed

predominantly by calcite weathering, in some of the other zones, silicate weathering is the governing process (Fig. 55a).

- Due to cation exchange processes, Ca^{2+} is exchanged by Na^+ in the deeper levels (Borzi et al., 2021).
- As the occurrence of nitrate is commonly related to agriculture and livestock, its presence in OSM groundwater (cluster 8) points towards the vulnerability of shallow OSM, particularly where these layers are not covered by impermeable clays or silts.
- According to Bertleff et al. (1993) and Heine et al. (2021), ion exchange waters of the Na – HCO_3 type were recharged during colder-than-present climatic conditions. This is confirmed by the stable water isotopes results, which present much lower values than modern waters.
- In previous studies of the OSM (Andres and Egger, 1985; Wagner et al., 2003) a distinction between deeper and shallow groundwater was made based on the tritium content; waters occurring deeper than 30 m were usually free of tritium. Tritium content data from the data bank of LfU and previous studies were used as a supporting argument in classifying wells. An interface of tritium-free old water and young tritium-containing water was estimated at a depth of ~30 m (Andres and Egger, 1985). This estimation of depth is still in use by local authorities for distinguishing between the shallow and deep OSM (Chavez-Kus et al., 2016; e.g. Wagner et al., 2003). However, ~30 years ago, Rauert et al. (1993) observed that, in the Munich area, under hydraulic stress (by intensive exploitation of deeper aquifers), young tritium-containing waters have reached the depths of 60 m. Tritium-free water was observed in deeper aquifers as well as in the well-isolated shallow OSM aquifer, mostly in the southern part of the project area. The former establishment of the tritium-interface depth is therefore unjustified.
- The data set was inhomogeneous in many ways, e.g. it was collected over a few decades and, therefore, characterized by multiple limits of detection for the same parameters. It was challenging to work with censored data (“censored” meaning data that have been reported above a predetermined value). Simple methods, such as replacing censored data with the detection limit or half of the detection limit, cause loss of valuable data. For that reason, descriptive statistics can be calculated using the NADA package in the statistic programme R (R Core Team, 2021) with “regression on order statistics” (ROS; Helsel, 2012). ROS is a semi-parametric method used to estimate summary statistics and plot model distributions with censored data; it assumes that data can be fit to a known distribution by a least-squares regression on a probability plot (ITRC, 2013).

7.6 Conclusions

The presented investigation of the hydrogeochemical characteristics of groundwater in the shallow aquifers of the greater area of Munich was a continuation of extensive research on the shallow deposits of the Quaternary and Neogene subsurface in the wider area of Munich,

conducted at the Chair of Hydrogeology, TUM, Germany (Albarrán-Ordás and Zosseder, 2022, 2020; Böttcher et al., 2019; Böttcher and Zosseder, 2022; Kerl et al., 2012; Theel et al., 2020; Zosseder et al., 2022b).

In this study, different methods were applied in order to characterise the groundwater chemistry in the most suitable way. It was found that the integration of descriptive and multivariate statistical techniques with 3D geological modelling gave the most satisfying outcome. The methods used posed different lines of evidence and were complementary to one another. The presented workflow of dealing with inhomogeneous data sets and the methodology of quality assurance demonstrate the importance of adequate data management. Presented procedures can be (after adaptation) implemented elsewhere.

Three water types were classified according to their hydrogeochemical composition and location in the 3D geological system. It was recognized that deeper aquifer systems are characterised by the most separate hydrogeochemical signature of the Na – HCO₃ water type. Also, a transition from deeper (alkaline) to shallow (alkaline-earth) groundwater was observed, as well as an anthropogenic impact on water quality in the shallow aquifers. The outcomes of this study improve understanding of the regional hydrogeology. The results can be utilised as a stimulus to other studies (in particular the geological 3D model and the derived architectural model) for improved groundwater management and sustainable usage of geopotentials.

This study has, as usual, some limitations resulting, for instance, from selected methodologies. First of all, the goal of this work was to capture the spatial variability of hydrogeochemical facies. Therefore, from the available analyses, only one fulfilling the defined criteria (actuality and number of analysed parameters) was selected for each well. Investigation of the temporal variability of physio-chemical parameters can be an interesting possibility for future research.

7.7 Acknowledgements

Grateful acknowledgment is given to the Bavarian Environment Agency (LfU) for their support and supervision, as well as for access to the borehole database of the Soil Information System of Bavaria. The authors thank Manuel Gossler (TUM) and Florian Heine (TUM) for their help in R programming, Marco Kerl (TUM) for productive cooperation within the project, Susanne Thiemann (TUM) for analysing water stable isotopes, Günter Kus (LfU) for instructions on the standardized sampling methods of the Bavarian Environment Agency and for information to hydrogeochemical aspects of the study area, Thomas Schaller (TUM) for help in the sampling campaigns, and finally all the institutions that provided us with data. Lastly, Emerson E&P is kindly acknowledged for providing licenses for the Software product SKUA™ Engineering Modelling in the scope of the Emerson Academic Program, which supported the results of this publication.

CHAPTER 8**Main findings and discussion**

This chapter emphasizes and discusses the main findings of the thesis presented in Chapters 4, 5, 6, and 7 and in five case studies presented in the first part of this chapter (8.1). This enables exploring the transferability of the research findings in different geological contexts and applications. The principles of this thesis have been utilized as a supporting tool for planning both a road and a subway tunnel (8.1.1 and 8.1.2), as well as to account for intra-zonal variability in hydraulic conductivity for groundwater model calibration (8.1.3). Furthermore, the research findings have been applied in a multi-layered aquifer in Augsburg (8.1.4), and in the Low Lech Valley (8.1.5) to investigate the degree of certainty associated with the connectivity between aquifers, and estimate spatial aquifer parameters for assessing the shallow geothermal potential for GWHP in accordance with applicable regulations from the water authority, respectively. The second part of the chapter presents and discusses the main research findings of this thesis (8.2).

8.1 Evaluation of transferability to other geological settings and areas of application on selected case studies

This chapter analyses the degree to which the main findings of this thesis can be applied effectively in different geological settings or practical applications. Transferability supports the trustworthiness of the research findings (Koch and Harrington, 1998) and is used to argue for the potential of wider relevance of the results in Chapter 8.2.

8.1.1 Case study: Tunnel planning of the Starnberg Road Tunnel

The State Construction Authority of Weilheim plans the construction of a tunnel to relieve road traffic congestion on the federal road B2 in the city of Starnberg, located 30 km southwest of Munich (see Fig. 58a). This federal road is the main communication axis between Munich and the municipalities of Starnberg, Weilheim, Peißenberg, and Schongau in the south. The total tunnel length is expected to be approximately 1.7 km, as depicted from Fig. 58b.

The planned tunnel is situated in extremely heterogeneous geological and hydrogeological conditions (Fillibeck and Lachmann, 2011). A simplified geological 2-D profile is shown in Fig. 58c. The pre-existing Miocene land surface was modified by glacier erosion during the alternating glacial periods in the Quaternary, thus creating troughs and depressions (see Fig. 58c). Like other lakes in the Bavarian Alpine foothills, the Starnberg Lake was created by the exaration of a glacier foreland and the subsequent filling up of the depression with water. When the glacier retreated

during the Würm glacial period, the melting glaciers exposed large areas with loose sediments in the form of complex moraines systems, which also reached the study area (see deposits indicated in light and dark grey in Fig. 58c). Post-glacial deposits formed by gravelly terraces with the presence of conglomerate boulders also occur at the northern end of Starnberg Lake. In the planned Starnberg Tunnel area, the cohesive moraines may also act as confining layers, thus leading to three aquifer tiers with different groundwater levels, as shown in Fig. 58c (Fillibeck and Lachmann, 2011). It is assumed that the tiers are separated from each other by vertical or inclined confining beds. However, less is known about the geometries of the aquifers and the impermeable beds. Furthermore, the tunnel construction requires the prediction of groundwater inflows in order to design suitable drainable systems. In its course, the tunnel passes through large portions of the aquifer, especially in the middle section, where high hydraulic conductivity values and hydraulic gradients are expected to occur (Fillibeck and Lachmann, 2011).

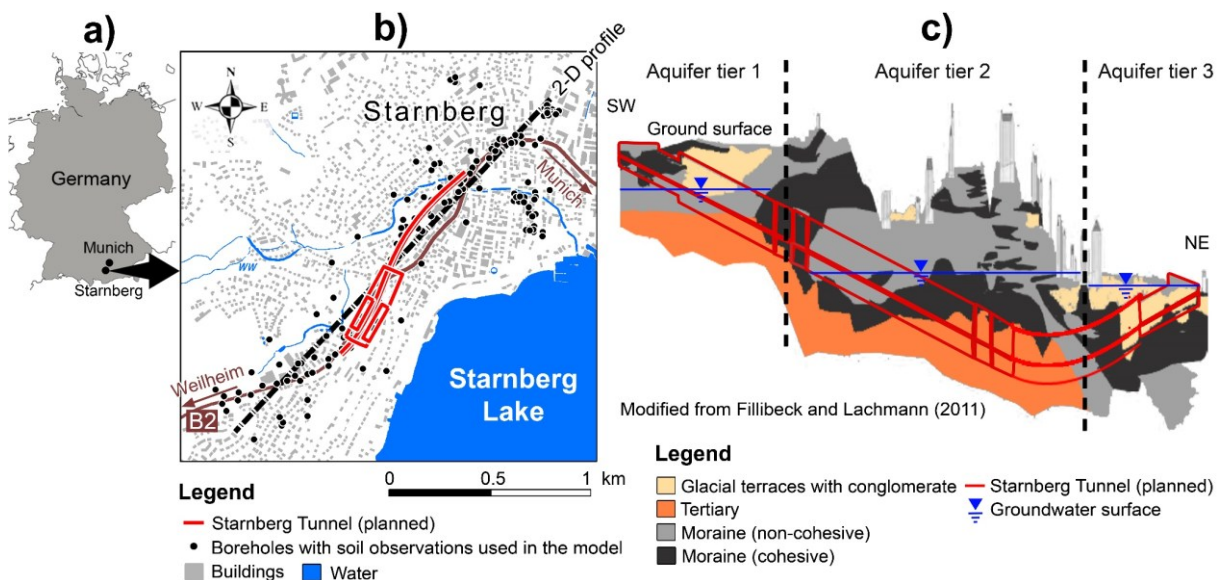


Fig. 58: Geological setting in the Starnberg Road Tunnel: **a)** Location map; **b)** Planned tunnel course and borehole data used for geological 3-D modeling; **c)** Schematic 2-D geological profile

The main research goal is to investigate the groundwater dynamics by capturing the geological and hydrogeological conditions near the planned tunnel in as much detail as possible. The specific objectives were, thus, *i)* the determination of the geometries of the aquifers relevant in the area and *ii)* the estimation of the groundwater inflows into the tunnel excavation.

To achieve the aforementioned goals, the D_i models method was implemented to build a 3-D geo-model with an area of approximately 1.3 km², comprising 183 boreholes with soil observations (see black dots in Fig. 58b). The grid has a 5 by 5 m aerially and 1 m vertically resolution with approximately 16 million voxels. The model provides four ($C=4$) simulated fractions at grain-sizes limits between 0.001-0.002 mm (silt), 0.002-0.063 mm (clay), 0.063-2 mm (sand), and 2-63 mm (gravel). A constant step in the GSD of 10% was fixed.

The water inflows into the tunnel, especially in unconsolidated sand and gravel deposits, might lead to severe water problems (Freeze and Cherry, 1979). Thus, the correct quantification of the water inflow rates likely to appear is a relevant task in designing the requirements of the dewatering system. Consequently, a scenario analysis based on the scheme introduced in Chapter 4.4.7 was proposed to determine a conservative and optimistic prediction regarding the expected dewatering demand (Fig. 59). An optimistic case, i.e., the less demanding dewatering, is generated by the minimal expected aquifer geometries with water-saturated deposits having at least 60% of coarse-grained sediments (see coarse-grained sediments in D_{40} -model in Fig. 59a-b). However, a conservative estimate, i.e., the most demanding dewatering, is generated by the maximal expected extension of the aquifer. This is given by the 3-D distribution of water-bearing deposits having at least 40% coarse-grained sediments (see coarse-grained sediments in D_{60} -model in Fig. 59c-d).

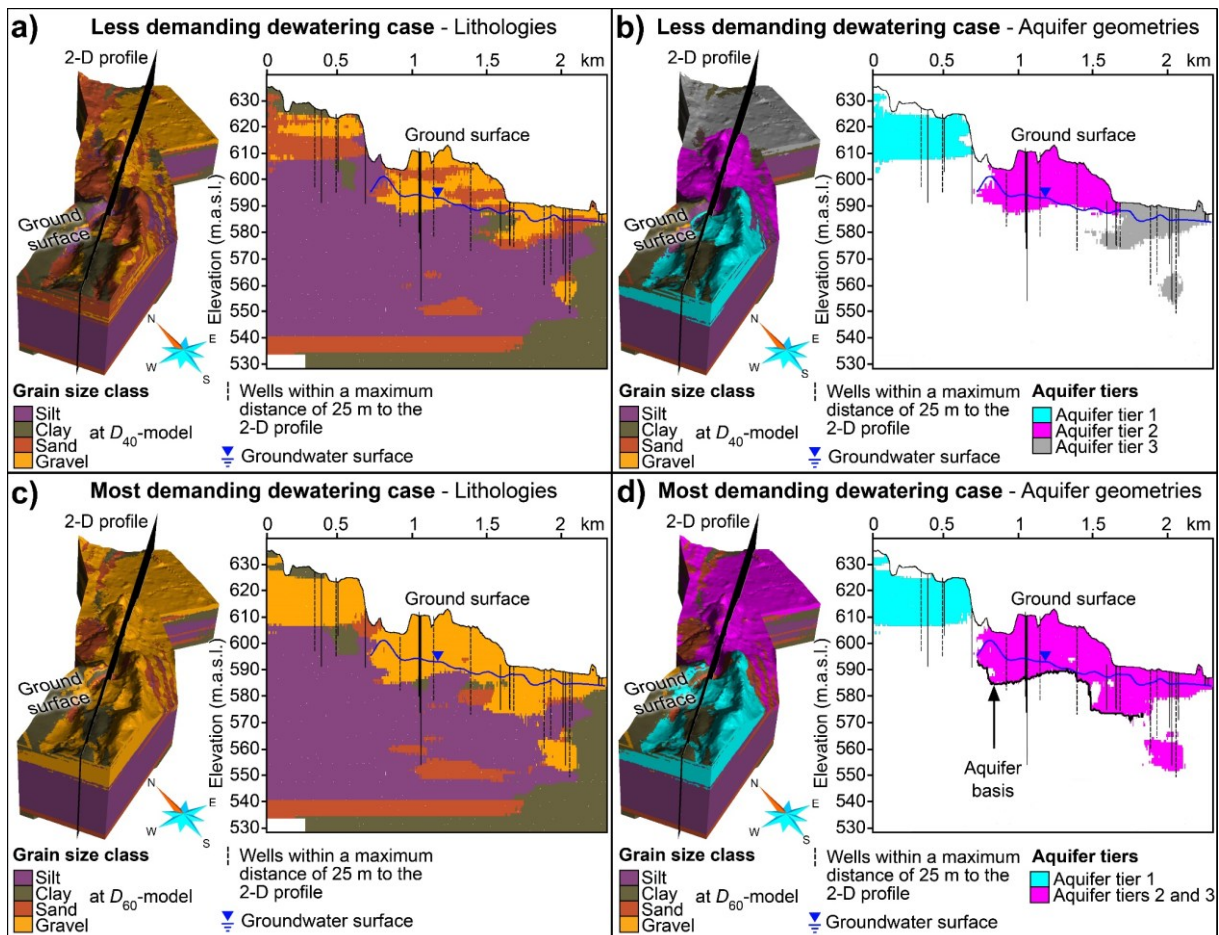


Fig. 59: Geological 3-D model in the Starnberg Road Tunnel: 3-D distribution (left panel) and 2-D profile (right panel) representing the less and most demanding dewatering scenarios: **a)** Lithologies at the less demanding dewatering case; **b)** Aquifer geometries at the less demanding dewatering case; **c)** Lithologies at the most demanding dewatering case; **d)** Aquifer geometries at the most demanding dewatering case

Further works, such as determining the aquifer basis indicated in Fig. 59d, focused on the most demanding dewatering requirements within the aquifer tier 2. Subsequently, the inflow areas were identified after modeling a groundwater table based on available measurements and

generating a transect across the geological 3-D model, as shown in Fig. 60a. As we can see, this transect is divided into eight distinct segments, each of which may contain an inflow area delimited on the top by the groundwater table and at the bottom by the confining layer represented by the aquifer basis (see Fig. 60a-b). A total of five possible inflow zones were inferred within the aquifer tier 2, with a total area of 3,600 m² (see Fig. 60b). The groundwater inflow calculation assumed a constant averaged hydraulic conductivity and a separate hydraulic gradient in each inflow zone. Moreover, the groundwater flow is assumed to follow Darcy's law in each zone separately, which was used to calculate the volume rate of flow through any cross-sectional area perpendicular to the flow direction. The results show that inflow rates may reach maximal values of 2,000 l/s for extreme inflows, with an average of 243 l/s. The largest groundwater inflows into the tunnel were encountered in the southwest parts in zones 1 to 3, with a combined area of 3,200 m² and an average of 220 l/s, thus representing 90% of the total expected inflow rates. Moreover, based on the 3-D distribution of grain-size fractions in the conservative scenario, an itemization of the well screens in the study area was carried out in order to selectively group the groundwater measurements together for each aquifer and generate reasonable separated hydraulic potentiometric surface maps.

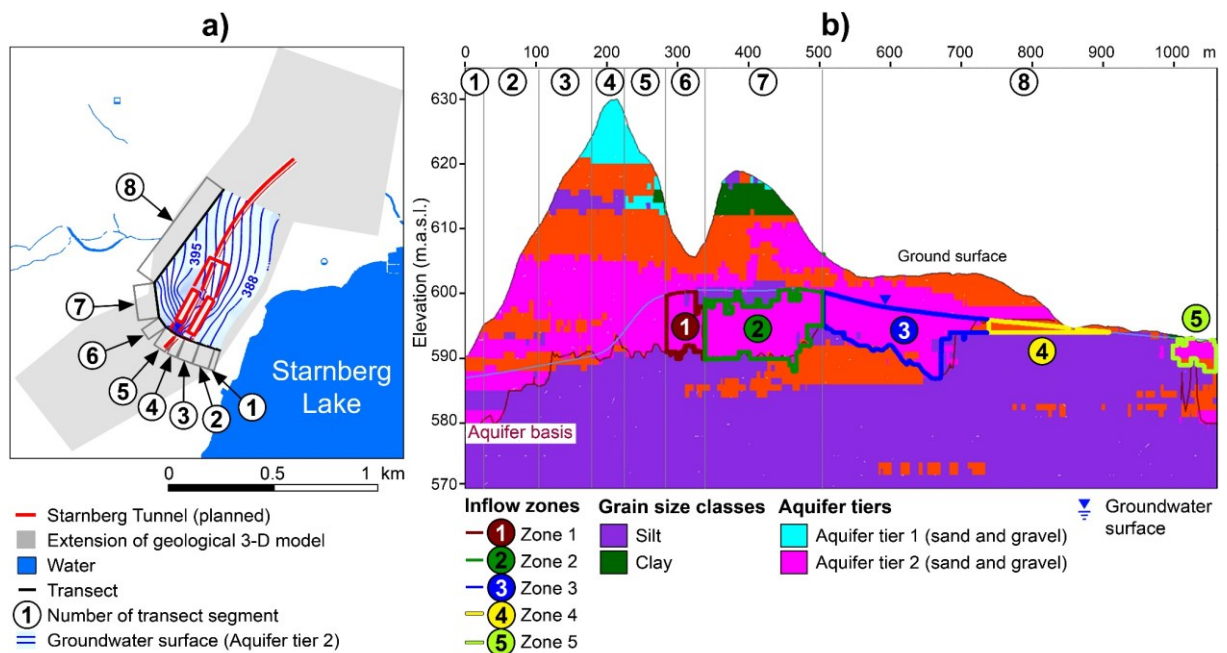


Fig. 60: Analysis of groundwater inflows in aquifer tier 2 into the Starnberg Road Tunnel based on the 3-D geo-model: **a)** Position of the transect divided into eight segments; **b)** Identification of inflow zones along the transect delimited on the top by the groundwater table and at the bottom by the confining layer

The results show that the 3-D geo-model provides useful insights to design the tunnel drainage system by means of the identification and quantification of the non-constant inflows along the tunnel based on the geological heterogeneities inferred from the model. Possible extreme water inflows, which are very difficult to predict, are addressed by considering the most demanding

dewatering based on the expectation of coarse-grained components in the sediment mixture derived from the D_i models method.

8.1.2 Case study: Tunnel planning of the U9 Subway Tunnel in Munich

Stadtwerke München (SWM), Munich's municipal utilities company, plans the construction of a tunnel as part of the new subway line U9 to relieve and provide additional mobility in Munich's transport network. The tunnel's length will be approximately 10.5 km and is intended to connect the districts of Schwabing and Sendling via the main train station in the city of Munich, as shown in Fig. 61b. The excavation itself will be approximately 35 m deep (see Fig. 61c), thus comprising sediments of the Quaternary and Upper Freshwater Molasse sequences.

Planning the exploration works to be undertaken before the tunnel construction requires identifying the hydrogeological conditions that are likely to be encountered in the underground space during the construction phase. In particular, this includes understanding the geometries and properties of the water-bearing and low-permeability formations affected by the tunnel, as well as their interactions. The initial thorough review of all available literature provides the main geological characteristics in the area, which need to be later verified by drilling.

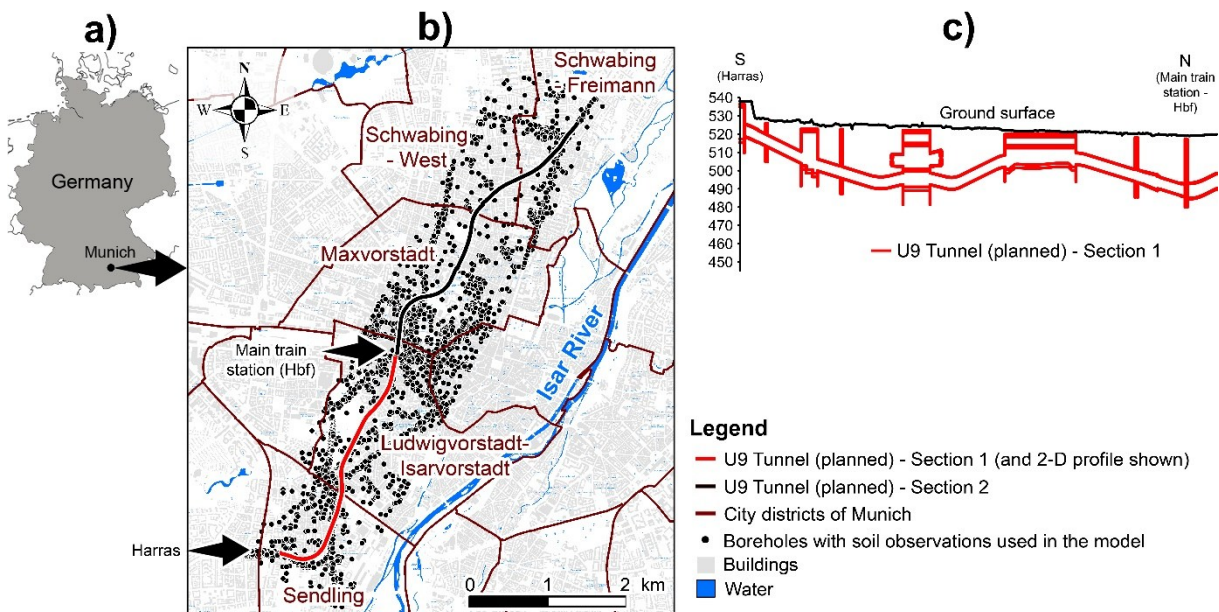


Fig. 61: Setting in the U9 Subway Tunnel in Munich: **a)** Location map; **b)** Planned tunnel course and borehole data used for geological 3-D modeling; **c)** Schematic 2-D profile of section 1 of tunnel's course

The main objective of this work is to investigate the geological and hydrogeological conditions in the vicinity of the course of the planned U9 Tunnel. The specific goals include: *i)* the creation of a high-resolution 3-D geo-model to improve the prediction capability of the characteristics of the sediments, *ii)* the determination of the reservoir architecture, *iii)* the itemization of the existing piezometers in the area for further groundwater monitoring, and *iv)* the optimization of the drilling program to increase confidence at the next construction phases.

The D_i models method was applied in the vicinity of the planned tunnel course in an area of 10 km² and a maximum depth of ~150 m below ground surface. The selected grid size was 25 x 25 x 0.5 m and 3,620 boreholes with soil observations were used (see black dots in Fig. 61b). The model provides three simulated fractions at grain-sizes limits between 0.001-0.063 mm (silt and clay), 0.063-2 mm (sand), and 2-63 mm (gravel), and a constant step in the GSD of 10% was fixed.

The geological 3-D model of the most dominant grain size classes in the sediment mixture and the resulting reservoir architecture are shown in Fig. 62a and b, respectively.

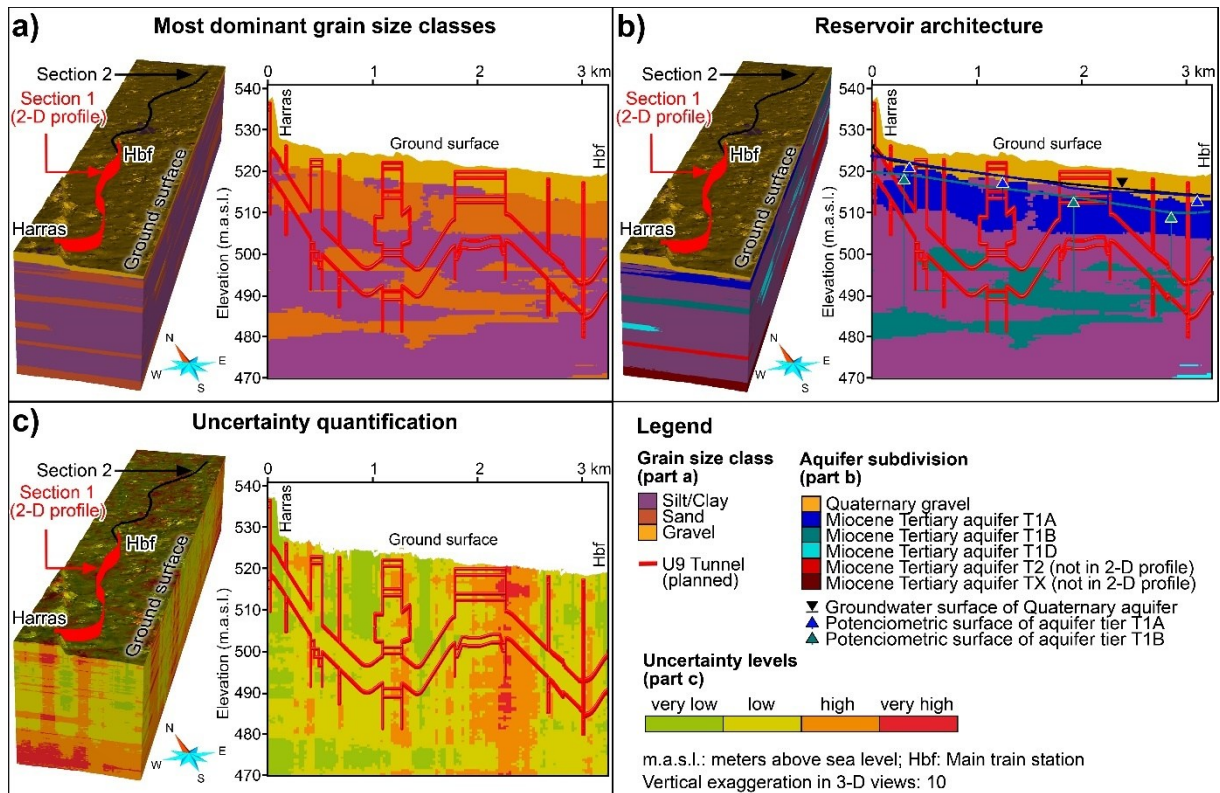


Fig. 62: Geological 3-D model in the U9 Subway Tunnel: 3-D distribution (left panel) and 2-D profile (right panel): **a)** Most dominant grain size classes; **b)** Reservoir architecture; **c)** Uncertainty quantification

The geological conditions simulated in the vicinity of the planned tunnel are exemplarily discussed here using a 2-D profile for the first section of the tunnel located between the district of Harras and the main train station (see at right of Fig. 62a-b). From south to north, the U9 Tunnel will first be drilled in Quaternary gravels at a high groundwater level (see Fig. 62a-b). Except for the heading, the tunnel will be excavated for most of its route passing through two different Miocene sandy formations, i.e., T1A and T1B, as shown in Fig. 62b. Both formations are separated by a 5-10 m thick clayed and silty impermeable layer throughout the profile at depths of approximately 20 m below ground (see Fig. 62b). Underneath various sandy bodies were simulated in depths greater than 45 m, i.e., 475 m.a.s.l. The project will not penetrate these aquifers, namely, T1D, T2, and TX (see Fig. 62b). Compared to T1A, which has a relatively constant thickness of ~10 m along the 2-D profile and is only locally confined, the T1B formation has a

highly variable thickness and lateral continuity. Besides, T1B is under confined conditions (Fig. 62b).

The 3-D geo-model was also used to identify the most suitable regions for new drilling. The UQ supports the decision-making process for identifying the areas with relatively high uncertainties regarding the lithological composition. These areas are proposed as preferred drilling targets along the tunnel route, thus reducing uncertainty and optimizing the amount of drilling required. The uncertainty model is given in Fig. 62c. The 3-D geo-model was also used to itemize the piezometers in the area in groups of water-bearing geological formations. The installation of piezometers in existing and newly drilled boreholes enables monitoring of the hydraulic heads in separate aquifers. An itemization of the well-screen segments based on the water-bearing formations where they are set should precede any groundwater monitoring if the hydrogeological conditions are well-known, which is not always the case. This knowledge is critical to determine the directions of groundwater flow for each aquifer separately.

8.1.3 Case study: Groundwater model calibration using 3-D K fields in Munich

The estimation of local-dependent values for K exposed in Chapter 6 has also been found to be applicable in calibrating numerical groundwater models. In this sense, within the Geo.KW project, a large-scale 3-D groundwater model was developed to improve the efficiency of thermal groundwater use in urban environments, specifically in the city of Munich (Böttcher, 2024; Zosseder et al., 2022a, 2020). This model is employed to describe the flow and heat transport in the Quaternary aquifer in the city of Munich by numerical simulation. The calibration process of the model aims at modifying the input data to increase the accuracy of the observed data, and its effectiveness is the most challenging for simulating the hydraulic head (Rabemaharitra et al., 2022). The numerical model requires a continuous 2-D K field of the aquifer under study whose spatial calibration represents the most critical step in the groundwater model calibration (Zosseder et al., 2022a). However, K constitutes a very sensitive parameter and it is only known at locations with pumping-test data. The calibration of the K field has to tackle the problem of introducing as much detailed information as possible about the local fluctuations of K while reducing the possible impacts of this sensitive parameter. The Geo.KW project addressed this issue and used the software package PEST (Model-Independent Parameter Estimation) (Doherty, 2003) for automated model calibration. PEST uses the pilot point technique, which introduces pilot points, i.e., discrete points distributed across the domain, assigns K values, and subsequently reproduces real hydraulic head measurements. K values from pumping tests were first assigned to the pilot points. The remaining regular pilot points lacked information on the K field and there are no set guidelines for how this attribution can be optimized. After this process, an interpolation takes place between the pilot points.

To optimize the model calibration, the remaining pilot points were assigned with the information provided by the 3-D geo-model of Munich (Chapter 4). This is shown schematically in Fig. 63.

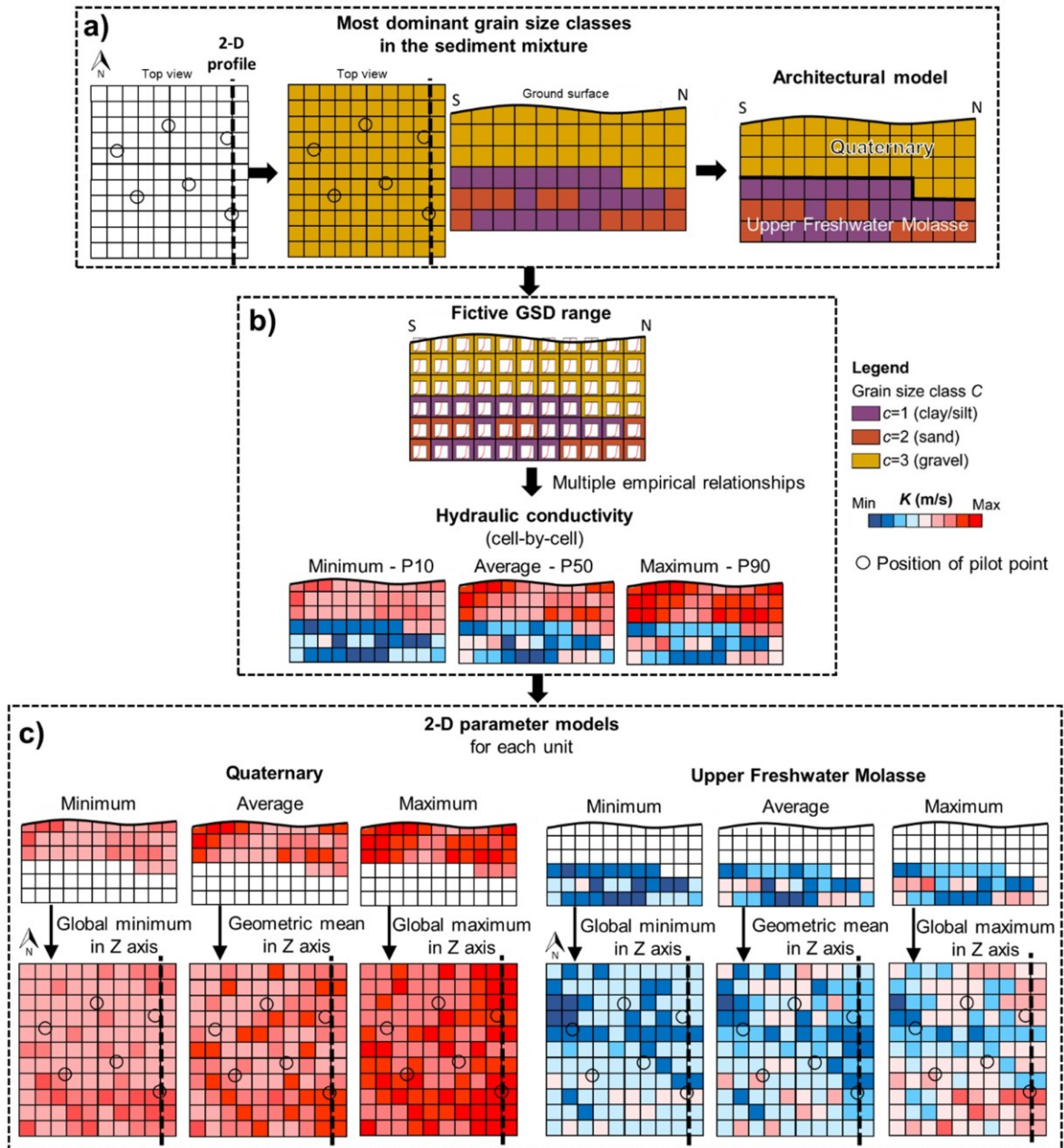


Fig. 63: Deriving fluctuations of K from the 3-D geo-model for groundwater model calibration: **a)** Results from simulation after applying the D_i models method and stratigraphic units shown at top view and in a 2-D profile; **b)** Fictive GSD range and 3-D K field at every location; **c)** 2-D K fields for assigning a preferred value and the variation range of K at the location of each pilot point

The use of the D_i models method enables deriving a fictive GSD range and a multiple estimation of K by using various empirical relationships at each location (Chapter 6 and Fig. 63a-b). This ultimately provides a high-resolution estimation of the range of K (Fig. 63b), which is used to calibrate the 2-D K field in the groundwater model. If domain subdivisions are available, as in the case of the city of Munich (see at the right of Fig. 63a), the need for a 2-D K field made specifically for the Quaternary aquifer is addressed by considering the set of underlying cells in this unit. The vertical cells forming voxel stacks covering the extension of the aquifer can be aggregated to determine the total variation of K in the Quaternary unit, as shown at the left of Fig. 63c. The

calibration of the groundwater model used the geometric mean at the location of each pilot point as the preferred value (Fig. 63c). The global minimum and maximum value from the collection of all empirical results and cells in the Quaternary was used to define the variation range, as shown at the left of Fig. 63c. Moreover, the same procedure was implemented in the Upper Freshwater Molasse, as shown at the right of Fig. 63c. This enables the integration of the contribution of K from the Miocene formations into the so-called geological window structures. As exposed in Chapter 1.3, a vertical groundwater flow and connectivity of the Quaternary aquifer with the underlying Miocene sequences may occur in these areas. Further details of the groundwater model calibration in the Geo.GW project are given in Zosseder et al. (2022a) and Böttcher (2024). The research findings of this thesis lead to an optimization of the groundwater model calibration using pilot plots. The use of the 3-D K fields derived from the D_i models method was intended to account for the fluctuation band of the intra-zonal hydraulic conductivity heterogeneity using pilot points, in order to get an acceptable fit between observed and simulated heads.

8.1.4 Case study: Optimizing the reservoir architecture in the city of Augsburg

The thesis findings also found various applications in the geological settings of the city of Augsburg and the Low Lech Valley, respectively, as part of the GeoSPOT project (2020 - 2023). While this chapter concentrates on the geological 3-D model in the city of Augsburg (see solid red line, Fig. 64b), Chapter 8.1.5 focuses on a wider area stretching over approximately 60 km between Landsberg am Lech in the south and the Danube in the north (see dashed red line, Fig. 64b).

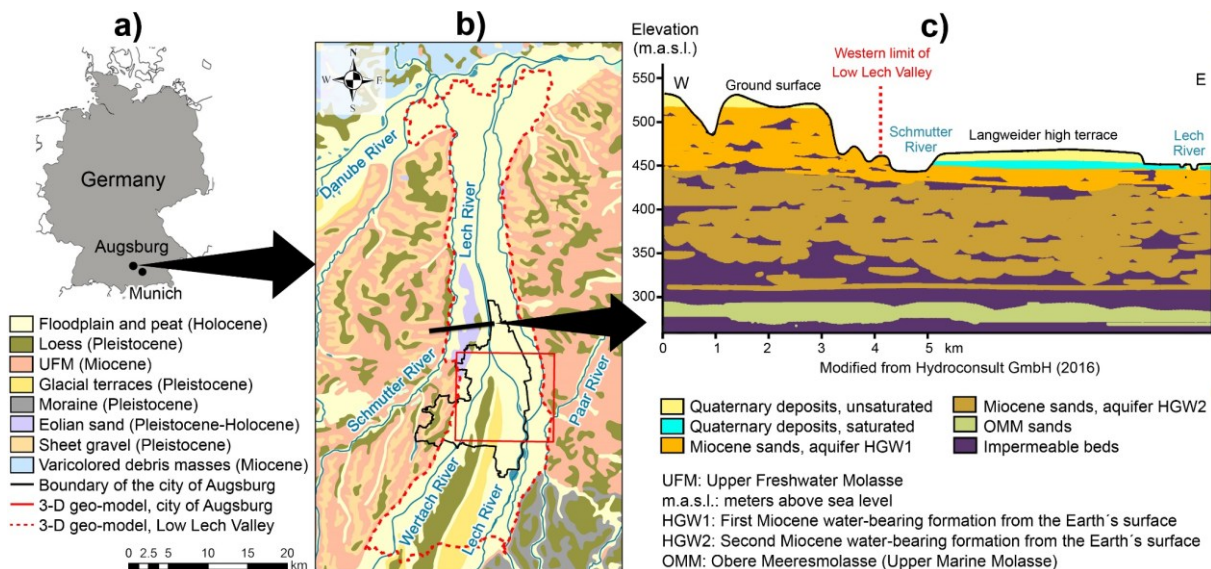


Fig. 64: Geological setting in the city of Augsburg and the Low Lech Valley: **a)** Location map; **b)** Simplified geological map and domains for 3-D models; **c)** Schematic geological profile (modified after HydroConsult GmbH, 2016)

With ~300,000 inhabitants and an area of 147 km², the city of Augsburg is located in southwestern Bavaria in Germany, about 35 km north-west of Munich (see Fig. 64a). The city lies in the Low

Lech Valley in the Northern Alpine Foreland at the convergence of the Alpine rivers Lech and Wertach. A simplified geological map is given in Fig. 64b. The morphological architecture in this valley is characterized by Quaternary terraces formed by terrace levels related to the Pleistocene glaciations and modern Holocene sediments (Schielein et al., 2011). The Quaternary glacio-fluvial deposits constitute significant groundwater resources used mainly for industrial and domestic water supply, as well as for GWHP in open-loop geothermal systems. Sandy and clayed sediments of the UFM of Miocene age underlie these deposits, and outcrop on both sides of the valley (see Fig. 64b-c). However, the deeper UFM aquifers are mainly used for drinking, brewing, and emergency water supply. Although studies have highlighted the interconnectedness between the Quaternary and the underlying Miocene water-bearing formations (HydroConsult GmbH (2016, 2003)), the reservoir architecture and geometries of the complex multi-layer shallow aquifer system and the deeper formations represented schematically in Fig. 64c have not been addressed yet in detail in 3-D. This, together with the existence of the above-mentioned competing subsurface functions and the high potential growth of the groundwater uses in the area due to the dense residential and industrial land use, necessitates a better understanding of the subsurface conditions leading to improved regional aquifer management.

The specific objectives were: *i*) the determination of the reservoir architecture of the water-bearing formations in the city of Augsburg, with a special focus on the connectivity between the Quaternary and the Miocene aquifers, and *ii*) the quantification of the associated uncertainty.

A 3-D geo-model was built based on 3,000 boreholes with soil observations. Herein, a grid was constructed with a resolution of 25 by 25 m aerially and 0.5 m vertically in the Quaternary, and a resolution of 100 x 100 x 2 m in the Miocene. The model provides three ($C=3$) simulated fractions, i.e., silt/clay, sand, and gravel. As mentioned in previous 3-D geo-models, a constant step in the GSD of 10% was defined. Fig. 65 shows the results obtained for the most dominant grain fractions (see left panel of Fig. 65) and the UQ (see right panel of Fig. 65) up to a depth of 225 m.a.s.l.

The near-surface Quaternary was simulated with higher confidence than the UFM (see blue-green colors in the Quaternary compared to the red color in the UFM in the right panel of Fig. 65a). However, the Augsburg high terrace, indicated by ① in Fig. 65a, is an exception due to the higher heterogeneity of the Riss deposits, which is in line with Landmeyer (2019). The distribution of uncertainties in the UFM clearly shows that a higher borehole density leads to a lower uncertainty, as shown at the top of the UFM marked by ② in Fig. 65a (right panel) and across the 2-D profiles AA' and BB' in Fig. 65b and c (right panel). In addition, the stronger pixel effect shown in the distribution of grain fractions in some areas, such as ⑤ in Fig. 65c (left panel), indicates a higher randomness in the prediction and is, thus, associated with a higher degree of uncertainty (see ⑤ in the right panel of Fig. 65c). Positions marked by ③ and ④ in Fig. 65b-c are subject to a higher uncertainty explained by the unexpected presence of gravel in one borehole log at depths of 181-215 m below ground level. Fig. 66 provides an overview of the reservoir architecture obtained in the UFM by including the uncertainty linked to the prediction.

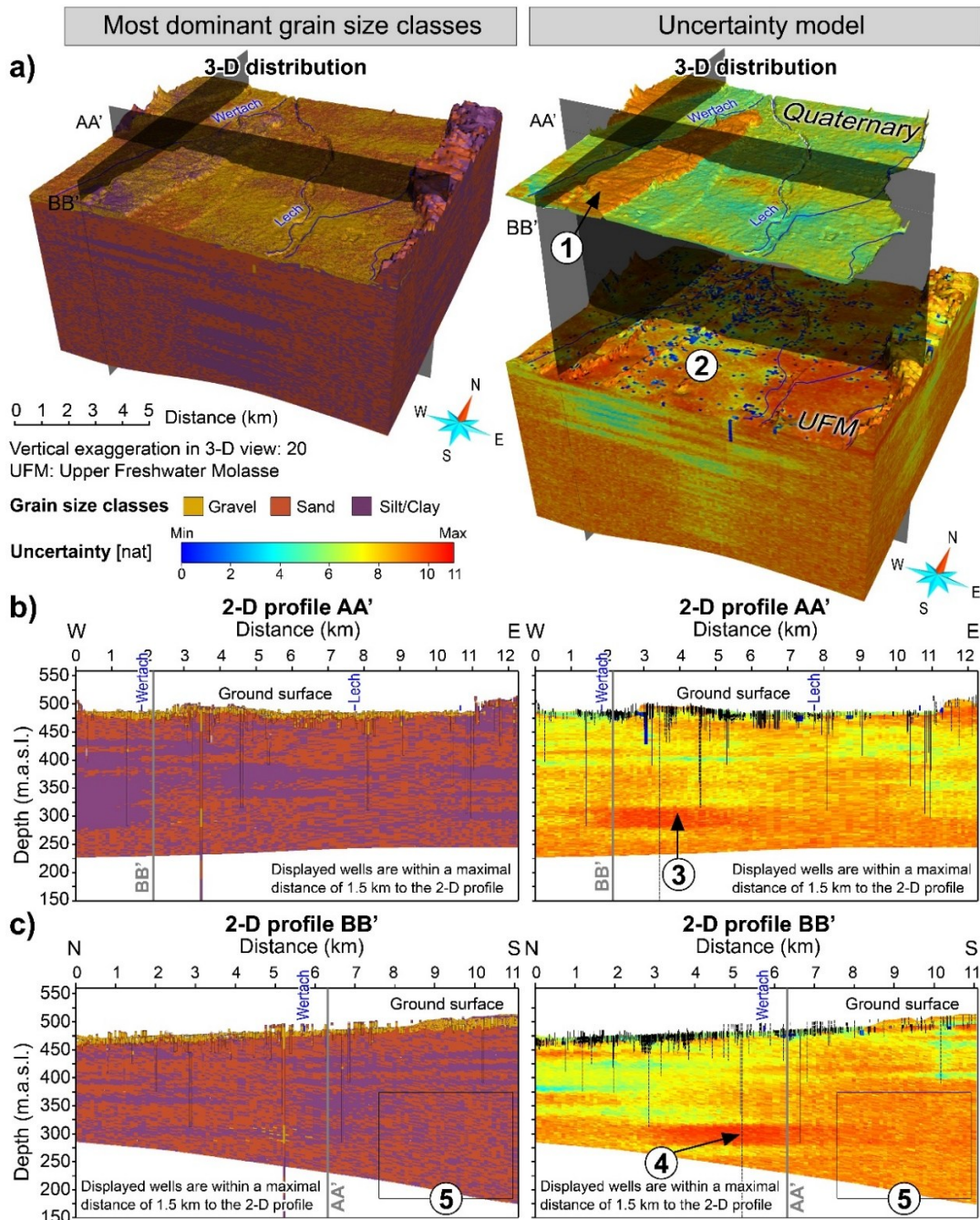


Fig. 65: Geological 3-D model in the city of Augsburg: Most dominant grain size classes (left panel) and uncertainty model (right panel): **a)** 3-D spatial distribution; **b)** 2-D profile AA'; **c)** 2-D profile BB'

Fig. 66a shows that almost the whole area at the top altitude of the Miocene is formed by sandy UFM formations, thus suggesting a connectivity between the Quaternary and the underlying Miocene aquifers. The combination of the information related to uncertainties with the distribution of the most dominant grain fractions is given in Fig. 66b. Focused exclusively on the certain areas (see lithologies shown in light colors in Fig. 66b), the analysis of the geometries of the main geological features and their interactions resulted in four coarse-grained formations separated by fine-grained successions in the UFM, termed as T1A, T1B, T2, and T3-OMM (Fig. 66c).

Thus, Fig. 66c reveals a high degree of certainty interconnectivity between the Quaternary aquifer and large parts of the highest UFM aquifer, i.e., the water-bearing T1A formation. Thus, the application of the D_i models and the subsequent integration of the UQ provides a more realistic assessment of the aquifer geometries, their spatial relationships, and interactions, which provide useful insights for improving the regional hydrogeological management.

8.1.5 Case study: Estimating spatial aquifer parameters for assessing the shallow geothermal potential in a multi-layered aquifer in the Low Lech Valley

As exposed in Chapter 8.1.4, the 3-D geo-model in Augsburg revealed the presence of isolated and non-laterally-extensive aquitards below the Quaternary, thus leading to an area-wide interconnection between the Quaternary water-saturated gravels and the underlying water-bearing UFM sands. As such, the geological window structures are not local effects but rather are found almost over the whole area. This is clearly seen in the distribution of lithologies in the top view of the Miocene in Fig. 66a. This is highly relevant in terms of resource management challenges. In their application of the EU water policy in every Member State in each river basin district, the regional water authorities implement measures promoting the long-term protection of water resources (European Parliament, 2000; StMUV, 2014). In the particular case of Germany, some of the factors limiting the groundwater use are the exclusion of restricted areas, i.e., water and spring protection areas, and a drilling depth limit (Born et al., 2022; LfU, 2009). The latter restriction of the drilling depth, abbreviated as RDD (Tissen et al., 2019), aims to protect the underlying aquifers from pollutant inputs and anthropogenic alterations in the shallow aquifer. Thus, the RDD is usually limited to the low-permeability upper substratum underlying the shallow aquifer, thus acting as a confining layer (LfU, 2009).

As such, the drilling length and, ultimately, the potential for underground uses are limited. If the geological conditions are sufficiently known and a continuous substratum underlies the uppermost Quaternary aquifer, the stratigraphic contact can be assumed as the RDD, and, thus, as the aquifer basis for potential assessments (Albarrán-Ordás and Zosseder, 2020; Böttcher et al., 2019). However, the stratigraphic contacts lose their practical value if the Quaternary aquifer is extensively underlain by permeable formations of the next stratigraphic unit. Herein, both units can be considered partially as a multi-layered aquifer system, which is lithologically vertically zoned, and the RDD depends solely on the aquifer geometries controlled by small-scale lithological heterogeneities. The greatest source of uncertainty in assessing the geothermal potential for GWHP stems from the spatial information on K and the aquifer basis (Böttcher, 2024). As we can see, this issue is even magnified in presence of multi-layered aquifers. In addition, the city of Augsburg has reported an extremely varying distribution of groundwater in the shallow aquifer. The presence of areas having very high thicknesses of groundwater contrasts with areas having very little or no groundwater resources at very short distances.

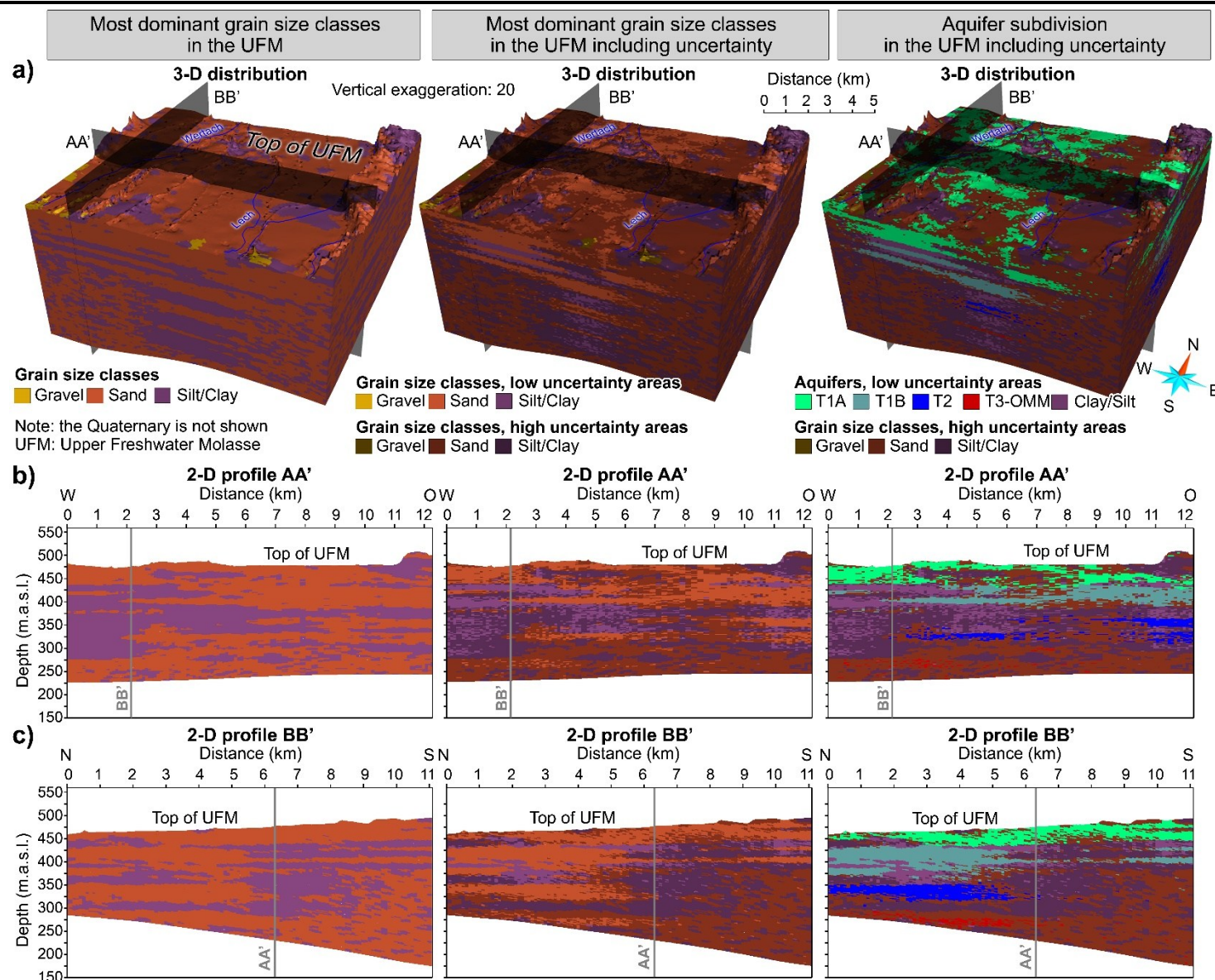


Fig. 66: Geological 3-D model in the city of Augsburg. Most dominant grain size classes (left panel), including UQ (center panel), and reservoir architecture including UQ in the Miocene sequences (right panel): **a)** 3-D spatial distribution; **b)** 2-D profile AA'; **c)** 2-D profile BB'

In view of the above, the research objectives were: *i)* determination of the reservoir architecture in the Low Lech Valley, *ii)* determination of the RDD defining the maximum allowed drilling depth in the aquifer in accordance with current regulations from regional water authorities, and *iii)* estimation of the aquifer parameters needed for assessing the geothermal potential for GWHP in a multi-layered aquifer system with significant vertical lithological changes.

The Low Lech Valley is located north of the Alps and stretches over approximately 60 km in the districts of Augsburg, city of Augsburg, Donau-Ries, Landsberg am Lech, and Aichach-Friedberg in Germany. The city of Augsburg is situated at the confluence of the Lech and Wertach rivers in the middle of this extensively stretched area, serving as a major urban center. The Low Lech Valley, around 660 km² large, encompasses the vast valley plains of the rivers Lech and Wertach between Landsberg am Lech in the South and the confluence of the Lech into the Danube in the North (see dashed line in red in Fig. 64b). The demarcation is based on the degree of relief of the landscape, which is higher south of the boundary than north of it.

A geological 3-D model was created with the D_i models method using the information provided by ~7,500 boreholes with soil observations. The resolution of the grid was 100 by 100 m aerially and 1 m vertically and three simulated fractions were defined, i.e., silt/clay, sand, and gravel.

Fig. 67 and Fig. 68 show the results obtained by means of a 3-D view and two exemplary cross sections along a north-south transect, i.e., 2-D profile AA', and a west-east transect, i.e., 2-D profile BB', across the Low Lech Valley. The 3-D lithological composition in the left panel of Fig. 67 shows clearly the presence of gravels in the high terraces of glacial age oriented in the north-south direction (see ①, ②, and ③ in Fig. 67) along the valley, which are covered by fine-grained loess and eolian sand deposits of few meters (see Fig. 67a, left panel). The low terraces of the Lech, Wertach, and Schmutter rivers stretch along the valley and are mainly formed by gravelly deposits, becoming more sandy north of Augsburg (see ④ in the left panel of Fig. 67a). This is due to the change into the Lech-Moisach mixed facies dominated by gravels in a sandy matrix (Schellmann et al., 2016; Schreiber, 1985). This makes it increasingly difficult to achieve lithological differentiation between the Quaternary and the UFM sediments in this area. In addition, as we can see along the 2-D profiles presented in the left panel of Fig. 67b-c, the uppermost Quaternary sediments and the underlying UFM sands are seldom separated by a fine-grained succession, thus leading to an interconnectedness of water-bearing Quaternary and UFM permeable deposits in most areas. The reservoir architecture shown in the middle left panel of Fig. 67 reveals an interbedded system of aquifers separated by aquitards. The permeable formations consist of an uppermost gravelly and sandy multi-layered aquifer system (see aquifer shown in green and light blue along the 2-D profiles in the middle left panel of Fig. 67b-c), and the deeper T1B, T2, and T3-OMM aquifers (see aquifers shown dark blue and red in the middle left panel of Fig. 67b-c). Based on this aquifer subdivision, geological window structures between aquifers were identified and mapped, and an itemization of ~2,400 well screens in the area was carried out in order to selectively group the groundwater measurements together for each

aquifer. In the absence of a continuous confining layer underlying the shallow aquifer, the uppermost aquitard is given by the simulated uppermost clay or silt in the 3-D model, representing the RDD according to the regional water authority regulations. The resulting RDD from the 3-D geo-model is shown in the middle right panel of Fig. 67. Subsequently, the saturated thickness of the groundwater in the shallow aquifer up to the RDD was calculated from the groundwater table and the RDD allowed in the shallow aquifer, inferred from the geological 3-D model, as shown in the right panel of Fig. 67.

The saturated thickness of the aquifer, the depth of the top of the aquitard, and the thickness distribution of the fine-grained intercalations within the uppermost aquifer were mapped for the whole Low Lech Valley and are represented in Fig. 93a, b, and c of Appendix F. As shown in the middle right panel of Fig. 67 and in Fig. 93a, the RDD constitutes an uneven boundary. This is due to the irregular presence of the low-permeability upper substratum at varying depths. The differential erosion of the UFM sediments causes the fine-grained intercalations to pinch out extensively in the valley (see white areas in Fig. 93 of Appendix F). This results in an extremely variable distribution of saturated aquifer thickness in the shallow aquifer, thus revealing a very heterogeneous potential for groundwater extraction (see ⑤ to ⑨ in the right panel of Fig. 67b-c and in Fig. 93b of Appendix F).

In terms of the parameter estimation for assessing the potential of shallow geothermal energy for GWHP, the horizontal equivalent K in the uppermost aquifer was also calculated. For this purpose, first, the K -values at each grid cell of the 3-D geo-model, down to a depth of 200 m.a.s.l., were estimated as exposed in Chapter 6. The expected range of K is provided using a conservative (P10, 10th percentile, see Fig. 68a), an average (P50, 50th percentile, see Fig. 68b), and an optimistic estimate (P90, 90th percentile, see Fig. 68c). Subsequently, the horizontal equivalent K values were calculated in the entire uppermost aquifer by adapting Eq. (49) to the aquifer case as follows:

$$K_{xeq,aquifer} = \sum_{v=0}^{N_{v,aquifer}} \frac{K_{predicted,v,aquifer} \times m_{v,aquifer}}{m_{aquifer}}. \quad (54)$$

where $m_{v,aquifer}$ is the thickness of each voxel v with permeable material vertically within the aquifer, $m_{aquifer}$ is the saturated aquifer thickness, and $N_{v,aquifer}$ is the number of voxels vertically within the aquifer. The distribution of the horizontal equivalent K values is shown in Fig. 94.

The results of the present case provides a detailed characterization of a complex multi-layer aquifer system with vertical lithological changes in regards to their groundwater management. Both the spatial variations of subsurface properties and the spatial restrictions in accordance with current regulations from regional water authorities are taken into account in order to estimate the parameters required for assessing the potential of shallow geothermal energy for GWHP.

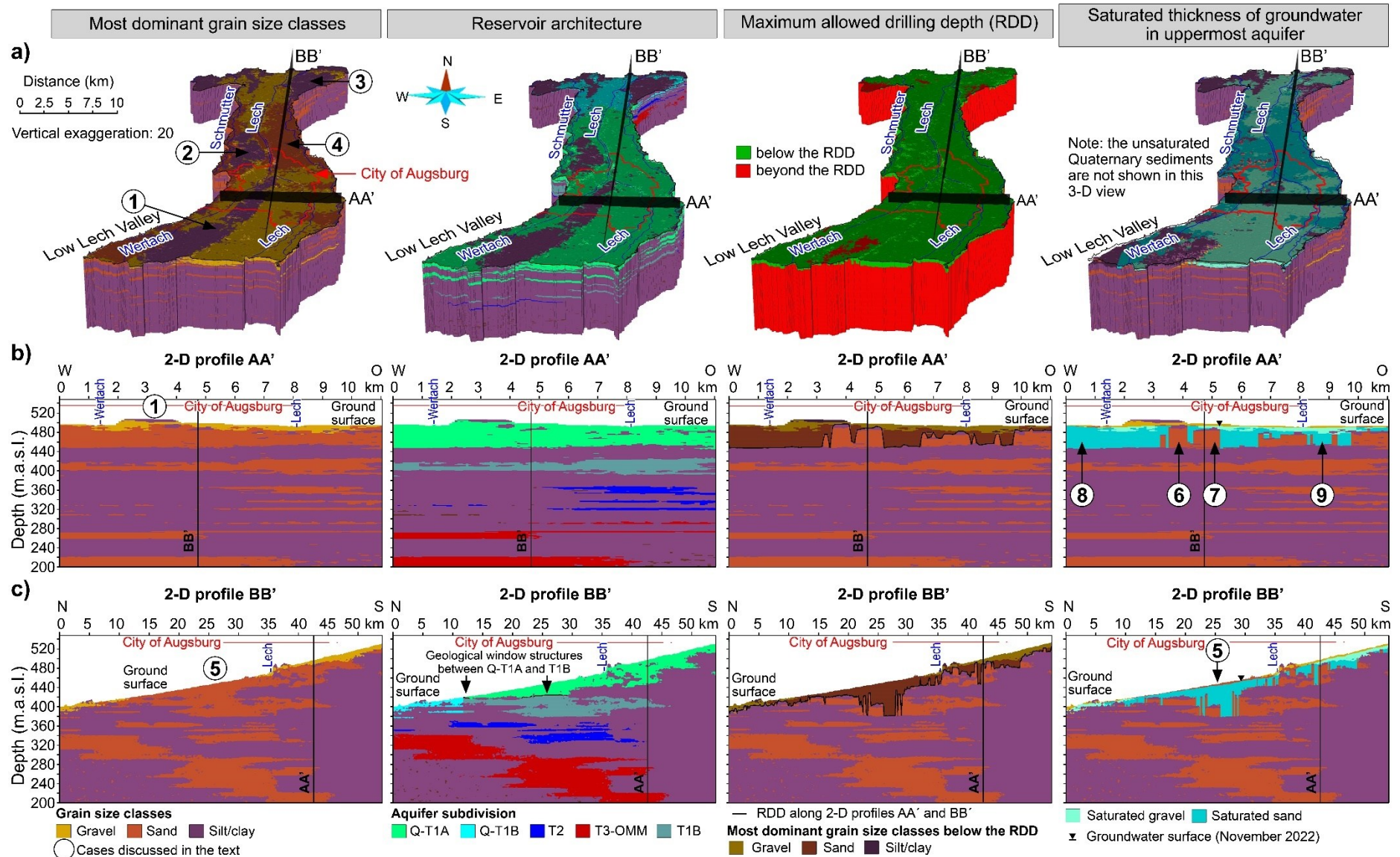


Fig. 67: Geological 3-D model in the Low Lech Valley. Most dominant grain size classes (left panel), reservoir architecture (middle left panel), RDD (middle right panel), and saturated thickness of groundwater in uppermost aquifer (right panel): **a)** 3-D spatial distribution; **b)** 2-D profile AA'; **c)** 2-D profile BB'

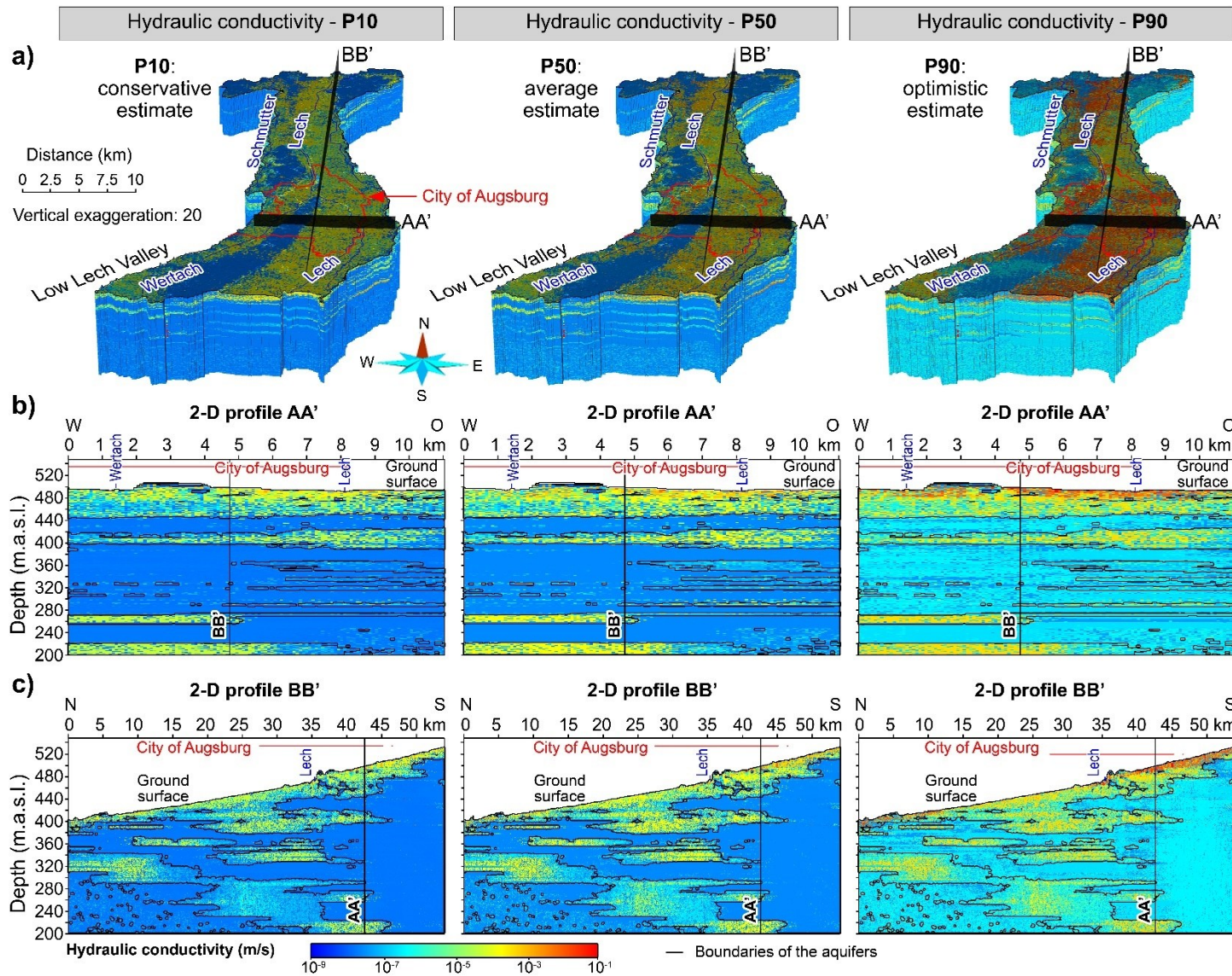


Fig. 68: Estimated 3-D hydraulic conductivity fields in the Low Lech Valley: conservative estimate (P10, 10th percentile) (left panel), average estimate (P50, 50th percentile) (center panel), and optimistic estimate (P90, 90th percentile) (left panel): **a)** 3-D spatial distribution; **b)** 2-D profile AA'; **c)** 2-D profile BB'

8.2 Discussion of main findings

The main contributions of this thesis are directly linked to the proposed research hypothesis exposed in Chapter 3 and can be summarized by the following four points:

8.2.1 Development of a 3-D novel approach simulating fictive grain size distributions: the D_i models method

The heart of the conducted research relies on the first research hypothesis: predicting the essential features of the natural heterogeneity of unconsolidated sediments by means of a fictive GSD preserving geological realism. The 3-D novel approach has been successfully applied across five case study areas. The cases include the city of Munich and the settings presented in Chapter 8.1, i.e., the Starnberg Road Tunnel, the U9 Subway Tunnel, the city of Augsburg, and the Low Lech Valley, all in Germany. The approach implements SIS for every selected cumulative frequency of the GSD, proposing categorizing heterogeneities at a grain-size scale at three levels. The first level addresses including all coded information contained in the input data used, i.e., direct soil observations from drilled materials, susceptible to being part of unconsolidated deposits. This includes major and minor components in the sediment mixture and is preceded by an intensive quality control, plausibility analysis and homogenization. The second level allows the modeler to define a user-defined number of grain fractions to be simulated. The third level fixes the number of cumulative frequencies of the GSD to be simulated. The resulted simulated grain size range represents a significant improvement in predicting the geological reality of highly non-constant mixtures of particles of different grain sizes compared to categorical schemes based on gross lithologies (Hademenos et al., 2019; Kearsley et al., 2015; Stafleu et al., 2011), lithofacies (Bianchi et al., 2011; Høyer et al., 2015; Jørgensen et al., 2010; Stafleu et al., 2011), hydrofacies (Comunian et al., 2011), geotechnical (Khojasteh, 2013), and lithostratigraphic schemes (Hademenos et al., 2019; Høyer et al., 2015; Merritt et al., 2007; Royse, 2010; Stafleu et al., 2011).

However, three limitations of the design of this approach must be highlighted. First, the gradual variation of clast mixtures is simulated in 3-D considering only a certain number of grain fractions and cumulative frequencies of the GSD. Although technically possible, addressing an unrealistic high number of grain fractions and cumulative frequencies within the geostatistical framework results in an overly arduous process. This is overcome by a log-cubic interpolation (PCHIP) to achieve completeness and accuracy in the fictive GSD. Despite this, the validation schemes carried out, i.e., the cross-validation procedure (Chapter 4.5) and the comparison of fictive GSD against real GSD from sieving (Chapter 6.2.2.2), revealed a strong prediction ability. Second, the incorporation of 3-D categorical trend models in the D_i models method, and especially the trend evaluation, is a laborious process and can pose some difficulties when dealing with large 3-D models combined with complex conceptual models (Chapter 5.5). Lastly, the approach strongly benefits from the level of detail of the soil observations. As such, in the absence of grain-size-based soil observations, the approach loses its innovative added value of simulating gradual variations

of clast mixtures, and other categorization schemes, such as classifications based on lithofacies or gross lithologies (Chapter 2.2.3), may be considered instead.

8.2.2 Reinterpretation of coded soil observation data as fictive GSD

The hypothesis concerning the reinterpretation of drilling descriptions is confirmed by addressing the interpretation of the semi-quantitative and qualitative descriptions of direct soil observations from drilled materials described in the field, i.e., sequences of symbols marking the soil, according to the standards for soil description in a way that addresses the grain-size-based heterogeneities and integrates uncertainties associated with imprecise input data. This is achieved by identifying the observed grain sizes, quantifying their proportion ranges (%), and finally capturing the lower and upper limits of the fictive GSD of the clastic sediments inferred from the soil observations.

The reinterpretation is initially conceived for soil observations described in the field according to the standards for soil description used in Bavaria (Germany) (DIN EN ISO 14688-1, 2020; DIN EN ISO 14688-2, 2020). Although adapting this process to other federal or national standards is feasible, it poses some constraints due to the considerable time and effort required, especially the quality control and plausibility analysis. This has become evident in another case study not addressed in this thesis, i.e., the 3D-GeoModell Berlin project. Within this ongoing four-year project, the Chair of Hydrogeology focuses on building a geological 3-D model in the city of Berlin (Germany) based on a borehole database with different standards for soil description (LBEG, 2011; NLfB, 2002). Thus, requiring all drilling data from ground investigations to be reported and incentivizing the subsurface data sharing and standardization in soil description at the federal and national levels would enable using the approach across borders in unconsolidated deposits in vast areas. The findings of this thesis strongly unlock the value of the subsurface data, in particular, borehole records from ground investigations. In addition, as mentioned in Chapter 8.2.1, the reinterpretation procedure also strongly benefits from the level of detail of the soil observations.

8.2.3 Uncertainty integration from input data using fictive GSD and UQ measures

This section discusses the main contributions achieved in the research of the hypothesis related to the uncertainty integration in the geo-modeling process as well as the development of UQ measures for sediment mixtures. The interpretation of soil observations as grain-size ranges delimited by a lower and upper fictive GSD implies introducing some degree of lithological noise inferred from the soil observations, which is conceptually consistent with model perturbations in structural models (Wellmann and Caumon, 2018). This ensures the integration of uncertainties associated with imprecise input data, thus avoiding uncertainty underestimation, as highlighted by Bárdossy and Fodor (2004). This idea is incorporated into the 3-D geostatistical framework for simulating the fictive GSD, which overcomes potential bias caused by ignoring imprecise input data, thus providing a more realistic uncertainty assessment. This was demonstrated in Chapter

5 and confirms the hypothesis regarding the uncertainty integration and propagation presented in Chapter 3.2.

Furthermore, the hypothesis associated with the UQ was equally validated by applying the concepts of entropy and joint entropy for UQ of the main outputs of the D_i models method. This is in line with the research need indicated by Wellmann and Caumon (2018) to develop UQ frameworks that integrate various possible model scenarios with stochastic simulations. The UQ measures provide very useful scalar measures for quantifying local uncertainties and for comparison purposes, as demonstrated in the simulation conducted in a domain located in the city of Munich (Chapter 6) and in the settings of the U9 Subway Tunnel (Chapter 8.1.2) and the city of Augsburg (Chapter 8.1.4). However, the entropy-based UQ measures presented in Chapter 5 and the case study in Chapter 8.1.4 use natural units (nats) as the calculation units. Although these calculation units are mathematically correct, the choice of binary digits (bits), which are directly tied to binary systems, may lead to more intuitive results, as the entropy value can be interpreted as the minimum number of yes/no questions required to determine the sediment mixtures.

The current approach considers the simulation of the GSD as a collection of RVs following the logical order of sieving. Since SIS is implemented independently for each cumulative frequency, it is assumed that the RVs are conditionally independent and the joint entropy is the sum of the marginal entropies. This assumption may be contrasted with the alternative interpretation that the RVs are conditionally dependent (MacKay, 2003; Stone, 2015).

8.2.4 Multiple parameter estimation and user-oriented scenario analysis based on the fictive GSD

The fourth contribution of this thesis is related to the last research hypothesis formulated in Chapter 3.3. It demonstrates the multiple parameter estimation and user-defined scenario analysis derived from estimating the full range of the fictive GSD for all voxels in the 3-D space. These aspects are crucial to estimate the different potential uses of underground space and, ultimately, to support data-driven decision-making for urban subsurface planning and sustainable management of the UUS as a multifunctional resource.

The 3-D distribution of the geological patterns defined by the fictive GSD enables defining the geometries and the spatial relationships of the geological features. On the one hand, the physical limits of aquifers and aquitards, i.e., the reservoir architecture, can be characterized in terms of their small-scale grain-size-based heterogeneities (Chapter 8.2.1), extent and thickness, as demonstrated in the settings of Munich (Chapter 4.4.6), the U9 Tunnel (Chapter 8.1.2), the city of Augsburg (Chapter 8.1.4), and the Low Lech Valley (Chapter 8.1.5). These findings support the necessary task of further characterizing the groundwater bodies to assess their use (European Parliament, 2000) and signify an advancement compared to other geo-modeling strategies whose

resulting reservoir architecture is based on gross lithologies, lithofacies, or stratigraphic units, as discussed in Chapter 8.2.1. The reservoir configuration in the city of Munich constitutes a significant step forward in improving hydrogeological knowledge in three fundamental aspects. First, this work dispels the existing doubts about the a priori arbitrary spatial distribution of sands at the top altitude of the substratum (see Fig. 4 of Chapter 1.3) (Blasy, 1974; Gebhardt, 1968; Schirm, 1968) by providing a grain-size based detailed prediction at the base of the Quaternary, which is shown in Fig. 69 and Fig. 70a. Second, it clarifies the spatial relationships of the underlying Miocene aquifers, allowing the differentiation of a main aquifer system, i.e., T1, subdivided into a complex system of aquifer tiers T1A to T1D, as well as the deeper aquifers T2-T4, which are clearly separated from the overlying aquifers (see Fig. 70b). Finally, this work highlights the connectivity of the Quaternary aquifer with different aquifer parts of the UFM in multiple areas throughout the city (see Fig. 70b).

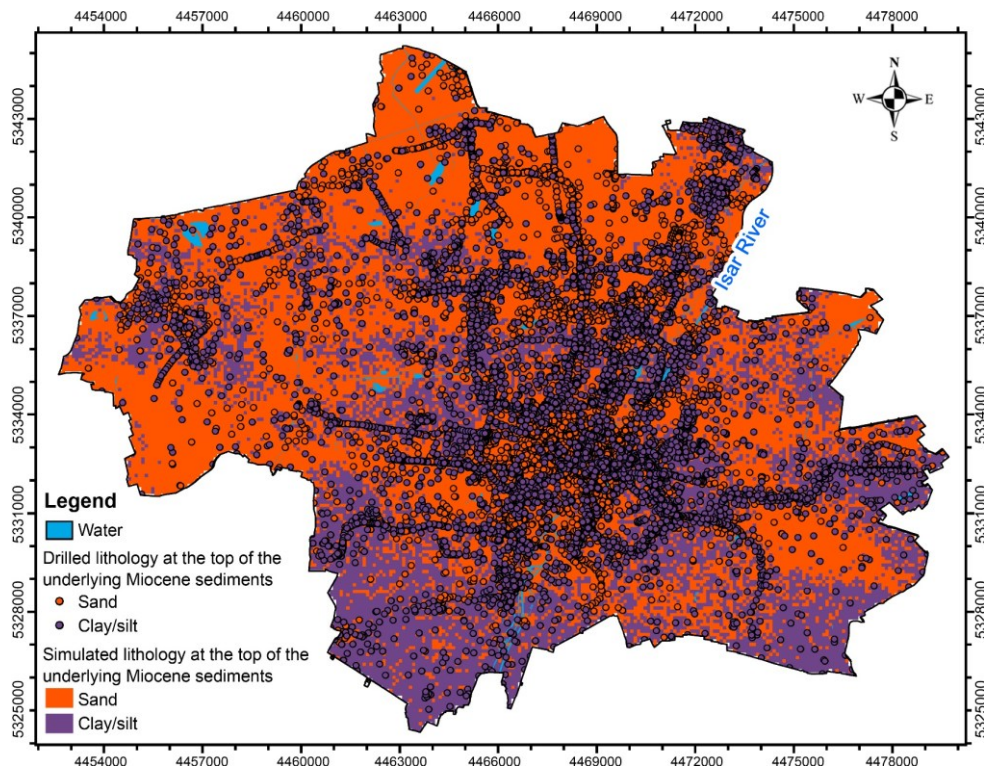


Fig. 69: Map of the distribution of most dominant grain size classes at the top of the Miocene sediments from the geological 3-D model in the city of Munich

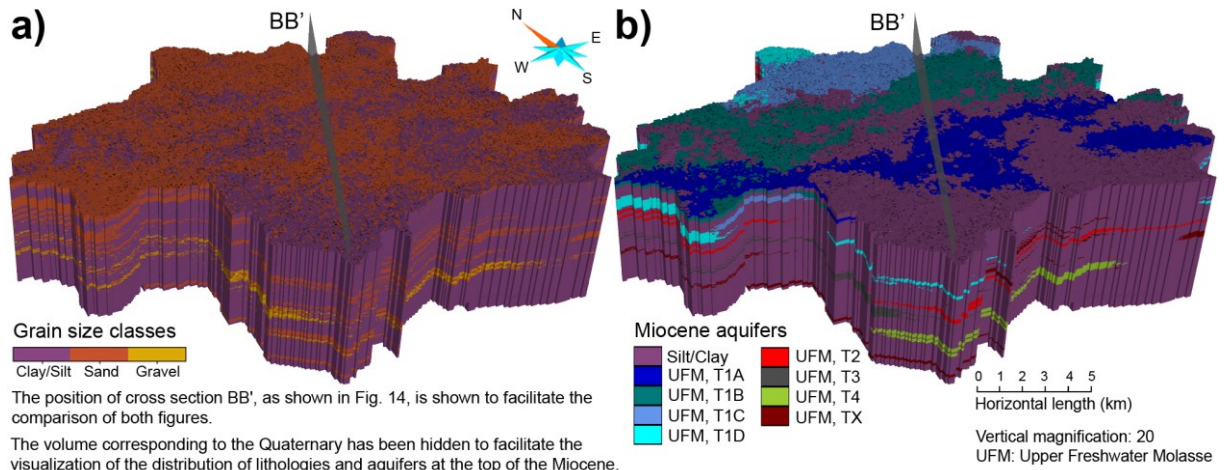


Fig. 70: 3-D views of the Miocene sediments from the geological 3-D model in the city of Munich: **a)** Most dominant grain size classes; **b)** Reservoir architecture, showing at its uppermost part the Miocene aquifers interacting with the overlying Quaternary

These findings represent a refinement over previous concepts of the reservoir architecture of the Miocene aquifers in the area, particularly the subdivision into parts of the T1 aquifer, and the ability to infer geological interaction zones between aquifers (Prösl and Anders, 2011). The reservoir configuration was qualitatively verified by considering the hydraulic head patterns existing in the subsurface (Zosseder et al., 2023, 2022b, 2019) and by integrating the hydrogeochemical characteristics of the aquifers (Chapter 7).

The geometries of the geological features may be determined based on the prediction uncertainty, as shown in Augsburg (Chapter 8.1.4), and on the expectation of a given content of a grain fraction, as shown in the predictive analysis of the dewatering demand of groundwater inflows in the Starnberg Tunnel (Chapter 8.1.1). On the other hand, the approach is particularly useful for identifying potential interconnectedness between water-bearing formations, serving as a basis for recommendation in decision-making in regional aquifer management strategies. In addition, other relevant reservoir anatomical components associated with regulatory constraints from the water authority, e.g., the restriction of the drilling depth (RDD) (Born et al., 2022; LfU, 2009), can be determined in 3-D to enhance the sustainable management of the subsurface resources (Chapter 8.1.5).

The research findings also revealed the added value of coupling the insights provided by the 3-D geo-models with knowledge gathered from other disciplines, such as hydrogeochemistry. Herein, the 3-D geo-model in the city of Munich (Chapter 4) provided a distinction of aquifers depending on the presence or absence of interaction with the overlying Quaternary shallow aquifer. The integration of hydrogeochemical groups within the involved aquifers leads to validate the separations of aquifers mentioned above (Chapter 7). This approach is highly transferable to other geological settings. However, a minimum set of representative hydrogeochemical samples is required, and discrepancies arise when long well screen lengths reach across various aquifers.

This thesis also demonstrated that estimating the fictive GSD of the sediment mixture enables deriving relevant grain-size-based soil properties in high resolution, such as K , as proven in the city of Munich (Chapter 6) and the Low Lech Valley (Chapter 8.1.5). The obtained 3-D K field in Munich preserves the variability and the central tendency of the K values obtained from pumping-test analysis in the Quaternary and Miocene aquifer systems (Egger, 1978; Exler, 1967; Gebhardt, 1968; Theel et al., 2020; Zosseder et al., 2022b). The insights obtained from estimating local-dependent K using multiple empirical relationships relating K with the grain-size property highlighted multiple applications. First, the 3-D K fields provide useful reliable information about the local fluctuation of K to calibrate numerical groundwater models (Chapter 8.1.3) and explicitly address the aquifer heterogeneity, as demanded by Zheng et al. (2011). Second, as shown in the Low Lech Valley (Chapter 8.1.5), the determination of horizontal equivalent K values vertically within aquifers enables estimating the key parameters for assessing the aquifer yields or the geothermal potential for GWHP in complex geological settings, such as multi-layer aquifer systems with strong vertical lithological changes and non-laterally-extensive aquitards. This includes the determination of the two most uncertain parameters necessary to estimate such potential, namely, K and groundwater thickness (Böttcher, 2024), whose determination based on interpolating sparse data accompanied by averaging or homogenization procedures in the presence of vertical lithological zoning presents many difficulties (de Marsily et al., 2005). Third, averaging K horizontally within the individual beds along well screens enables capturing the representativeness of aquifer heterogeneity and spatial geometries closer to the field scale, which as been reported as a limitation of K estimates based on GSD analysis from soil samples or petrographical descriptions (D'Andrea, 2001; Devlin, 2015; Schultz and Ruppel, 2002; Uma et al., 1989). This process emulates different lateral extents of the cone of depression, which can be very useful when planning water withdrawals. Despite the advantages of these developments, there are also some limitations. First, using empirical relationships may lead to an underestimation of K , as reported when using empirical methods with GSD from sieving or petrographical descriptions (Chandel and Shankar, 2021; Cheng and Chen, 2007; Fuchs, 2010; Oh et al., 2013; Vuković and Soro, 1992). The second limitation comes from the stronger presence of fine-grained sediments and highly heterogeneous clast mixtures. Those deposits raise difficulties linked to the reduced applicability of the existing empirical methods. Another point to consider is that the empirical formulas used in the thesis to relate K from the simulated grain-size range yield a scalar value, typically representing isotropic or predominantly horizontal conductivity. However, K is generally anisotropic and varies with direction and can therefore be treated as a full 3-D tensor.

CHAPTER 9**Conclusions and outlook**

The present chapter concludes highlighting the main achievements of the thesis and proposes future research and development directions.

The transition to more sustainable urban development in response to land use, geotechnical engineering challenges, climate change mitigation, decarbonization, and resource protection requires understanding the subsurface geological conditions, especially in urban areas, from a digital 3-D perspective. Achieving this requires robust prediction capabilities to generate high-quality scientific information that characterizes the geological structures and properties of unconsolidated sediments mantling nearly all cities and regions of the developing world. This characterization is a essential for assessing engineering geology constraints, evaluating sustainable energy uses, and balancing the competing and coexisting functions of the subsurface space.

This thesis makes an important contribution to enhancing 3-D prediction capabilities for unconsolidated sediments by addressing three key priorities linked to the proposed research hypothesis:

- **Prediction of small-scale grain-size-based heterogeneities in 3-D.** The findings provide valuable insights into successfully predicting the essential features of small-scale heterogeneity in unconsolidated sediments, i.e., the fictive GSD. This overcomes oversimplification issues that affect model usability.
- **Uncertainty integration and quantification.** The proposed 3-D geo-modeling framework incorporates uncertainties arising from systematic imprecisions in input data and provides robust uncertainty information about model outputs.
- **Development of a framework enabling multiple parameter estimation and user-oriented scenarios.** This thesis contributes to interdisciplinary subsurface management by providing:
 - a) Reservoir architecture insights, i.e., geometries of groundwater bodies, aquitards, and regions complying with a specific content of a grain fraction.

- b) Spatial relationships among reservoir constituents, i.e., interconnectedness among aquifers and 3-D implementation of geology-based regulatory constraints.
- c) High-resolution estimations of grain-size-based soil properties, such as K , for improved groundwater modeling and geothermal potential assessment in complex multi-layer aquifer systems. Thus, the approach is particularly useful as a base for identifying and quantifying uses in the underground space.

The research conducted across five case studies demonstrates the strong transferability of the findings to diverse geological contexts. The user-defined nature of the method enhances its adaptability to various applications, such as hydrogeological and hydrogeochemical characterization, tunnel planning, groundwater model calibration, and parameter estimation for potential assessment.

Future research directions

The following additional research and development is proposed in a variety of areas:

Further developments in grain-size-based property modeling and potential assessment

Future methodological enhancements could integrate multiple hierarchical structures to account for heterogeneity at different scales. Moreover, the use of variable cell sizes could enhance model resolution in areas of higher variability and optimize computational efficiency.

In estimating K , several research directions are proposed. First, the limitations of existing empirical methods in poorly sorted sediments can be further investigated by exploring multiple linear regression analysis between K and sediment mixture properties. However, the reference data available, i.e., K values from pumping tests, are not related to individual voxels with unique fictive GSD but to groups of voxels within a specific aquifer volume defined by the screened interval. This ultimately hinders the fitting capability of the pumping-test data on a cell-by-cell basis. Alternatively, the stochastic modeling of K in each voxel with poorly sorted sediments or the introduction of a weighting scheme according to the accuracy of the method can be implemented, if the accuracy is provided. Second, the approach also opens opportunities to combine and compare K estimates with the inverse numerical modeling of K . Third, defining horizontal and vertical anisotropy ratios—potentially through 3-D variogram analysis to assess the spatial continuity of the 3-D- K -field—would allow for the derivation of an anisotropic K tensor, enhancing predictions of groundwater flow directionality, which is particularly important for numerical modeling. Fourth, adapting vertical averaging to stratification might also be useful to assess groundwater protection potential and vulnerability to contamination. The present approach offers also possibilities for exploring the potential for estimating storage capacity for managed aquifer recharge (MAR) schemes (Dillon et al., 2009; Gale, 2005).

An ambition for future research involves expanding the applicability of the approach to other grain-size-based soil properties. This includes estimating the effective thermal conductivity λ_{eff} , to support the assessment of the geothermal potential for ground source heat pumps (GSHP) and borehole thermal energy storage (BTES), as initiated in the GeoSPOT project (2024 - 2023) (Zosseder et al., 2023) and continued in the GeoMaN project (2024 - 2027). Additionally, unconsolidated sediments are fundamental in foundation, earthwork, and earthquake engineering, requiring further investigation of their geotechnical characteristics. Research into estimating the shear wave velocity V_s , a crucial mechanical property providing the input parameters for the design of earthquake-resistant structures, based on GSD, would support assessments of seismic hazard areas through seismic microzonation, required in the geothermal energy sector, as highlighted by Bundesverband Geothermie e.V., (2017).

Coupling with other 3-D geo-modeling techniques and disciplines

In geological settings where small-scale heterogeneities cannot be represented by a fictive GSD, constructing a detailed 3-D structural model of unconsolidated and consolidated deposits becomes essential. This challenge is being addressed in the ongoing 3D-GeoModell Berlin project of the Chair of Hydrogeology. Additionally, faulted systems increase the complexity of 3-D structural modeling. This circumstance is addressed in the GeoMaN project (2024 - 2027), which focuses on constructing a geological 3-D model in the area of Nuremberg (Germany).

Furthermore, the evaluation of uncertainty correlations in a spatial context, which has been applied in structural geological modeling (Wellmann, 2013), may also be applied in the context of the modeling outputs for sediment mixtures proposed in this thesis. This line of research may provide insights into how additional information on clast mixtures at one location leads to a reduction of uncertainties in the remaining locations.

The combination of the developed 3-D novel approach with other disciplines in the future is highly desirable. As demonstrated in Munich's 3-D model, the integration of hydrogeochemistry is particularly relevant for validating the spatial relationships among the reservoir constituents. This ultimately enables providing support to regulators for facilitating the deployment of adequate resource protection measures.

The impact of climate change on groundwater level dynamics is normally assessed by analysing the time scale change patterns of the groundwater level fluctuations. The insights gained in this thesis, especially those gathered in multi-layered aquifer systems with non-uniform stratification patterns and varying fine-grained intercalations pinching out in the aquifer, strongly recommend including as much detailed information as possible about the subsurface conditions. This could improve a wider understanding of the groundwater vulnerability to groundwater-level decline within the context of the aquifer system.

Coupling of 3-D geo-models with digital twin or BIM approaches

The results of the 3-D geo-models generated in this thesis align with digital urban planning initiatives, such as Geo-CIM (Bricker et al., 2024). The data can support urban planners, users, policy-makers, regulators, and local governments through online geospatial data platforms. Making these models widely accessible will facilitate data-driven decision-making for urban sustainable subsurface planning at all levels.

The findings of this thesis provide valuable contributions to advancing 3-D subsurface modeling for sustainable urban development. By improving prediction capabilities, integrating uncertainty, and facilitating interdisciplinary applications, this research supports more informed decision-making in geological and engineering contexts.

It can be concluded that the main goal of the thesis have been successfully achieved.

References

- Admiraal, H., Cornaro, A., 2016. Why underground space should be included in urban planning policy - And how this will enhance an urban underground future. *Tunn. Undergr. Sp. Technol.* 55, 214–220. <https://doi.org/10.1016/j.tust.2015.11.013>
- Albarrán-Ordás, A., Zosseder, K., 2024. Estimation of 3-D hydraulic conductivity fields from fictive grain-size distributions obtained by geological 3-D modeling [Manuscript submitted for publication] (First submitted: 26 February 2024 / Revised submitted: 11 July 2024).
- Albarrán-Ordás, A., Zosseder, K., 2023. Uncertainties in 3-D stochastic geological modeling of fictive grain size distributions in detrital systems. *Appl. Comput. Geosci. Spec. issue Appl. 3D Geosci. Model. Artic.* 100127 19. <https://doi.org/10.1016/j.acags.2023.100127>
- Albarrán-Ordás, A., Zosseder, K., 2022. The Di models method: geological 3-D modeling of detrital systems consisting of varying grain fractions to predict the relative lithological variability for a multipurpose usability. *Bull. Eng. Geol. Environ.* 81. <https://doi.org/10.1007/s10064-021-02538-2>
- Albarrán-Ordás, A., Zosseder, K., 2020. Geostatistical relief modelling of the Quaternary aquifer basis in the Munich Gravel Plain with the use of big datasets. *Zeitschrift der Dtsch. Gesellschaft fur Geowissenschaften* 171, 1–19. <https://doi.org/10.1127/zdgg/2020/0206>
- Albarrán-Ordás, A., Zosseder, K., 2019. 3D facies modelling based on particle size distributions of borehole data. A case study of georesource management in the city of Munich, in: 5th European Meeting on 3D Geological Modelling. Bern, Switzerland.
- Alpay, O.A., 1972. A practical approach to defining reservoir heterogeneity. *J. Pet. Technol.* 1, 42–46. <https://doi.org/10.1108/eb025468>
- Alvarado Blohm, F.J., 2016. Determination of Hydraulic Conductivities through Grain-Size Analysis. Master's Thesis. Boston College University.
- Andres, G., Egger, R., 1985. A new tritium interface method for determining the recharge rate of deep groundwater in the Bavarian Molasse basin. *J. Hydrol.* 82, 27–38. [https://doi.org/10.1016/0022-1694\(85\)90044-7](https://doi.org/10.1016/0022-1694(85)90044-7)
- Appelo, C.A.J., Postma, D., 2004. *Geochemistry, groundwater and pollution*, CRC. ed. London.
- Arabkoohsar, A., 2023. *Future Grid-Scale Energy Storage Solutions Mechanical and Chemical Technologies and Principles*. Academic Press.
- Arpat, G.B., 2005. *Sequential Simulation with Patterns*. PhD Thesis. Stanford University, Department of Petroleum Engineering.
- Aughenbaugh, J.M., Paredis, C.J.J., 2007. Probability bounds analysis as a general approach to sensitivity analysis in decision making under uncertainty. *SAE Tech. Pap.* <https://doi.org/10.4271/2007-01-1480>
- Babak, O., Bergey, P., Deutsch, C. V., 2014. Facies trend modeling for SAGD application at Surmont. *J. Pet. Sci. Eng.* 119, 85–103. <https://doi.org/10.1016/j.petrol.2014.04.015>

- Bachmann, G.H., Muller, M., 1992. Sedimentary and structural evolution of the German Molasse Basin. *Eclogae Geol. Helv.* 85, 519–530.
- Backhaus, K., Erichson, B., Plinke, W., Weiber, R., 2016. *Multivariate Analysemethoden, Multivariate Analysemethoden*. Springer Berlin Heidelberg, Berlin, Heidelberg. <https://doi.org/10.1007/978-3-662-46076-4>
- Banning, A., Demmel, T., Rde, T.R., Wrobel, M., 2013. Groundwater uranium origin and fate control in a river valley aquifer. *Environ. Sci. Technol.* 47, 13941–13948. <https://doi.org/10.1021/es304609e>
- Barahona-Palomo, M., 2014. Estimation of aquifers hydraulic parameters by three different techniques: geostatistics, correlation and modeling. PhD Thesis. Universitat Politcnica de Catalunya, UPC. Hydrogeology Group (GHS) Dept.
- Brdossy, G., Fodor, J., 2004. Evaluation of Uncertainties and Risks in Geology, Lecture Notes in Economics and Mathematical Systems. Springer Berlin Heidelberg, Berlin, Heidelberg. <https://doi.org/10.1007/978-3-662-07138-0>
- Brdossy, G., Fodor, J., 2001. Traditional and new ways to handle uncertainty in geology. *Nat. Resour. Res.* 10, 179–187. <https://doi.org/10.1023/A:1012513107364>
- Bassani, M.A.A., Costa, J.F.C.L., 2022. Geostatistics with Data of Different Support Applied to Mining Engineering, Topics in Mining, Metallurgy and Materials Engineering. Springer International Publishing, Cham. <https://doi.org/10.1007/978-3-030-80193-9>
- Bauer, M., Neumann, P., Scholz, M., Thuro, K., 2005. The geology of the city of Munich and its significance for ground modelling in urban areas. *IAEG2006 Pap. number 454 28*, 83–92.
- Bayer, P., Attard, G., Blum, P., Menberg, K., 2019. The geothermal potential of cities. *Renew. Sustain. Energy Rev.* 106, 17–30. <https://doi.org/10.1016/j.rser.2019.02.019>
- Bayer, P., Huggenberger, P., Renard, P., Comunian, A., 2011. Three-dimensional high resolution fluvio-glacial aquifer analog: Part 1: Field study. *J. Hydrol.* 405, 1–9. <https://doi.org/10.1016/j.jhydrol.2011.03.038>
- Bear, J., 1972. Dynamics of Fluids in Porous Media. *Soil Sci. Soc. Am. J.* 37, vi–vi. <https://doi.org/10.2136/sssaj1973.03615995003700040004x>
- Berg, R.C., Mathers, S.J., Kessler, H., Keefer, D. a, 2011. Synopsis of current three-dimensional geological mapping and modeling in Geological Survey organizations. *Circ.* 578 104.
- Bertleff, B., Ellwanger, D., Szenkler, C., Eichinger, L., Trimborn, P., Wolfendale, N., 1993. Interpretation of hydrochemical and hydroisotopical Hydrogeology measurements on paleogroundwaters in Oberschwaben, South German Alpine Foreland, with focus on quaternary geology, in: *Isotope Techniques in the Study of Past and Current Environmental Changes in the Hydrosphere and the Atmosphere*. Proceedings of a Symposium, Vienna, 19–23 April 1993. International Atomic Energy Agency, Vienna, pp. 337–357.
- Beyer, W., 1964. Zur Bestimmung der Wasserdurchlssigkeit von Kiesen und Sanden aus der Kornverteilungskurve. *WWT* 14 165–168.
- Bialas, Z., Kleczkowski, A., 1970. ber den praktischen Gebrauch von einigen empirischen Formeln zur Berechnung des Durchlssigkeitskoeffizienten K. *Arch Hydrotechniki* 17.3, 405–417.
- Bianchi, M., Kearsley, T., Kingdon, A., 2015. Integrating deterministic lithostratigraphic models in

- stochastic realizations of subsurface heterogeneity. Impact on predictions of lithology, hydraulic heads and groundwater fluxes. *J. Hydrol.* 531, 557–573. <https://doi.org/10.1016/j.jhydrol.2015.10.072>
- Bianchi, M., Zheng, C., 2016. A lithofacies approach for modeling non-Fickian solute transport in a heterogeneous alluvial aquifer. *Water Resour. Res.* 52, 552–565. <https://doi.org/10.1002/2015WR018186>
- Bianchi, M., Zheng, C., Wilson, C., Tick, G.R., Liu, G., Gorelick, S.M., 2011. Spatial connectivity in a highly heterogeneous aquifer: From cores to preferential flow paths. *Water Resour. Res.* 47, 1–18. <https://doi.org/10.1029/2009WR008966>
- Blasy, L., 1974. Die Grundwasserverhältnisse in der Münchner Schotterebene westlich der Isar. PhD Thesis. Technical University of Munich (Germany).
- Bloomfield, J., 1994. Unconsolidated sedimentary aquifers: Review no 5- The use of laboratory techniques in the characterization of unconsolidated sedimentary aquifer physical properties. Keyworth, Nottingham.
- Bond, C.E., Gibbs, A.D., Shipton, Z.K., Jones, S., 2007. What do you think this is? “Conceptual uncertainty” in geoscience interpretation. *GSA Today* 17, 4–10. <https://doi.org/10.1130/GSAT01711A.1>
- Born, H., Bracke, R., Eicker, T., Rath, M., 2022. Roadmap for near-surface geothermal energy. Fraunhofer IEG. <https://doi.org/https://doi.org/10.24406/publica-552>
- Borzi, G., Idaszkin, Y.L., Tanjal, C., Galliari, J., Carol, E., 2021. Assessment of anthropogenic pollution using multiple hydrogeochemical tools and statistical analysis in rural plain basins of the Argentinian Pampean Plain. *River Res. Appl.* 37, 826–842. <https://doi.org/10.1002/rra.3800>
- Böttcher, F., 2024. The potential of thermal groundwater use in urban environments. PhD Thesis. Technical University of Munich (Germany), Chair of Hydrogeology, Geothermal Energy Group.
- Böttcher, F., Casasso, A., Götzl, G., Zosseder, K., 2019. TAP - Thermal aquifer Potential: A quantitative method to assess the spatial potential for the thermal use of groundwater. *Renew. Energy* 142, 85–95. <https://doi.org/10.1016/j.renene.2019.04.086>
- Böttcher, F., Zosseder, K., 2022. Thermal influences on groundwater in urban environments – A multivariate statistical analysis of the subsurface heat island effect in Munich. *Sci. Total Environ.* 810, 152193. <https://doi.org/10.1016/j.scitotenv.2021.152193>
- Bricker, S., Jelenek, J., van der Keur, P., La Vigna, F., O’Connor, S., Ryzynski, G., Smith, M., Schokker, J., Venvik, G., 2024. Geoscience for Cities: Delivering Europe’s Sustainable Urban Future. *Sustainability* 16, 2559. <https://doi.org/10.3390/su16062559>
- Brunetti, G.F.A., Lauria, A., Fallico, C., 2021. Comparison among variation models of the hydraulic conductivity with the effective porosity in confined aquifer. *IOP Conf. Ser. Earth Environ. Sci.* 958, 012003. <https://doi.org/10.1088/1755-1315/958/1/012003>
- Bundesverband Geothermie e.V., 2017. Stand der Forschung und Forschungsbedarf in der Geothermie. Positionspapier des Bundesverbandes Geothermie e. V. (BVG) zum 7. Energieforschungsprogramm des Bundesministeriums für Wirtschaft und Energie (BMWi) 1–19.
- Cabalar, A.F., Akbulut, N., 2016. Evaluation of actual and estimated hydraulic conductivity of sands

- with different gradation and shape. Springerplus 5. <https://doi.org/10.1186/s40064-016-2472-2>
- Caers, J., 2011. Modeling Uncertainty in the Earth Sciences. Wiley. <https://doi.org/10.1002/9781119995920>
- Campbell, S.D.G., Merritt, J.E., Dochartaigh, B.É.Ó., Mansour, M., Hughes, A.G., Fordyce, F.M., Entwisle, D.C., Monaghan, A.A., Loughlin, S.C., 2010. 3D geological models and their hydrogeological applications: supporting urban development – a case study in Glasgow-Clyde, UK. *Zeitschrift der Dtsch. Gesellschaft für Geowissenschaften* 161, 251–262. <https://doi.org/10.1127/1860-1804/2010/0161-0251>
- Carman, P., 1956. Flow of gases through porous media. Butterworths Scientific Publications, London.
- Carman, P., 1939. Permeability of saturated sands, soils and clays. *J Agric Sci* 29, 262–273.
- Chandel, A., Shankar, V., 2022. Assessment of Hydraulic Conductivity of Porous Media Using Empirical Relationships. *Sediment Transp. Publ. IntechOpe*. <https://doi.org/10.5772/intechopen.103127>
- Chandel, A., Shankar, V., 2021. Evaluation of empirical relationships to estimate the hydraulic conductivity of borehole soil samples. *ISH J. Hydraul. Eng.* 00, 1–10. <https://doi.org/10.1080/09715010.2021.1902872>
- Chapuis, R.P., 2012. Predicting the saturated hydraulic conductivity of soils: A review. *Bull. Eng. Geol. Environ.* 71, 401–434. <https://doi.org/10.1007/s10064-012-0418-7>
- Chapuis, R.P., 2004. Predicting the saturated hydraulic conductivity of sand and gravel using effective diameter and void ratio. *Can. Geotech. J.* 41, 787–795. <https://doi.org/10.1139/T04-022>
- Chapuis, R.P., Aubertin, M., 2003. Predicting the coefficient of permeability of soils using the Kozeny-Carman equation. Montreal, QC, Canada.
- Chapuis, R.P., Dallaire, V., Marcotte, D., Chouteau, M., Acevedo, N., Gagnon, F., 2005. Evaluating the hydraulic conductivity at three different scales within an unconfined sand aquifer at Lachenaie, Quebec. *Can. Geotech. J.* 42, 1212–1220. <https://doi.org/10.1139/t05-045>
- Chavez-Kus, L., Kainzmeier, B., Muhr, C., Paul, R., Riße, I., Scholz, M., Wilferth, T., Pokowietz, C., Blumenhofer, A., 2016. Geowissenschaftliche Landesaufnahme in der Planungsregion 18 Südoberbayern. Bayerisches Landesamt für Umwelt.
- Cheng, C., Chen, X., 2007. Evaluation of methods for determination of hydraulic properties in an aquifer-aquitard system hydrologically connected to a river. *Hydrogeol. J.* 15, 669–678. <https://doi.org/10.1007/s10040-006-0135-z>
- Cheong, J.Y., Hamm, S.Y., Kim, H.S., Ko, E.J., Yang, K., Lee, J.H., 2008. Estimating hydraulic conductivity using grain-size analyses, aquifer tests, and numerical modeling in a riverside alluvial system in South Korea. *Hydrogeol. J.* 16, 1129–1143. <https://doi.org/10.1007/s10040-008-0303-4>
- Chilès, J. -P., Delfiner, P., 2012. Geostatistics: Modeling Spatial Uncertainty, Second Edi. ed. Wiley, New Jersey.
- Cloutier, V., Lefebvre, R., Therrien, R., Savard, M.M., 2008. Multivariate statistical analysis of geochemical data as indicative of the hydrogeochemical evolution of groundwater in a

- sedimentary rock aquifer system. *J. Hydrol.* 353, 294–313. <https://doi.org/10.1016/j.jhydrol.2008.02.015>
- Coburn, T.C., Yarus, J.M., Chambers, R.L., 2006. *Stochastic Modeling and Geostatistics: Principles, Methods, and Case Studies, Volume II*. American Association of Petroleum Geologists. <https://doi.org/10.1306/CA51063>
- Comunian, A., De Micheli, L., Lazzati, C., Felletti, F., Giacobbo, F., Giudici, M., Bersezio, R., 2016. Hierarchical simulation of aquifer heterogeneity: implications of different simulation settings on solute-transport modeling. *Hydrogeol. J.* 24, 319–334. <https://doi.org/10.1007/s10040-015-1343-1>
- Comunian, A., Renard, P., Straubhaar, J., Bayer, P., 2011. Three-dimensional high resolution fluvio-glacial aquifer analog - Part 2: Geostatistical modeling. *J. Hydrol.* 405, 10–23. <https://doi.org/10.1016/j.jhydrol.2011.03.037>
- Conway, J.M., Huffcutt, A.I., 2003. A Review and Evaluation of Exploratory Factor Analysis Practices in Organizational Research. *Organ. Res. Methods* 6, 147–168. <https://doi.org/10.1177/1094428103251541>
- Cornelis, W.M., Ronsyn, J., Van Meirvenne, M., Hartmann, R., 2001. Evaluation of Pedotransfer Functions for Predicting the Soil Moisture Retention Curve. *Soil Sci. Soc. Am. J.* 65, 638–648. <https://doi.org/10.2136/sssaj2001.653638x>
- Curtis, Z.K., Li, S.G., Liao, H.S., Lusch, D., 2018. Data-Driven Approach for Analyzing Hydrogeology and Groundwater Quality Across Multiple Scales. *Groundwater* 56, 377–398. <https://doi.org/10.1111/gwat.12584>
- D’Andrea, R., 2001. Hydraulic conductivity of soils from grain-size distribution: New models. *J. Geotech. Geoenviron. Eng.* 127, 899–900.
- De Bartolo, S., Fallico, C., Veltri, M., 2013. A note on the fractal behavior of hydraulic conductivity and effective porosity for experimental values in a confined aquifer. *Sci. World J.* 2013. <https://doi.org/10.1155/2013/356753>
- de Marsily, G., Delay, F., Gonçalves, J., Renard, P., Teles, V., Violette, S., 2005. Dealing with spatial heterogeneity. *Hydrogeol. J.* 13, 161–183. <https://doi.org/10.1007/s10040-004-0432-3>
- Deutsch, C. V., 2006. A sequential indicator simulation program for categorical variables with point and block data: BlockSIS. *Comput. Geosci.* 32, 1669–1681. <https://doi.org/10.1016/j.cageo.2006.03.005>
- Deutsch, C. V., 2002. *Geostatistical reservoir modeling*. Oxford University Press. Applied Geostatistics Series, New York.
- Deutsch, C. V., Journel, A.G., 1997. *GSLIB: geostatistical software library and user’s guide*, Second ed. ed. Oxford University Press, New York.
- Deutsch, C. V., 2021. Citation in *Applied Geostatistics*, 2021 Editi. ed.
- Devlin, J.F., 2015. HydrogeoSieveXL: an Excel-based tool to estimate hydraulic conductivity from grain-size analysis. *Hydrogeol. J.* 23, 837–833. <https://doi.org/10.1007/s10040-015-1255-0>
- Diaz-Maurin, F., Saaltink, M.W., 2021. Model validation for subsurface dynamics, GEOTHERMICA – ERA NET Cofund Geothermal.
- Dillon, P., Pavelic, P., Page, D., Beringen, H., Ward, J., 2009. Managed aquifer recharge: An

- Introduction (Waterlines Report Series No. 13). Australian Government. National Water Commission. <https://doi.org/10.1007/BF01929660>
- DIN 18196, 2023. (DIN 18196:2023-02) Erd- und Grundbau – Bodenklassifikation für bautechnische Zwecke. Earthworks and foundations – Soil classification for civil engineering purposes. DIN Deutsches Institut für Normung e. V.
- DIN 18300, 2019. (DIN 18300:2019-09) VOB Vergabe- und Vertragsordnung für Bauleistungen - Teil C: Allgem. Technische Vertragsbedingungen für Bauleistungen (ATV) - Erdarbeiten.
- DIN 4023, 2006. (DIN 4023:2006-02) Geotechnische Erkundung und Untersuchung – Zeichnerische Darstellung der Ergebnisse von Bohrungen und sonstigen direkten Aufschlüssen. DIN Deutsches Institut für Normung e. V.
- DIN EN ISO 14688-1, 2020. (DIN EN ISO 14688-1:2020-11) Geotechnische Erkundung und Untersuchung — Benennung, Beschreibung und Klassifizierung von Boden — Teil 1: Benennung und Beschreibung (ISO 14688-1:2017); Deutsche Fassung EN ISO 14688-1:2018. DIN Deutsches Institut für Normung e. V.
- DIN EN ISO 14688-2, 2020. (DIN EN ISO 14688-2:2020-11) Geotechnische Erkundung und Untersuchung — Benennung, Beschreibung und Klassifizierung von Boden — Teil 2: Grundlagen für Bodenklassifizierungen (ISO 14688-2:2017); Deutsche Fassung EN ISO 14688-2:2018. DIN Deutsches Institut für Normung e. V.
- DIN EN ISO 14689, 2018. (DIN EN ISO 14689:2018-05) Geotechnische Erkundung und Untersuchung – Benennung, Beschreibung und Klassifizierung von Fels (ISO 14689:2017); Deutsche Fassung EN ISO 14689:2018. DIN Deutsches Institut für Normung e. V.
- Doherty, J., 2003. Ground water model calibration using pilot points and regularization. *Ground Water* 41, 170–177.
- Domenico, P.A., Schwartz, F.W., 1997. *Physical and Chemical Hydrogeology*. John Wiley and Sons, New York.
- Doppler, G., Heissig, K., Reichenbacher, B., 2005. Die Gliederung des Tertiärs im süddeutschen Molassebecken. *Newsletters Stratigr.* 41, 359–375. <https://doi.org/10.1127/0078-0421/2005/0041-0359>
- Doppler, G., Kroemer, E., Rögner, K., Wallner, J., Jerz, H., Grottenthaler, W., 2011. Quaternary Stratigraphy of Southern Bavaria. *E G Quat. Sci. J.* 60, 329–365. <https://doi.org/10.3285/eg.60.2-3.08>
- Egger, F., 1978. *Das Grundwasser in der Oberen Süßwassermolasse im Raum München und Augsburg*. PhD Thesis. Ludwig-Maximilians-Universität, Munich (Germany).
- Ehlers, J., Gibbard, P.L., 2004a. *Quaternary Glaciations- Extent and Chronology, Part I: Europe*. Elsevier.
- Ehlers, J., Gibbard, P.L., 2004b. *Quaternary Glaciations- Extent and Chronology, Part II: North America*. Elsevier.
- Enemark, T., Andersen, L.T., Høyer, A.S., Jensen, K.H., Kidmose, J., Sandersen, P.B.E., Sonnenborg, T.O., 2022. The influence of layer and voxel geological modelling strategy on groundwater modelling results. *Hydrogeol. J.* 30, 617–635. <https://doi.org/10.1007/s10040-021-02442-9>
- English, M., 2017. Package ‘hydrogeo’: groundwater data presentation and interpretation (Version

0.6-1).

- Entenmann, W., 1992. Das hydrogeologische Beweissicherungsverfahren für Hausmülldeponien. – Band 1: Verfahren, Fallbeispiele, Erkundung und Erfassung hydraulischer Daten. Clausthaler geologische Abhandlungen, Köln.
- Epting, J., Böttcher, F., Mueller, M.H., García-Gil, A., Zosseder, K., Huggenberger, P., 2020. City-scale solutions for the energy use of shallow urban subsurface resources – Bridging the gap between theoretical and technical potentials. *Renew. Energy* 147, 751–763. <https://doi.org/10.1016/j.renene.2019.09.021>
- Esfandiari, R.S., 2017. Numerical Methods for Engineers and Scientists Using MATLAB. CRC Press.
- European Parliament, 2000. Directive 2000/60/EC of the European Parliament and of the Council establishing a framework for the community action in the field of water policy.
- Exler, H.J., 1967. Hydrogeologische Profile der U-Bahn-Trasse zwischen Haupt- und Ostbahnhof der Landeshauptstadt München [Hydrogeological profiles of the underground railway line between the main and eastern railway stations of the City of Munich]. Dtsch. Gewässerkundliche Mitteilungen.
- Fallico, C., De Bartolo, S., Troisi, S., Veltri, M., 2010. Scaling analysis of hydraulic conductivity and porosity on a sandy medium of an unconfined aquifer reproduced in the laboratory. *Geoderma* 160, 3–12. <https://doi.org/10.1016/j.geoderma.2010.09.014>
- Fallico, C., Vita, M.C., De Bartolo, S., Straface, S., 2012. Scaling effect of the hydraulic conductivity in a confined aquifer. *Soil Sci.* 177, 385–391. <https://doi.org/10.1097/SS.0b013e31824f179c>
- FAO, 2016. Global Framework for Action to achieve the Vision on Groundwater Governance. Food and Agricultural Organization of the United Nations (FAO).
- Fillibeck, J., Lachmann, D.M., 2011. B2 – Tunnel Starnberg – Erkundung des heterogenen Baugrundes und Auswirkungen auf die Planung, in: Tagungsband Geotechnik-Tag „Wasser Und Boden“, München, 4. März 2011. N. Vogt, pp. 31–45.
- Fogg, G.E., Zhang, Y., 2016. Debates-Stochastic subsurface hydrology from theory to practice: A geologic perspective. *Water Resour. Res.* 52, 9235–9245. <https://doi.org/10.1002/2016WR019699>
- Frape, S.K., Blyth, A., Blomqvist, R., McNutt, R.H., Gascoyne, M., 2003. Deep Fluids in the Continents: II. Crystalline Rocks. *Treatise on Geochemistry* 5–9, 541–580. <https://doi.org/10.1016/B0-08-043751-6/05086-6>
- Freedman, V., Connelly, M., Rockhold, M., Hasan, N., Mehta, S., McMahon, W.J., Kozak, M., Hou, Z.J., Bergeron, M., 2019. A multiple lines of evidence approach for identifying geologic heterogeneities in conceptual site models for performance assessments. *Sci. Total Environ.* 692, 450–464. <https://doi.org/10.1016/j.scitotenv.2019.07.213>
- Freeze, R.A., Cherry, J.A., 1979. Groundwater. Prentice-Hall, Inc., Englewood Cliffs, New Jersey.
- Freudenberger, W., Schwerd, K., 1996. Erläuterungen zur Geologischen Karte von Bayern 1 : 500000, Geol. Kt. Bayern 1 : 500000. Bayerisches Geologisches Landesamt.
- Fritsch, F.N.; Carlson, R.E., 1980. Monotone piecewise cubic interpolation. *Soc. Ind. Appl. Math.* 17, 238–246. <https://doi.org/10.1137/0717021>
- Froidevaux, R., 1992. Probability field simulation, in: Soares, A. (ed) (Ed.), *Geostatistics Toria '92*.

pp. 73–83.

- Fuchs, S., 2010. Deterministische kf-Wert-Schätzung nach petrographischer Bohrgutansprache. *Grundwasser* 15, 177–189. <https://doi.org/10.1007/s00767-010-0143-8>
- Gale, I., 2005. Strategies for Managed Aquifer Recharge (MAR) in semi-arid areas. International Association of Hydrogeologists. Commission on Managed Aquifer Recharge.
- Galloway, W.E., Hobday, D.K., 1983. Terrigenous Clastic Depositional Systems. Springer US, New York, NY. <https://doi.org/10.1007/978-1-4684-0170-7>
- Gebhardt, P., 1968. Die geologischen und hydrologischen Verhältnisse beim Münchner U-Bahn-Bau. PhD Thesis. Ludwig-Maximilians-Universität, Munich (Germany).
- Ghesquière, O., Walter, J., Chesnaux, R., Rouleau, A., 2015. Scenarios of groundwater chemical evolution in a region of the Canadian Shield based on multivariate statistical analysis. *J. Hydrol. Reg. Stud.* 4, 246–266. <https://doi.org/10.1016/j.ejrh.2015.06.004>
- Gibling, M.R., 2006. Width and Thickness of Fluvial Channel Bodies and Valley Fills in the Geological Record: A Literature Compilation and Classification. *J. Sediment. Res.* 76, 731–770. <https://doi.org/10.2110/jsr.2006.060>
- Gilabert-Alarcón, C., Daesslé, L.W., Salgado-Méndez, S.O., Pérez-Flores, M.A., Knöller, K., Kretzschmar, T.G., Stumpp, C., 2018. Effects of reclaimed water discharge in the Maneadero coastal aquifer, Baja California, Mexico. *Appl. Geochemistry* 92, 121–139. <https://doi.org/10.1016/j.apgeochem.2018.03.006>
- Göktepe, A.B., Sezer, A., 2010. Effect of particle shape on density and permeability of sands. *Proc. Inst. Civ. Eng. Geotech. Eng.* 163, 307–320. <https://doi.org/10.1680/geng.2010.163.6.307>
- Gómez-Hernández, J.J., 1997. Issues on environmental risk assessment, in: Baafi, E.Y., Schofield, N.A. (Eds.), *Geostatistics Wollongong '96*. Kluwer Academic Publishing, Dordrecht, pp. 15–26.
- Gómez-Hernández, J.J., Srivastava, R.M., 2021. One Step at a Time: The Origins of Sequential Simulation and Beyond. *Math. Geosci.* 53, 193–209. <https://doi.org/10.1007/s11004-021-09926-0>
- González, E., McLennan, J.A., Deutsch, C. V., 2007. Non-stationary Gaussian Transformation: A New Approach to SGS in Presence of a Trend. APCOM 2007, Santiago, Chile.
- Goovaerts, P., 1997. *Geostatistics for Natural Resource Evaluation*. Oxford University Press, New York.
- Goretzko, D., Pham, T.T.H., Bühner, M., 2019. Exploratory factor analysis: Current use, methodological developments and recommendations for good practice. *Curr. Psychol.* 40, 3510–3521. <https://doi.org/10.1007/s12144-019-00300-2>
- Griffioen, J., van Wensem, J., Oomes, J.L.M., Barends, F., Breunese, J., Bruining, H., Olsthoorn, T., Stams, A.J.M., van der Stoel, A.E.C., 2014. A technical investigation on tools and concepts for sustainable management of the subsurface in The Netherlands. *Sci. Total Environ.* 485–486, 810–819. <https://doi.org/10.1016/j.scitotenv.2014.02.114>
- Gringarten, E., Deutsch, C.V., 1999. Methodology for Variogram Interpretation and Modeling for Improved Reservoir Characterization. *Soc. Pet. Eng.* <https://doi.org/https://doi.org/10.2118/56654-MS>
- Güler, C., Thyne, G.D., McCray, J.E., Turner, A.K., 2002. Evaluation of graphical and multivariate

- statistical methods for classification of water chemistry data. *Hydrogeol. J.* 10, 455–474. <https://doi.org/10.1007/s10040-002-0196-6>
- Hadavand, M., Deutsch, C. V., 2017. Facies proportion uncertainty in presence of a trend. *J. Pet. Sci. Eng.* 153, 59–69. <https://doi.org/10.1016/j.petrol.2017.03.036>
- Hademenos, V., Stafleu, J., Missiaen, T., Kint, L., Van Lancker, V.R.M., 2019. 3D subsurface characterisation of the Belgian Continental Shelf: A new voxel modelling approach. *Geol. en Mijnbouw/Netherlands J. Geosci.* 98. <https://doi.org/10.1017/njg.2018.18>
- Hajji, S., Karoui, S., Nasri, G., Allouche, N., Bouri, S., 2021. EFA-CFA integrated approach for groundwater resources sustainability in agricultural areas under data scarcity challenge: case study of the Souassi aquifer, Central-eastern Tunisia. *Environ. Dev. Sustain.* 23, 12024–12043. <https://doi.org/10.1007/s10668-020-01155-5>
- Halilovic, S., Böttcher, F., Kramer, S.C., Piggott, M.D., Zosseder, K., Hamacher, T., 2022. Well layout optimization for groundwater heat pump systems using the adjoint approach. *Energy Convers. Manag.* 268, 116033. <https://doi.org/10.1016/j.enconman.2022.116033>
- Harleman, D.R.F., Mehlhorn, P.F., Rumer, R.R., 1963. Dispersion-Permeability Correlation in Porous Media. *J. Hydraul. Div.* 89, 67–85. <https://doi.org/10.1061/JYCEAJ.0000863>
- Harris, C.R., Millman, K.J., van der Walt, S.J., Gommers, R., Virtanen, P., Cournapeau, D., Wieser, E., Taylor, J., Berg, S., Smith, N.J., Kern, R., Picus, M., Hoyer, S., van Kerkwijk, M.H., Brett, M., Haldane, A., del Río, J.F., Wiebe, M., Peterson, P., Gérard-Marchant, P., Sheppard, K., Reddy, T., Weckesser, W., Abbasi, H., Gohlke, C., Oliphant, T.E., 2020. Array programming with NumPy. *Nature* 585, 357–362. <https://doi.org/10.1038/s41586-020-2649-2>
- Hassanpour, R., Deutsch, C., 2010. An Introduction to Grid-Free Object-based Facies Modeling. *CCG Annu. Rep.* 12, Pap. 107 107, 1–6.
- Hazen, A., 1892. Some physical properties of sands and gravels with special reverence to their use in filtration. *Twenty-fourth ann. rep. state board Heal. Mass., Bost.* 541–556.
- Heine, F., Zosseder, K., Einsiedl, F., 2021. Hydrochemical zoning and chemical evolution of the deep upper jurassic thermal groundwater reservoir using water chemical and environmental isotope data. *Water (Switzerland)* 13. <https://doi.org/10.3390/w13091162>
- Helsel, D.R., 2012. *Statistics for Censored Environmental Data Using Minitab and R*. 2nd Edition, John Wiley & Sons, Hoboken, New Jersey.
- Hölting, B., Coldewey, W.G., 2013. *Einführung in die Allgemeine und Angewandte Hydrogeologie*, 8. Auflage. ed, Springer Spektrum. Spektrum Akademischer Verlag, Heidelberg. <https://doi.org/10.1007/978-3-8274-2354-2>
- Hönes, J.A.E., 2021. *The Impact of Autonomous Parking on Land-Use and Transport With a Case Study of Munich*. Technical University of Munich.
- Hong, S., 2010. *Multivariate Analysis of Diverse Data for Improved Geostatistical Reservoir Modeling*. PhD Thesis. University of Alberta, Edmonton (Canada). Faculty of Graduate Studies and Research.
- Hong, S., Deutsch, C. V., 2009. Evaluation of Probabilistic Models for Categorical Variables. *CCG Annu. Rep.* 11, Pap. 131 2009, 1–6.
- Høyer, A.S., Jørgensen, F., Sandersen, P.B.E., Viezzoli, A., Møller, I., 2015. 3D geological modelling of a complex buried-valley network delineated from borehole and AEM data. *J. Appl.*

- Geophys. 122, 94–102. <https://doi.org/10.1016/j.jappgeo.2015.09.004>
- Hunter, J., 2007. Matplotlib: A 2D Graphics Environment. *Comput. Sci. Eng.* 9, 90–95.
- HydroConsult GmbH, 2016. Hydrogeologische Studie zum Tertiärgrundwasser in Bayerisch-Schwaben. Report (unpublished). Augsburg, Germany.
- HydroConsult GmbH, 2003. Tertiärgrundwasser im Raum Augsburg. Studie zur Grundwasserbilanzierung. Report (unpublished). Augsburg, Germany.
- IAEA/WMO, 2020. Global Network of Isotopes in Precipitation. The GNIP Database [WWW Document]. URL <https://nucleus.iaea.org/wiser>
- IEA, 2019. Renewables 2019: Analysis and forecasts to 2024, Market Report Series: Renewables. International Energy Agency (IEA), Paris. <https://doi.org/10.1787/b3911209-en>
- Isaaks, E.H., Srivastava, R.M., 1989. Applied geostatistics. Oxford University Press, Inc., New York, Oxford.
- Ishaku, J.M., Gadzama, E.W., Kaigama, U., 2011. Evaluation of empirical formulae for the determination of hydraulic conductivity based on grain-size analysis. *J. Geol. Min. Res.* 3, 105–113.
- ITRC, 2013. Groundwater statistics and monitoring compliance: statistical tools for the Project Life Cycle. The Interstate Technology & Regulatory Council Groundwater Statistics and Monitoring Compliance Team. Washington, DC. <https://doi.org/10.13140/RG.2.2.11083.59685>
- Jerz, H., 1993. Geologie von Bayern II - Das Eiszeitalter in Bayern: Erdgeschichte, Gesteine, Wasser, Boden [Geology of Bavaria part 2: stratigraphy, rocks, water, soil]. E. Schweizerbart'sche Verlagsbuchhandlung, Stuttgart, Germany.
- Jones, R.R., McCaffrey, K.J.W., Wilson, R.W., Holdsworth, R.E., 2004. Digital field data acquisition: Towards increased quantification of uncertainty during geological mapping. *Geol. Soc. Spec. Publ.* 239, 43–56. <https://doi.org/10.1144/GSL.SP.2004.239.01.04>
- Jørgensen, F., Møller, R.R., Sandersen, P.B.E., Nebel, L., 2010. 3-D Geological Modelling of the Egebjerg Area, Denmark, Based on Hydrogeophysical Data. *Geol. Surv. Denmark Greenl. Bull.* 27–30. <https://doi.org/10.34194/geusb.v20.4892>
- Journel, A.G., 1989. Fundamentals of Geostatistics in Five Lessons, Fundamentals of Geostatistics in Five Lessons. 28th International Geological Congress, Washington, D.C.
- Journel, A.G., 1983. Nonparametric estimation of spatial distributions. *J. Int. Assoc. Math. Geol.* 15, 445–468. <https://doi.org/10.1007/BF01031292>
- Journel, A.G., Deutsch, C. V., 1993. Entropy and spatial disorder. *Math. Geol.* 25, 329–355. <https://doi.org/10.1007/BF00901422>
- Kahnt, R., Gabriel, A., Seelig, C., Freund, A., Homilius, A., 2015. Unterirdische Raumplanung - Vorschläge des Umweltschutzes zur Verbesserung der über- und untertägigen Informationsgrundlagen, zur Ausgestaltung des Planungsinstrumentariums und zur nachhaltigen Lösung von Nutzungskonflikten - Teilvorhaben 1: Geologische D. Umweltbundesamt, Forschungskennzahl 3711 16 103 1, Reihe Texte | 11/2015, Dessau-Roßlau.
- Kainzmeier, B., Thom, P., Wrobel, M., Pukowietz, C., Lischeid, G., Pamer, R., 2007. Geowissenschaftliche Landesaufnahme in der Planungsregion 13 Landshut. Bayerisches

- Landesamt für Umwelt, Augsburg, Germany.
- Kassambara, A., 2017. *Multivariate Analysis I: Practical Guide To Cluster Analysis in R. Unsupervised Machine Learning*. Taylor Fr. Gr. 188.
- Kaubisch, M., 1986. Zur indirekten Ermittlung hydrogeologischer Kennwerte von Kippenkomplexen, dargestellt am Beispiel des Braunkohlenbergbaus. PhD Thesis. TU Bergakademie Freiberg, Freiberg, Germany.
- Kearsey, T., Williams, J., Finlayson, A., Williamson, P., Dobbs, M., Marchant, B., Kingdon, A., Campbell, D., 2015. Testing the application and limitation of stochastic simulations to predict the lithology of glacial and fluvial deposits in Central Glasgow, UK. *Eng. Geol.* 187, 98–112. <https://doi.org/10.1016/j.enggeo.2014.12.017>
- Kerl, M., Runge, N., Tauchmann, H., Goldscheider, N., 2012. Conceptual hydrogeological model of the City of Munich, Germany, as a basis for geothermal groundwater utilisation. *Grundwasser* 17, 127–135. <https://doi.org/10.1007/s00767-012-0199-8>
- Kessler, H., L. Terrington, R., Sobisch, H.-G., Gunnink, J., Ludwig, R., Harms, E., Turner, K., Moore, R., 2010. The need for improved management of the subsurface. *First Int. Conf. Front. Shallow Subsurf. Technol.* Delft, Netherlands, 20–22 January 2010, 43–50. <https://doi.org/10.3997/2214-4609-pdb.150.b03>
- Kessler, H., Lelliott, M., Bridge, D., Ford, J., Sobisch, H.-G., Mathers, S., Price, S., Merritt, J., Royse, K., 2005. 3D geoscience models and their delivery to customers. *Geol. Surv. Canada, Open File* 5048, 39–42.
- Khojasteh, E.R., 2013. Geostatistical three-dimensional modeling of the subsurface unconsolidated materials in the Göttingen area. Georg-August-University School of Science (GAUSS), Göttingen, Germany.
- Kiecak, A., Huch, J., Albarrán-Ordás, A., Chavez-Kus, L., Zosseder, K., 2023. Interpretation of hydrogeochemistry of the Upper Freshwater Molasse (Obere Süßwassermolasse) in the Munich area (Bavaria, Germany) using multivariate analysis and three-dimensional geological modelling. *Hydrogeol. J.* <https://doi.org/10.1007/s10040-023-02761-z>
- Kirabo Kacyira, A., 2012. Addressing the sustainable urbanization challenge. *UN Chron.* 49, 58–60. <https://doi.org/10.18356/f813137d-en>
- Koch, T., Harrington, A., 1998. Reconceptualizing rigour: The case for reflexivity. *J. Adv. Nurs.* 28, 882–890. <https://doi.org/10.1046/j.1365-2648.1998.00725.x>
- Koltermann, C.E., Gorelick, S.M., 1996. Heterogeneity in sedimentary deposits: A review of structure-imitating, process-imitating, and descriptive approaches. *Water Resour. Res.* 32, 2617–2658. <https://doi.org/10.1029/96WR00025>
- Kozeny, J., 1927. Via capillary conduit the water in the ground. *R. Acad. Sci. Vienna Proc. Cl. I.* 136, 271–306.
- Kresse, W., Danko, D.M. (Eds.), 2012. *Springer Handbook of Geographic Information, Choice Reviews Online*. Springer Berlin Heidelberg, Berlin, Heidelberg. <https://doi.org/10.1007/978-3-540-72680-7>
- Kruiver, P.P., van Dedem, E., Romijn, R., de Lange, G., Korff, M., Stafleu, J., Gunnink, J.L., Rodriguez-Marek, A., Bommer, J.J., van Elk, J., Doornhof, D., 2017. An integrated shear-wave velocity model for the Groningen gas field, The Netherlands. *Bull. Earthq. Eng.* 15, 3555–3580. <https://doi.org/10.1007/s10518-017-0105-y>

- Kruseman, G.P., de Ridder, N.A., 2000. Analysis and Evaluation of Pumping Test Data, Second. ed, International Institute for Land Reclamation and Improvement, AA Wageningen, The Netherlands, Second Edition (Completely Revised). International Institute for Land Reclamation and Improvement/ILRI. <https://doi.org/10.2136/sssaj1971.03615995003500040014x>
- Kuhlemann, J., Kempf, O., 2002. Post-Eocene evolution of the North Alpine Foreland Basin and its response to Alpine tectonics. *Sediment. Geol.* 152, 45–78. [https://doi.org/10.1016/S0037-0738\(01\)00285-8](https://doi.org/10.1016/S0037-0738(01)00285-8)
- Lai, Y., Wang, Y., Cheng, J., Chen, X., Liu, Q., 2023. Review of constraints and critical success factors of developing urban underground space. *Undergr. Sp.* 12, 137–155. <https://doi.org/10.1016/j.undsp.2023.03.001>
- Landmeyer, N., 2019. Geologisches 3D-Modell Augsburg. Bayerisches Landesamt für Umwelt (LfU). *Umweltspezial*.
- Langguth, H.-R., Voigt, R., 2004. *Hydrogeologische Methoden*. Springer Berlin Heidelberg, Berlin, Heidelberg. <https://doi.org/10.1007/978-3-642-18655-4>
- LBEG, 2011. Verschlüsselung und Erfassung von Bohrdaten in Niedersachsen (GeoBerichte 17). Landesamt für Bergbau, Energie und Geologie (LBEG). Hannover, Germany. https://doi.org/10.48476/geober_17_2011
- Leij, F., Alves, W., van Genuchten, Mt., Williams, J., 1994. *Unsaturated Soil Hydraulic Database, UNSODA 1.0 User's Manual*. Office of Research and Development, United States Environmental Protection Agency, Ada, OK.
- Lemcke, K., 1988. *Geologie von Bayern I. Das bayerische Alpenvorland vor der Eiszeit - Erdgeschichte Bau Bodenschätze*. E. Schweizerbart'sche Verlagsbuchhandlung, Stuttgart.
- Leung, Y., Goodchild, M.F., Lin, C.C., Leung, Y., Goodchild, M.F., Lin, C.C., 1992. Visualization of fuzzy scenes and probability fields. *Comput. Sci. Stat.*
- LfU, 2009. *Oberflächennahe Geothermie - Wasserwirtschaftliche Aspekte*. Fachtagung am 11. März 2009. Bayerisches Landesamt für Umwelt (LfU). *UmweltSpezial*. May 2009.
- LHM, 2022. *Nachhaltigkeitsbericht München 2022*. Landeshauptstadt München (LHM), Referat für Gesundheit und Umwelt, Munich.
- Lindsay, M.D., Aillères, L., Jessell, M.W., de Kemp, E.A., Betts, P.G., 2012. Locating and quantifying geological uncertainty in three-dimensional models: Analysis of the Gippsland Basin, southeastern Australia. *Tectonophysics* 546–547, 10–27. <https://doi.org/10.1016/j.tecto.2012.04.007>
- Lo Russo, S., Taddia, G., 2009. Groundwater in the Urban Environment: Management Needs and Planning Strategies. *Am. J. Environ. Sci.* 5, 493–499. <https://doi.org/10.3844/ajessp.2009.493.499>
- Ma, X., 2018. Data science for geoscience: leveraging mathematical geosciences with semantics and open data, in: *Handbook of Mathematical Geosciences: Fifty Years of IAMG*. Springer International Publishing, Cham, Switzerland, pp. 687–702. <https://doi.org/10.1007/978-3-319-78999-6>
- Machuca-Mory, D.F., Deutsch, C. V., 2009. Validation and Confirmation of Non-Stationary Models with the Ventersdorp Reef Data. *CCG Annu. Rep.* 11, Pap. 307 2009, 1–10.

- MacKay, D.J.C., 2003. *Information Theory, Inference, and Learning Algorithms*. Cambridge University Press. <https://doi.org/10.1166/asl.2012.3830>
- Maljers, D., Stafleu, J., Van Der Meulen, M.J., Dambrink, R.M., 2015. Advances in constructing regional geological voxel models, illustrated by their application in aggregate resource assessments. *Geol. en Mijnbouw/Netherlands J. Geosci.* 94, 257–270. <https://doi.org/10.1017/njg.2014.46>
- Małozzewski, P., Rauert, W., Stichler, W., Herrmann, A., 1983. Application of flow models in an alpine catchment area using tritium and deuterium data. *J. Hydrol.* 66, 319–330. [https://doi.org/10.1016/0022-1694\(83\)90193-2](https://doi.org/10.1016/0022-1694(83)90193-2)
- Manchuk, J.G., Deutsch, C. V., 2011. A Short Note on Trend Modeling using Moving Windows. *CCG Annu. Rep.* 13, Pap. 403 2011, 1–8.
- Mann, C.J., 1993. Uncertainty in geology, in: Davis, J.C., Herzfeld, U.C. (Eds.), *Computers in Geology - 25 Years of Progress*. Oxford University Press, Oxford, UK, pp. 241–254.
- Mariethoz, G., Caers, J., 2015. *Multiple-point geostatistics: stochastic modeling with training image*. Wiley-Blackwell.
- Marotz, G., 1968. Technische Grundlagen einer Wasserspeicherung im natürlichen Untergrund. *Schriftenr. des KWK*, 18 228 S., 95 Abb., 14 Tab., 1 Anl.; Hambg. (Wasser u. Boden).
- Marti, R., 2019. Was gilt unter dem Boden? Im Untergrund | Dans le sous-sol. *Themenh. von Hochparterre*. Hochparterre.
- Martinez, J.L., Raiber, M., Cendón, D.I., 2017. Using 3D geological modelling and geochemical mixing models to characterise alluvial aquifer recharge sources in the upper Condamine River catchment, Queensland, Australia. *Sci. Total Environ.* 574, 1–18. <https://doi.org/10.1016/j.scitotenv.2016.09.029>
- Maurer, H., Buchner, E., 2007. Fluvial systems of the Upper Freshwater Molasse (North Alpine Foreland Basin, SW-Germany). *Zeitschrift der Dtsch. Gesellschaft für Geowissenschaften* 158, 249–270. <https://doi.org/10.1127/1860-1804/2007/0158-0249>
- McCaffrey, K.J.W., Jones, R.R., Holdsworth, R.E., Wilson, R.W., Clegg, P., Imber, J., Holliman, N., Trinks, I., 2005. Unlocking the spatial dimension: Digital technologies and the future of geoscience fieldwork. *J. Geol. Soc. London.* 162, 927–938. <https://doi.org/10.1144/0016-764905-017>
- McLennan, J.A., 2007. *The Decision of Stationarity*. PhD Thesis. University of Alberta, Edmonton (Canada).
- Menció, A., Mas-Pla, J., 2008. Assessment by multivariate analysis of groundwater-surface water interactions in urbanized Mediterranean streams. *J. Hydrol.* 352, 355–366. <https://doi.org/10.1016/j.jhydrol.2008.01.014>
- Merritt, J.E., Monaghan, A.A., Entwisle, D.C., Hughes, A.G., Campbell, D., Browne, M.A.E., 2007. 3D attributed models for addressing environmental and engineering geoscience problems in areas of urban regeneration – a case study in Glasgow, UK. *First Break* 25, 1–16. <https://doi.org/10.3997/1365-2397.25.1110.27598>
- Miall, A., 2014. *Fluvial depositional systems*. Springer-Verlag, Berlin. <https://doi.org/10.5860/choice.51-4454>
- Moler, C., 2004. *Numerical Computing with MATLAB*. MathWorks, Natick, Mass, USA.

- Montcoudiol, N., Molson, J., Lemieux, J.M., 2015. Groundwater geochemistry of the Outaouais Region (Québec, Canada): a regional-scale study. *Hydrogeol. J.* 23, 377–396. <https://doi.org/10.1007/s10040-014-1190-5>
- Mukim, M., Roberts, M., 2023. *Thriving : Making Cities Green, Resilient, and Inclusive in a Changing Climate, Making Cities Work.* © Washington, DC: World Bank. <https://doi.org/10.4324/9780429051678>
- Münichsdorfer, F., 1922. Das geologische Querprofil von München. Kenntnis der Geologie von München und Umgebung. Sonderabdruck aus dem Geognostischen Jahresh. 1921. XXXIV. Jahrgang. München. Verlag von Pilot. Loehle.
- Nemes, A., Rawls, W.J., 2006. Evaluation of different representations of the particle-size distribution to predict soil water retention. *Geoderma* 132, 47–58. <https://doi.org/10.1016/j.geoderma.2005.04.018>
- Nemes, A., Wösten, J.H.M., Lilly, A., Oude Voshaar, J.H., 1999. Evaluation of different procedures to interpolate particle-size distributions to achieve compatibility within soil databases. *Geoderma* 90, 187–202. [https://doi.org/10.1016/S0016-7061\(99\)00014-2](https://doi.org/10.1016/S0016-7061(99)00014-2)
- Newman, B.D., Havenor, K.C., Longmire, P., 2016. Identification of hydrochemical facies in the Roswell Artesian Basin, New Mexico (USA), using graphical and statistical methods. *Hydrogeol. J.* 24, 819–839. <https://doi.org/10.1007/s10040-016-1401-3>
- NLFB, 2002. Anleitung zur Erfassung von Bohrungs- und Schichtdaten mit SEP 3. Arbeitsgruppe Bohrdaten. Niedersächsisches Landesamt für Bodenforschung (NLfB). Hannover, Germany.
- Odong, J., 2007. Evaluation of Empirical Formulae for Determination of Hydraulic Conductivity based on Grain-Size Analysis. *J. Am. Sci.* 4, 1–6.
- Odziomek, K., Rybinska, A., Puzyn, T., 2017. Unsupervised learning methods and similarity analysis in chemoinformatics, in: *Handbook of Computational Chemistry*. Springer, Cham, Switzerland, pp. 2095–2132.
- Oh, Y.Y., Hamm, S.Y., Chung, S.Y., Lee, B.D., 2013. Characterizing hydraulic properties by grain-size analysis of fluvial deposits depending on stream path in Korea. *Environ. Eng. Res.* 18, 129–137. <https://doi.org/10.4491/eer.2013.18.3.129>
- Olea, R.A., 1999. *Geostatistics for Engineers and Earth Scientists*. Springer US, Boston, MA. <https://doi.org/10.1007/978-1-4615-5001-3>
- Pakyuz-Charrier, E., Giraud, J., Ogarko, V., Lindsay, M., Jessell, M., 2018a. Drillhole uncertainty propagation for three-dimensional geological modeling using Monte Carlo. *Tectonophysics* 747–748, 16–39. <https://doi.org/10.1016/j.tecto.2018.09.005>
- Pakyuz-Charrier, E., Lindsay, M., Ogarko, V., Giraud, J., Jessell, M., 2018b. Monte Carlo simulation for uncertainty estimation on structural data in implicit 3-D geological modeling, a guide for disturbance distribution selection and parameterization. *Solid Earth* 9, 385–402. <https://doi.org/10.5194/se-9-385-2018>
- Peterson, P., Jones, E., Oliphant, T., 2001. Scipy: Open source scientific tools for Python. *SciPy: Open Source Scientific Tools for Python*.
- Potter, K., Gerber, S., Anderson, E.W., 2013. Visualization of uncertainty without a mean. *IEEE Comput. Graph. Appl.* 33, 75–79. <https://doi.org/10.1109/MCG.2013.14>
- Potter, K., Kniss, J., Riesenfeld, R., Johnson, C.R., 2010. Visualizing summary statistics and

- uncertainty. *Comput. Graph. Forum* 29, 823–832. <https://doi.org/10.1111/j.1467-8659.2009.01677.x>
- Prinz, H., Strauß, R., 2011. *Ingenieurgeologie*, 5th ed. ed. Springer Spektrum, Heidelberg.
- Privett, K.D., 2019. The lines of evidence approach to challenges faced in engineering geological practice. *Q. J. Eng. Geol. Hydrogeol.* 52, 141–172. <https://doi.org/10.1144/qjgeh2018-131>
- Prösl, K.-H., Anders, E., 2011. Bilanzierung der Grundwasservorkommen innerhalb der Gesteine der tertiären Oberen Süßwassermolasse im Großraum München (Amtsbereich WWA München: Stadt München und die Landkreise Fürstentfeldbruck, Dachau, München, Freising und Erding). Technical Report, Sachverständigenbüro für Grundwasser Dr. Karl-Heinz Prösl. WWA München.
- Prudic, D., 1991. Estimates of hydraulic conductivity from aquifer-test analyses and specific-capacity data, Gulf Coast regional aquifer systems, south-central United States. *Water-Resources Investig. Rep.* 90-4121 38 pp. <https://doi.org/10.3133/wri904121>
- Pucko, T., Verbovšek, T., 2015. Comparison of hydraulic conductivities by grain-size analysis, pumping, and slug tests in Quaternary gravels, NE Slovenia. *Open Geosci.* 7, 308–317. <https://doi.org/10.1515/geo-2015-0032>
- Pusch, R., 2002. *The Buffer and Backfill Handbook. Part 1: Definitions, basic relationships and laboratory methods.* Technical Report TR-02-20. Svensk Kärnbränslehantering AB Swedish Nuclear Fuel and Waste Management Co. Stockholm.
- Pyrzcz, M.J., Deutsch, C. V., 2014. *Geostatistical Reservoir Modeling*, Second Edi. ed. Oxford University Press, New York, NY.
- R Core Team, 2021. R: A language and environment for statistical computing [WWW Document]. URL <https://www.gbif.org/tool/81287/r-a-language-and-environment-for-statistical-computing>
- Rabemaharitra, T.P., Zou, Y., Yi, Z., He, Y., Khan, U., 2022. Optimized Pilot Point Emplacement Based Groundwater Flow Calibration Method for Heterogeneous Small-Scale Area. *Appl. Sci.* 12. <https://doi.org/10.3390/app12094648>
- Raiber, M., White, P.A., Daughney, C.J., Tschirter, C., Davidson, P., Bainbridge, S.E., 2012. Three-dimensional geological modelling and multivariate statistical analysis of water chemistry data to analyse and visualise aquifer structure and groundwater composition in the Wairau Plain, Marlborough District, New Zealand. *J. Hydrol.* 436–437, 13–34. <https://doi.org/10.1016/j.jhydrol.2012.01.045>
- Rauert, W., Wolf, M., Weise, S.M., Andres, G., Egger, R., 1993. Isotope-hydrogeological case study on the penetration of pollution into the deep tertiary aquifer in the area of Munich, Germany. *J. Contam. Hydrol.* 14, 15–38. [https://doi.org/10.1016/0169-7722\(93\)90039-U](https://doi.org/10.1016/0169-7722(93)90039-U)
- Rebala, G., Ravi, A., Churiwala, S., 2019. *Handbook of computational chemistry.* Springer, Cha, Switzerland.
- Revelle, W., 2020. psych: procedures for psychological, psychometric, and personality research. R package version 2.0.12.
- Revil, A., 2000. Thermal conductivity of unconsolidated sediments with geophysical applications. *J. Geophys. Res.* 105, 749–768.
- Říha, J., Petrula, L., Hala, M., Alhasan, Z., 2018. Assessment of empirical formulae for determining

- the hydraulic conductivity of glass beads. *J. Hydrol. Hydromechanics* 66, 337–347. <https://doi.org/10.2478/johh-2018-0021>
- Ringrose, P., Bentley, M., 2015. *Reservoir Model Design*. Springer Netherlands, Dordrecht. <https://doi.org/10.1007/978-94-007-5497-3>
- Roberson, S., Weltje, G.-J., 2011. 3D modelling of particle-size distributions in the shallow subsurface: Zeeland, The Netherlands, in: *IAMG Conference*, Salzburg, Austria, 5-9 September. <https://doi.org/10.5242/iamg.2011.0076>
- Rosas, J., Lopez, O., Missimer, T.M., Coulibaly, K.M., Dehwah, A.H.A., Sesler, K., Lujan, L.R., Mantilla, D., 2014. Determination of hydraulic conductivity from grain-size distribution for different depositional environments. *Groundwater* 52, 399–413. <https://doi.org/10.1111/gwat.12078>
- Ross, M., Parent, M., Lefebvre, R., 2005. 3D geologic framework models for regional hydrogeology and land-use management: A case study from a Quaternary basin of southwestern Quebec, Canada. *Hydrogeol. J.* 13, 690–707. <https://doi.org/10.1007/s10040-004-0365-x>
- Rossi, M.E., Deutsch, C. V., 2014. *Mineral Resource Estimation*. Springer Netherlands, Dordrecht. <https://doi.org/10.1007/978-1-4020-5717-5>
- Royse, K.R., 2010. Combining numerical and cognitive 3D modelling approaches in order to determine the structure of the Chalk in the London Basin. *Comput. Geosci.* 36, 500–511. <https://doi.org/10.1016/j.cageo.2009.10.001>
- Sahu, S., Saha, D., 2016. Empirical methods and estimation of hydraulic conductivity of fluvial aquifers. *Environ. Eng. Geosci.* 22, 319–340. <https://doi.org/10.2113/gseegeosci.22.4.319>
- Sánchez-Vila, X., Carrera, J., Girardi, J.P., 1996. Scale effects in transmissivity. *J. Hydrol.* 183, 1–22. [https://doi.org/10.1016/S0022-1694\(96\)80031-X](https://doi.org/10.1016/S0022-1694(96)80031-X)
- Sauerbrey, I., 1932. On the Problem and Determination of the Permeability Coefficient, in: *Proceedings VNIIG*, No. 3–5.
- Schellmann, G., Schielein, P., Gesslein, B., 2016. *Bamberger physisch-geographische Studien 2008 - 2015 : Teil III: Geomorphologisch-quartärgeologische Kartierungen im bayerischen Lech-, Wertach- und Schmuttertäl. Bamberger Geogr. Schriften, Sonderfolge 12.*
- Schielein, P., Schellmann, G., Lomax, J., 2011. Stratigraphy of Late Quaternary fluvial terraces at the confluence of the Lech and Danube valleys. *E G Quat. Sci. J.* 60, 414–424. <https://doi.org/10.3285/eg.60.4.02>
- Schirm, E., 1968. *Die hydrogeologischen Verhältnisse der Münchener Schotterebene östlich der Isar*. PhD Thesis. Ludwig-Maximilians-Universität, Munich (Germany).
- Schirmer, M., Leschik, S., Musolff, A., 2013. Current research in urban hydrogeology - A review. *Adv. Water Resour.* 51, 280–291. <https://doi.org/10.1016/j.advwatres.2012.06.015>
- Schokker, J., Sandersen, P., de Beer, H., Eriksson, I., Kallio, H., Kearsey, T., Pfeleiderer, S., Seither, A., 2017. 3D urban subsurface modelling and visualisation: a review of good practices and techniques to ensure optimal use of geological information in urban planning. *TU1206 COST Sub-Urban WG2 Report*.
- Schreiber, U., 1985. *Das Lechtal zwischen Schongau und Rain im Hoch-, Spät- und Postglazial*. Sonderveröffentlichung d. Geol. Inst. d. Uni. Köln 58, 192.
- Schuhmann, R., Koniger, F., Emmerich, K., Stefanescu, E., Stacheder, M., 2011. Determination of

- Hydraulic Conductivity Based on (Soil) - Moisture Content of Fine Grained Soils, in: Hydraulic Conductivity - Issues, Determination and Applications. <https://doi.org/10.5772/20369>
- Schultz, G., Ruppel, C., 2002. Constraints on hydraulic parameters and implications for groundwater flux across the upland-estuary interface. *J. Hydrol.* 260, 255–269. [https://doi.org/10.1016/S0022-1694\(01\)00616-3](https://doi.org/10.1016/S0022-1694(01)00616-3)
- Schumacker, R.E., 2016. Using R with multivariate statistics. Sage, Thousand Oaks, CA. <https://doi.org/10.1214/lnms/1196285102>
- Schweizer, D., Blum, P., Butscher, C., 2017. Uncertainty assessment in 3-D geological models of increasing complexity. *Solid Earth* 8, 515–530. <https://doi.org/10.5194/se-8-515-2017>
- Schwerd, K., Doppler, G., Unger, H.-J., 1996. Gesteinsfolge des Molassebeckens und der inneralpinen Tertiärbecken, Kap. 4.1 Allgemeiner Überblick, in: Bayerisches Geologisches Landesamt (Ed.), Erläuterungen Zur Geologischen Karte von Bayern 1: 500 000. München, pp. 141–149.
- Seelheim, F., 1880. Methode zur Bestimmung der Durchlässigkeit des Bodens. *Z Anal Chem* 19 387–418.
- Seiler, K.-P., 1973. Durchlässigkeit, Porosität und Kornverteilung quartärer Kies-Sand-Ablagerungen des bayerischen Alpenvorlandes. *GWF, Wasser, Abwasser* 114, 353–400.
- Senbayram, M., Gransee, A., Wahle, V., Thiel, H., 2015. Role of magnesium fertilisers in agriculture: Plant-soil continuum. *Crop Pasture Sci.* 66, 1219–1229. <https://doi.org/10.1071/CP15104>
- Shahabi, A.A., Das, B.M., Tarquin, A.J., 1984. An empirical relation for coefficient of permeability sand. *Proc. Fourth Aust. - New Zeal. Conf. Geomech.*
- Shang, S., 2013. Log-cubic method for generation of soil particle size distribution curve. *Sci. World J.* 2013. <https://doi.org/10.1155/2013/579460>
- Shannon, C.E., 1948. A Mathematical Theory of Communication. *Bell Syst. Tech. J.* 27, 379–423. <https://doi.org/10.1002/j.1538-7305.1948.tb01338.x>
- Silva, D., 2018. Enhanced Geologic Modeling of Multiple Categorical Variables. PhD Thesis. University of Alberta, Edmonton (Canada). Department of Civil and Environmental Engineering. <https://doi.org/https://doi.org/10.7939/R30G3HD9R>
- Singhal, B.B.S., Gupta, R.P., 1999. Applied Hydrogeology of Fractured Rocks. Springer Netherlands, Dordrecht. <https://doi.org/10.1007/978-94-015-9208-6>
- Skaballanowitsch, J., 1954. Hydrogeologische Berechnungen über die Dynamik des Unterirdischen Wassers. Vlg. UgleTechIsdat, Moskau.
- Slichter, C., 1899. Theoretical investigation of the motion of ground waters, in: The 19th Ann. Rep., US Geophys Survey. pp. 304–319.
- Stafleu, J., Dubelaar, C.W., 2016. Product specification – Subsurface model GeoTOP (TNO 2016 R10133 | 1.3). Geological Survey of the Netherland. Utrecht.
- Stafleu, J., Maljers, D., Gunnink, J.L., Menkovic, A., Busschers, F.S., 2011. 3D modelling of the shallow subsurface of Zeeland, The Netherlands. *Netherlands J. Geosci.* 16, 5647. <https://doi.org/10.5242/iamg.2011.0076>
- StMUV, 2014. Bekanntmachung des Bayerischen Staatsministeriums für Umwelt und Verbraucherschutz über die Verwaltungsvorschrift zum Vollzug des Wasserrechts (VWWas)

vom 27. Januar 2014 (AllMBL S. 57), die durch Bekanntmachung vom 12. November 2021 (BayMBL Nr. 849) ge. Bayerisches Staatsministerium für Umwelt und Verbraucherschutz (StMUV).

- Stone, J. V., 2015. *Information Theory: A Tutorial Introduction*, First Edit. ed. Sebtel Press.
- Storz, K., Steger, H., Wagner, V., Bayer, P., Blum, P., 2017. Methodenvergleich zur Bestimmung der hydraulischen Durchlässigkeit. *Grundwasser* 22, 103–111. <https://doi.org/10.1007/s00767-017-0353-4>
- Stumpp, C., Klaus, J., Stichler, W., 2014. Analysis of long-term stable isotopic composition in German precipitation. *J. Hydrol.* 517, 351–361. <https://doi.org/10.1016/j.jhydrol.2014.05.034>
- Szymczak, P., Wassiliew, M., Behnke, A., 2012. Bedienhinweise zum Programm für die Auswertung von Korngrößenanalysen im Fachinformationssystem Hydrogeologie. Programm UK32. Version 1.2. G.E.O.S. Freiberg Ingenieurgesellschaft mbH, HGC Hydro-Geo-Consult GmbH, Freiberg, Sächsisches Landesamt für Umwelt, Landwirtschaft und Geologie.
- Team GM, 2003. *GeoMol - Assessing subsurface potentials of the Alpine Foreland Basins for sustainable planning and use of natural resources*. Project Report. Augsburg, Germany.
- Terzagui, K., Peck, R.B., Mesri, G., 1996. *Soil Mechanics in Engineering Practice*, Soil Science. John Wiley & Sons, Inc. <https://doi.org/10.1097/00010694-194911000-00029>
- Theel, M., Huggenberger, P., Zosseder, K., 2020. Assessment of the heterogeneity of hydraulic properties in gravelly outwash plains: a regionally scaled sedimentological analysis in the Munich gravel plain, Germany. *Hydrogeol. J.* 28, 2657–2674. <https://doi.org/10.1007/s10040-020-02205-y>
- Timpe, C., Kenkmann, T., Hesse, T., Mundt, J., Maaß, C., Kapfer, J., Claas-Reuther, J., Rudolf, A., Kluth, T., 2021. *Maßnahmenplan Klimaneutralität München*. Öko-Institut e.V., HIC Hamburg Institut Consulting GmbH, INTRAPLAN Consult GmbH.
- Tissen, C., Menberg, K., Bayer, P., Blum, P., 2019. Meeting the demand: geothermal heat supply rates for an urban quarter in Germany. *Geotherm. Energy* 7. <https://doi.org/10.1186/s40517-019-0125-8>
- Todd, D.K., Mays, L.W., 2005. *Groundwater hydrology*, Groundwater Hydrology. John Wiley & Sons, Inc, Third Edition.
- Torres-Martínez, J.A., Mora, A., Knappett, P.S.K., Ornelas-Soto, N., Mahlkecht, J., 2020. Tracking nitrate and sulfate sources in groundwater of an urbanized valley using a multi-tracer approach combined with a Bayesian isotope mixing model. *Water Res.* 182, 115962. <https://doi.org/10.1016/j.watres.2020.115962>
- Turner, A.K., 2006. Challenges and trends for geological modelling and visualisation. *Bull. Eng. Geol. Environ.* 65, 109–127. <https://doi.org/10.1007/s10064-005-0015-0>
- Tweed, S., Leblanc, M., Cartwright, I., Bass, A., Travi, Y., Marc, V., Bach, T.N., Duc, N.D., Massuel, S., Kumar, U.S., 2019. Stable Isotopes of Water in Hydrogeology. *Encycl. Water* 1–10. <https://doi.org/10.1002/9781119300762.wsts0154>
- Uma, K.O., Egboka, B.C.E., Onuoha, K.M., 1989. New statistical grain-size method for evaluating the hydraulic conductivity of sandy aquifers. *J. Hydrol.* 108, 343–366. [https://doi.org/10.1016/0022-1694\(89\)90293-X](https://doi.org/10.1016/0022-1694(89)90293-X)

- UNESCO, 2022. GROUNDWATER Making the invisible visible. 2022 edition of the United Nations World Water Development Report. Paris. <https://doi.org/10.12968/bjon.2023.32.19.922>
- Urumović, K., Borović, S., Urumović, K., Navratil, D., 2020. Validity range and reliability of the United States Bureau of Reclamation (USBR) method in hydrogeological investigations. *Hydrogeol. J.* 28, 625–636. <https://doi.org/10.1007/s10040-019-02080-2>
- van der Meulen, M.J., Maljers, D., van Gessel, S.F., Gruijters, S.H.L.L., 2007. Clay resources in the Netherlands. *Geol. en Mijnbouw/Netherlands J. Geosci.* 86, 117–130. <https://doi.org/10.1017/S001677460002312X>
- van der Meulen, M.J., van Gessel, S.F., Veldkamp, J.G., 2005. Aggregate resources in the Netherlands. *Geol. en Mijnbouw/Netherlands J. Geosci.* 84, 379–387. <https://doi.org/10.1017/S0016774600021193>
- van Geldern, R., Baier, A., Subert, H.L., Kowol, S., Balk, L., Barth, J.A.C., 2014. Pleistocene paleo-groundwater as a pristine fresh water resource in southern Germany - Evidence from stable and radiogenic isotopes. *Sci. Total Environ.* 496, 107–115. <https://doi.org/10.1016/j.scitotenv.2014.07.011>
- Vázquez-Suñé, E., Carrera, J., Tubau, I., Sánchez-Vila, X., Soler, A., 2010. An approach to identify urban groundwater recharge. *Hydrol. Earth Syst. Sci.* 14, 2085–2097. <https://doi.org/10.5194/hess-14-2085-2010>
- Venables, W., Ripley, B., 2002. *Modern applied statistics with S*, Fourth. ed. Springer, New York.
- Vernes, R.W., van Doorn, T.H.M., 2005. *Van Gidslaag naar Hydrogeologische Eenheid - Toelichting op de totstandkoming van REGIS II*. TNO-rapport NITG 05-038. Utrecht.
- Villalba, M.E., Deutsch, C. V, 2010. Computing Uncertainty in the Mean with a Stochastic Trend Approach. *CCG Annu. Rep.* 12 2010, 1–6.
- Volchko, Y., Norrman, J., Ericsson, L.O., Nilsson, K.L., Markstedt, A., Öberg, M., Mossmark, F., Bobylev, N., Tengborg, P., 2020. Subsurface planning: Towards a common understanding of the subsurface as a multifunctional resource. *Land use policy* 90, 104316. <https://doi.org/10.1016/j.landusepol.2019.104316>
- Vuković, M., Soro, A., 1992. *Determination of Hydraulic Conductivity of Porous Media from Grain-Size Composition*. Water Resources Publications, Littleton, Colorado.
- Wagner, B., Töpfner, C., Lischeid, G., Scholz, M., Klinger, R., Klaas, P., 2003. *Hydrochemische Hintergrundwerte der Grundwässer Bayerns [Hydrogeochemical background values of groundwater in Bavaria]*. Bayerisches Geologisches Landesamt, Munich, Germany.
- Wagner, B., Walter, T., Himmelsbach, T., Clos, P., Beer, A., Budziak, D., Dreher, T., Fritsche, H.G., Hübschmann, M., Marczinek, S., Peters, A., Poeser, H., Schuster, H., Steinel, A., Wagner, F., Wirsing, G., 2011. *Hydrogeochemische Hintergrundwerte der Grundwässer Deutschlands als Web Map Service*. *Grundwasser* 16, 155–162. <https://doi.org/10.1007/s00767-011-0161-1>
- Wakode, H.B., Baier, K., Jha, R., Azzam, R., 2018. Impact of urbanization on groundwater recharge and urban water balance for the city of Hyderabad, India. *Int. Soil Water Conserv. Res.* 6, 51–62. <https://doi.org/10.1016/j.iswcr.2017.10.003>
- Wehrens, P., Volken, S., 2019. BIM and geological data at the Swiss Geological Survey, status and outlook . BIM and geological data at the Swiss Geological Survey , status and outlook, in: *5th European Meeting on 3D Geological Modelling*. Bern, Switzerland.

- Wei, T., Simko, T., 2021. R package “corrplot”. Visualization of a correlation matrix (Version 0.92) [WWW Document]. URL <https://github.com/taiyun/corrplot>
- Weight, W.D., 2001. Manual of Applied Field Hydrogeology. McGraw Hill, Inc., New York.
- Wellmann, F., Caumon, G., 2018. 3-D Structural geological models: Concepts, methods, and uncertainties, 1st ed, Advances in Geophysics. Elsevier Inc. <https://doi.org/10.1016/bs.agph.2018.09.001>
- Wellmann, J.F., 2013. Information Theory for Correlation Analysis and Estimation of Uncertainty Reduction in Maps and Models. *Entropy* 15, 1464–1485. <https://doi.org/10.3390/e15041464>
- Wellmann, J.F., Horowitz, F.G., Schill, E., Regenauer-Lieb, K., 2010. Towards incorporating uncertainty of structural data in 3D geological inversion. *Tectonophysics* 490, 141–151. <https://doi.org/10.1016/j.tecto.2010.04.022>
- Wellmann, J.F., Regenauer-Lieb, K., 2012. Uncertainties have a meaning : Information entropy as a quality measure for 3-D geological models. *Tectonophysics* 526–529, 207–216. <https://doi.org/10.1016/j.tecto.2011.05.001>
- Wentworth, C.K., 1922. A Scale of Grade and Class Terms for Clastic Sediments. Published by: The University of Chicago Press Stable URL : <http://www.jstor.org/stable/30063207> . *J. Geol.* 30, 377–392. <https://doi.org/10.1086/622910>
- Wickham, H., 2009. ggplot2. Elegant Graphics for Data Analysis. Springer, New York.
- Wild, L.M., Mayer, B., Einsiedl, F., 2018. Decadal Delays in Groundwater Recovery from Nitrate Contamination Caused by Low O₂ Reduction Rates. *Water Resour. Res.* 54, 9996–10,012. <https://doi.org/10.1029/2018WR023396>
- Wild, L.M., Rein, A., Einsiedl, F., 2020. Monte Carlo Simulations as a Decision Support to Interpret $\delta^{15}\text{N}$ Values of Nitrate in Groundwater. *Groundwater* 58, 571–582. <https://doi.org/10.1111/gwat.12936>
- Williams, J.D.O., Dobbs, M.R., Kingdon, A., Lark, R.M., Williamson, J.P., MacDonald, A.M., Dochartaigh, B., 2019. Stochastic modelling of hydraulic conductivity derived from geotechnical data; an example applied to central Glasgow. *Earth Environ. Sci. Trans. R. Soc. Edinburgh* 108, 141–154. <https://doi.org/10.1017/S1755691018000312>
- Woessner, W.W., Poeter, E.P., 2020. Hydrogeologic Properties of Earth Materials and Principles of Groundwater Flow, *Groundwater*. <https://doi.org/10.1111/gwat.13085>
- Wycisk, P., Hubert, T., Gossel, W., Neumann, C., 2009. High-resolution 3D spatial modelling of complex geological structures for an environmental risk assessment of abundant mining and industrial megasites. *Comput. Geosci.* 35, 165–182. <https://doi.org/10.1016/j.cageo.2007.09.001>
- Yong, A., Pearce, S., 2013. A beginner’s guide to factor analysis: focusing on exploratory factor analysis. *Tutor Quant Methods Psychol* 9, 79–94. <https://doi.org/https://doi.org/10.20982/tqmp.092.p079>
- Zadeh, L., 1978. Fuzzy sets as a basis for a theory of possibility. *Fuzzy Sets Syst.* 1, 3–28. [https://doi.org/10.1016/0165-0114\(78\)90029-5](https://doi.org/10.1016/0165-0114(78)90029-5)
- Zheng, C., Bianchi, M., Gorelick, S.M., 2011. Lessons learned from 25 years of research at the MADE site. *Ground Water* 49, 649–662. <https://doi.org/10.1111/j.1745-6584.2010.00753.x>

- Zimmermann, H.J., 2000. Application-oriented view of modeling uncertainty. *Eur. J. Oper. Res.* 122, 190–198. [https://doi.org/10.1016/S0377-2217\(99\)00228-3](https://doi.org/10.1016/S0377-2217(99)00228-3)
- Zosseder, K., Böttcher, F., Davis, K., Haas, C., Halilovic, S., Hamacher, T., Heller, H., Odersky, L., Pauw, V., Schramm, T., Schulte, M., 2022a. Schlussbericht Verbundprojekt GEO-KW: Kopplung des geoth. Speicherpotenzials mit den wechselnden Anforderungen des urbanen Energiebedarfs zur effizienten Nutzung der regen. Energiequelle Grundwasser für die dez. Kälte- und Wärmebereitstellung in der Stadt. <https://doi.org/10.14459/2022md1692003>
- Zosseder, K., Böttcher, F., Haas, C., 2020. Das Projekt GEO.KW: Optimierung der Grundwassernutzung für die dezentrale Wärme- und Kältebereitstellung in der Stadt. *Geotherm. Energ.* 95, 12–13.
- Zosseder, K., Chavez-Kus, L., Kerl, M., Albarrán-Ordás, A., Beichel, K., Kotyla, Pa., Somogyi, G., 2015. Abschlussbericht zum GEPO-Forschungsvorhaben “Erstellung einer Datengrundlage für die Abschätzung des geothermischen Potenzials im oberflächennahen Untergrund des quartären Grundwasserleiters des Großraum Münchens”. Research report (unpublished).
- Zosseder, K., Chavez-Kus, L., Kerl, M., Albarrán-Ordás, A., Gossler, M.A., Kiecak, A., Küster, S., Schmetzer, T., 2023. Abschlussbericht zum GeoSPOT-Forschungsvorhaben “Geologische Nutzungs- und Speicherpotenziale im quartären und tertiären Untergrund des Großraums Augsburg”. Research report (unpublished).
- Zosseder, K., Chavez-Kus, L., Kerl, M., Albarrán-Ordás, A., Gossler, M.A., Theel, M., Kiecak, A., Huch, J., Schaller, T., 2019. Abschlussbericht zum GeoPot-Forschungsvorhaben “Parameterbestimmung für die Abschätzung der geologischen Nutzungspotenziale in der Planungsregion 14 und im tertiären Untergrund des Großraums München”. Research report (unpublished).
- Zosseder, K., Kerl, M., Albarrán-Ordás, A., Gossler, M., Kiecak, A., Chavez-Kus, L., 2022b. Die hydraulischen Grundwasserverhältnisse des quartären und des oberflächennahen tertiären Grundwasserleiters im Großraum München [The hydraulic groundwater conditions in the Quaternary and shallow Tertiary aquifer in the greater Munich area]. Bayerisches Landesamt für Umwelt (LfU). *Geologica Bavarica* 122 (2022).
- Zuber, A., Michalczyk, Z., Maloszewski, P., 2001. Great tritium ages explain the occurrence of good-quality groundwater in a phreatic aquifer of an urban area, Lublin, Poland. *Hydrogeol. J.* 9, 451–460. <https://doi.org/10.1007/s100400100149>

Appendices

Appendix A: Supporting information to Chapter 2

Tab. 6: Overview of the stochastic simulation methods with their main features.

Stochastic simulation method	Input data integration			Geological complexity	Applicability
	Well data	Soft data	Spatial continuity		
A Object-based	Limited	Not guaranteed		Crisp geometries	Crisp reservoir element geometries
A-1 Object-based A-2 Event-based			- Geometric rules - Temporal rules		
B Cell-based	Limitless	Limitless, high resolution			Geological complex systems
B-1 Variogram-based B-1.1 Sequential simulation SIS SGS B-1.2 <i>p</i> -field B-1.3 LU decomposition B-1.4 Simulated annealing			Variogram	Small-scale features with non-stationary	
B-2 Texture-based (e.g. MPS)			Training images	Repeating small-scale features with non-stationary	

Tab. 7: Literature review of the criteria used for defining the discrete values of a categorical variable when modeling unconsolidated sediments.

Classification criterion	Author	Area and depositional environment	Classes
Lithofacies	Stafleu et al. (2011)	- The Zeeland (The Netherlands) - Shallow marine, estuarine, and fluvial	17
	Bianchi et al. (2015)	- Glasgow (UK) - Glacial-fluvial	4: (1) soft clay, (2) stiff clay diamicton, (3) silt and sand, (4) sand and gravel
	Høyer et al. (2015)	- Central part of Denmark - Glacial-fluvial	6: (1) Paleogene clay, (2) Miocene sand, (3) sand till, (4) meltwater sand, (5) clay till, (6) meltwater clay
	Jørgensen et al. (2010)	- Egebjerg area (Denmark) - Glacial	6: (1) Paleogene clay, (2) clay till, (3) sand till, (4) meltwater sand/gravel, (5) sand, (6) diatomite
Lithostratigraphy	Stafleu et al. (2011)	- The Zeeland (The Netherlands) - Shallow marine, estuarine and fluvial	7
	Hademoos et al. (2019)	- Belgian Continental Shelf (Belgium) - Sediment-depleted shallow shelf	5
	Merritt et al. (2007)	- Glasgow (UK) - Glacial-fluvial	9
	Royse (2010)	- London (UK) - Marine, shallow marine to fluvial	5

	Høyer et al. (2015)	- Central part of Denmark - Glacial-fluvial	42
Lithology and/or grain-size	Stafleu et al. (2011)	- The Zeeland (the Netherlands) - Shallow marine, estuarine and fluvial	7: (1) Organic deposits, (2) clay, (3) clayey sand and sandy clay, (4) fine sand, (5) medium sand, (6) coarse sand, gravel and shells, (7) sand, grain size unknown
	Hademoos et al. (2019)	- Belgian Continental Shelf (Belgium) - Sediment-depleted shallow shelf	6: (1) gravel, (2) coarse sand, (3) medium sand, (4) fine sand, (5) silt, (6) clay
	Kearsey et al. (2015)	- Glasgow (UK) - Glacial-fluvial	6: (1) organic, (2) soft clay, (3) stiff clay, (4) diamicton, (5) sand, (6) sand and gravel
Hydrofacies	Bayer et al. (2011), Comunian et al. (2011)	- The Herten site (Germany) - Glacial	10: Poorly sorted, matrix supported gravel, normal (1, Gcm), cobble-rich (2, cGcm), sand-rich (3, sGcm); alternating gravel, Matrix-free, clast-supported open framework coarse - fine pebbles (4, Gcg, o), cobbles-coarse pebbles openwork (5, cGcg, o), granules/sand open framework (6, sGcg, o), bimodal basal subunit with sand matrix (7, sGcm, b), bimodal basal subunit with silt/clay matrix (8, fGcm, b), well sorted gravel (and coarse sand) (9, GS-x), pure, well sorted sand (10, S-x)
Geotechnics	Khojasteh (2013)	- The Göttingen test site (Germany) - Fluvial	4: (1) coarse-grained sediments, (2) mixed grain-size sediments, (3) fine-grained sediments, (4) organogenetic sediments of sediments with organic constituents

Tab. 8: Considerations of geological uncertainties according to different authors

Author	Considerations of uncertainties
Mann (1993)	<p style="text-align: center;"><u>Types of uncertainties</u></p> <ol style="list-style-type: none"> 1. Observation errors, bias and measurement imprecisions 2. Inherent variability and stochasticity 3. Ignorance, lack of knowledge, model imperfections and generalizations
Zimmermann (2000)	<p style="text-align: center;"><u>Causes of uncertainty</u></p> <ol style="list-style-type: none"> 1. Lack of information 2. Abundance of information (complexity) 3. Conflicting evidence 4. Ambiguity 5. Measurement 6. Belief (subjective belief of observer about a certain situation)
Jones et al. (2004) McCaffrey et al. (2005)	<p style="text-align: center;"><u>Types of uncertainties in the mapping campaigns</u></p> <ol style="list-style-type: none"> 1. Data acquisition (position, measurement, scale-dependent, observational, temporal, sampling) 2. Primary interpretation (correlation, interpolation, inference from topography) 3. Compound interpretation (2-D map, cross-section, 3-D structural model)
Bárdossy and Fodor (2004)	<p style="text-align: center;"><u>Types of uncertainties</u></p> <ol style="list-style-type: none"> 1. Inherent natural variability (independent of geologic investigations) 2. Sampling error 3. Observation error 4. Measurement error 5. Errors of the mathematical evaluation of geological data 6. Propagation of errors 7. Conceptual and model uncertainty <p style="text-align: center;"><u>Aspects</u></p> <ol style="list-style-type: none"> 1. Important contribution to uncertainty from the inherent natural variability 2. Uncertainty evaluation should start at the level of the input data and avoid the use of crisp values 3. Need to avoid the propagation of errors by not repeating parameters
Wellmann et al. (2010)	<p style="text-align: center;"><u>Types of uncertainties in 3-D structural models, adaptation of Mann (1993)</u></p>

	<ol style="list-style-type: none"> 1. Input data 2. Interpolation and extrapolation from known data points 3. Incomplete knowledge about the structural existence
Wellmann and Caumon (2018)	<p style="text-align: center;"><u>Levels of uncertainty in the construction of 3-D structural models</u></p> <ol style="list-style-type: none"> 1. Conceptual model (e.g. complexity, scale) 2. Structure of the mathematical model (e.g. number of layers) 3. Parameters of mathematical model (e.g. variogram) 4. Input data for interpolation (e.g. interface positions)

Appendix B: Supporting information to Chapter 4

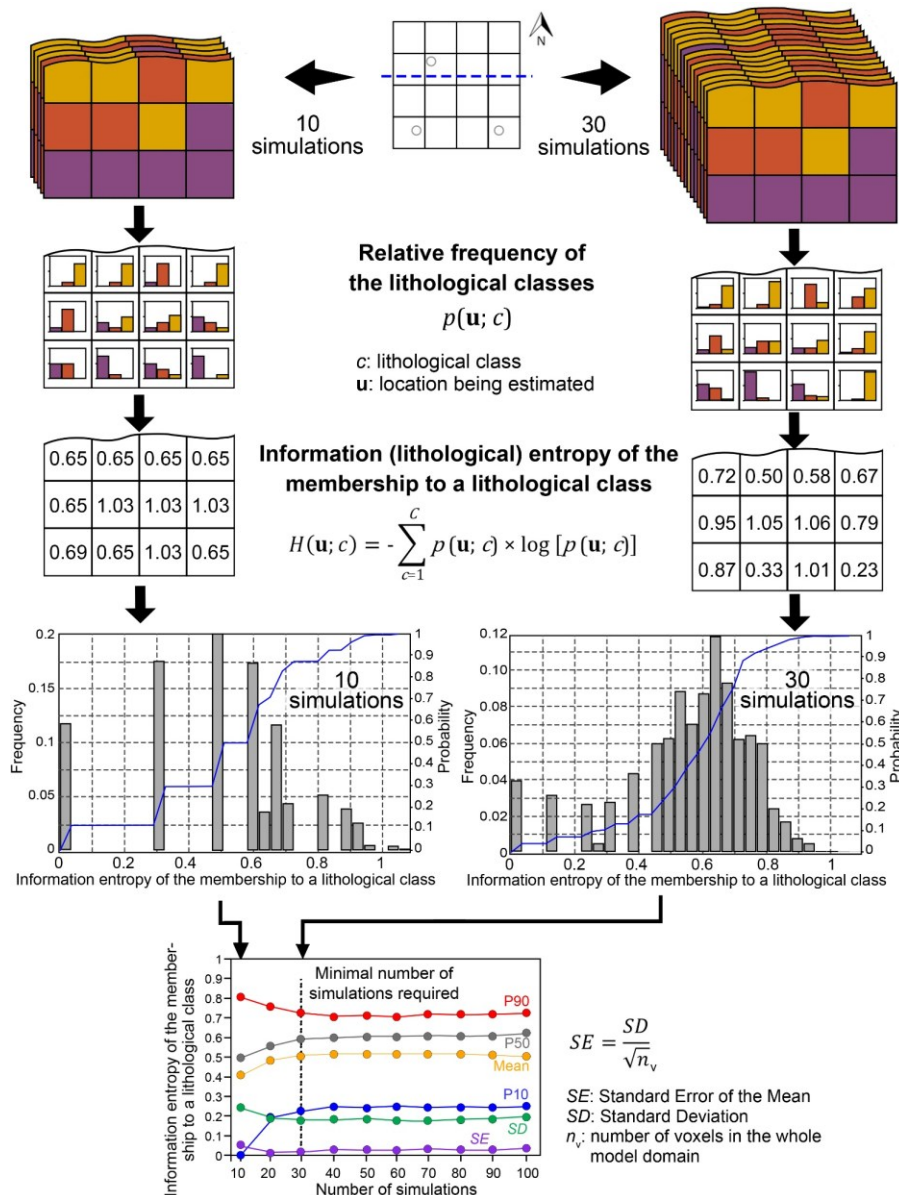


Fig. 71: Illustration showing the process of quantifying the summary statistics of the information entropy of the membership to a lithological class for two simulation sets consisted of 10 and 30 simulations. The procedure is the same for the remaining sets of 20, 40, 50, 60, 70, 80, 90, etc. simulations, respectively. The minimal number of simulations required was obtained when the summary statistics converged to a constant value so that an increase in the number of realizations did not lead to a significant change in the lithological attribution in the whole model. Modified after Albarrán-Ordás and Zosseder (2022)

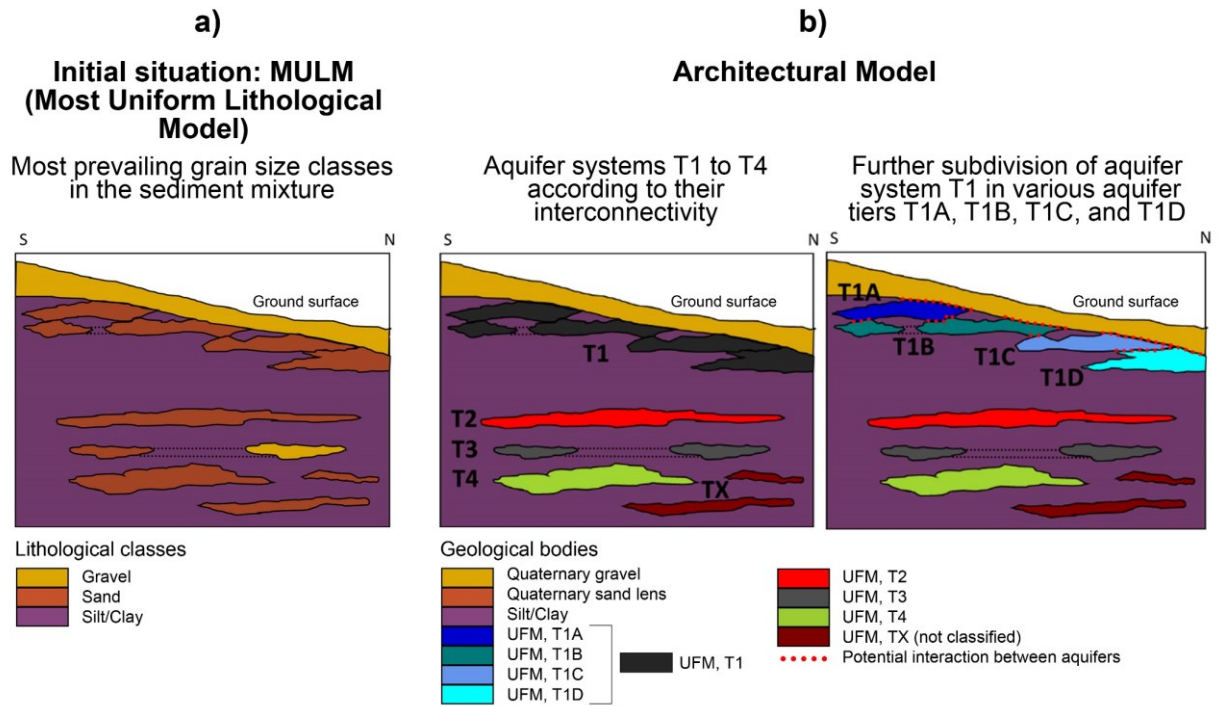


Fig. 72: Schematic graph showing the architectural model of the Quaternary and UFM deposits in the case study in the city of Munich. UFM: Upper Freshwater Molasse. The red dots represent the different areas of preferential connectivity between aquifer tiers

Tab. 9: Overview of the aquifer systems and tiers from the architectural model of the Quaternary and UFM deposits in the case study in the city of Munich. m.a.s.l.: meters above sea level; UFM: Upper Freshwater Molasse; P10: 10th percentile; P50: 50th percentile; P90: 90th percentile, M: arithmetic mean; SD: Standard deviation; min: minimum value; max: maximum value

Aquifer system/ tier	Description	Thickness (m)	Stratigraphy and lithology	Area (km ²)	Elevation (m.a.s.l.)	Aquifer interactions
T1A	T1: First Tertiary aquifer system from the Earth's surface. A: Highest aquifer tier located in T1 aquifer system	P10=2.00, P50=7.00, P90=12.99, M=7.10, min=1.00, max=23.00, SD=4.08	Tertiary, UFM Sandy	95	492-533	-Quaternary -T1B
T1B	T1: First Tertiary aquifer system from the Earth's surface. B: Second highest aquifer tier located in T1 aquifer system	P10=3.00, P50=8.02, P90=14.99, M=8.67, min=1.00, max=28.00, SD=4.66	Tertiary, UFM Sandy	163	476-518	-Quaternary -T1A -T1C
T1C	T1: First Tertiary aquifer system from the Earth's surface. C: Third highest aquifer tier located in T1 aquifer system	P10=2.02, P50=8.00, P90=15.02, M=8.56, min=1.00, max=23.00, SD=4.84	Tertiary, UFM Sandy	115	465-496	-Quaternary -T1B -T1D
T1D	T1: First Tertiary aquifer system from the Earth's surface. D: Forth highest aquifer tier located in T1 aquifer system	P10=2.01, P50=9.02, P90=22.00, M=11.03, min=1.00, max=28.00, SD=7.37	Tertiary, UFM	144	435-474	-Quaternary -T1C
T2	T2: Second Tertiary aquifer system from the Earth's surface	P10=3.00, P50=7.03, P90=16.02, M=8.61, min=1.00, max=26.00, SD=5.37	Tertiary, UFM Sandy, locally gravelly	235	381-448	No
T3	T3: Second Tertiary aquifer system from the Earth's surface	P10=2.99, P50=6.98, P90=29.00, M=11.48, min=1.00, max=46.00, SD=10.52	Tertiary, UFM Sand and gravelly	134	352-414	No
T4	T4: Second Tertiary aquifer system from the Earth's surface	P10=4.01, P50=14.00, P90=19.00, M=12.79, min=1.00, max=22.00, SD=5.45	Tertiary, UFM Sandy and gravelly	154	157-170	No

Appendix C: Supporting information to Chapter 5

Fig. 73 illustrates an exemplary application of the UQ measures in three direct soil observations from drilled materials. Whereas the main components with relative percentages of at least 40% are identified by a capital letter, e.g., G for gravel, fG for fine-grained gravel or mG for medium-grained gravel, the secondary components are represented by lowercase letters with a quantifier denoting the relative percentage (quantifier ‘: 5-15%, no quantifier: 15-30%).

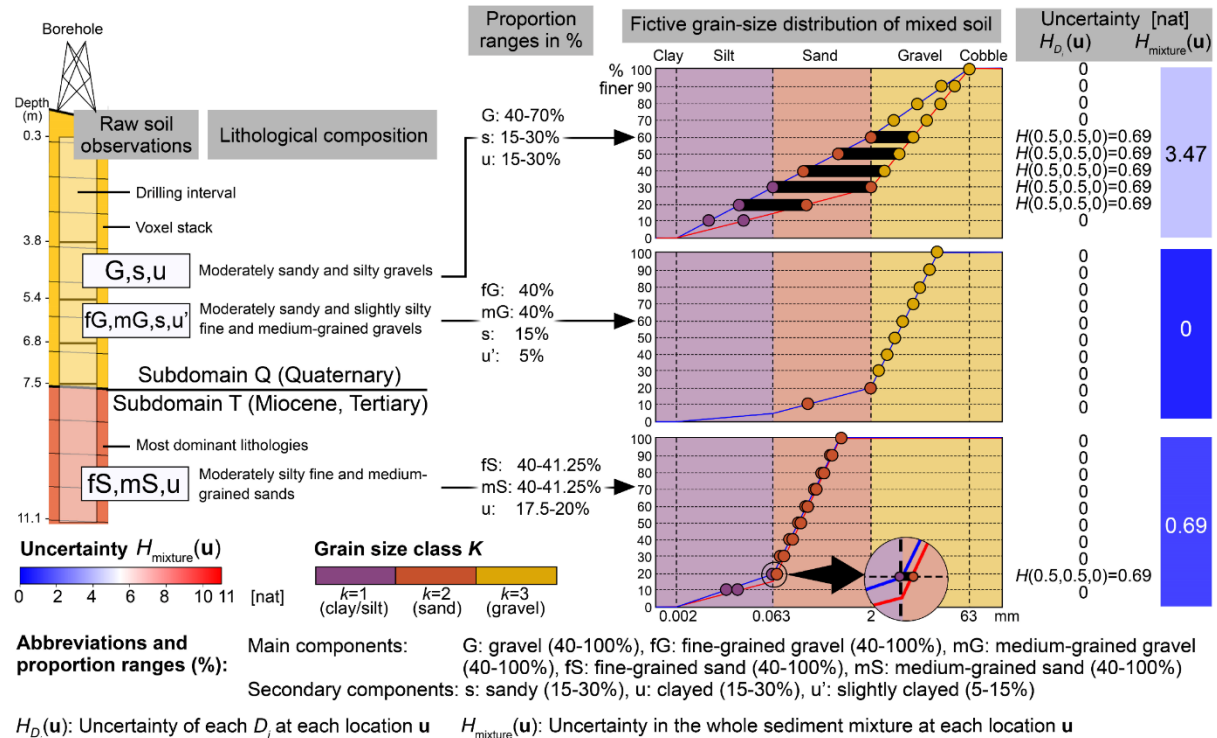


Fig. 73: Exemplary application of the UQ measures in three soil observations from drilled material

The imprecise proportion ranges leave much room for variation in the code (G,s,u), since the gravel fraction may vary between 40% and 70% and both the sand and clay fractions also fluctuate considerably (15-30%). This imprecise description leads to obtain two equiprobable grain size classes at some cumulative frequencies, indicated by the black bars in Fig. 73 right top. This translates in complete certainty ($H=0$) for $i=10, 70, 80, 90$ and 100 , some uncertainty measured by $H(0.5,0.5,0)$ for the remaining cumulative frequencies and an uncertainty about the entire GSD of $H=3.47$ nat on a maximum scale of 11 (see Fig. 73). However, the code (fG,mG,s,u) leaves no room for variation according to the standards used for soil description. Consequently, only one grain size class can be inferred for every cumulative frequency, thus leading to complete certainty for all i and for the entire GSD (see Fig. 73). The quantification of the third soil description, i.e., (fS,mS,u), is subject to uncertainty only for $i=20$. Since the silt fraction may vary only between 17.5% and 20% and the sand fraction fluctuates also very little (80-82.5%), two equiprobable grain size classes can be only obtained at one cumulative frequency, i.e., for $i=20$.

Simulation setup 3 (Non-stationary SK, sub-domains Q and T, trend highly overfit)

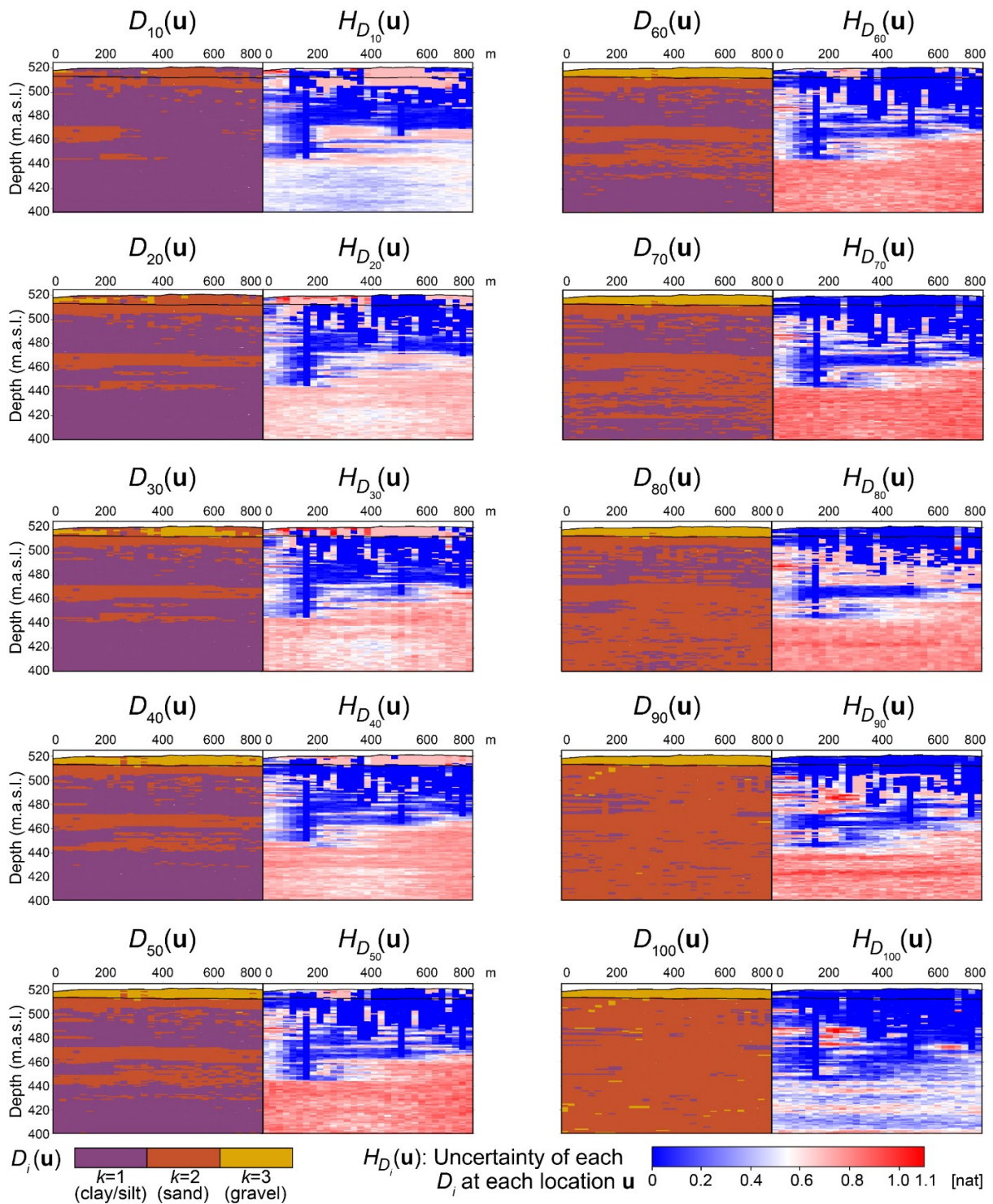


Fig. 74: Results of UQ in the partial lithological models of Simulation setup 3

Simulation setup 4 (Non-stationary SK, sub-domains Q and T, trend slightly overfit)

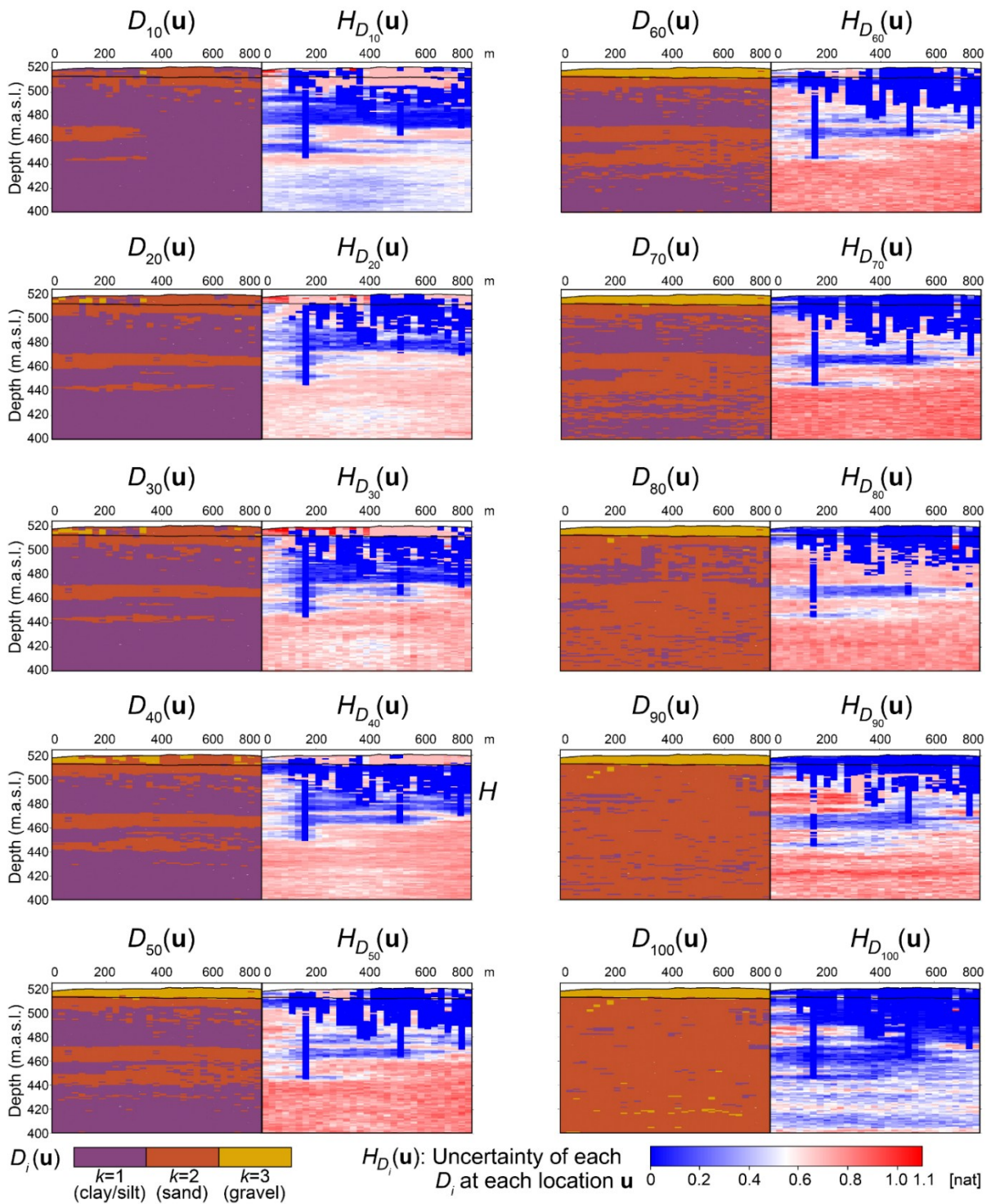


Fig. 75: Results of UQ in the partial lithological models of Simulation setup 4

Simulation setup 5 (Non-stationary SK, sub-domains Q and T, trend non overfit)

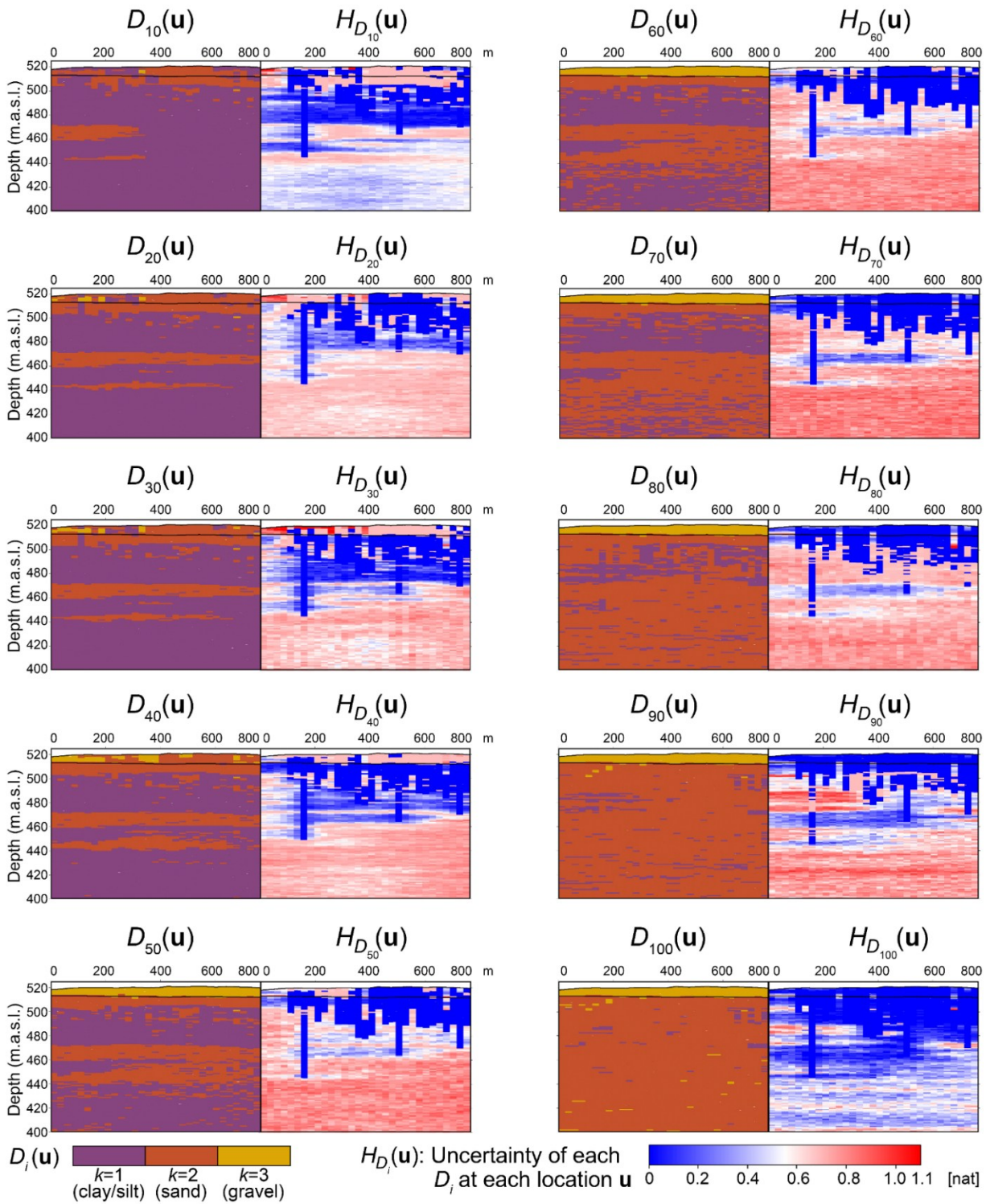


Fig. 76: Results of UQ in the partial lithological models of Simulation setup 5

Appendix D: Supporting information to Chapter 6

Appendix D-1: Summary of the main steps of the D_i models method

The present appendix summarizes the main features of the stochastic 3-D modeling using GSD with the D_i models method. It is structured based on the information outlined in Albarrán-Ordás and Zosseder (2023, 2022). The D_i models method was conceived as a stochastic approach to make predictions of the 3-D lithological composition of detrital systems based on estimating the fictive grain size distribution of the sediment mixture by using soil observations from drilled materials. The implementation of the method can be summarized in the following steps:

Step 1 - Conceptual model

1.1 Definition of a number C of mutually exclusive and exhaustive grain size classes:

$$c=1, 2, \dots, C \quad (\text{see Fig. 77, at left}).$$

1.2 Definition of a set of cumulative frequencies in the GSD i by fixing a constant percentile step p divisor of 100. The GSD is then characterized by a number $N = 100/p$ of cumulative frequencies.

$i=p, 2p, 3p, \dots, Np$; where $Np=100$ (see Fig. 77, the part immediately to the left of the GSD plot)

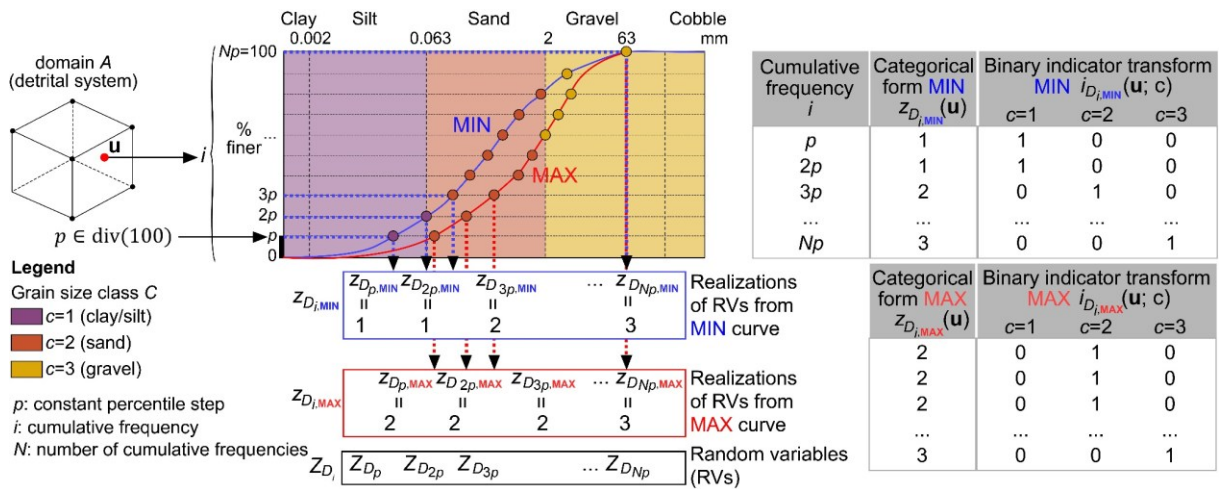


Fig. 77: Concept of the random 3-D modeling of GSD with the D_i models method: Introduction of a series of RVs representing a grain size class for each i . Modified after Albarrán-Ordás and Zosseder (2023)

These two parameters lead to introduce two categorical random variables (RVs) representing the grain size class per each i , whereas $Z_{D_i,MIN}(\mathbf{u})$ represents the RV with the finest-grained class and $Z_{D_i,MAX}(\mathbf{u})$ represents the coarsest-grained class (see Fig. 77, at right). The categorical RVs can be also be expressed as a series of two indicator RVs, i.e., $I_{D_i,MIN}(\mathbf{u})$ and $I_{D_i,MAX}(\mathbf{u})$ (see far right table in Fig. 77).

Step 2 - Transformation of input data: soil descriptions from drilled material

The input data are direct soil descriptions from drilled materials described in the field comprising a sequence of symbols marking the soil in terms of the types of the observed grain sizes and their proportion range (%) in the soil. These raw data are transformed for further integration in the geo-modeling framework of the D_i models method so that they are converted into fictive grain size ranges of the different grain fractions contained in the sequence of symbols (see Fig. 78).

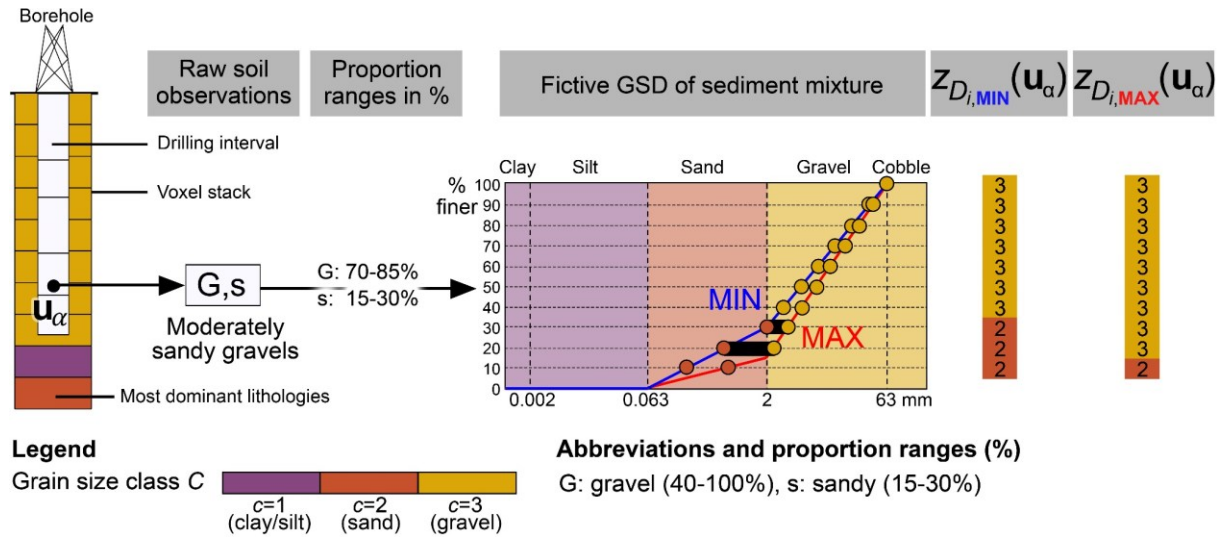


Fig. 78: Exemplary soil observation used as hard data in the D_i models method: transformation of raw soil observations for their further integration in the geo-modeling framework Modified after Albarrán-Ordás and Zosseder (2023)

Step 3 - Spatial statistical inference

The geostatistical simulation is conditioned to both prior models of local proportions $P_{D_i,MIN}(\mathbf{u}; c)$ and $P_{D_i,MAX}(\mathbf{u}; c)$. The assumption of stationarity implies consideration of the prior proportions to be constant and equal to the global mean probabilities of each grain size class in each domain. However, opting for integrating non-stationarities implies consideration of a 3-D trend model consisting of locally varying proportions.

Step 4 - Spatial continuity model

The indicator 3-D variograms $\gamma_{I_{D_i,MIN}}(\mathbf{h}; c)$ and $\gamma_{I_{D_i,MAX}}(\mathbf{h}; c)$ are inferred for each cumulative frequency i , where \mathbf{h} denotes the separation vector between points pairs.

Step 5 - Geostatistical simulation

Application of Sequential Indicator Simulation (SIS) for each cumulative frequency by sampling of the conditional cumulative distribution function (CCDF). The indicator kriging estimators $I_{D_i,MIN}^*(\mathbf{u}; c)$ and $I_{D_i,MAX}^*(\mathbf{u}; c)$ provide the local conditional probability for each c at an unsampled location, which is integrated into a CCDF.

Step 6 - Lithological predictability

6.1 Calculation of the probability of each grain size class c at each location for each i over a large number of realizations L based on the set of possible equiprobable realizations of the categorical RVs at any location, i.e., $z_{D_i}^*(\mathbf{u})$:

$$p_{D_i}(\mathbf{u}; c) = \frac{1}{L} \sum_{l=1}^L z_{D_i}^{*l}(\mathbf{u}; c); \quad \mathbf{u} \in A.$$

6.2 Calculation of the partial percentile lithological models or D_i models, $D_i(\mathbf{u})$, representing the grain size classes at a location with the highest probabilities, expressed as follows:

$$D_i(\mathbf{u}) = c; \text{ if } \max\{p_{D_i}(\mathbf{u}; c)\} = p_{D_i}(\mathbf{u}; c); \quad c = 1, \dots, C; \quad \mathbf{u} \in A.$$

6.3 Calculation of the distribution of the most dominant grain size classes for the whole GSD at each location, expressed by the Most Uniform Lithological Model, denoted by MULM(\mathbf{u}) (Albarrán-Ordás and Zosseder, 2022).

Step 7 - Multipurpose usability

The availability of fictive GSD in individual voxels strongly encourages the model usability from various viewpoints, summarized in Fig. 79.

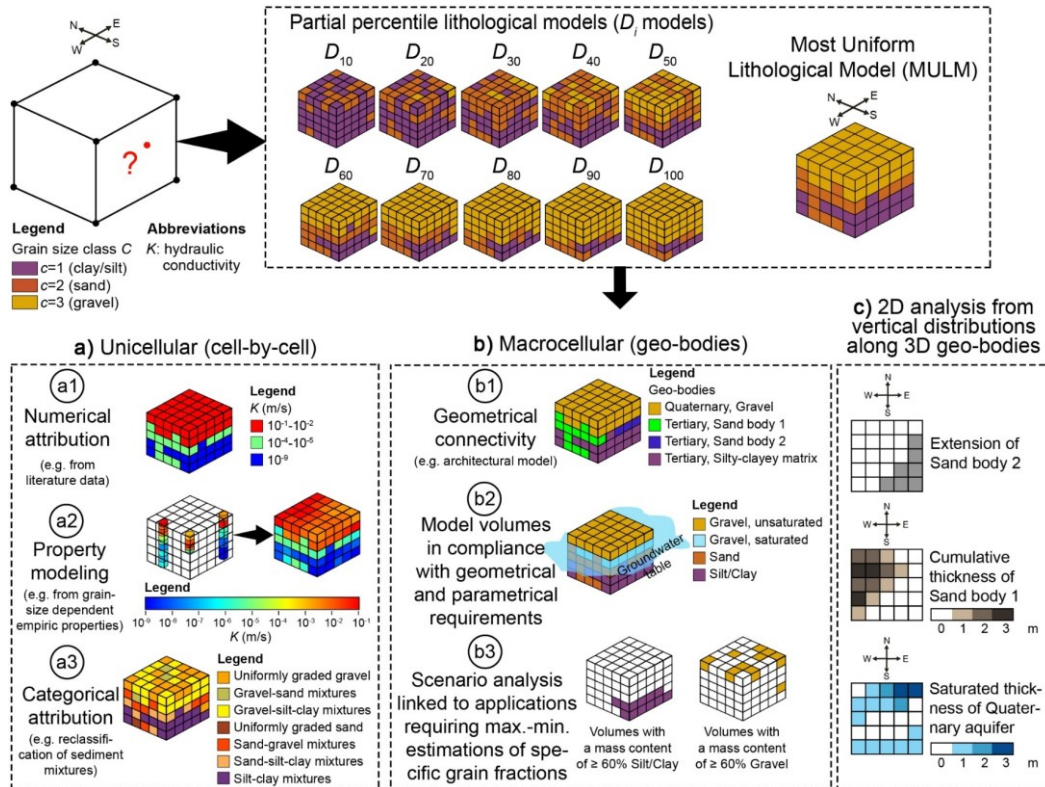


Fig. 79: Step 7 of the D_i models method: Multipurpose usability. Modified after Albarrán-Ordás and Zosseder (2022)

Appendix D-2: Selected empirical relationships relating hydraulic conductivity K and the size property of porous media used in the article

Tab. 10: Selected empirical relationships relating hydraulic conductivity K and the size property of porous media used in the article

Author	Empirical equation K (m/s)	Domain of applicability and limitations according to the literature review	Implemented criteria in the geological 3-D model
Seelheim (1880)	$K = 0.00357 * d_{50}^{2.3}$ <p>where: d_{50}: grain diameter for 50% finer d_{10}: grain diameter for 10% finer (at right) C_U: coefficient of uniformity ($C_U = d_{60}/d_{10}$) d_{60}: grain diameter for 60% finer (at right)</p>	Applicable to uniformly graded sands with $C_U < 5$ (Brunetti et al., 2021; Entenmann, 1992). This method might provide inaccurate results (Entenmann, 1992)	$C_U < 5$ $0.06 \text{ mm} \leq d_{10} \leq 0.6 \text{ mm}$ Gravel proportion: < 40%
Hazen (1892)	$K = C_U * d_{10}^2$ <p>where: C_U: coefficient of uniformity ($C_U = d_{60}/d_{10}$) $C_U = 0.0139$ ($1 < C_U < 3$) $C_U = 0.0116$ ($3 < C_U < 5$) (Skaballanowitsch, 1954) d_{10}: grain diameter for 10% finer d_{60}: grain diameter for 60% finer</p>	Applicable to uniformly graded sands with low fines (Entenmann, 1992; Fuchs, 2010) and fine sands to gravels, provided the sediment has a C_U less than 5 and a d_{10} value between 0.1 mm and 3 mm (Cheng and Chen, 2007; Devlin, 2015; Odong, 2007; Williams et al., 2019). It provides intermediate K values in Quaternary gravels (Pucko and Verbovšek, 2015) and good results for filter sands (Entenmann, 1992).	$C_U < 5$ $0.1 \text{ mm} \leq d_{10} \leq 3 \text{ mm}$
Beyer (1964)	$K = x * d_{10}^2$ <p>where: $x = f(C_U)$ (correction factor) d_{10}: grain diameter for 10% finer C_U: coefficient of uniformity ($C_U = d_{60}/d_{10}$) d_{60}: grain diameter for 60% finer (at right)</p>	Applicable to sands and gravels (Entenmann, 1992; Fuchs, 2010), materials with heterogeneous distributions and poorly sorted grains (Alvarado Blohm, 2016; Göktepe and Sezer, 2010; Odong, 2007), sediments with a d_{10} value between 0.06 mm and 0.6 mm (Cheng and Chen, 2007; Devlin, 2015). It provides intermediate K values in Quaternary gravels (Pucko and Verbovšek, 2015). If $C_U > 20$, the method is too inaccurate and should be used only as an approximation (Szymczak et al., 2012). Deviations of +/- 30% from pumping-test data (Entenmann, 1992). Accurate results for sands (Entenmann, 1992).	$1 \leq C_U < 20$ $0.06 \text{ mm} \leq d_{10} \leq 0.6 \text{ mm}$
Kozeny-Carman (Carman, 1956, 1939; Kozeny, 1927)	$K = \frac{g}{v} * 8.3 * 10^{-3} \left[\frac{n^3}{(1-n)^2} \right] * d_{10}^2$ <p>where: n: porosity ($n = 0.255 * (1 + 0.83^{C_U})$) (Vuković and Soro, 1992) C_U: coefficient of uniformity g: gravitational acceleration v: kinematic viscosity of water d_{10}: grain diameter for 10% finer</p>	Applicable to coarse-grained sands (Říha et al., 2018), sands (Chapuis, 2012), gravels, sands, and silty soil (Chandel and Shankar, 2022). Not recommended to: clayed sediments (Alvarado Blohm, 2016; Ishaku et al., 2011) and coarse-grained deposits with $d_{10} > 3 \text{ mm}$ (Williams et al., 2019). The clay-silt percentage should be smaller than 25% (Williams et al., 2019). This method might lead to underestimating K (Oh et al., 2013) and intermediate K values in Quaternary gravels (Pucko and Verbovšek, 2015). In gravels and coarser soils, a more advanced formula must be used (Barahona-Palomo, 2014; Chapuis and Aubertin, 2003).	$d_{10} \leq 3 \text{ mm}$ Silt and clay proportion: < 25% Gravel proportion: < 40%
Adaptation of Kozeny-Carman for high conductive gravels (HCG) (Bianchi and Zheng, 2016)	$K = \frac{g}{v} * 8.3 * 10^{-3} \left[\frac{n^3}{(1-n)^2} \right] * \left(\frac{d_{10} + d_{25}}{2} \right)^2$ <p>where: n: porosity ($n = 0.255 * (1 + 0.83^{C_U})$) (Vuković and Soro, 1992) C_U: coefficient of uniformity ($C_U = d_{60}/d_{10}$)</p>	Applicable to HCG (high conductive gravels) with a gravel proportion higher than 50%, a proportion of fines less than 5%, a d_{10} value higher than 0.25 mm, and a d_{25} value higher than 1 mm (Bianchi and Zheng, 2016).	$d_{10} > 0.25 \text{ mm}$ $d_{25} > 1 \text{ mm}$ Gravel proportion: > 50% Silt and clay proportion: < 5%

	<p>g: gravitational acceleration ν: kinematic viscosity d_{10}: grain diameter for 10% finer d_{25}: grain diameter for 25% finer d_{60}: grain diameter for 60% finer</p>		
Slichter (1899)	$K = \frac{g}{\nu} * 1 * 10^{-2} * n^{3.287} * d_{10}^2$ <p>where: n: porosity ($n = 0.255 * (1 + 0.83^{C_U})$) (Vuković and Soro, 1992) C_U: coefficient of uniformity ($C_U = d_{60}/d_{10}$) g: gravitational acceleration ν: kinematic viscosity d_{10}: grain diameter for 10% finer d_{60}: grain diameter for 60% finer</p>	<p>Applicable to sediments with a d_{10} value between 0.01 mm and 5 mm (Alvarado Blohm, 2016; Brunetti et al., 2021; Cabalar and Akbulut, 2016; Cheng and Chen, 2007; Ishaku et al., 2011; Odong, 2007). It provides good results in uniformly graded sands (Urumović et al., 2020) and very low K values in gravels (Brunetti et al., 2021; Chandel and Shankar, 2022; Cheng and Chen, 2007; Pucko and Verbovšek, 2015).</p>	<p>0.01 mm $\leq d_{10} \leq$ 5 mm Gravel proportion: < 40%</p>
USBR (Bialas and Kleczkowski, 1970)	$K = 0.0036 * d_{20}^{2.3}$ <p>where: d_{20}: grain diameter for 20% finer d_{10}: grain diameter for 10% finer (at right)</p>	<p>For glacial till and mixed-grained soils (Entenmann, 1992; Szymczak et al., 2012), medium-grained sands with $C_U < 5$ (Cheng and Chen, 2007; Ishaku et al., 2011; Odong, 2007; Říha et al., 2018). This method might lead to underestimating K (Chandel and Shankar, 2022; Oh et al., 2013; Urumović et al., 2020), especially in Quaternary gravels (Pucko and Verbovšek, 2015). It should be used only as an approximation in glacial till (Entenmann, 1992). It provides good results in sediments with $C_U < 5$ and $0.1 \text{ mm} \leq d_{10} \leq 3 \text{ mm}$ (Cheng and Chen, 2007; Vuković and Soro, 1992). However, Alvarado Blohm (2016) and Sahu and Saha (2016) reported good results in sediments with $C_U > 5$. Alvarado Blohm (2016) reported an application range of $0.063 \text{ mm} \leq d_{10} \leq 2 \text{ mm}$.</p>	<p>0.063 mm $\leq d_{10} \leq$ 2 mm This method will be applied in gravels only if no other methods can be used.</p>
USCRO (Urumović et al., 2020)	$K = 0.0117 * d_{20}^{2.32} (C_U < 5)$ <p>(uniformly graded sand)</p> $K = 0.0323 * d_{20}^{2.32} (5 < C_U < 92)$ <p>(sandy gravels)</p> <p>where: C_U: coefficient of uniformity ($C_U = d_{60}/d_{10}$) d_{20}: grain diameter for 20% finer d_{60}: grain diameter for 60% finer d_{10}: grain diameter for 10% finer</p>	<p>Applicable to uniformly graded sands and sandy gravels (Urumović et al., 2020)</p>	<p>Uniformly graded sands: $C_U < 5$ and gravel proportion < 40%. Sandy gravels: $5 < C_U < 92$, silty and clay proportion equals zero</p>
Seiler (1973)	$K = x * d_{10}^2 \quad x = f(C_U) \quad (C_U \leq 17)$ $K = x * d_{25}^2 \quad x = f(C_U) \quad (17 < C_U \leq 100)$ <p>where: x: correction factor C_U: coefficient of uniformity ($C_U = d_{60}/d_{10}$) d_{10}: grain diameter for 10% finer d_{25}: grain diameter for 25% finer d_{60}: grain diameter for 60% finer</p>	<p>Applicable to sands and gravels with a coefficient of uniformity between 5 and 100 (Seiler, 1973)</p>	<p>5 $\leq C_U \leq$ 100 Silt and clay proportion: < 40%</p>
Harleman et al. (1963)	$K = \frac{g}{\nu} * \beta * d_{10}^2$ <p>where: g: gravitational acceleration</p>	<p>Applicable to sands (Chapuis, 2012), coarse and well distributed samples (Chandel and Shankar, 2022). It provides inaccurate results in gravels (Oh et al., 2013). This method might lead to an underestimation of K (Chandel and Shankar, 2022). When using this method, the deviations</p>	<p>Gravel proportion: < 40% Sand proportion: \geq 40%</p>

	<p>v: kinematic viscosity d_{10}: grain diameter for 10% finer $\beta = 0.000654$ (Říha et al., 2018)</p>	become more severe for heterogeneous materials where grain sizes vary greatly (Uma et al., 1989).	
Chapuis (2004)	$K = 2.4622 * 10^{-2} * [d_{10}^2 * e^3 / (1 + e)]^{0.7825}$ <p>where: e: void ratio ($e = \frac{n}{1-n}$) n: porosity ($n = 0.255 * (1 + 0.83^{C_U})$) (Vuković and Soro, 1992) C_U: coefficient of uniformity ($C_U = d_{60}/d_{10}$) d_{10}: grain diameter for 10% finer d_{60}: grain diameter for 60% finer</p>	Applicable to uniformly graded sands and gravels with $C_U < 12$ (Chapuis, 2004) and $0.003 \text{ mm} \leq d_{10} \leq 3 \text{ mm}$ (Chapuis, 2012). This method can be extended to silty soils (Chapuis, 2004). It might lead to underestimating K (Chandel and Shankar, 2022). It provides inaccurate results in gravels (Oh et al., 2013).	$C_U < 12$ $0.3 \leq e \leq 1$ $0.003 \text{ mm} \leq d_{10} \leq 3 \text{ mm}$ Gravel proportion: < 40%
Sauerbrey (1932)	$K = \frac{g}{v} * C_Z * \frac{n^3}{(1-n)^2} * d_{17}^2$ <p>where: n: porosity ($n = 0.255 * (1 + 0.83^{C_U})$) (Vuković and Soro, 1992) C_U: coefficient of uniformity ($C_U = d_{60}/d_{10}$) g: gravitational acceleration v: kinematic viscosity d_{17}: grain diameter for 17% finer $C_Z = 0.00375$ d_{60}: grain diameter for 60% finer d_{10}: grain diameter for 10% finer</p>	Applicable to sands and sandy clays (Cheong et al., 2008; Devlin, 2015), with a domain of application of $d_{17} \leq 0.5 \text{ mm}$ (Cheong et al., 2008; Oh et al., 2013). This method provides inaccurate results in gravels (Oh et al., 2013).	$d_{17} \leq 0.5 \text{ mm}$ Gravel proportion: < 40% This method will be applied in gravels only if no other methods can be applied.
NAVFAC (Chapuis et al., 2005)	$K = 10^{-2} * 10^{1.2921 * e - 0.6435} * d_{10}^{10^{0.5504 - 0.2937 * e}}$ <p>where: e: void ratio ($e = \frac{n}{1-n}$) n: porosity ($n = 0.255 * (1 + 0.83^{C_U})$) (Vuković and Soro, 1992) C_U: coefficient of uniformity ($C_U = d_{60}/d_{10}$) d_{10}: grain diameter for 10% finer d_5: grain diameter for 5% finer d_{60}: grain diameter for 60% finer</p>	Applicable to sands and gravels with $2 \leq C_U \leq 12$, $d_{10} / d_5 > 1.4$, $0.3 \leq e \leq 0.7$, $0.1 \text{ mm} \leq d_{10} \leq 2 \text{ mm}$ (Cabalar and Akbulut, 2016; Chapuis, 2012, 2004).	$2 \leq C_U \leq 12$ $d_{10} / d_5 > 1.4$ $0.3 \leq e \leq 0.7$ $0.1 \text{ mm} \leq d_{10} \leq 2 \text{ mm}$
Kaubisch (1986)	$K = 10^{0.0005 * P^2 - 0.12 * P - 3.59}$ <p>where: P: percentage for grains with $d < 0.06 \text{ mm}$ (Brunetti et al., 2021; Williams et al., 2019) d: grain size diameter</p>	Applicable to any soil (Chapuis, 2012), especially to mixed-grained soils with a higher content of fines in the range of K lower than 10^{-6} m/s (Szymczak et al., 2012).	Silt and clay proportion: 10-60%
Shahabi et al. (1984)	$K = 0.012 * C_U^{0.735} * d_{10}^{0.89} * \frac{e^3}{1 + e}$ <p>where: e: void ratio ($e = \frac{n}{1-n}$) n: porosity ($n = 0.255 * (1 + 0.83^{C_U})$) (Vuković and Soro, 1992) C_U: coefficient of uniformity ($C_U = d_{60}/d_{10}$) d_{10}: grain diameter for 10% finer d_{60}: grain diameter for 60% finer</p>	Applicable to sands with $1.2 \leq C_U \leq 8$, $0.38 \leq e \leq 0.73$ and $0.15 \text{ mm} \leq d_{10} \leq 0.59 \text{ mm}$ (Chapuis, 2012)	$1.2 \leq C_U \leq 8$ $0.38 \leq e \leq 0.73$ $0.15 \text{ mm} \leq d_{10} \leq 0.59 \text{ mm}$

Appendix D-3: Averaging of hydraulic conductivity K in alternating beds of heterogeneous detrital systems in the geological 3-D model

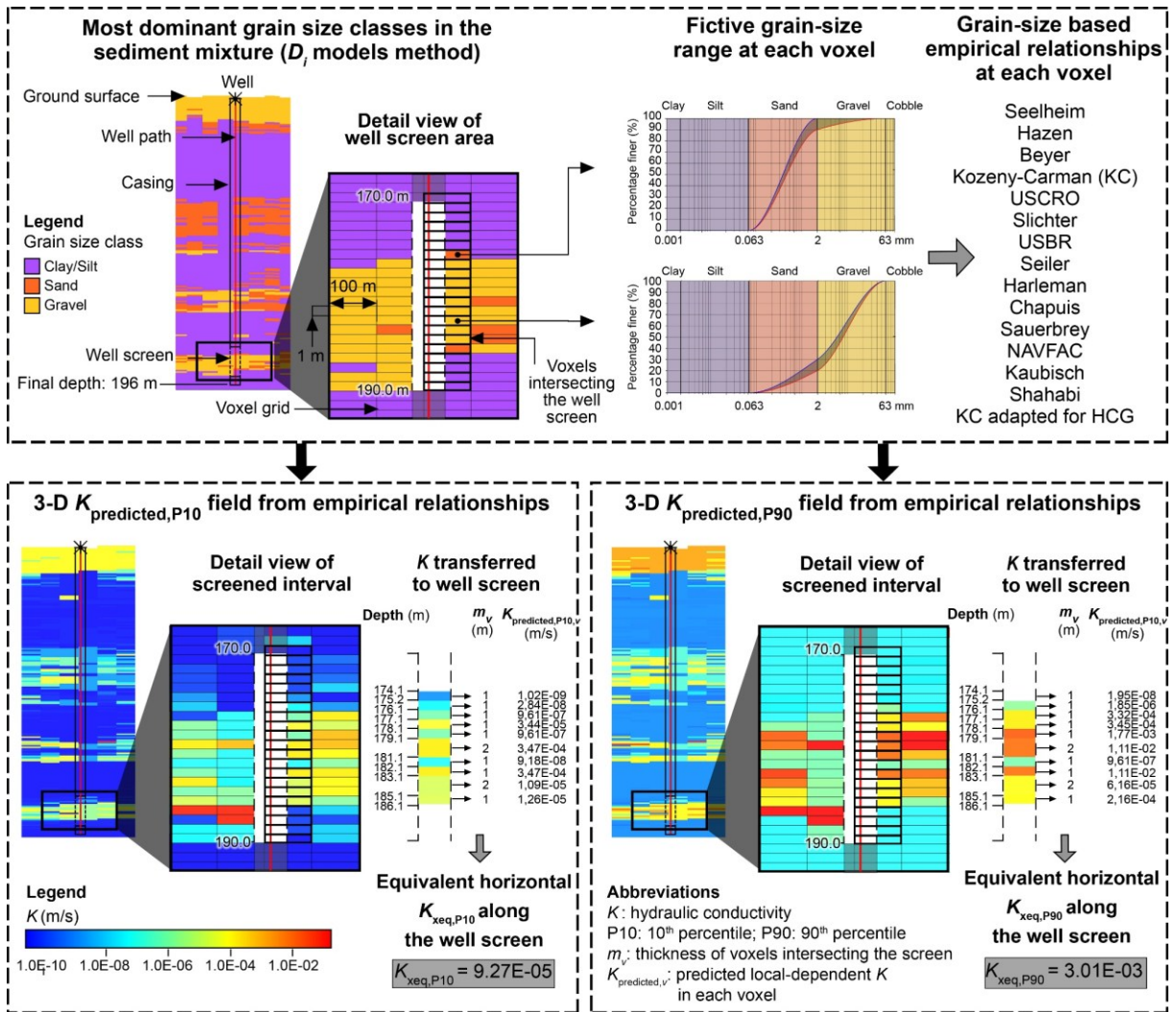


Fig. 80: Averaging of hydraulic conductivity K in alternating beds in the immediate vicinity of the wells

Appendix D-4. Prediction performance in the immediate vicinity of the well screens in the city of Munich: Relationship between predicted K_{xeq} and measured K_{pump} versus the proportion of each grain size class in the screened aquifer portion

The minimum and maximum proportion of each grain size class was estimated as thickness-weighted arithmetic mean, as exposed in Section 6.2.5.1. As we can see in Fig. 81, most of the worst-case predictions in T in the graph are associated with aquifer portions having high proportions of silt and clay, between 20% and 40% on average.

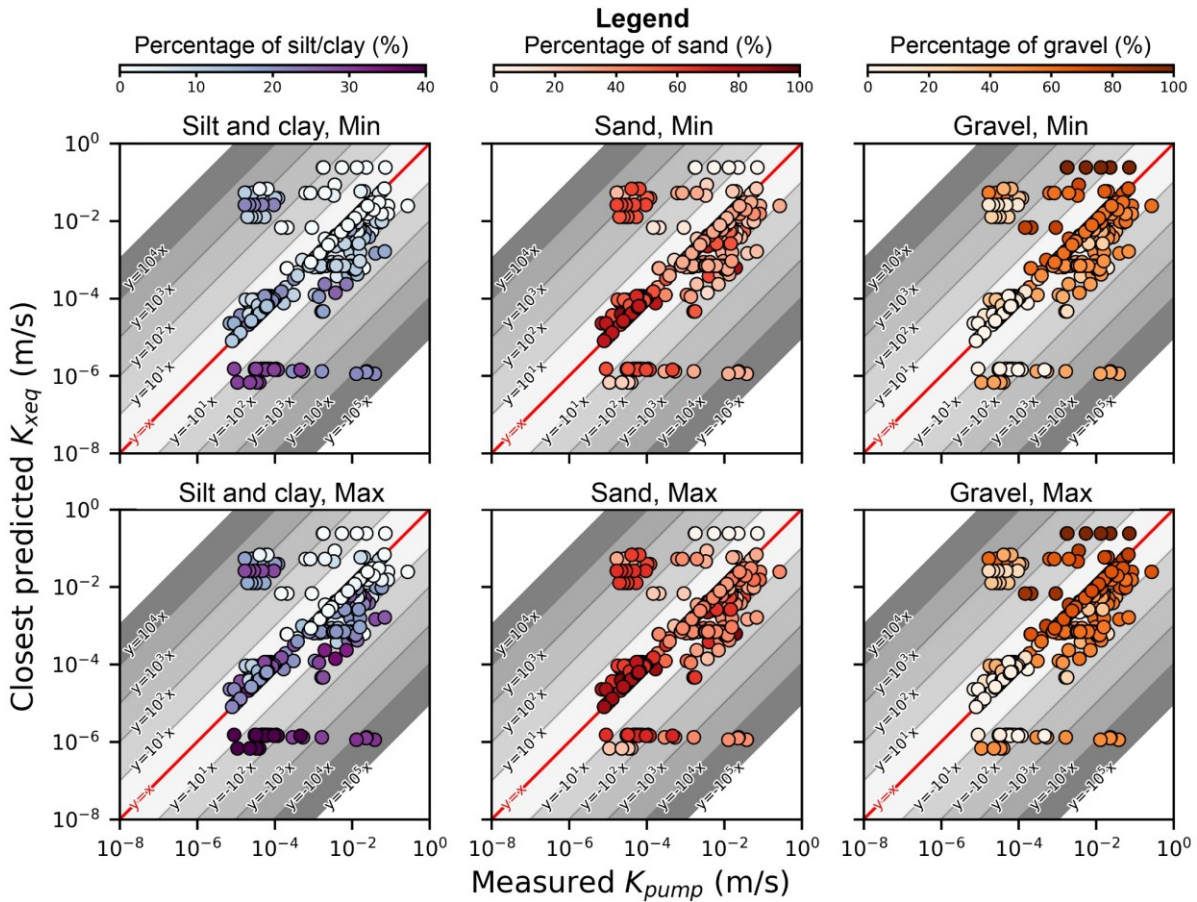


Fig. 81: Prediction performance in the immediate vicinity of the well screens in the city of Munich: Relationship between predicted K_{xeq} and measured K_{pump} versus the proportion of each grain size class in the screened aquifer portion

Appendix E: Supporting information to Chapter 7

Appendix E-1: Supporting Figures and Tables

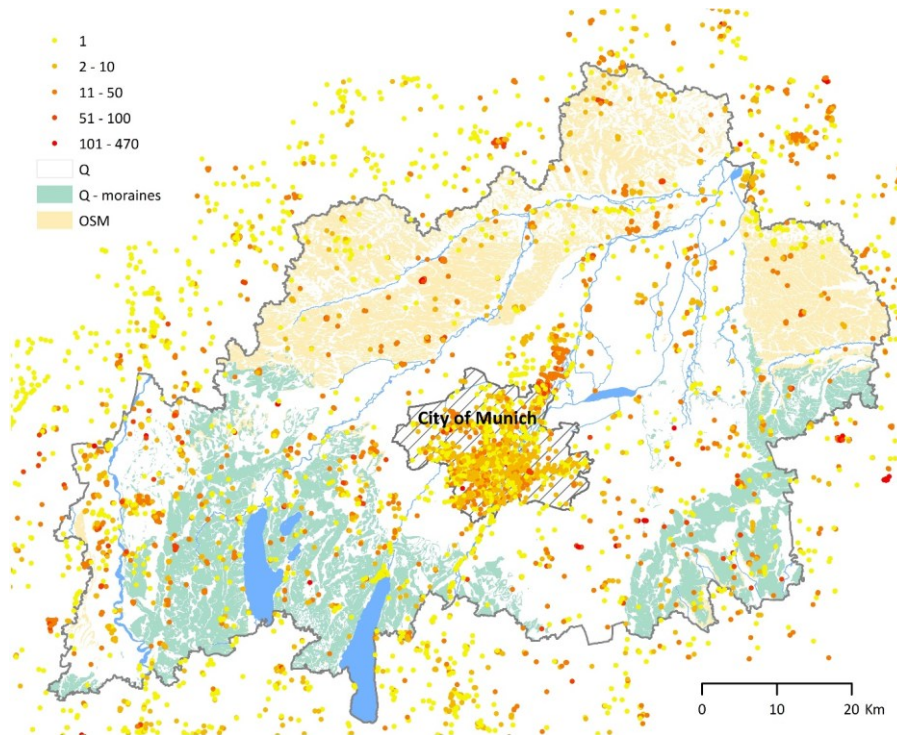


Fig. 82: Location of all available data points. The colour scale indicates the number of single chemical analyses performed at a particular well or piezometer

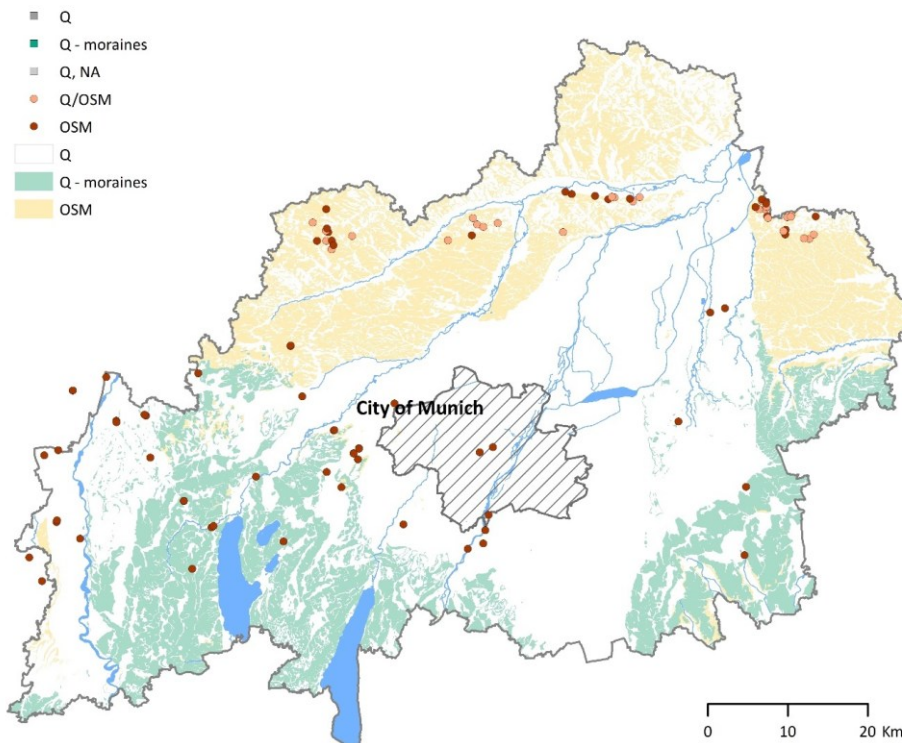


Fig. 83: Location of data points associated with samples taken during three sampling campaigns in 2017-2019

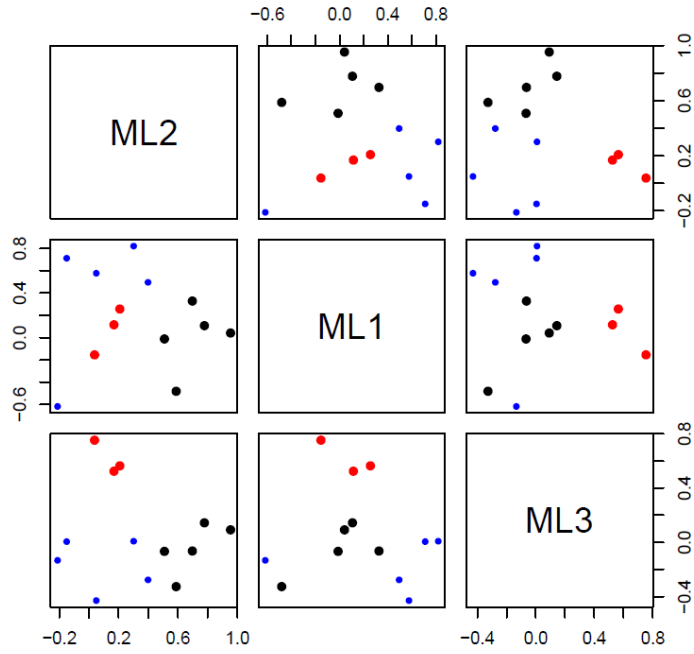


Fig. 84: Factor loadings obtained in EFA

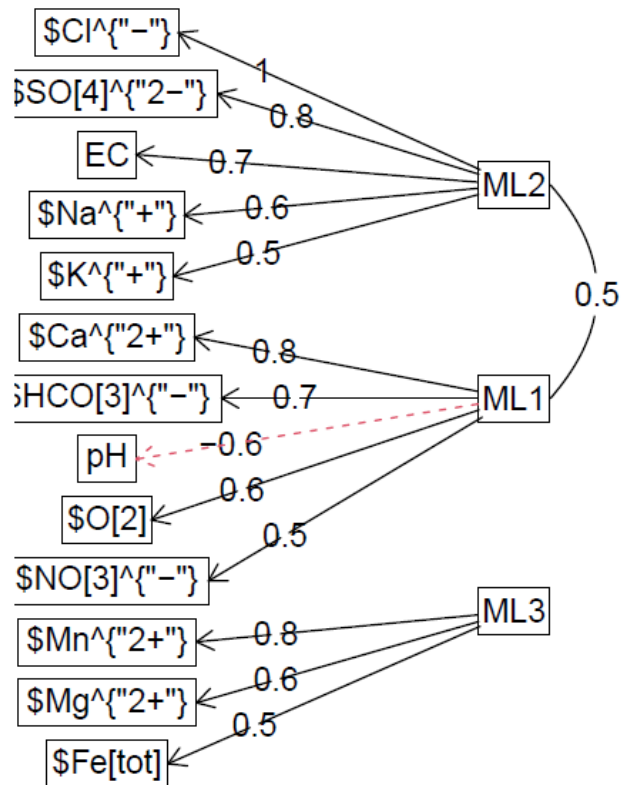


Fig. 85: Factor loadings for the exploratory factor analysis (EFA) with the maximum likelihood method and oblique (oblimin) rotation

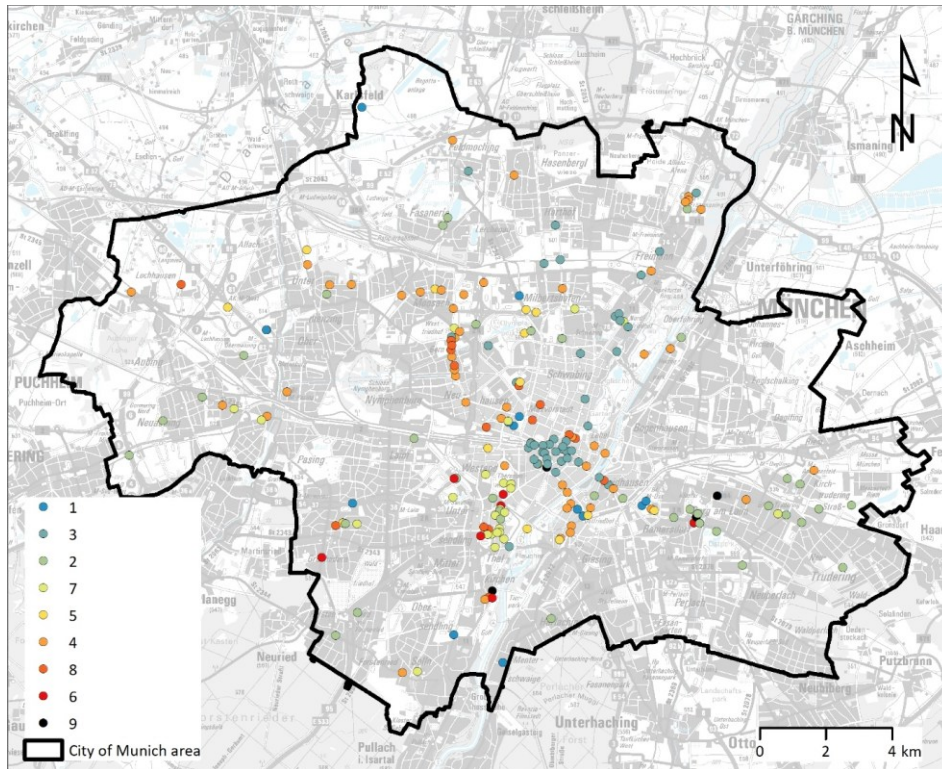


Fig. 86: The location of wells assigned to clusters in the City of Munich area. Numbers 1-8 indicate clusters, number 9 indicates outliers, excluded from HCA

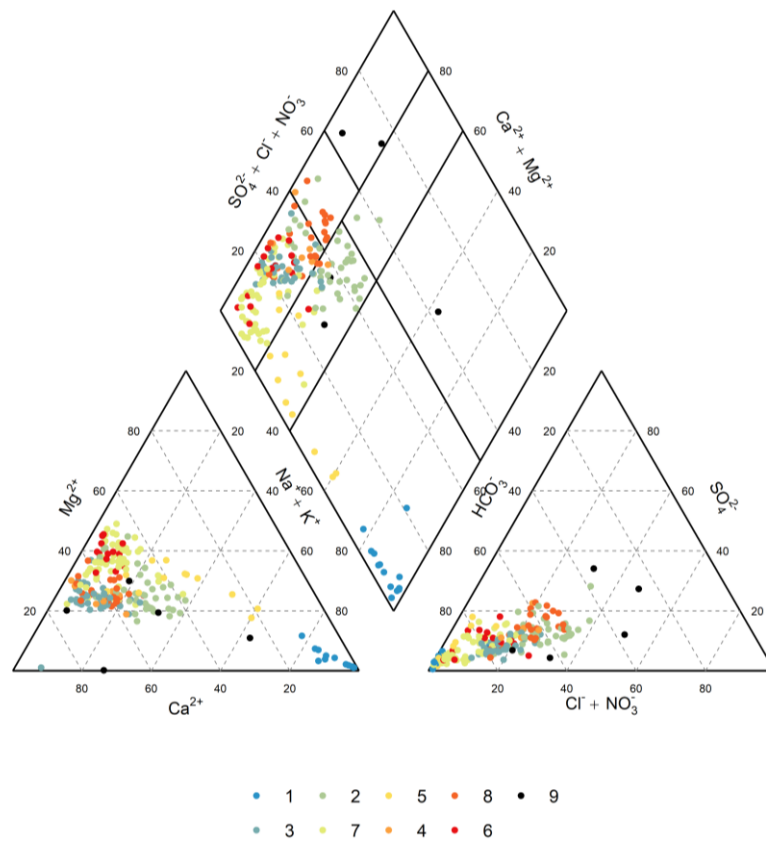


Fig. 87: Piper plot presenting clusters in the city area. Numbers 1-8 indicate clusters, number 9 indicates outliers, excluded from HCA

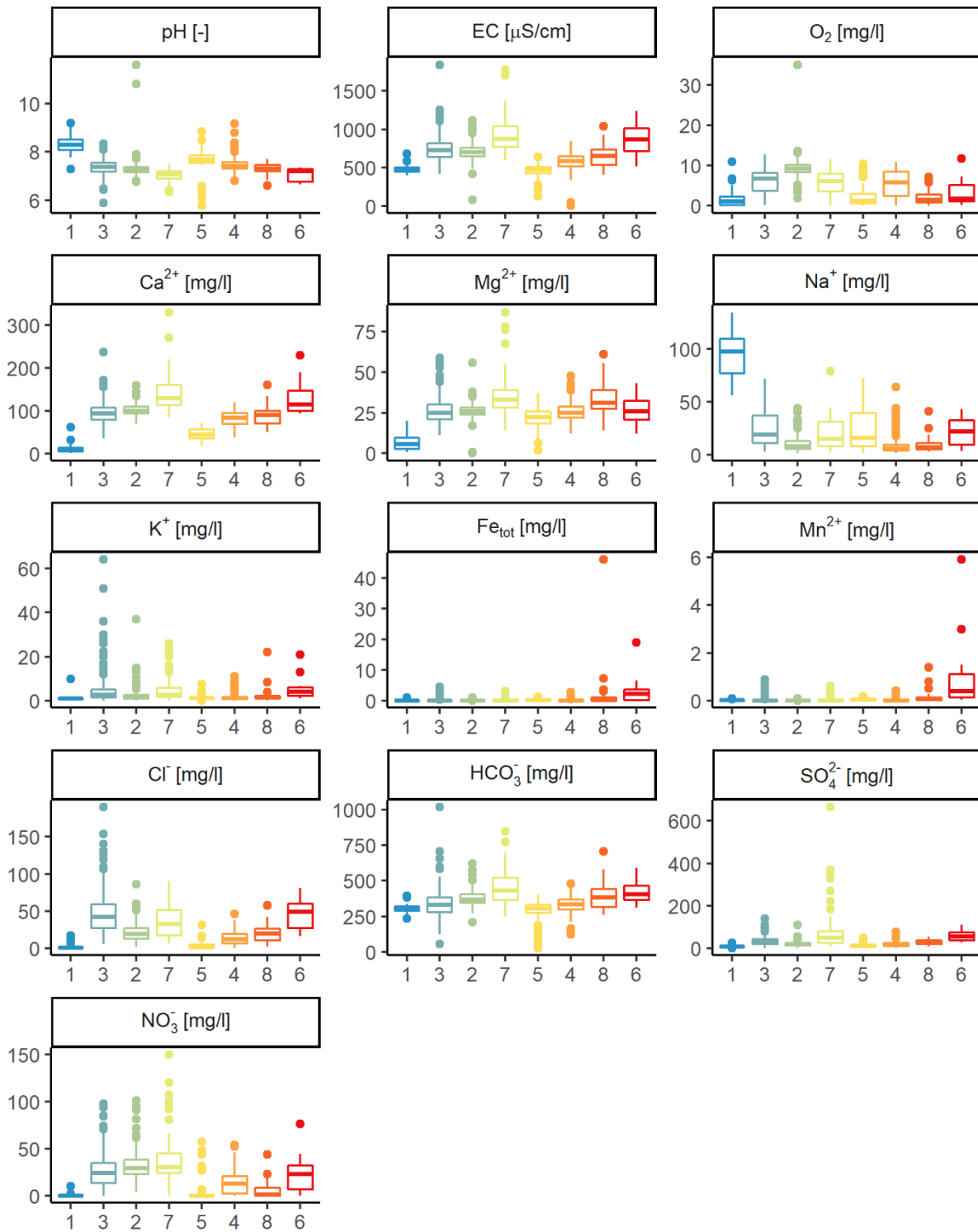


Fig. 88: Box plots for clusters associated with the whole study area

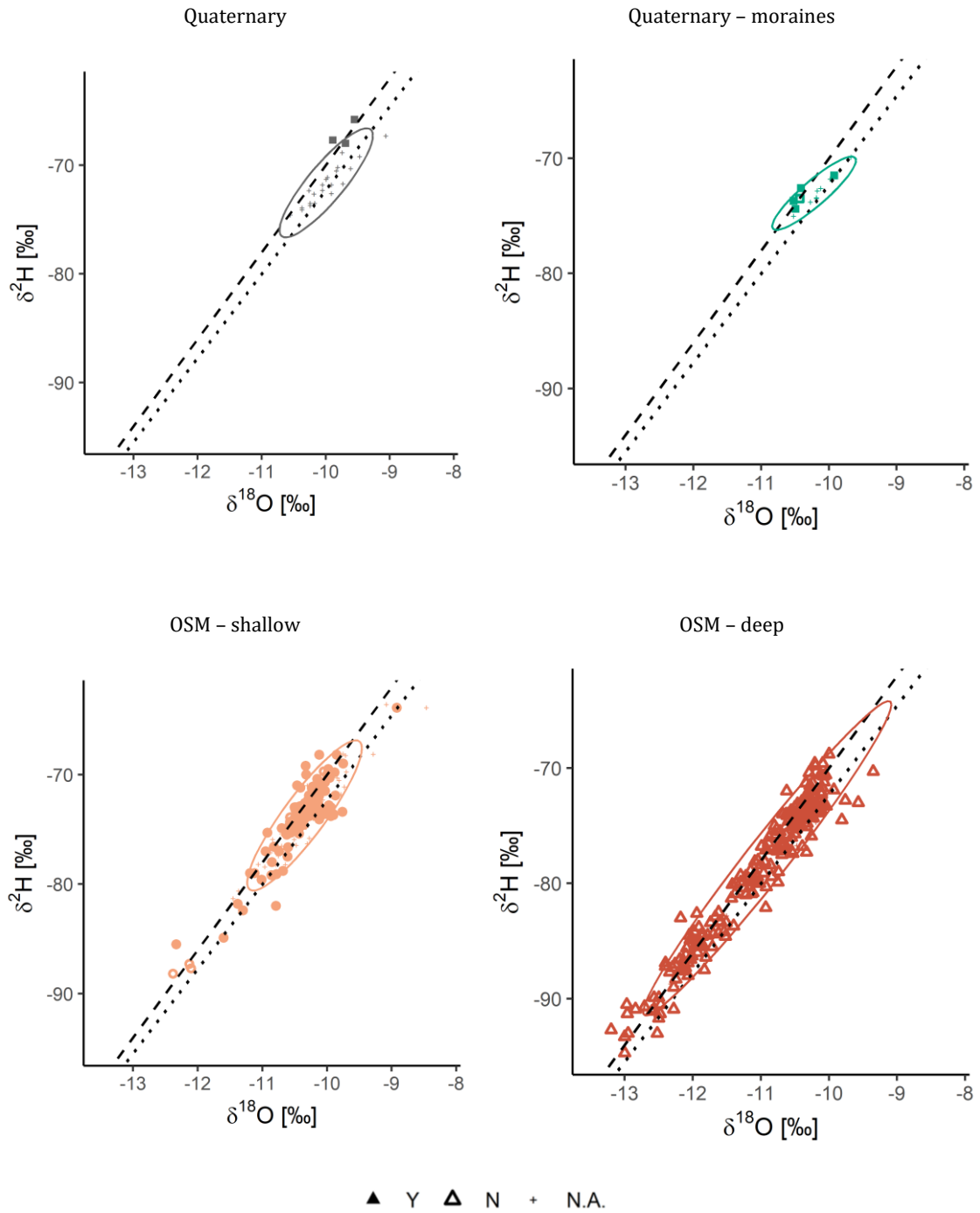


Fig. 89: $\delta^2\text{H}$ versus $\delta^{18}\text{O}$ for each hydrogeological unit. Tritium content is presented as follows: filled symbols (Y) – tritium is present in the water sample, empty symbol (N) – no tritium present, + (N.A.) – no tritium-data available. The colours indicate the hydrogeological unit (see Fig. 52a in the paper)

Tab. 11: Relationship between clusters and groundwater horizons from the 3D lithofacies model of the City of Munich

		C1	C3	C2	C7	C5	C4	C8	C6	Total
Q	Q			9	1		5			15
Q/T1	Q/OSM		2	4	1	1	3			11
T1	OSM-shallow	3	40	25	22	7	41	16	7	161
T1/T2		1	1			3	3			8
T2	OSM-deep	2				2	2			6
T3		1								1
T4		4								4
TX		2								2
Total			13	43	38	24	13	54	16	7

Appendix E-2: Descriptive statistics

1. Methods

Descriptive statistics were calculated for four predefined hydrogeological units. The statistics were minimum, maximum, median, quantiles (10%, 25%, 75%, 90%).

Additionally, censored box plots were prepared. Values of some water constituents (e.g. NO_3^- , SO_4^{2-} , minor elements) were below the detection limit, i.e. censored. Moreover, as already mentioned, the detection limits in the available historical data varied over time. Therefore, simple methods such as replacing censored data with the detection limit or $\frac{1}{2}$ of the detection limit couldn't be applied. For that reason, descriptive statistics were calculated using the NADA package in the statistic programme R (R Core Team, 2021) with "regression on order statistics" (ROS) (Helsel, 2012). ROS is a semi-parametric method used to estimate summary statistics and plot model distributions with censored data; it assumes that data can be fit to a known distribution by a least-squares regression on a probability plot (ITRC, 2013). For each observation a number and a logical value of a censoring indicator was assigned (TRUE for censored, FALSE for uncensored). In the resulting censored boxplots, the line indicating the limit of detection is drawn at the highest detection limit in the data set. Percentiles above this line are unaffected by censoring, while percentiles below this line are estimated, for example by ROS.

2. Results

The statistics were summarised in tables separately for each hydrogeological unit (Tab. 12). The censored boxplots allowed one to compare the values of parameters in each unit (Fig. 90). A Piper diagram graphically represents the hydrogeochemical facies of groundwater in the study area (Fig. 91). Stiff diagrams show the medians as well as quantiles (10%, 90%) of the main constituents of groundwater samples in particular hydrogeological units (Fig. 92).

Tab. 12: Table of descriptive statistics of selected parameters (23 out of 64) calculated for Quaternary groundwater samples

Parameter	Unit	No of samples	No < LOD	LOD	Minimum	10% - Quantile	25% - Quantile	Median	75% - Quantile	90% - Quantile	Maximum
Temperature	°C	590	0		4.7	8.5	9.2	10.1	11.4	13.3	24.1
pH		604	0		6.03	7.00	7.13	7.29	7.40	7.50	9.10
EC (25 °C)	µS/cm	457	0		83.7	560	617	703	781	943	1840
DO	mg/l	588	4	0.3	<LOD	2.7	5.5	8.3	9.7	10.5	15.5
DO-saturation	%	449	5		<LOD	20.6	49.5	75.2	88.0	96.9	137.1
F ⁻	mg/l	379	96	1	<LOD	<LOD	0.059	0.088	0.1	0.2	12
Cl ⁻	mg/l	612	3	5	<LOD	7.2	12	19	29	51	200
Br ⁻	mg/l	34	27	1	<LOD	<LOD	<LOD	<LOD	0.1	1	1
NO ₃ ⁻	mg/l	612	10	1	<LOD	8	15	23.2	33	50.1	192
NO ₂ ⁻	mg/l	441	388	0.16	<LOD	<LOD	<LOD	<LOD	<LOD	0.02	0.5
SO ₄ ²⁻	mg/l	606	2	0.1	<LOD	9.2	13	18	27	43	66.5
S ²⁻	mg/l	35	34	0.5	<LOD	<LOD	<LOD	<LOD	<LOD	<LOD	0.5
PO ₄ ³⁻	mg/l	82	60	0.02	<LOD	<LOD	<LOD	<LOD	0.044	0.1	0.88
orth.-PO ₄ ³⁻	mg/l	387	253	0.2	<LOD	<LOD	<LOD	0.008	0.03	0.08	0.84
HCO ₃ ⁻	mg/l	612	0		64.1	306.3	336.3	368.9	408.8	452.7	1150.2
NH ₄ ⁺	mg/l	549	353	0.26	<LOD	<LOD	<LOD	0.006	0.023	0.053	15
K ⁺	mg/l	606	30	1	<LOD	0.7	1	1.8	3.3	6	64
Na ⁺	mg/l	612	0		0.3	3.3	5	8.7	15	29.05	113
Ca ²⁺	mg/l	612	0		21	82	91	100	112	130	330
Mg ²⁺	mg/l	612	0		7.3	19	22.1	25	28	32	87
Fe _{tot}	mg/l	557	300	0.05	<LOD	<LOD	<LOD	0.00279	0.035	0.16	22
Mn ²⁺	mg/l	534	369	0.05	<LOD	<LOD	<LOD	<LOD	0.006	0.0523	1.6
Si	mg/l	123	0		0.43	2.3	2.8	3.2	3.8	5.4	18

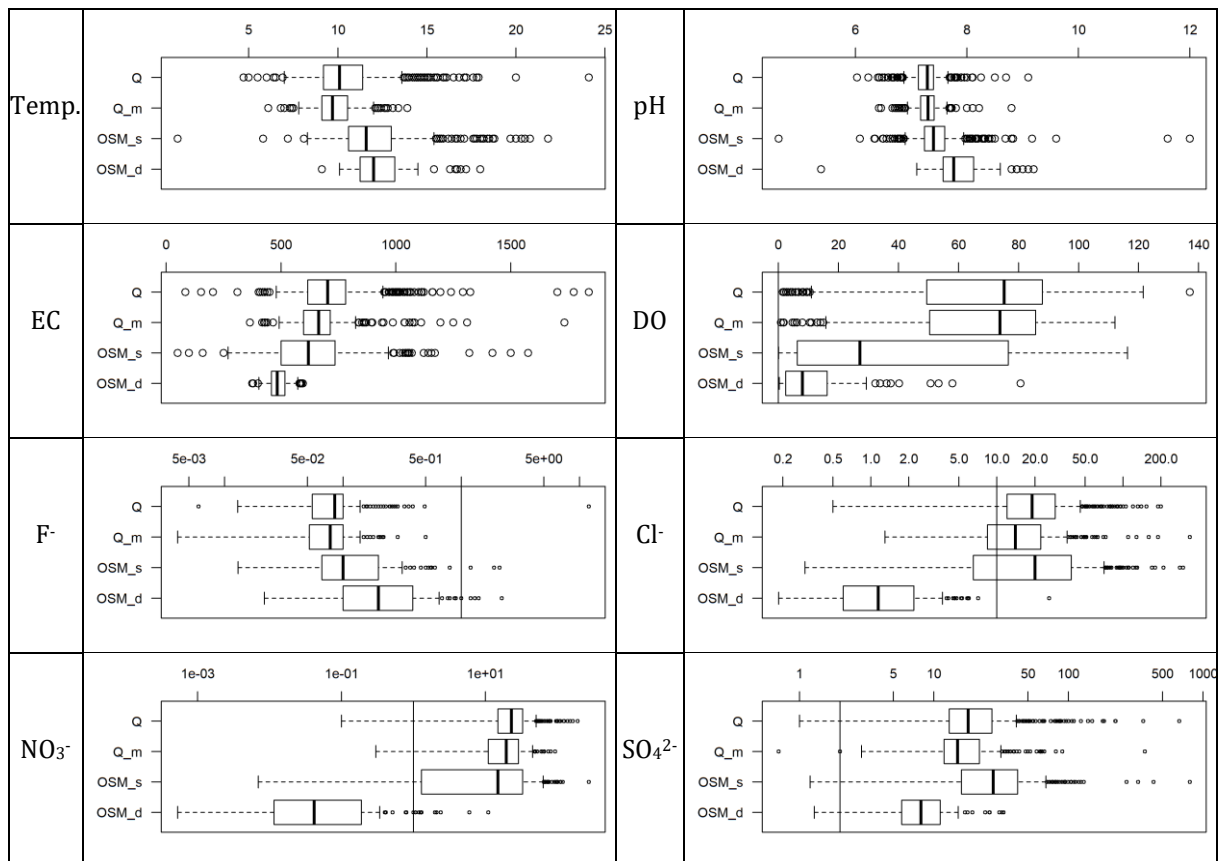


Fig. 90: Selected box plots

Anthropogenic impacts (mostly diffuse contamination sources i.e. use of fertilizers or road-salt in winter) are visible through elevated contents of nitrate, chloride, potassium, and sodium (Wagner et al., 2011, 2003). For example, German limit-values for drinking water of nitrate (> 50 mg/L)

were exceeded in 62 analysed samples for Quaternary waters, in 10 waters samples in moraines, and in 54 samples of shallow OSM aquifers. Previous studies conducted in the immediate vicinity of the study area have shown that elevated concentrations of nitrate are caused by releasing high amounts of manure and, to a lesser extent, synthetic fertilizers due to intensified agriculture (Wild et al., 2020, 2018).

Quaternary groundwater in the study area is typically represented by a Ca – HCO₃ water type with total mineralisation varying from 138 to 1890 mg/L (477-580-766 mg/L). The pH-values (7.0-7.3-7.5) classify these water samples as neutral or low alkaline. DO median (8.3 mg/L) was the highest among all the four units. The iron and manganese concentrations are mostly low. Among the trace elements, the following are present: with the median above 100 µg/L; B, Ba – above 10 µg/L, Cs, Hg, Li, U, Zn – above 1 µg/L. The presence of uranium above 1 µg/L in more than 50 % of samples is noteworthy, not only in Quaternary deposits, but also in moraines and shallow OSM. As concluded by Banning et al. (2013), uranium primarily originates from lignitic inclusions in OSM sediment, was transported to and accumulated in lowland moor peats, and nowadays gets mobilised e.g. by agricultural fertiliser (nitrate) application.

The hydrogeochemical signatures of groundwater samples from the Quaternary moraine deposits are similar to the waters occurring in alluvial Quaternary deposits and belong to alkali mostly carbonated water facies. Total mineralisation varies between 276 and 2268 mg/L (460-571-704 mg/L) and EC between 365 and 1733 µS/cm (540-663-825 µS/cm).

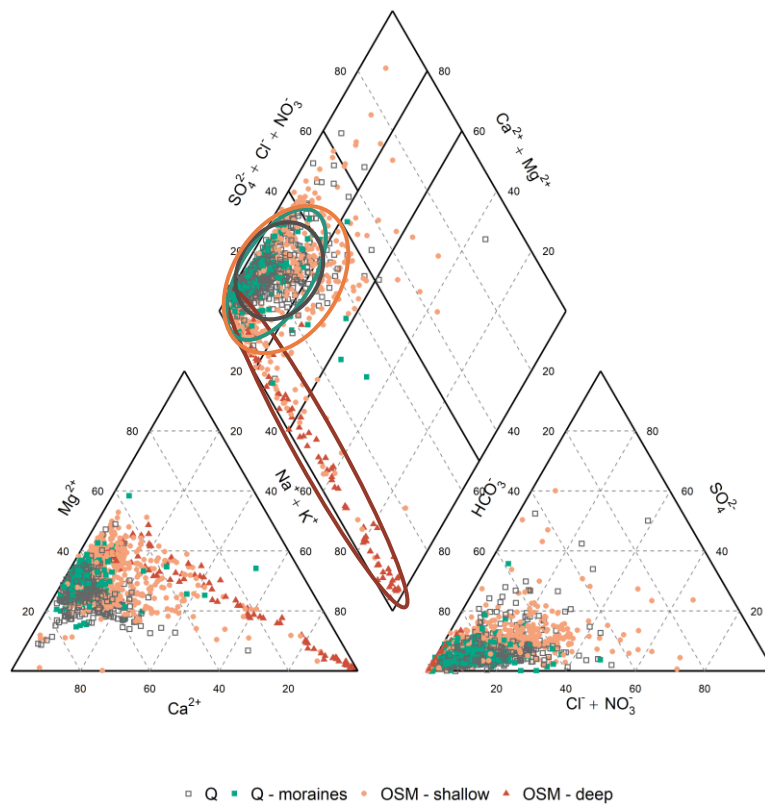


Fig. 91: Piper diagram of groundwater samples (the ellipses for each group are drawn approximately)

The main constituents of shallow OSM waters are calcium, magnesium and hydrogen carbonate. Some water samples represent the hydrogencarbonated-sulfatic water type. Total mineralization is 391-521-710mg/L. 80 % of pH-values range between 7.1 and 7.8 (7.4), which classifies the waters of the shallow as low alkaline. Relatively high concentrations of silica are observed, which may be related to the occurrence of feldspar in the OSM sediments (Wagner et al., 2003). Iron and manganese concentrations were higher in both OSM units in comparison with Quaternary horizons.

Groundwater samples from the level of deeper OSM show a broader typification, from Ca – HCO₃ to Na, K – HCO₃ waters. The pH-values are higher than samples from the “shallower” three units on average. DO is low (0.8 mg/L), similar to nitrate (<LOD), indicating reductive conditions. Also, chloride (1.1 mg/L), sulphate (8 mg/L), calcium (37 mg/L), and magnesium (20 mg/L) were lower than in other units. Sodium concentrations are the highest in this unit, the same as ortho phosphate and fluoride. According to lower content of major ions, total mineralisation and EC are lower. However, some trace elements (B, Ba, Li, Mo, Sr, Ti) show higher concentrations in these deeper-level samples than in shallower-OSM samples or in the Quaternary. The opposite case is observed for Hg (<LOD), though. Also, uranium concentrations were the lowest among the four hydrogeological units (1.3 µg/L).

It is worth mentioning that some (47 out of 108) of the deep OSM samples show specialized hydrogeochemical signatures, characterized by little total mineralization (<500 mg/L), low EC, higher pH, and lower hardness. Besides other trace elements, also selenium and strontium reveal relatively high concentrations, which can be explained by the occurrence of weathered feldspars in the OSM sediments (Kainzmeier et al., 2007). In previous studies also from OSM, but located east from the study area (region 13-Landshut and 18-Südostbayern), the waters of low EC, low DO, high pH and specific chemistry were described as ion exchange waters (Chavez-Kus et al., 2016; Kainzmeier et al., 2007). The authors related these waters to uprising Malm waters and recalled that higher concentrations of tracer elements (B, Cz, Li, Rb, Th, Ta) present in some OSM wells are typical for Malm waters.

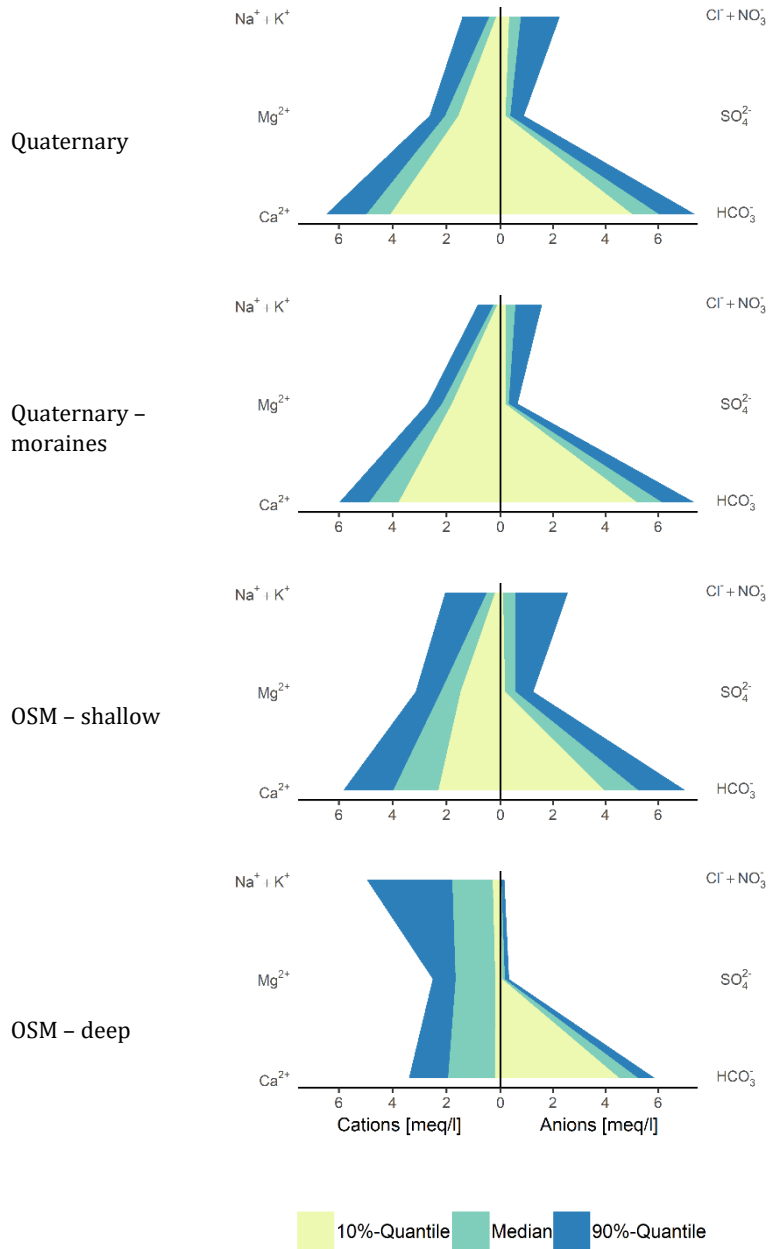


Fig. 92: Stiff diagrams

Appendix F: Supporting information to Chapter 8

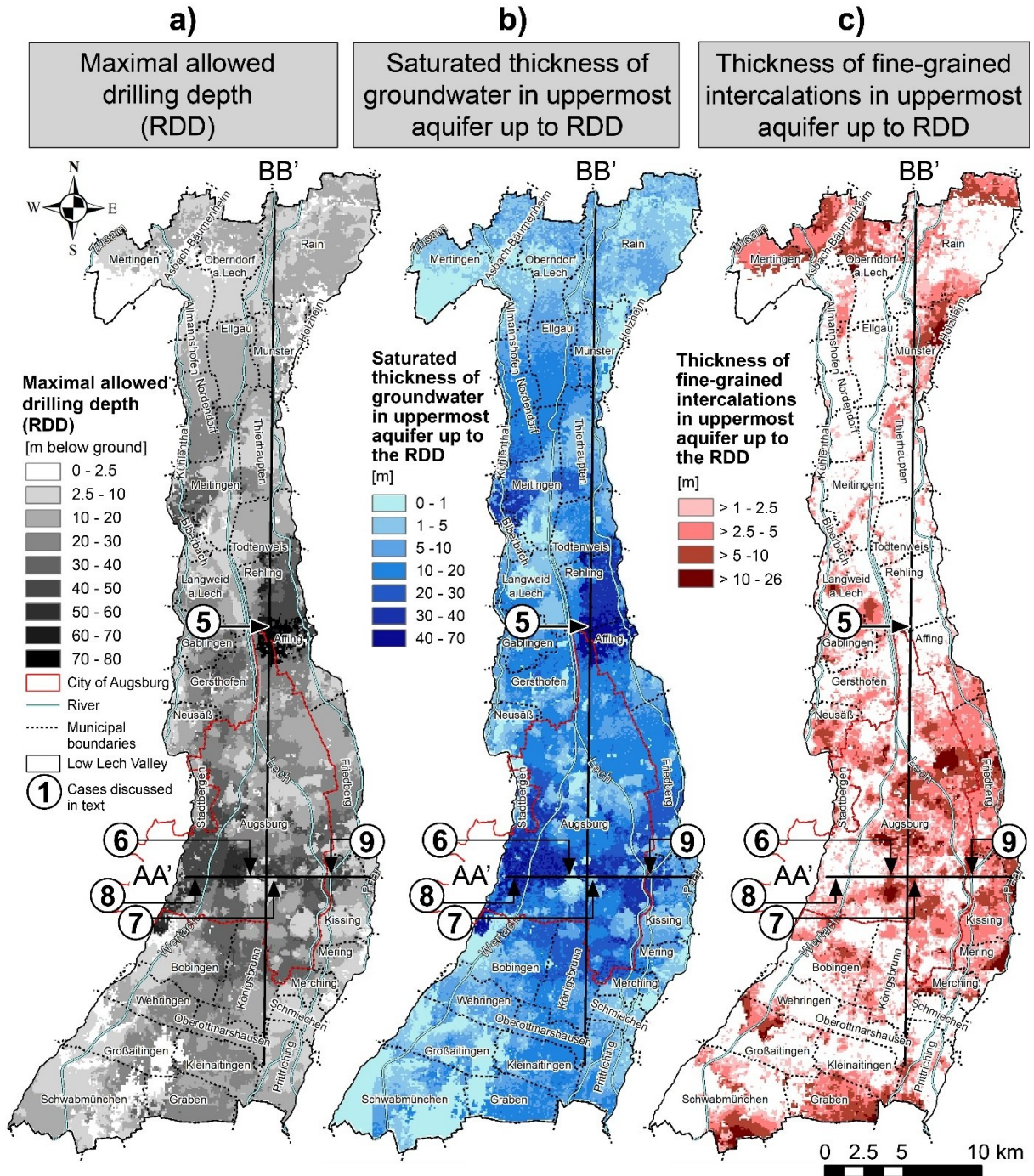


Fig. 93: Mapped results from the geological 3-D model in the Lower Lech Valley: **a)** Maximal allowed drilling depth (RDD); **b)** Saturated thickness of groundwater in uppermost aquifer up to the RDD; **c)** Thickness of fine-grained intercalations in uppermost aquifer up to RDD

Equivalent horizontal hydraulic conductivity in uppermost aquifer up to the RDD

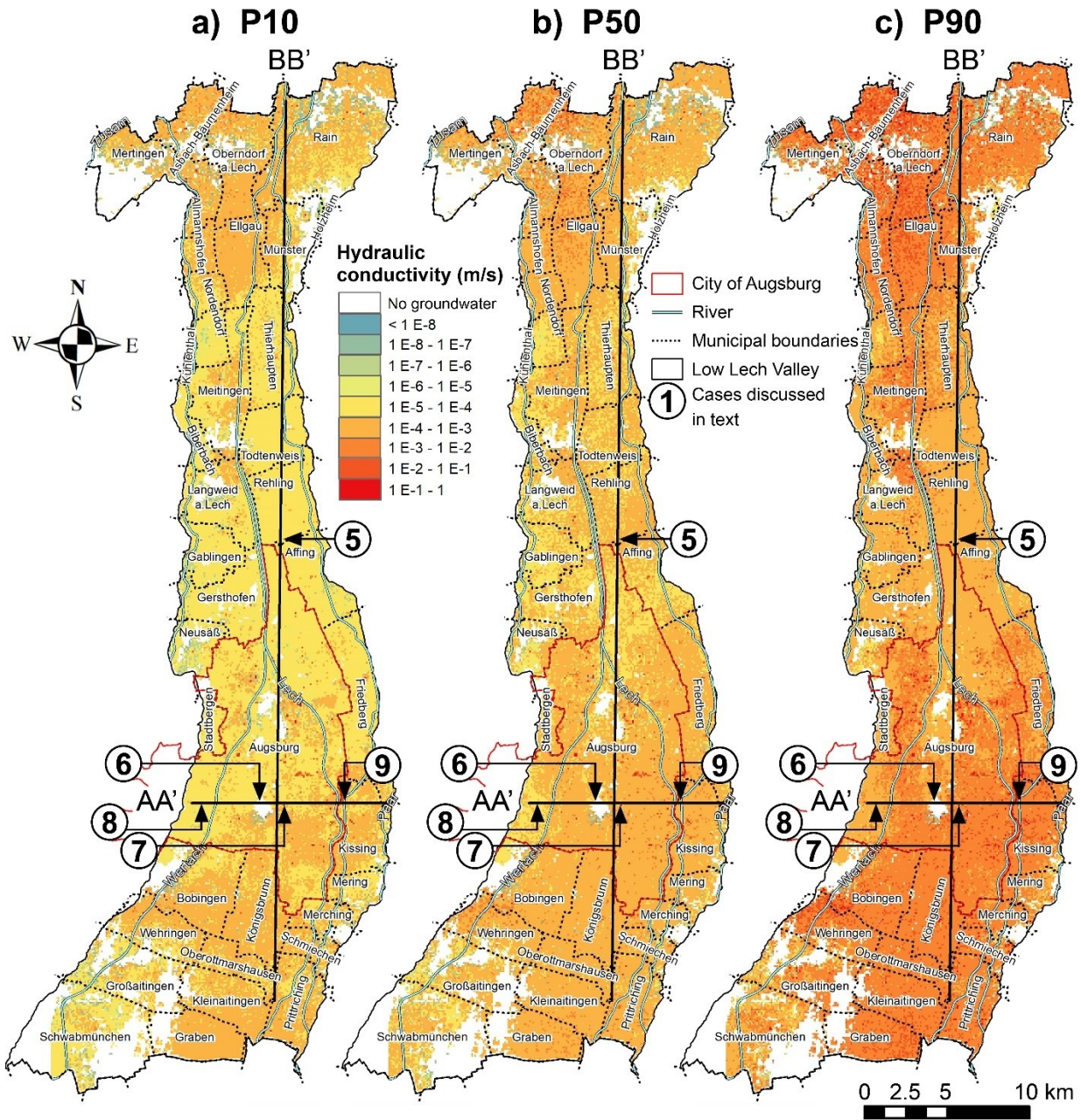


Fig. 94: Calculated equivalent horizontal hydraulic conductivity in uppermost aquifer up to the RDD from the geological 3-D model in the Lower Lech Valley: **a)** conservative estimate (P10, 10th percentile); **b)** average estimate (P50, 50th percentile); **c)** optimistic estimate (P90, 90th percentile)